António César Galvão Soares

Mestre em Engenharia Mecânica

Fatigue life assessment of exhaust systems for naval gas turbines

Dissertação para obtenção do Grau de Mestre em
Engenharia Mecânica

Orientador: Prof. Doutor Rui Fernando Martins, FCT/UNL, DEMI

Co-orientador: Eng. Rodrigues Mateus, Marinha Portuguesa, DN

Júri:

Presidente: Prof. Doutor João Mário Burguete Botelho Cardoso
Vogais: Eng. Celso Jacinto Branco Moreira Guerreiro
Eng. António Fernando dos Santos Rodrigues Mateus
Prof. Doutor Rui Fernando dos Santos Pereira Martins

FACULDADE DE
CIÊNCIAS E TECNOLOGIA
UNIVERSIDADE NOVA DE LISBOA

Setembro de 2011

Copyright

Resumo

Os ciclos de aquecimento e arrefecimento (choque térmico), conjugados com os esforços mecânicos a que condutas de evacuação de gases de escape são submetidas, levam à nucleação e propagação de defeitos junto ao pé do cordão de soldaduras de canto e topo a topo, resultando numa diminuição das vidas à fadiga das estruturas consideradas. A precipitação de carbonetos de crómio, nos limites de grão do material base e do material que compõe as ligações soldadas, também potenciam o efeito localizado de nucleação e propagação de fissuras devido à diminuição da resistência à corrosão do material de fabrico das condutas (corrosão por picada). Para além do referido, os defeitos de soldadura introduzidos durante o fabrico e o acabamento superficial de tipo laminado das chapas que formam a conduta resultam numa diminuição do valor da tensão limite de fadiga do material e, consequentemente, da vida à fadiga das estruturas.

A presente tese apresenta o estudo do comportamento térmico e mecânico, de duas condutas de evacuação de gases de escape com geometrias diferentes, através da análise pelo método dos elementos finitos.

Foram efectuadas e analisadas modificações na geometria actual de cada conduta de evacuação de gases de escape, de modo a se obter uma redução nas tensões a que as mesmas estão sujeitas e assim aumentar as suas vidas à fadiga. Estas modificações consistiram na alteração das espessuras das chapas que constituem as condutas, na adição de reforços especificamente localizados, assim como na alteração do material de fabrico das condutas.

A possibilidade de aplicação de três materiais foi estudada, nomeadamente o aço inoxidável austenítico AISI 316L (material de que são fabricadas as condutas), o aço inoxidável austenítico Crómio-Manganês e o aço inoxidável ferrítico 445M2, uma vez que este último possui propriedades térmicas (condutividade e coeficiente de expansão linear) mais vantajosas do que as apresentadas pelos aços inoxidáveis austeníticos.

Foi feita uma previsão de vida à fadiga de diferentes detalhes estruturais presentes nas estruturas estudadas, assim como uma previsão de vida à fadiga das secções críticas, onde foi considerada a existência de fissuras devidas à montagem e soldadura das chapas das condutas de evacuação de gases de escape em estudo.

No que concerne à redução do nível de tensões, os melhores resultados foram obtidos nas modificações que consistiram na alteração do tipo de material das condutas de evacuação de gases de escape, bem como nas modificações onde se tentou obter uma uniformização das espessuras das chapas destas mesmas condutas. Estes resultados levaram à confirmação de que as fissuras foram principalmente criadas pelos choques térmicos a que as condutas são submetidas. Foi igualmente verificado que o comportamento térmico e mecânico varia bastante em função da geometria da conduta em estudo.

Palavras-Chave:

Condutas de evacuação de gases de escape

Método dos Elementos Finitos (FEM)

Previsão de vida à fadiga a alta temperatura

Aços inoxidáveis austeníticos (AISI 316L e Cr-Mn)

Aço inoxidável ferrítico 445M2

Choque térmico

Abstract

Cracks have nucleated and propagated from the weld toe of some fillet and butt welded joints in the exhaust systems of naval gas turbines, resulting in a reduction of the fatigue life. These cracks were originated by thermal shock along with mechanical stresses to which exhaust systems of naval gas turbines are submitted to and also by the decrease of the pitting corrosion resistance due to the precipitation of chromium carbides in the grain boundaries of the base material of the welded joints. Furthermore, welding and surface finish defects, introduced during the fabrication of the exhaust systems, also result in a decrease of the fatigue strength of the material and, consequently, of the fatigue life of the structures.

This thesis presents the mechanical and thermal behaviour studies of two different exhaust systems which were carried out using the finite element method (FEM).

Modifications to the current geometry of these exhaust systems were also performed and then analysed in order to diminish the stresses and thus, increase the fatigue life of the exhaust systems. These modifications consisted in the change of the plates' thicknesses, addition of reinforcements and even changes in the type of material which the exhaust systems are made of.

Three different materials were studied namely: the AISI 316L austenitic stainless steel (the current material used in the exhaust systems), the Chromium-Manganese austenitic stainless steel, that has the better mechanical properties and the 445M2 ferritic marine type grade stainless steel, that has better thermal properties than the austenitic stainless steels.

Fatigue life assessments were done in different critical structural details where the existence of initial surface cracks was considered.

The uniformization of the plates' thicknesses and the use of a marine ferritic stainless steel type resulted in lower stresses applied on the critical locations of the exhaust systems. Also, it was verified different thermal and mechanical behaviour depending on the different exhaust system geometry analysed.

Keywords:

Exhaust system

Finite Element Method (FEM)

High temperature fatigue life assessment

Austenitic stainless steels (AISI 316L & Cr-Mn)

445M2 ferritic stainless steel

Thermal shock

Acknowledgements

I would like to express my deep gratitude to my supervisor, Professor Doctor Rui Fernando Martins, for providing me the opportunity to carry out such a good project and for all the support, knowledge and time granted.

I also wish to express my gratitude to my Co-orientator, MSc. Rodrigues Mateus, for all the support and information shared which was a great help to the accomplishment of this project.

My sincere appreciation to MSc. Cunha Gomes and Mr. Marques Brida, for the guided tour to one of the exhaust systems in study, as well as for the information shared on the existing problems in both exhaust systems.

I dedicate this work to my parents, Carlos and Maria Soares, and to my sister, Sara, to whom I express my deep gratitude for all the support, friendship and education given to me.

To my dear Joana, a special thanks for all the support, friendship and dedication given to me.

The author also expresses his deep appreciation towards MSc. Daniel Martins, Luís Alberty, Luís Santos, João Gandra, future MSc. Paulo Ferreira and many other colleagues, for the strong friendship and support given in the past years.

Contents

Table Index

Figure Index

List of abbreviations, acronyms and symbols

AISI – American Iron and Steel Institute
APDL – Ansys Parametric Design Language
CAD – Computer Aided Design
CFD – Computational Fluid Dynamics
EFS – Elastic Foundation Stiffness
EPFM – Elastic Plastic Fracture Mechanics
FAT – Fatigue class
FEA – Finite Element Analysis
FEM – Finite Element Method
HCF – High Cycle Fatigue
LCF – Low Cycle Fatigue
LEFM - Linear Elastic Fracture Mechanics
PREN – Pitting Resistance Equivalent Number
NDT – Non Destructive Test
NP – No crack Propagation

a – crack depth
a_f –final crack depth
a_i – intial crack depth
A – area
c – half the length of a surface crack
c' – fatigue ductility exponent
C – material contant of the S-N curve power law
C_0 – constant of the Paris law
F – force
f_w – finite width correction factor
G – gravitational aceleration
k – elastic constant
K_{IC} – fracture toughness value obtained under plain stress state
$K_{I\,max.}$ – maximum stress intensity factor
k_m – stress concentration factor
l - toe distance
m – slope of fatigue strength curves
M_k - local geometry correction factor
N – number of cycles
P – relative pressure
$r_{o\sigma}$ - size of the plastic region at the crack tip

q_m – mass flow rate

R – stress ratio

t – plate thickness

T – temperature

V – velocity of gas flow

x – axial displacement

$f(R)$ – fatigue strength reducing/enhancement factor

ΔK – cyclic stress intensity factor range

ΔK_I – mode I stress intensity factor

ΔK_{th} – fatigue threshold

ρ – density

σ – nominal stress

σ_1 – first principal stress

σ_y – yield stregth

$\Delta\sigma$ – nominal stress range applied perpendicular to the direction of crack propagation

$\frac{\Delta\varepsilon_p}{2}$ – plastic strain amplitude

$\varepsilon_f^{'}$ - fatigue ductility coefficient

$2N$ – number of strain reversals to failure

1. Introduction

Heating and cooling cycles (thermal shock) along with mechanical stresses, to which exhaust systems of naval gas turbines are submitted, lead to nucleation and propagation of cracks on fillet and butt welded joints of some exhaust systems, resulting in a reduction of its fatigue lives [1-3]. The decrease of the pitting corrosion resistance, due to the precipitation of chromium carbides in the grain boundaries of the base material of the welded joints, as well as welding and surface finish defects, introduced during the fabrication of the exhaust systems, result in a decrease of the fatigue strength of the material and, consequently, the fatigue life of the structures. In order to avoid the malfunction of the structures, periodic inspections are made on critical areas of the exhaust system [2].

One of the purposes of this thesis is to simulate and compare the structural and thermal behaviour of two different exhaust systems through the use of a finite element analysis (FEA) software, *Ansys*®. Furthermore, redesigned exhaust systems were studied and the mechanical properties of three different materials were compared, namely: the AISI 316L austenitic stainless steel, which is the material used in the fabrication of the exhaust systems currently used in service [4], the Chromium-Manganese austenitic stainless steel and the 445M2 ferritic stainless steel.

Thermal failures can occur due to the existence of large differences between the plates' thicknesses of the exhaust systems' pipes and the surrounding reinforcements and supports of such exhaust systems. This fact leads to different levels of expansion and contraction of the plates, due to different thermal inertia of the structural elements involved in. Moreover, thermal fatigue crack propagation near the welded joints will be expected due to the high stress concentration values presented. Also, the existence of defects introduced during the fabrication stage and the oxides and chromium carbide precipitation potentiates the effect of nucleation and propagation of these cracks [1, 5].

In order to improve the fatigue life of the exhaust systems, design modifications were studied and compared in order to choose the modifications that reduce the stresses and enhance the fatigue life of critical areas of the exhaust systems under study.

The introduction of different materials namely, one austenitic stainless steel and one ferritic stainless steel, will also be assessed. While the new austenitic stainless steel has different mechanical properties and similar physical and thermal properties as the AISI 316L austenitic stainless steel, the ferritic stainless steel has thermal properties more beneficial than the austenitic stainless steels, due to higher thermal conductivity and lower thermal expansion coefficient. This would result in lower expansion and contraction of the plates, therefore reducing the thermal stresses induced in the welded details and improving the fatigue life of those critical areas of the exhaust systems.

Chapter 2 includes a description and a discussion of the physical and mechanical properties of the three materials studied. Also, some axial tensile tests and fatigue tests at 500 ºC were performed to transverse butt welded specimens, manufactured from Chromium-Manganese austenitic stainless steel.

Chapter 3 shows the exhaust systems modelled using the computer aided design (CAD) software, *Solidworks*® and its dimensions.

Chapter 4 describes the program that was created to analyse the mechanical and thermal behaviour of the exhaust systems. This program was done using the Ansys Parametric Design Language (APDL) and includes all the in-service conditions of the exhaust systems under study.

Chapter 5 presents each design modification made to the exhaust systems.

Chapter 6 shows the structural details chosen to assess the fatigue life and describes the calculations made to determine the fatigue life of each assessed detail. Besides, a fatigue life assessment was performed considering the existence of initial cracks in the material of the exhaust systems.

Chapter 7 reports all the first principal nodal stress and fatigue life results obtained for each design modification made to the exhaust systems.

Conclusions and future work proposals are presented in chapter 8.

2. Materials

2.1 AISI 316L Austenitic Stainless Steel grade type:

The material currently used in the construction of the exhaust systems is the AISI 316L austenitic stainless steel grade type. At room temperature, it has a yield strength of 290 MPa and an ultimate strength of 560 MPa [6]. These values are in accordance with the experimental data obtained (Fig. 2.1).

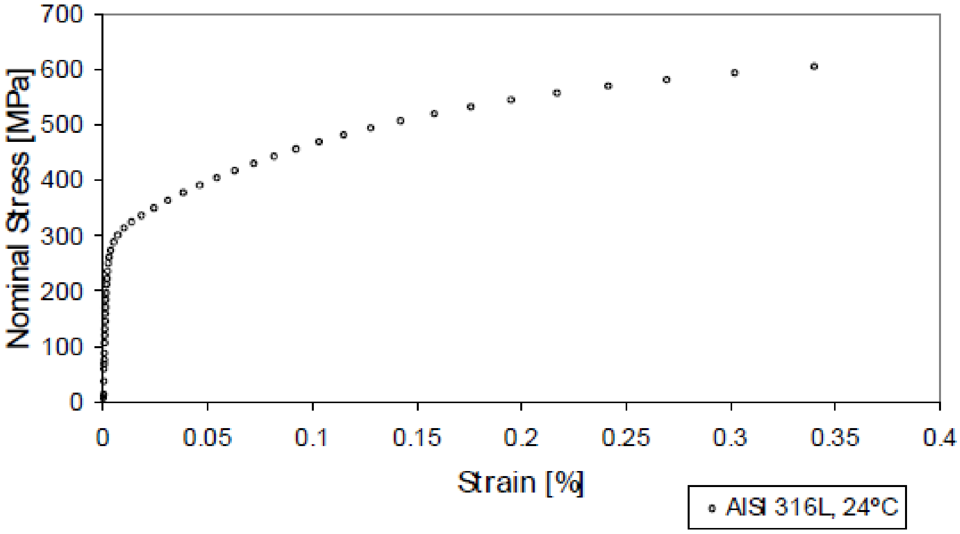

Figure 2.1: Nominal stress versus strain curve of the AISI 316L austenitic stainless steel. Axial tensile test performed at room temperature: 24 ºC.

A yield strength of 233 MPa and a ultimate strength of 484 MPa were obtained for the AISI 316L austenitic stainless steel at 350 ºC [5]. It was also obtained, from other studies, a yield strength of 210 MPa and a ultimate strength of 410 MPa for the AISI 316L austenitic stainless steel at 500 ºC [7].

The AISI 316L austenitic stainless steel has a high percentage of Chromium and Molybdenum elements (Table 2.1) which gives it a high corrosion resistance.

Table 2.1: Chemical composition of the AISI 316L austenitic stainless steel [8].

Chemical composition of the AISI 316L austenitic stainless steel										
C	Si	Mn	P	S	Cr	Mo	Ni	Cu	V	N
0.05	0.37	1.30	0.03	0.004	17.34	2.23	11.11	0.22	0.07	0.08

Considering that the exhaust systems work in a highly corrosive environment, a high pitting corrosion resistance is necessary. The pitting corrosion resistance is evaluated by the percentages of Chromium, Molybdenum and Nitrogen presented in the chemical composition of the materials in study and it can be calculated by the pitting resistance equivalent number (PREN-eq. 2.1) [8]:

$$PREN = \%Cr + 3.3 \times \%Mo + 16 \times \%N \tag{2.1}$$

Using this equation (eq. 2.1) and the chemical composition of the AISI 316L austenitic stainless steel (Table 2.1), the pitting resistance equivalent number was obtained (Table 2.2).

Table 2.2: Pitting resistance equivalent number of the AISI 316L austenitic stainless steel

	PREN (eq. 2.1)
AISI 316L austenitic stainless steel	17.34+3.3×2.23+16×0.08=25.98

Due to the high percentages of Chromium and Molybdenum present in its chemical composition and a pitting resistance equivalent number of nearly 26, the AISI 316L austenitic stainless steel is considered to have a very good corrosion resistance.

Table 2.3 shows some physical properties of the AISI 316L austenitic stainless steel [9].

Table 2.3: Physical properties of the AISI 316L austenitic stainless steel [9].

Density (Kg/m^3)	**Young´s Modulus (GPa)**
8000	193

Once the vessels' exhaust systems reach temperatures up to 500 ºC [2], the thermal properties of the material are very important to determine how the exhaust system will conduct heat and expand due to temperature distribution. Table 2.4 shows thermal conductivity and thermal expansion coefficients for some given temperatures [8].

Table 2.4: Thermal properties of the AISI 316L austenitic stainless steel [8].

Thermal conductivity (W/mm.K)		**Thermal expansion coefficient (K^{-1})**		
373 K	**773 K**	**373 K**	**588 K**	**811 K**
16.2×10^{-3}	21.5×10^{-3}	15.9×10^{-6}	16.2×10^{-6}	17.5×10^{-6}

When austenitic stainless steels are submitted to the temperature range of 427 ºC - 870 °C during a certain time range, they may become susceptible to intergranular corrosion by the precipitation of chromium carbides in the grain boundaries [8, 10]. The formation of these carbides implies the depletion of chromium from the inside of the grain's areas which would otherwise be available to form the protective chromium oxide. So, when welding austenitic stainless steels, in order to minimize the carbide precipitation, some stabilizing alloy elements, such as titanium (Ti) or niobium (Nb), should be added, and/or the content of carbon (C) should be ensured to be less than 0.03% [10].

Reducing the time during which the temperature of the austenitic stainless steels remains in the range of 427 ºC - 870°C will contribute to minimize the chromium carbide precipitation. Finally the application of an annealing heat-treatment would result in a complete solubilization of the carbides and is needed when maximum corrosion resistance is required [10].

2.2 Chromium-Manganese Austenitic Stainless Steel (Cr-Mn):

The Chromium-Manganese stainless steel is also an austenitic steel like the AISI 316L stainless steel, but has an higher mechanical resistance due to its higher percentage of Manganese and Nitrogen.

Since it is a recently developed steel, information about its mechanical properties is still scarce. From tests performed to the material at room temperature, it was determined a yield strength of 430 MPa and an ultimate strength of 800 MPa (Fig. 2.2) [8].

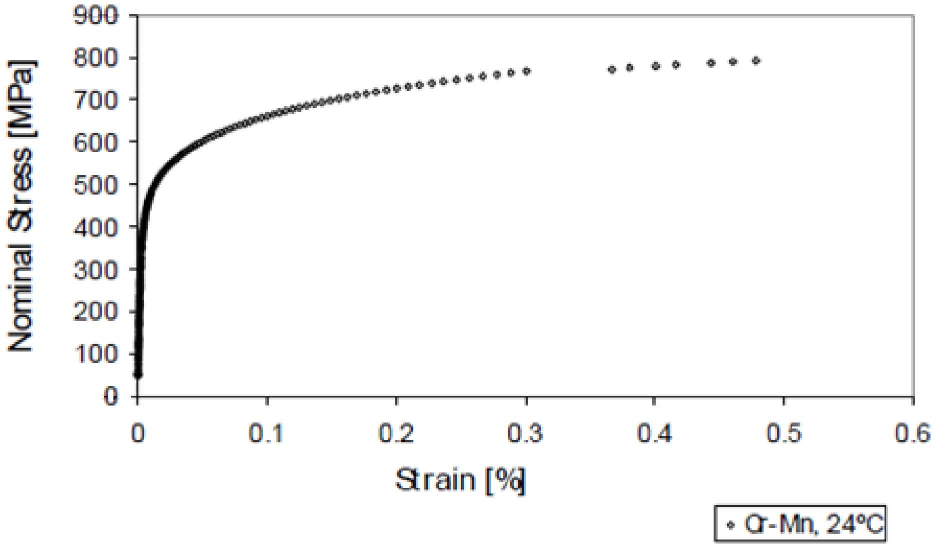

Figure 2.2: Nominal stress versus strain curve of the Chromium-Manganese austenitic stainless steel. Axial tensile test performed at room temperature: 24 ºC [8].

Comparing Stress-Strain curves (Figures 2.1 and 2.2) of both austenitic stainless steels obtained at room temperature, the Chromium-Manganese austenitic stainless steel has a higher yield strength than the AISI 316L austenitic stainless steel (+48%). In terms of ultimate strength, the Chromium-Manganese austenitic stainless steel has a higher value (+42%) than the AISI 316L austenitic stainless steel.

A yield strength of 270 MPa and a ultimate strength of 510 MPa were obtained for the Cr-Mn stainless steel at 350 ºC [7]. At this temperature (350 ºC), the Chromium-Manganese austenitic stainless steel has a higher yield strength than the AISI 316L austenitic stainless steel (+16%). In terms of ultimate strength, the Chromium-Manganese austenitic stainless steel has a higher value (+5%) than the AISI 316L austenitic stainless steel.

The chemical composition of the austenitic Chromium-Manganese is presented in table 2.5 [8]. Comparing the chemical compositions of the Chromium-Manganese stainless steel and the AISI 316L stainless steel, the percentage of Manganese and Nitrogen is higher in the former, which gives it higher mechanical resistance. On the other side, the Nickel content is lower in the Chromium-Manganese stainless steel, being the reason to be a cheaper steel, once Nickel is an expensive chemical compound.

Table 2.5: Chemical composition of the Chromium-Manganese austenitic stainless steel [8]

Chemical composition of the Chromium-Manganese austenitic stainless steel										
C	Si	Mn	P	S	Cr	Mo	Ni	Cu	V	N
0.05	0.34	6.54	0.02	0.001	18.31	0.10	4.40	0.16	0.06	0.18

Using equation 2.1 and the chemical composition of the austenitic Chromium-Manganese stainless steel (Table 2.5), the pitting resistance equivalent number was obtained (Table 2.6).

Table 2.6: Pitting resistance equivalent number of the Chromium-Manganese austenitic stainless steel

	PREN (eq. 2.1)
Chromium-Manganese austenitic stainless steel (Cr-Mn)	18.31+3.3×0.10+16×0.18=21.52

Comparing the pitting resistance equivalent number of each austenitic stainless steels under study (Table 2.2 and Table 2.6), the Chromium-Manganese stainless steel has a lower value, which indicates that it is more susceptible to pitting corrosion.

The density and Young´s modulus of the austenitic stainless steels under study are the same. Table 2.7 shows these physical properties of the austenitic Chromium-Manganese stainless steel [8].

Table 2.7: Physical properties of the Chromium-Manganese austenitic stainless steel [8].

Density (Kg/m^3)	**Young´s Modulus (GPa)**
8000	193

The Chromium-Manganese austenitic stainless steel has the same thermal properties of the AISI 316L austenitic stainless steel. Table 2.8 shows the thermal conductivity and expansion coefficients for this steel [8].

Table 2.8: Thermal properties of the Chromium-Manganese austenitic stainless steel [8].

Thermal conductivity (W/mm.K)		**Thermal expansion coefficient (K^{-1})**		
373 K	**773 K**	**373 K**	**588 K**	**811 K**
16.2×10^{-3}	21.5×10^{-3}	15.9×10^{-6}	16.2×10^{-6}	17.5×10^{-6}

Like the AISI 316L austenitic stainless steel, the Chromium-Manganese austenitic stainless steel may become prone to intergranular corrosion by the precipitation of chromium carbides in grain boundaries if heated within the temperature range of 427 ºC - 870 °C or cooled slowly through that range [8, 10]. The solutions to minimize the carbide precipitation are the same as those presented in chapter 2.1.

Some experimental tests were performed with the Chromium-Manganese austenitic stainless steel in order to evaluate its mechanical properties at 500 ºC (maximum temperature of the exhaust systems in normal service conditions). These experimental tests consisted in axial tensile tests of two specimens of Chromium-Manganese austenitic stainless steel at 500 ºC. Some fatigue tests were also performed to specimens of Chromium-Manganese austenitic stainless steel at 500 ºC. For these experimental tests, the specimens used were transverse butt welded specimens, manufactured from Chromium-Manganese austenitic stainless steel with the geometry and dimensions shown in Figure 2.3 [8].

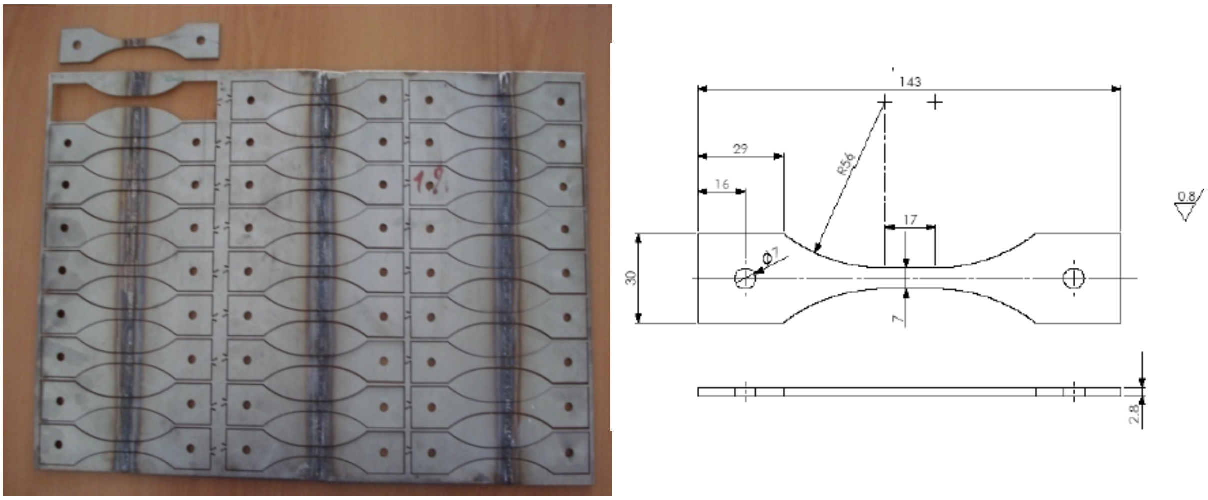

Figure 2.3: Geometry and dimensions of the transverse butt welded Cr-Mn specimens used on the experimental tests [8]

A servo-hydraulic machine coupled with a furnace was used to carry out the axial tensile and fatigue tests at 500 ºC.

Figure 2.4 shows the servo-hydraulic machine and furnace which were used to perform the axial tensile and fatigue tests.

Figure 2.4: Servo-hydraulic machine and furnace used to perform the axial tensile and fatigue tests

Figure 2.5 shows the nominal stress versus displacement curves obtained from the uniaxial tensile tests performed to two specimens of austenitic Chromium-Manganese stainless steel, at a temperature of 500 ºC.

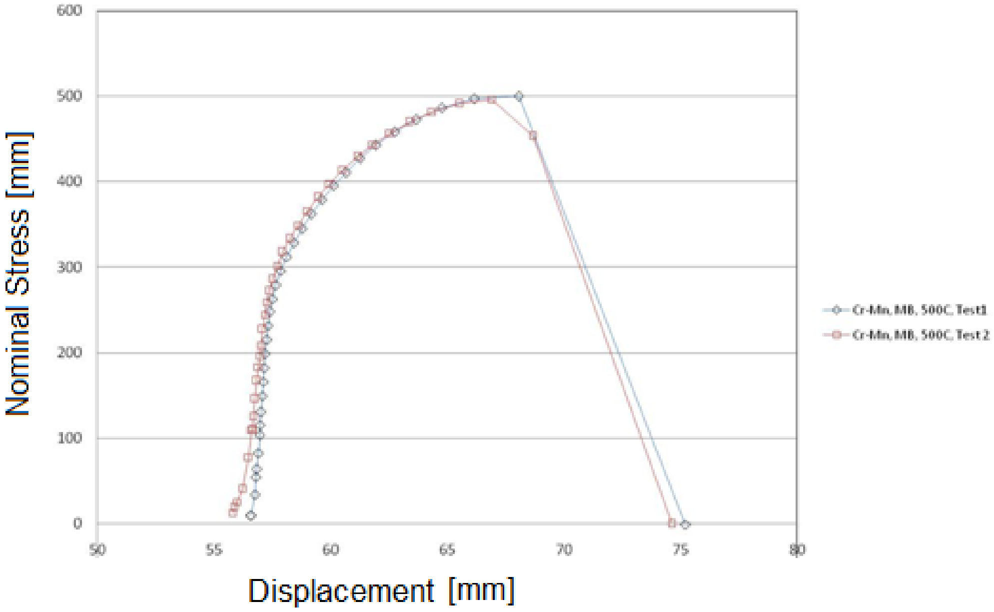

Figure 2.5: Nominal stress versus displacement curve of the austenitic Chromium-Manganese stainless steel. Test temperature: 500 ºC.

The two axial tests performed show that the Chromium-Manganese austenitic stainless steel has a yield strength of 260 MPa and an ultimate strength of 500 MPa at 500 ºC (Figure 2.6). Therefore, these results show that the austenitic Chromium-Manganese stainless steel, at 500 ºC, has, more or less, the same mechanical properties as the AISI 316L austenitic stainless steel at 24 ºC (Figures 2.1 and 2.5). At 500ºC, the Chromium-Manganese austenitic stainless steel has a higher yield strength than the AISI 316L austenitic stainless steel (+24%). In terms of ultimate strength, the

Chromium-Manganese austenitic stainless steel has a higher value (+22%) than the AISI 316L austenitic stainless steel.

Besides the axial tensile tests, three fatigue strength tests (R=0.1) were performed to transverse butt welded specimens, manufactured from Chromium-Manganese austenitic stainless steel. Table 2.9 shows the parameters and its values used for each fatigue test and the respective number of cycles obtained.

Table 2.9: Fatigue tests parameters and respective results

Tests	**Stress range applied (MPa)**	**Temperature of test (ºC)**	**Life prediction (cycles)**
1st	225	500	12397
2nd	162	500	6000000
3rd	193	500	86541

Given the reduced number of cycles obtained in the first test, the Chromium-Manganese austenitic stainless steel tested specimen is considered to have a reduced fatigue life for a maximum stress applied of 250 MPa (stress range of 225 MPa, with R=0.1). From the result obtained in the second test, the tested specimen is deemed to have infinite fatigue life for values of maximum stresses below 180 MPa. The third test revealed that the austenitic Chromium-Manganese stainless steel fatigue life reduces dramatically when maximum stress values above 180 MPa are applied (stress range of 162 MPa, with R=0.1). However, residual stresses measured in some specimens showed that they could play an important role in fatigue life results [7].

2.3 445M2 Ferritic Stainless Steel marine grade type:

The 445M2 ferritic stainless steel marine grade type is a recently developed ferritic stainless steel with mechanical properties very similar to the AISI 316Laustenitic stainless steel grade type, which makes it a viable alternative to the AISI 316L austenitic stainless steel. At room temperature it has a yield strength of 350 MPa and an ultimate strength of 520 MPa [6] which is very similar to the mechanical properties of the AISI 316L austenitic stainless steel.

In comparison with the AISI 316L and Cr-Mn austenitic stainless steels, the 445M2 ferritic stainless steel does not have Nickel and Nitrogen in its chemical composition. However, it has Titanium and Aluminum, which improve the toughness and corrosion resistance of this ferritic stainless steel [11].

The chemical composition of this ferritic steel is shown in table 2.10 [9].

Table 2.10: Chemical composition of the 445M2 ferritic stainless steel marine grade type [9].

Chemical composition of the 445M2 ferritic stainless steel marine grade type										
C	Si	Mn	P	S	Cr	Mo	Ni	Nb	Ti+Al	N
0.01	0.18	0.20	----	----	22.1	1.20	----	0.23	0.19+0.09	----

A common problem in the ferritic stainless steels is its poor corrosion resistance in comparison with the austenitic stainless steels. However, the 445M2 ferritic stainless steel marine grade type was developed considering the corrosive maritime environment, so it has more percentage of Chromium in its chemical composition. Using, once again, equation 2.1 and the chemical composition of the 445M2 ferritic stainless steel (Table 2.10), the pitting resistance equivalent number was obtained (Table 2.11).

Table 2.11: Pitting resistance equivalent number of the 445M2 ferritic stainless steel marine grade type

	PREN (eq. 2.1)
445M2 ferritic stainless steel marine grade type	$22.1+3.3\times1.20+16\times0=26.06$

As shown in table 2.11 by the PREN, even with the lack of Nitrogen in its chemical composition, the 445M2 ferritic stainless steel has better pitting corrosion resistance than the austenitic stainless steels in study, due to its higher percentage of Chromium.

Being a ferritic stainless steel, the 445M2 marine grade type is a less dense stainless steel than the austenitic stainless steels in study but it has a slightly higher Young´s modulus value. Table 2.12 shows these physical properties of the 445M2 ferritic marine grade type grade stainless steel [9].

Table 2.12: Physical properties of the 445M2 ferritic marine stainless steel grade type [9].

Density (Kg/m^3)	**Young´s Modulus (GPa)**
7750	199

The ferritic steels have higher thermal conductivity than the austenitic stainless steels, which allows them to dissipate heat better. They also have lower thermal expansion coefficients, which reduces the expansion of each plate, therefore reducing the stresses on the welded plates with different thicknesses. The thermal properties of the 445M2 ferritic stainless steel are shown in table 2.13.

Table 2.13: Thermal properties of the 445M2 ferritic stainless steel marine grade type [9].

Thermal conductivity (W/mm.K)		**Thermal expansion coefficient (K^{-1})**		
373 K	**773 K**	**373 K**	**588 K**	**811 K**
22.5×10^{-3}	22.6×10^{-3}	10.0×10^{-6}	10.5×10^{-6}	11.1×10^{-6}

When ferritic stainless steels are heated above 950°C, as during welding, or are submitted to prolonged heating in the 400 ºC to 600 ºC range, they may become brittle at room temperature, therefore loosing toughness and ductility. To avoid brittlement after welding, the weld and the affected zone must be annealed within the temperature range of 790 ºC to 815 ºC. Ideally, the weldment should be furnace cooled to 593 °C, but a slow cooling through the temperature range of 565 ºC to 399 °C should be avoided, in order to prevent embrittlement from precipitation or development of a brittle phase [10, 11].

One should note that the application of the 445M2 ferritic stainless steel, on the exhaust system of certain vessels, can be a drawback due to its magnetic properties [12].

3. Modelling the naval gas turbines’ exhaust systems

Two different exhaust systems for naval gas turbines, each from a different vessel, were modelled using a Computer Aided Design (CAD) software, *Solidworks*®, in order to simulate the structural and thermal behaviour of the exhaust systems using a Finite Element Analysis (FEA) software, *Ansys*®.

The exhaust systems are thermally insulated and are manufactured from AISI 316L austenitic stainless steel grade type plates that were bent in roll machines and mainly butt welded by MIG/MAG welding process [2].

Both exhaust systems, that will be designated this point forward as A and B (Fig.3.1 and Fig.3.3, respectively), were modelled according to their fabrication drawings and represent half of the height of each complete exhaust system. This means that they were only modelled from the outlet section of the gas turbines till half of the height of each complete exhaust system, representing the first collector.

Figures 3.2-(a) and 3.4-(a) are “front views” of the exhaust systems (exhaust system A and B, respectively), as seen from the port side of the vessels. Its right side is oriented to the stern of the vessel and the left side oriented in the bow direction.

This way, in figure 3.2-(a) and figure 3.4-(a) the X axis points to the stern of the vessel, the Y axis points to the top and the Z axis points to the port side of the vessel. These were the axial orientations used on the analysis.

3.1 Modelling the gas turbine´s exhaust system A (vessel A):

Exhaust system A was modelled according to the fabrication drawings. It has 7.847 m in height, a rectangular inlet section of 4.247 m^2 and an outlet section of 5.113 m^2. Figure 3.1 shows the dimensions of the gas turbine´s exhaust system A, as modelled using *Solidworks*®.

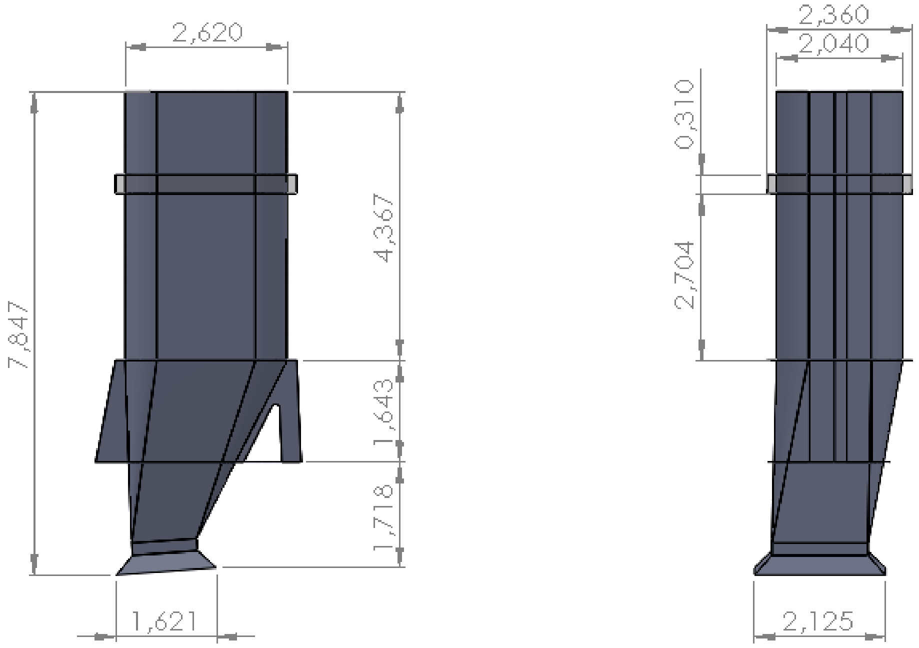

Figure 3.1: Dimensions of exhaust system A (meters)

Complete technical drawings of exhaust system A are shown in annex A, annexes A1 and A2.

Once modelled the exhaust system A, it was exported to the FEA software, *Ansys*®, in order to simulate its structural and thermal behaviour.

Figure 3.2 shows different views of the gas turbine´s exhaust system A, as shown in the FEA software, *Ansys*®.

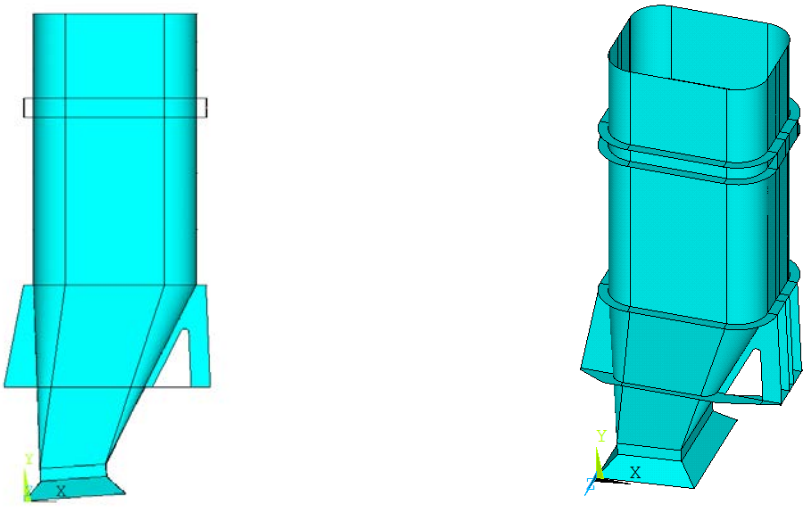

(a) (b)

Figure 3.2: Front view (a) and oblique view (b) of the exhaust system A

3.2 Modelling the gas turbine’s exhaust system B (vessel B):

Exhaust system B was modelled according to the fabrication drawings. It has 7.630 m in height, an inlet section of 1.902 m^2 and a circular outlet section of 2.274 m^2. Figure 3.3 shows the dimensions of the gas turbine´s exhaust system B, as modelled using *Solidworks*®

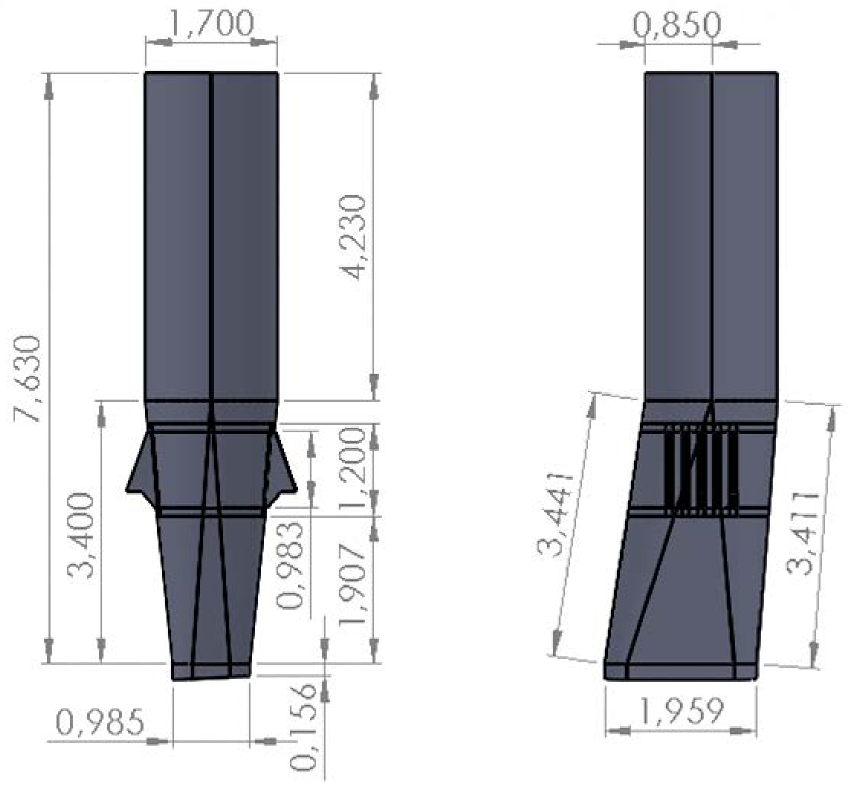

Figure 3.3: Dimensions of exhaust system B (meters)

Complete technical drawings of exhaust system B are shown in annex A, annexes A3 and A4.

Once modelled the exhaust system B, it was exported to the FEA software, *Ansys*®, in order to simulate its structural and thermal behaviour.

Figure 3.4 shows different views of the gas turbine´s exhaust system B, as shown in the FEA software, *Ansys*®.

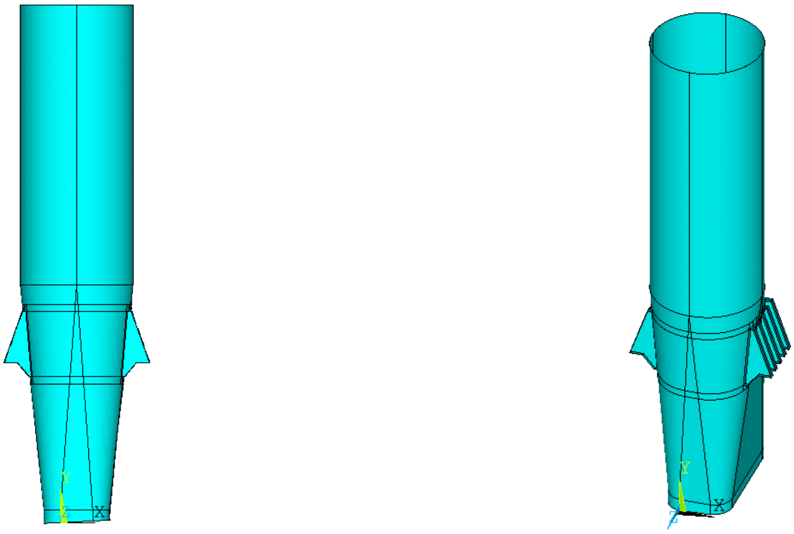

(a) (b)

Figure 3.4: Front view (a) and oblique view (b) of exhaust system B

Comparing the dimensions of both exhaust systems (Figures 3.1 and 3.3), one may observe that although having similar heights, they have different inlet and outlet section areas. They also have different geometries and different types of reinforcement ribs which will determine their structural behaviour.

4. Finite Element Analysis of the gas turbine exhaust systems

A finite element numerical software (*Ansys*®) was used to analyse the in-service conditions to which the exhaust systems are submitted and computational programs were written using Ansys Parametric Design Language (APDL). These programs proved to be very useful for easily verify all the input conditions and furthermore, once the programs were finished, it was also easy to implement new modifications in the exhaust systems design by simply making modifications in the code lines. In this chapter (Chapters 4.1 to 4.8), all the major inputs needed to simulate the thermal and structural behaviour of the exhaust systems, will be explained.

4.1 Finite element types:

As the thickness to radius ratio (t/R), in the different cross sections, was much smaller than 0.05 (1/20), the walls of the exhaust systems were modelled as shells, for the structural and thermal analysis performed [2].For these analyses, two finite element types were used: SHELL63 and SHELL57.

The finite element SHELL63 type is a structural bi-quadratic element that has both bending and membrane capabilities. The element has six degrees of freedom at each node: translations in the nodal x, y, and z directions and rotations about the x, y, and z-axes. Stress stiffening and large deflection capabilities are also included in the mathematical formulation of the finite element used.

The finite element SHELL57 type is a thermal element that has in-plane thermal conduction capability. The element has four nodes with a single degree of freedom, temperature, at each node and it was applied in a steady-state thermal analysis.

4.2 Thickness definition:

4.2.1 Specification of plate's thicknesses of exhaust system A (on vessel A):

The thickness of each plate was defined through the use of real constants in *Ansys*®. The exhaust system pipe, Figure 4.1-(1), has a wall thickness of 4 mm. The reinforcement ribs on the right side (2) have a thickness of 13 mm, while the left side reinforcement ribs (3) have a thickness of 11 mm. The lower supporting ring (4) has a 15 mm thickness, the intermediate supporting ring (5) has a 30 mm thickness and the upper supporting ring (6) has plates with 10 mm thickness. Figure 4.1 shows the exhaust system's plate thicknesses of the current geometry of exhaust system A.

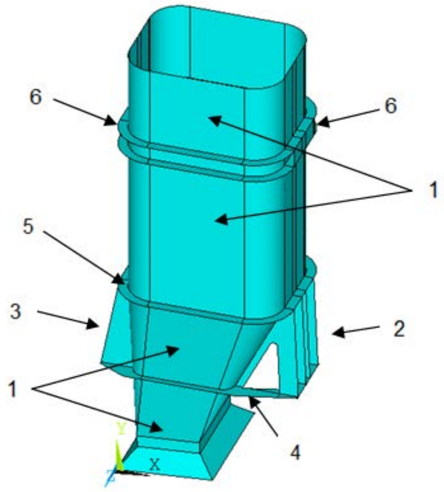

Figure 4.1: Distribution of the plate's thicknesses of the current geometry of exhaust system A

Note that, for a question of simplifying the model, it was considered that the intermediate supporting ring of exhaust system A is made of a thick plate with 30 mm, when infact it is composed by two thick flanges, each of which with a thickness of 15 mm, that are bolted together.

4.2.2 Specification of plate’s thicknesses of exhaust system B (on vessel B):

The use of real constants in *Ansys*® to define the thicknesses was also done for each plate that exists in exhaust system B. The exhaust system pipe, Figure 4.2-(1), has a wall thickness of 4 mm, the right and left side reinforcement ribs, Figure 4.2-(2) and Figure 4.3-(2), have a thickness of 12 mm, and the right and left doubler plates, Figure 4.3-(3), also have a thickness of 12 mm. In the APDL programs, the areas that correspond to the overlap of the exhaust system pipe with the doubler plates were defined as having a thickness of 16 mm (4 mm thickness of the exhaust pipe plus 12 mm thickness of the doubler plates). Figures 4.2 and 4.3 show the exhaust system’s plate thicknesses on the current geometry of exhaust system B.

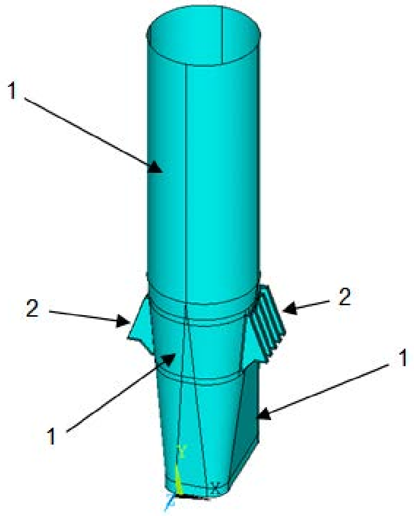

Figure 4.2 Distribution of the plate’s thicknesses of the current geometry of exhaust system B

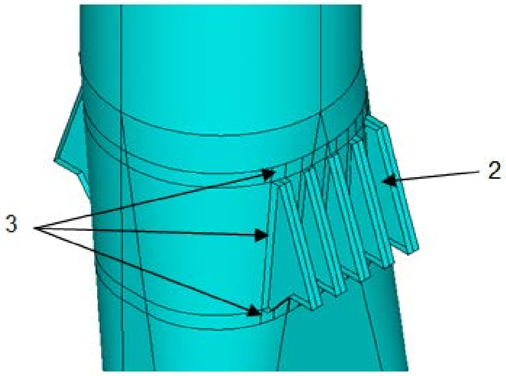

Figure 4.3: Distribution of the plate’s thicknesses of the current geometry of exhaust system B (magnification of the right reinforcement ribs and doubler plates)

4.3 Material model:

The same material model was considered in both exhaust systems.

The material model representing the AISI 316L austenitic stainless steel or the 445M2 ferritic stainless steel (according to the analysis that is being run) was assumed isotropic, homogeneous and used values of Young’s modulus, of thermal expansion coefficient and of thermal conductivity temperature-dependent. Consequently, due to the change of the thermal expansion coefficient and the thermal conductivity of the material, with temperature, nonlinear material behaviour, nonlinear boundary conditions and geometric nonlinearity were introduced and analysed in the model.

For the analysis of the exhaust systems made with the AISI 316L austenitic stainless steel, the Poisson´s ratio used was 0.33 and the material density and Young´s modulus values are those presented in table 2.3. The thermal properties of this material (austenitic stainless steel) were defined using a reference temperature of 293 K and the values of the thermal conductivity and of the thermal expansion coefficients were introduced in the material model from table 2.4.

In the exhaust systems’ analysis, that considered the structure made by the 445M2 ferritic stainless steel, the Poisson´s ratio used was 0.33 and the material density and Young´s modulus are those presented in table 2.11. The thermal properties of the ferritic stainless steel were defined using a reference temperature of 293 K and the values of the thermal conductivity and of the thermal expansion coefficients were introduced in the material model from table 2.12.

4.4 Mesh generation:

Mesh generation is one of the most critical aspects in the finite element method. Too many finite elements may result in long solver runs (large computational effort), and too few may lead to inaccurate results. So, in order to obtain the appropriate mesh for each simulation of the exhaust systems, some experiments were made using coarse and finer finite element meshes. Also, all the exhaust system’s mesh were checked in order to verify the correct connectivity between adjacent areas..

Three types of mesh were tested: an *Ansys*® automatic free mesh, with *smartsize 1*, which generates the most refined automatic free mesh in *Ansys*®, a manually defined mesh with quadrilateral elements with an edge length of 75 mm and finally a manually defined mesh with quadrilateral elements with an edge length of 50 mm.

In order to compare each mesh type tested, the principal stress distributions obtained on critical areas, near stress concentration details, the number of elements generated and the time taken by the program to solve the simulations were registered.

4.4.1 Mesh generation of exhaust system A:

The first type of mesh tested was an *Ansys*® automatic free mesh, with *smartsize 1*. This generates the most refined automatic mesh done by *Ansys*®. Figure 4.4 shows the mesh generated over exhaust system A.

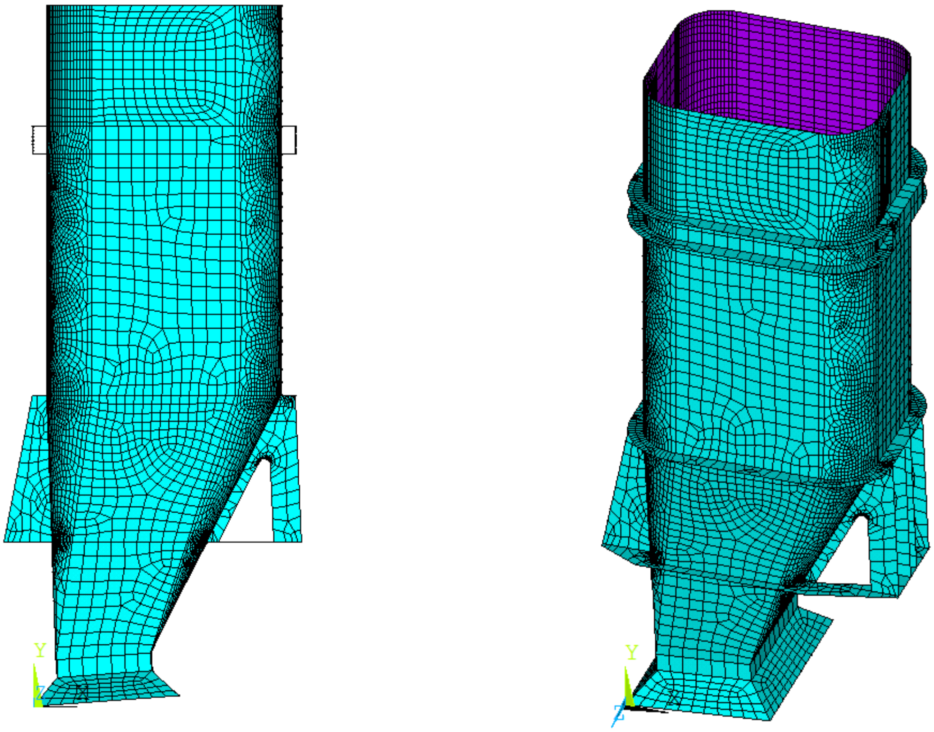

Figure 4.4: *Ansys*® automatic free mesh with *smartsize 1* generated over exhaust system A

The mesh shown is composed by 15614 finite elements and 15528 nodes.

To verify the level of stresses in critical areas of exhaust system A, in order to compare the different types of mesh, some simulations were made. In these simulations an internal pressure of 500 Pa was applied to the exhaust system pipe, in which the exhaust gases flow. Also, axial displacement constraints (UX=UY=UZ=0) were applied in the lines that delimit the right side of the lower supporting ring and in the lines (UY=0) correspondent to the left side of the lower supporting ring of exhaust system A. Figure 4.5 shows the first principal stresses obtained near the intermediate supporting ring with an automatic free mesh with *smartsize 1*.

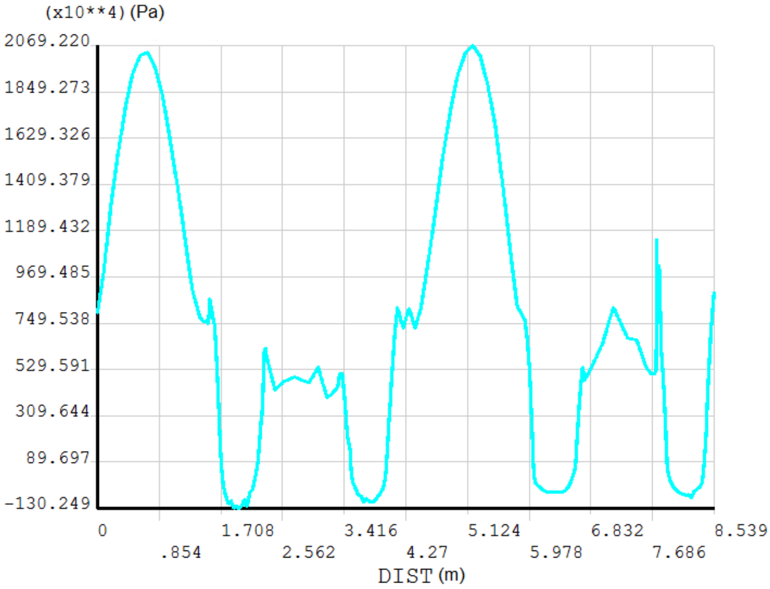

Figure 4.5: First principal stress distribution obtained near the intermediate supporting ring of exhaust system A with an automatic free mesh with *smartsize 1*

Figure 4.6 shows the first principal stresses obtained near the lower supporting ring with an automatic free mesh with *smartsize 1*.

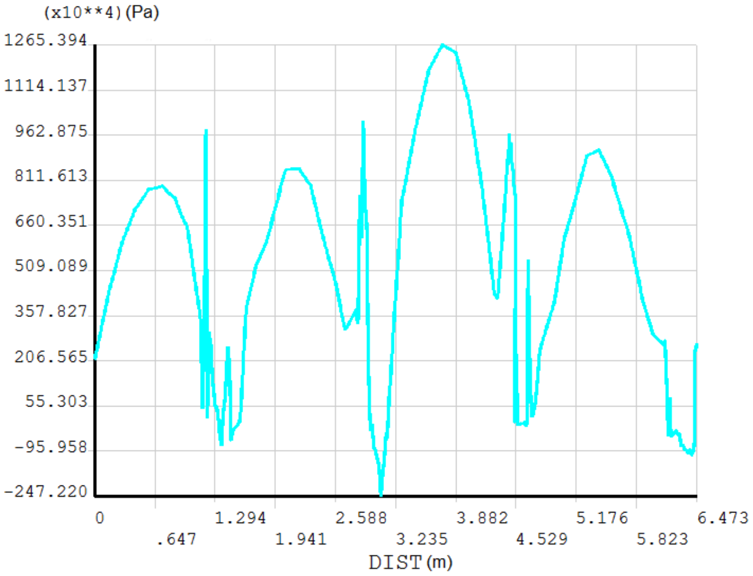

Figure 4.6: First principal stress distribution obtained near the lower supporting ring of exhaust system A with an automatic free mesh with *smartsize 1*

The second type of mesh tested was a manually defined mesh with quadrilateral elements with an edge length of 75 mm. Figure 4.7 shows the mesh generated over exhaust system A.

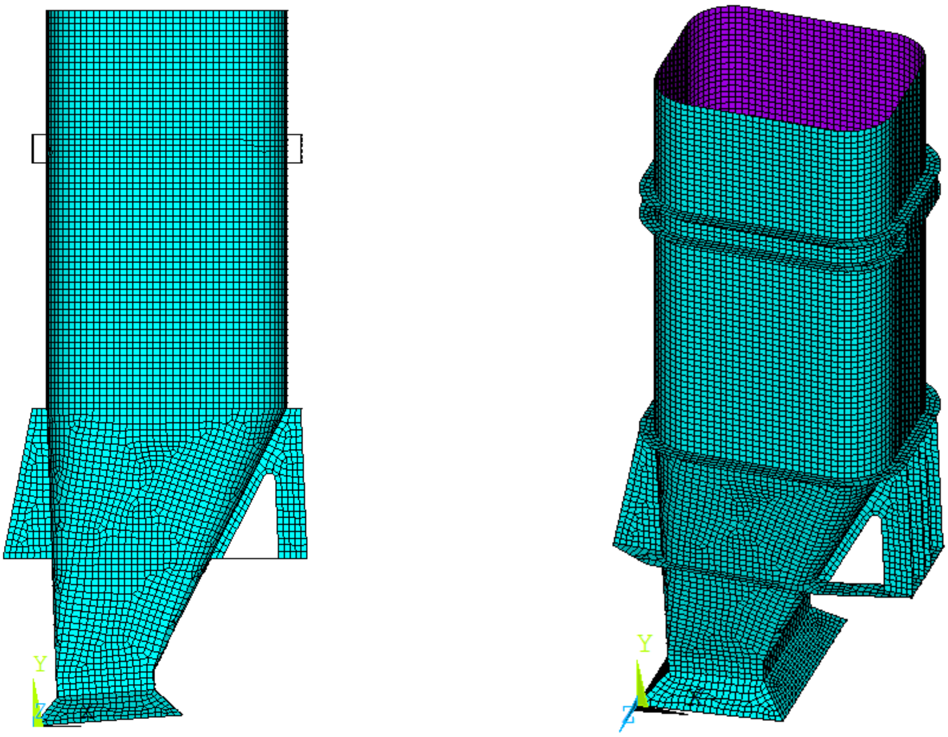

Figure 4.7: *Ansys*® manually defined mesh with quadrilateral elements with an edge length of 75 mm generated over exhaust system A

This mesh is composed by 15339 finite elements and 15472 nodes.

An identical simulation to the automatic free mesh with *smartsize 1* was made to this second type of mesh, applying both the same internal pressure value and constraints. Figure 4.8 shows the first principal stresses obtained near the intermediate supporting ring with a manually defined mesh with quadrilateral elements with an edge length of 75 mm.

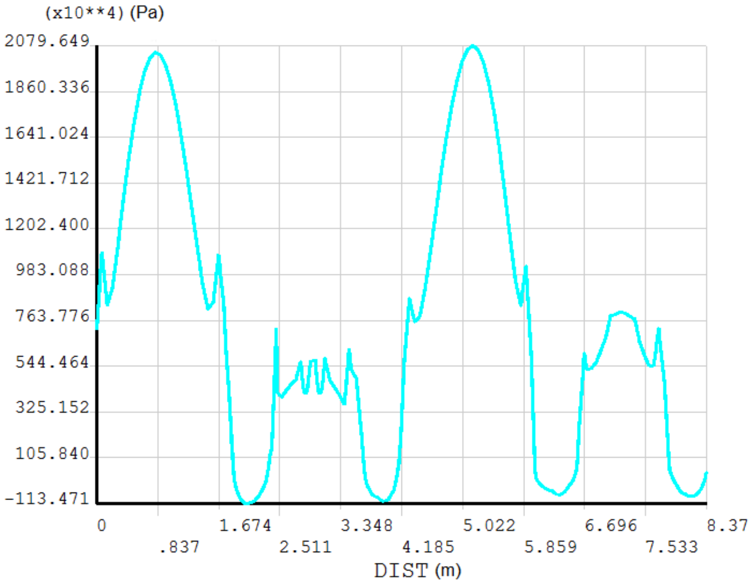

Figure 4.8: First principal stress distribution obtained near the intermediate supporting ring of exhaust system A with a manually defined mesh using quadrilateral elements with an edge length of 75 mm

Figure 4.9 shows the first principal stresses obtained near the lower supporting ring with a manually defined mesh with quadrilateral elements with an edge length of 75 mm.

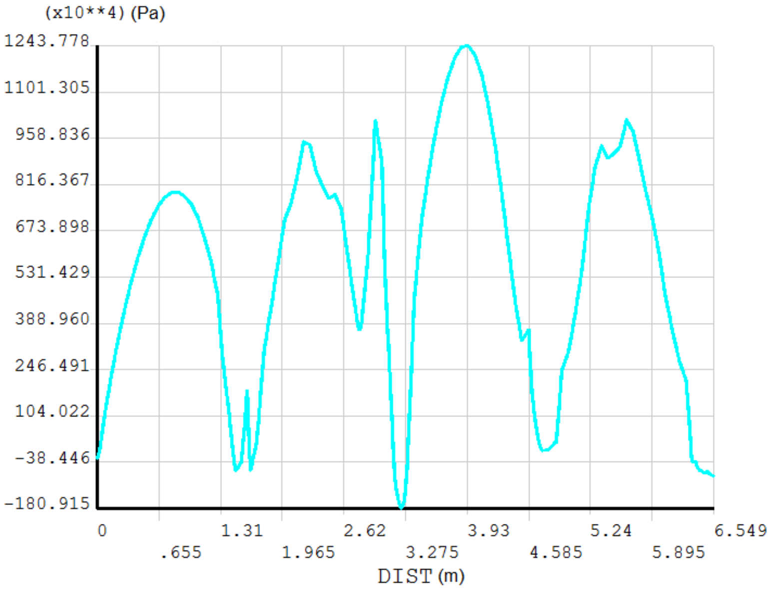

Figure 4.9: First principal stress distribution obtained near the lower supporting ring of exhaust system A with a manually defined mesh using quadrilateral elements with an edge length of 75 mm

The third type of mesh tested was a manually defined mesh with quadrilateral elements with an edge length of 50 mm. Figure 4.10 shows the mesh generated over exhaust system A.

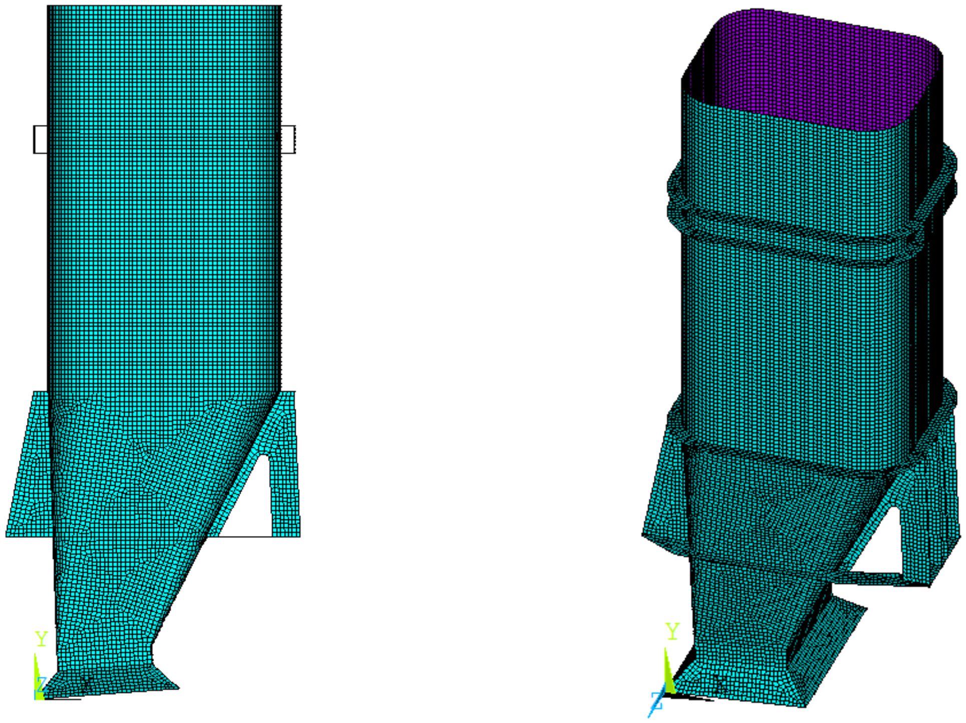

Figure 4.10: *Ansys*® manually defined mesh with quadrilateral elements with an edge length of 50 mm generated over exhaust system A

This mesh is composed by 31665 finite elements and 31878 nodes.

An identical simulation to the other two types of mesh was made to this third type of mesh, applying both the same internal pressure value and constraints. Figure 4.11 shows the first principal stresses obtained near the intermediate supporting ring with a manually defined mesh with quadrilateral elements with an edge length of 50 mm.

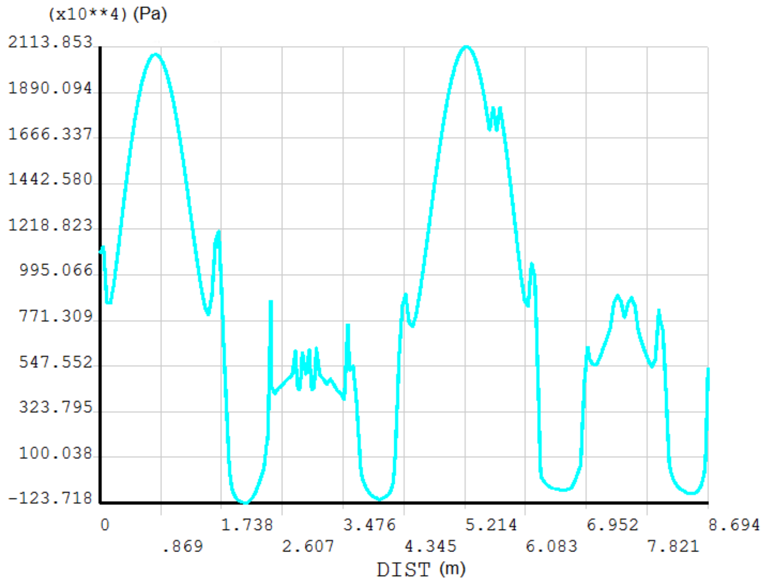

Figure 4.11: First principal stress distribution obtained near the intermediate supporting ring of exhaust system A with a manually defined mesh using quadrilateral elements with an edge length of 50 mm

Figure 4.12 shows the first principal stresses obtained near the lower supporting ring with a manually defined mesh with quadrilateral elements with an edge length of 50 mm.

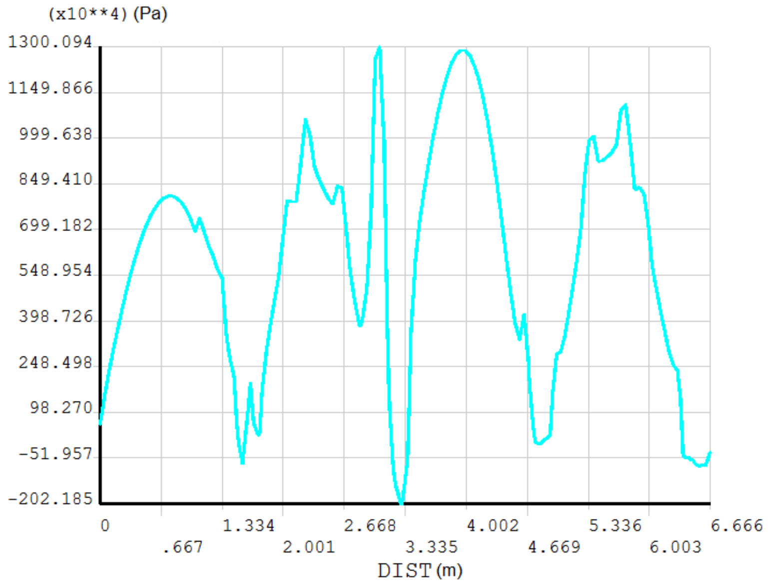

Figure 4.12: First principal stress distribution obtained near the lower supporting ring of exhaust system A with a manually defined mesh using quadrilateral elements with an edge length of 50 mm

The results of the highest first principal stress value obtained from the tests made to each of the three types of mesh on exhaust system A are shown in table 4.1.

Table 4.1: Highest first principal stress value obtained from the application of three refinement mesh tests made to exhaust system A

Type of mesh	Number of elements created /Number of nodes created	Intermediate supporting ring (MPa)	Lower supporting ring (MPa)
Automatic free mesh, *smartsize 1*	15614/15528	20.69	12.75
75 mm sized elements	15339/15472	20.80	12.44
50 mm sized elements	31665/31878	21.14	13.00

In terms of mesh refinement, the meshes that were manually defined generated finite element models with more uniform meshes applied in all the structure, while the *smartsize* option allowed to refine more the mesh near the stress concentration details where the stress gradients are larger. Also, the finite elements generated were not neither distorted nor elongated.

The program solved the simulations slightly faster when using the second type of mesh, the mesh manually defined with quadrilateral elements with an edge length of 75 mm. The first and third types of mesh took more or less the same time to solve the same simulations.

From the results obtained for the three types of mesh tested on exhaust system A (Table 4.1), one can see that the stresses do not change appreciably for the different cases studied (which is a sign of adequate mesh refinement). It was decided to use the manually defined mesh with quadrilateral elements with an edge length of 50 mm due to the fact that it created more elements per area, it obtained the highest value of stress in the first principal stress tests and it produced a more refined mesh.

4.4.2 Mesh generation of exhaust system B:

The first type of mesh tested was an *Ansys*® automatic free mesh, with *smartsize 1*. This generates the most refined automatic mesh done by *Ansys*®. Figure 4.13 shows the mesh generated over exhaust system B.

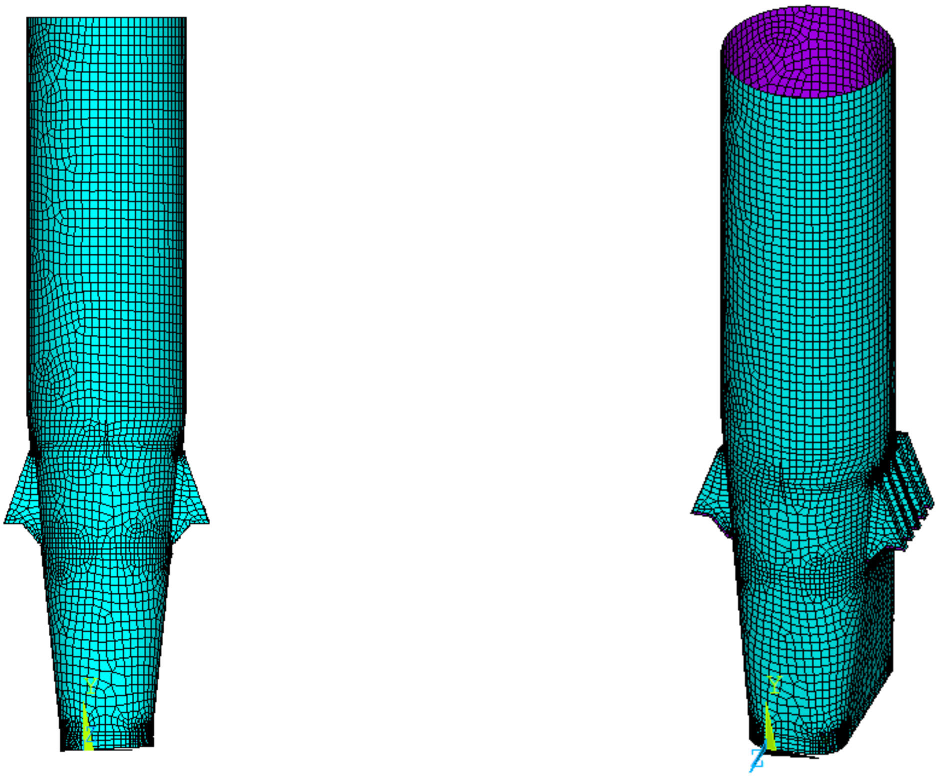

Figure 4.13: *Ansys*® automatic free mesh with *smartsize 1* generated over exhaust system B

The mesh shown is composed by 12696 finite elements and 13066 nodes.

To verify the level of stresses in critical areas of exhaust system B, in order to compare the different types of mesh, some simulations were made. In these simulations an internal pressure of 500 Pa was applied to the exhaust system pipe, in which the exhaust gases flow. Also, axial displacement constraints (UX=UY=UZ=0) were applied in the lines that delimit the right side of the reinforcement ribs and in the lines (UY=0) correspondent to the left side of the reinforcement ribs of exhaust system B. Figure 4.14 shows the first principal stresses obtained near the upper flanges of the reinforcement ribs with an automatic free mesh with *smartsize 1*.

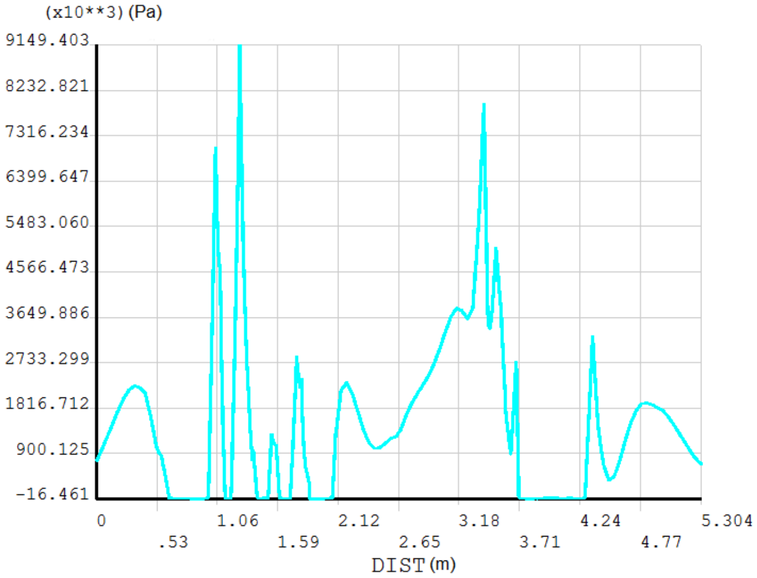

Figure 4.14: First principal stress distribution obtained near the upper flanges of the reinforcement ribs of exhaust system B with an automatic free mesh with smartsize 1

Figure 4.15 shows the first principal stresses obtained near the lower flanges of the reinforcement ribs with an automatic free mesh with *smartsize 1*.

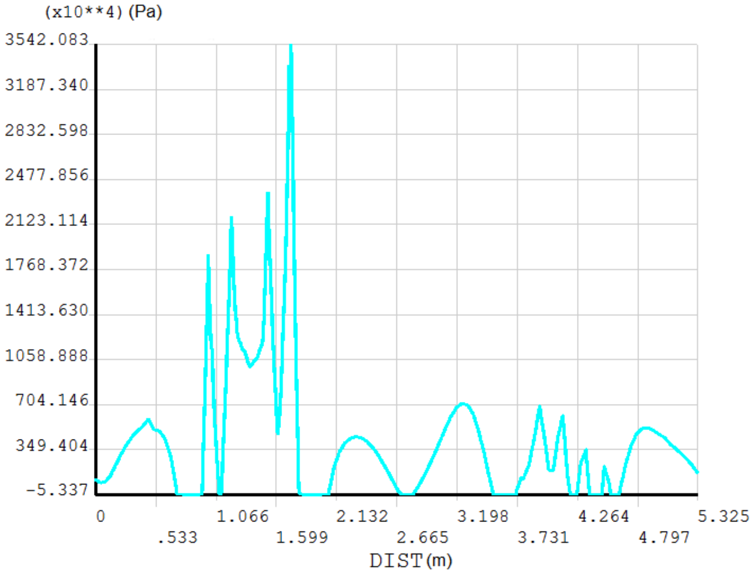

Figure 4.15: First principal stress distribution obtained near the lower flanges of the reinforcement ribs of exhaust system B with an automatic free mesh with smartsize 1

The second type of mesh tested was a manually defined mesh with quadrilateral elements with an edge length of 75 mm. Figure 4.16 shows the mesh generated over exhaust system B.

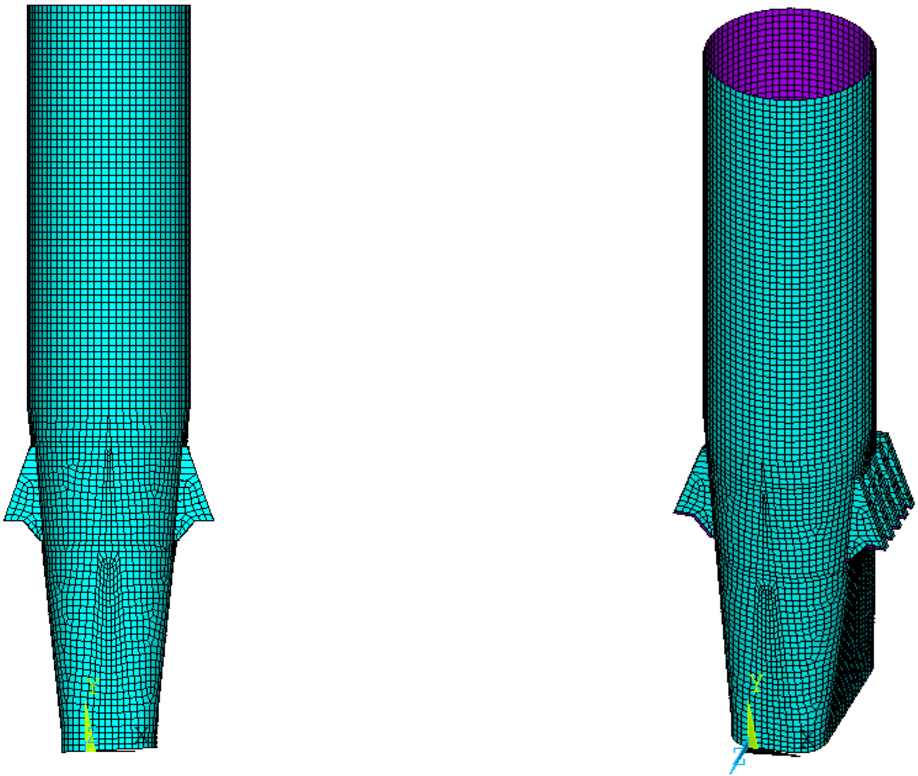

Figure 4.16: *Ansys*® manually defined mesh with quadrilateral elements with an edge length of 75 mm generated over exhaust system B

This mesh is composed by 9169 finite elements and 9219 nodes.

An identical simulation to the automatic free mesh with *smartsize 1* was made to this second type of mesh, applying both the same internal pressure value and constraints. Figure 4.17 shows the first principal stresses obtained near the upper flanges of the reinforcement ribs with a manually defined mesh with quadrilateral elements with an edge length of 75 mm.

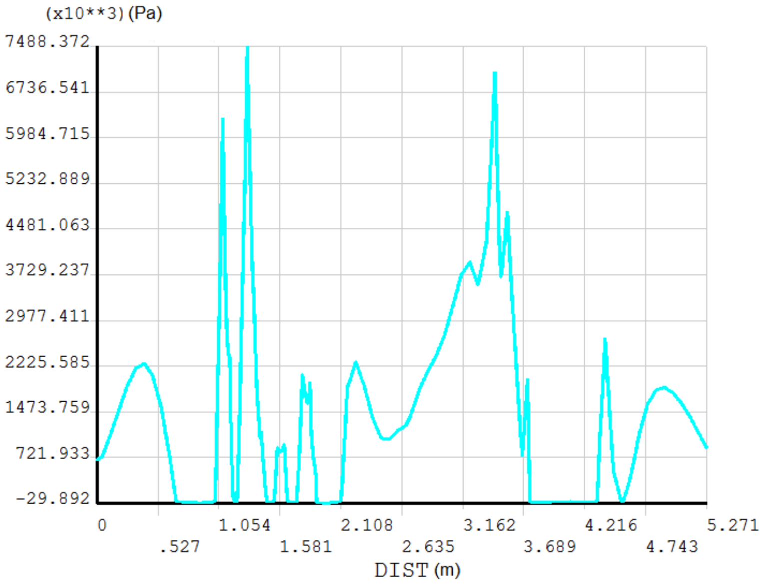

Figure 4.17: First principal stress distribution obtained near the upper flanges of the reinforcement ribs of exhaust system B with a manually defined mesh using quadrilateral elements with an edge length of 75 mm

Figure 4.18 shows the first principal stresses obtained near the lower flanges of the reinforcement ribs with a manually defined mesh with quadrilateral elements with an edge length of 75 mm.

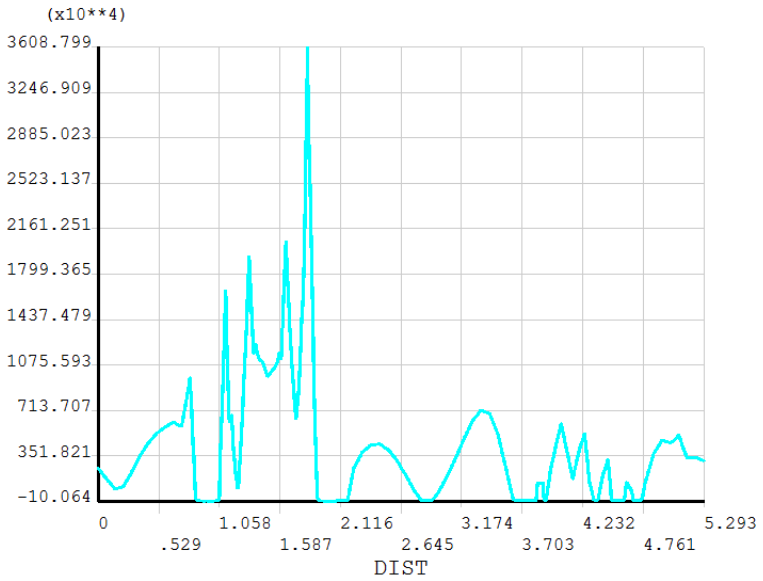

Figure 4.18: First principal stress distribution obtained near the lower flanges of the reinforcement ribs of exhaust system B with a manually defined mesh using quadrilateral elements with an edge length of 75 mm

The third type of mesh tested was a manually defined mesh with quadrilateral elements with an edge length of 50 mm. Figure 4.19 shows the mesh generated over exhaust system B.

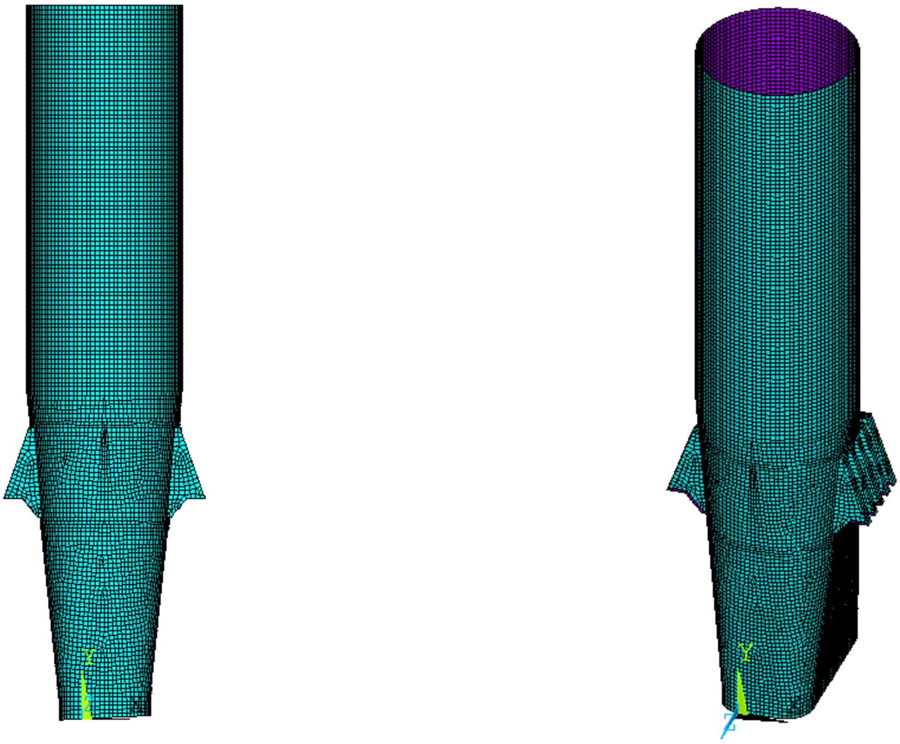

Figure 4.19: *Ansys*® manually defined mesh with quadrilateral elements with an edge length of 50 mm generated over exhaust system B

This mesh is composed by 19442 finite elements and 19539 nodes.

An identical simulation to the other two types of mesh was made to this third type of mesh, applying both the same internal pressure value and constraints. Figure 4.20 shows the first principal stresses obtained near the upper flanges of the reinforcement ribs with a manually defined mesh with quadrilateral elements with an edge length of 50 mm.

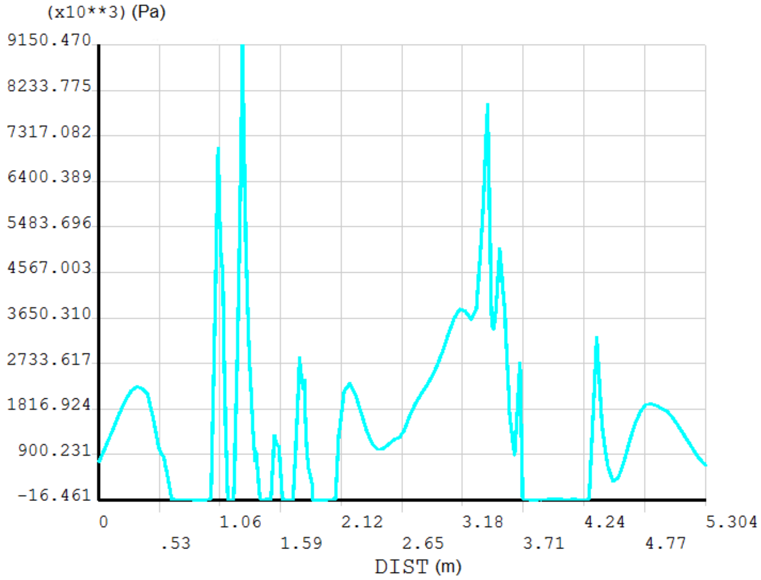

Figure 4.20 First principal stress distribution obtained near the upper flanges of the reinforcement ribs of exhaust system B with a manually defined mesh using quadrilateral elements with an edge length of 50 mm

Figure 4.21 shows the first principal stresses obtained near the lower flanges of the reinforcement ribs with a manually defined mesh with quadrilateral elements with an edge length of 50 mm.

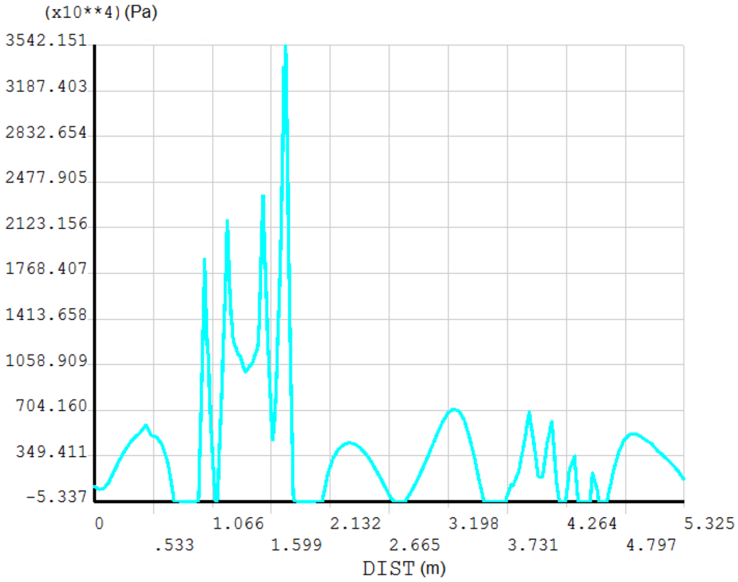

Figure 4.21: First principal stress distribution obtained near the lower flanges of the reinforcement ribs of exhaust system B with a manually defined mesh using quadrilateral elements with an edge length of 50 mm

The results of the highest first principal stress value obtained from the tests made to each of the three types of mesh on exhaust system B are shown in table 4.2.

Table 4.2: Highest first principal stress value obtained from the application of three refinement mesh tests made to exhaust system B

Type of mesh	Number of elements created /Number of nodes created	Upper flanges (MPa)	Lower flanges (MPa)
Automatic free mesh, *smartsize 1*	12696/13066	9.15	35.42
75 mm sized elements	9169/9219	7.41	35.42
50 mm sized elements	19442/19539	9.15	36.09

In terms of mesh refinement, the meshes that were manually defined generated finite element models with more uniform meshes applied in all the structure, while the *smartsize* option allowed to refine more the mesh near the stress concentration details where the stress gradients are larger. Also, the finite elements generated were not neither distorted nor elongated.

The program solved the simulations slightly faster when using the second type of mesh, the mesh manually defined with quadrilateral elements with an edge length of 75 mm. The first and third types of mesh took more or less the same time to solve the same simulations.

From the results obtained for the three types of mesh tested on exhaust system B (Table 4.2), one can see that the stresses do not change appreciably for the different cases studied (which is a sign of adequate mesh refinement). It was decided to use the manually defined mesh with quadrilateral elements with an edge length of 50 mm due to the fact that it created more elements per area, it obtained the highest value of stress in the first principal stress tests and it produced a more refined mesh.

4.5 Nodal temperature distribution:

4.5.1 Nodal temperature distribution on exhaust system A:

In order to obtain the nodal temperature distribution along exhaust system A, it was necessary to impose temperatures on lines (Fig. 4.22). Temperatures were measured on several points of exhaust system A while the gas turbine was operating, namely: 773 K at the inlet section, 623 K at the intermediate section, 373 K at the outside of the reinforcement ribs (both right and left sides) and 473 K at the outlet section of the exhaust system [2, 7].

Figure 4.22 shows the temperatures that were measured and that were used as an input for the thermal analysis using the finite element SHELL57 and the Ansys Parametric Design Language (APDL).

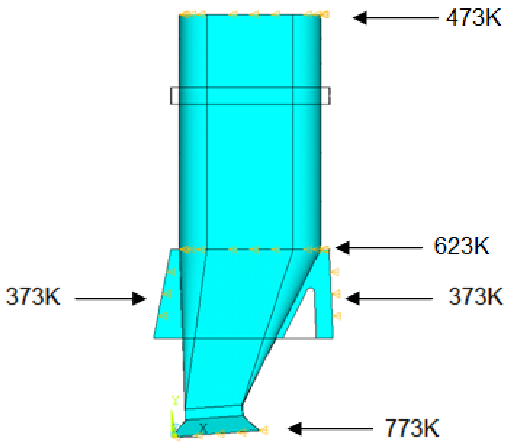

Figure 4.22: Temperature conditions defined in exhaust system A

Once all the steps mentioned in chapter 4.1 to 4.5 regarding exhaust system A were defined, a thermal analysis (foreseen in chapter 4.1) was run.

Figure 4.23 shows the nodal temperature distribution obtained in the thermal analysis of exhaust system A.

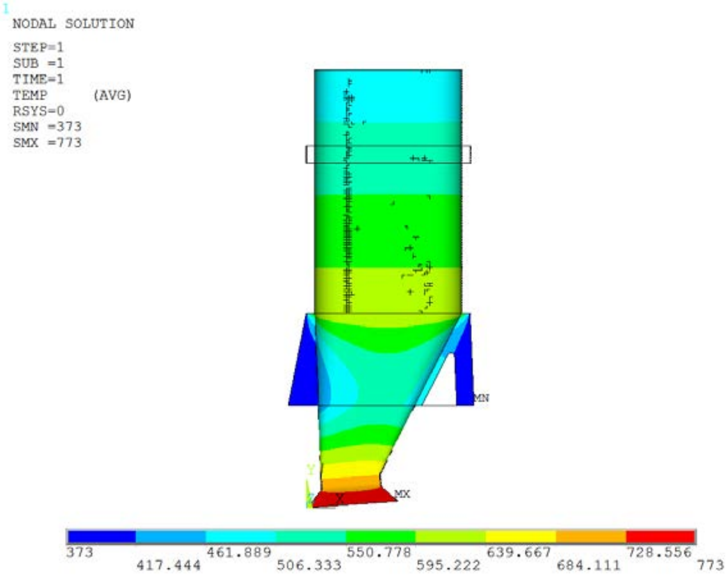

Figure 4.23: Nodal temperature distribution on exhaust system A (temperature scale in Kelvin)

After running the thermal analysis, a .RTH file (an *Ansys*® file) containing all the information about the thermal analysis – nodal temperature distribution (Fig. 4.23) - was obtained. This file was used as an input file during the structural analysis stage of exhaust system A.

4.5.2 Nodal temperature distribution on exhaust system B:

An identical procedure was applied to determine the nodal temperature distribution on exhaust system B. Taking as reference the temperatures measured in exhaust system A, three temperatures were imposed on three lines of the finite element model of exhaust system B (Fig. 4.24): 773 K at the inlet section, 623 K at the intermediate section and 473 K at the outlet section of the exhaust system.

Those temperatures were used as inputs for the thermal analysis of exhaust system B using the finite element SHELL57 and the Ansys Parametric Design Language (APDL).

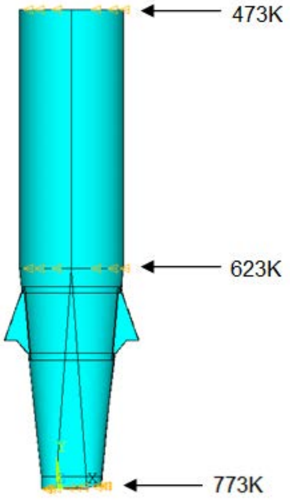

Figure 4.24: Temperature conditions defined in exhaust system B

Once all the steps mentioned in chapter 4.1 to 4.5 regarding exhaust system B were defined, a thermal analysis (foreseen in chapter 4.2) was run.

Figure 4.25 shows the nodal temperature distribution obtained in the thermal analysis of exhaust system B.

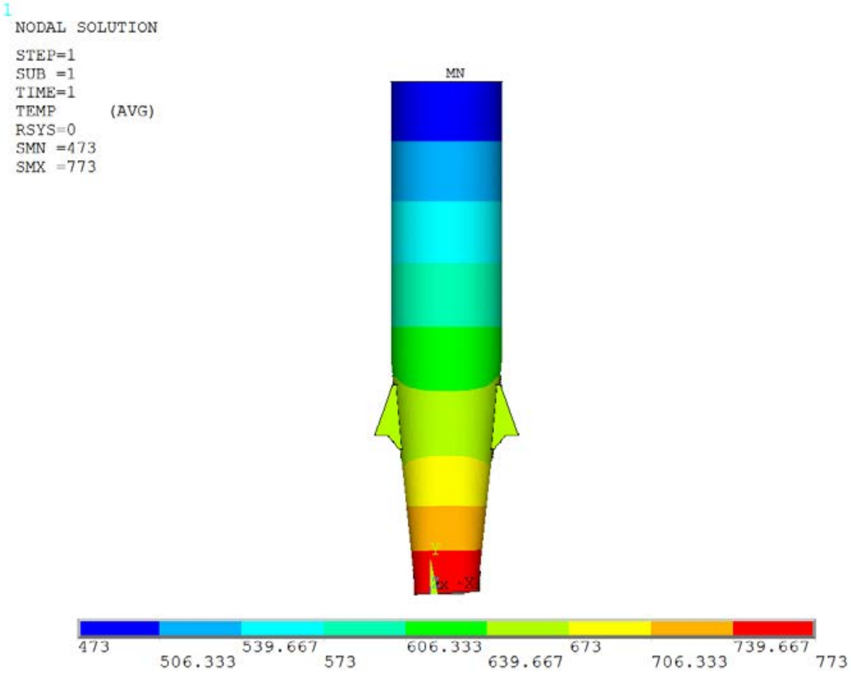

Figure 4.25: Nodal temperature distribution of exhaust system B (temperature scale in Kelvin)

After running the thermal analysis, a .RTH file (an *Ansys*® file) containing all the information about the thermal analysis – nodal temperature distribution (Fig. 4.25) - was obtained. This file was used as an input file during the structural analysis stage of exhaust system B.

4.6 Inertial loads:

Inertial loads were introduced in the model in order to simulate the accelerations/decelerations to which the exhaust systems are submitted to by the manoeuvres performed with the vessels. These inertial loads were applied in the center of mass of the exhaust systems under study.

In order to simulate the acceleration of gravity to which the exhaust systems are submitted, an acceleration of 1G was defined with opposite direction to the established Y axis.

A 2G deceleration (with opposite direction to the established X axis) was also defined in order to simulate the consequences of an emergency manoeuvre called Crashstop, which enables the ship to stop in a very short period of time. This manoeuvre can be considered as an overload condition as it is rarely used due to the imposition of high stresses in all the components of the vessels [2].

4.6.1 Inertial loads applied to exhaust system A:

The current geometry of exhaust system A weights 3118.1 kg and its center of mass, where the inertial loads are applied, is located on the following coordinates: X=0.2429 m, Y=3.6195 m, Z=-0.6868 m. These values were obtained through *Ansys*®, once all the thicknesses and the material model were defined.

There are also three silencers inside exhaust system A, each one weighting approximately 400 kg. In order to simulate the weight of such silencers, six forces were defined, each with a value of 2000 N and with opposite direction to the established Y axis. Figure 4.26 shows the location of these forces.

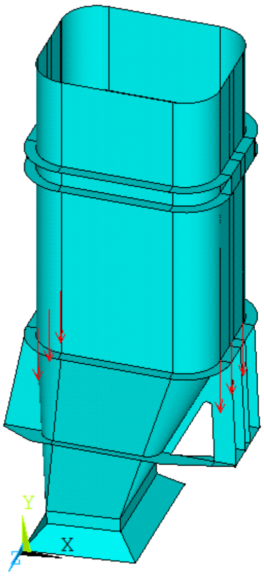

Figure 4.26: Location of the six forces that represent the silencers weight (red arrows)

As previously mentioned, in all the analyses made, the weight of the exhaust system was simulated through the definition of the acceleration of gravity (1G) which was defined in the opposite direction of the Y axis direction established.

In some analysis the overload condition was imposed, subjecting the exhaust system to a deceleration of 2G.

4.6.2 Inertial loads applied to exhaust system B:

The current geometry of exhaust system B weights 1743.2 kg and its center of mass, where the inertial loads are applied, is located on the following coordinates: X=1.3649 m, Y=3.8544 m, Z=-0.7899 m. These values were obtained through *Ansys*®, once all the thicknesses and the material model were defined.

No silencers exist inside exhaust system B.

The same inertial loads as those applied to exhaust system A, were applied to exhaust system B.

4.7 Boundary conditions:

In order to make an analysis as close as possible to the physical reality, some boundary conditions were defined. The introduction of boundary conditions is equivalent to introduce constraints on the displacements of the exhaust systems.

4.7.1 Axial constraints:

4.7.1.1 Axial constraints on exhaust system A:

Some axial constraints along Y direction were defined in some areas of the lower supporting ring in order to simulate the structural supports applied on the exhaust system A and are discussed in detail in section 4.7.2.1. In reality, the X and Z displacements are not totally constrained due to the existence of supporting springs that allow shear and rolling motions, respectively, in order to give the exhaust system some freedom in what concerns displacements due to thermal expansion and mechanical/inertial external forces applied and caused by the vessel´s manoeuvres. So, in order to simulate these physical constraints, the X and Z displacement constraints were only applied in the lines of the right side of the lower supporting ring, enabling displacement on the left side of the lower supporting ring. The displacement constraints defined are shown in figure 4.27.

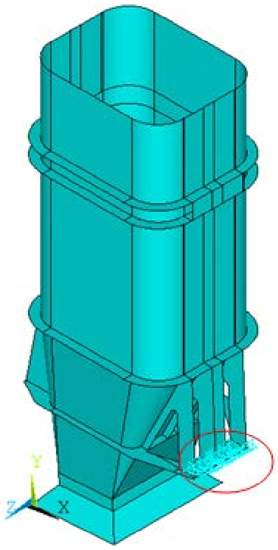

Figure 4.27: Displacement constraints applied on the lower supporting ring of exhaust system A (shown inside the oval line in red)

4.7.1.2 Axial constraints on exhaust system B:

Similar axial constraints, as those defined in exhaust system A, were defined in order to simulate the structural displacement constraints of exhaust system B. In reality, the X and Z displacements are not totally constrained due to the existence of elastomers that allow shear and rolling motions, respectively, in order to give the exhaust system some freedom in what concerns displacements due to thermal expansion and mechanical/inertial external forces applied and caused by the vessel´s manoeuvres. So, in order to simulate these physical constraints, the X and Z displacement constraints were only applied in the lines of the right side of the reinforcement ribs, enabling displacement on the left side of the reinforcement ribs. The displacement constraints defined are shown in figure 4.28.

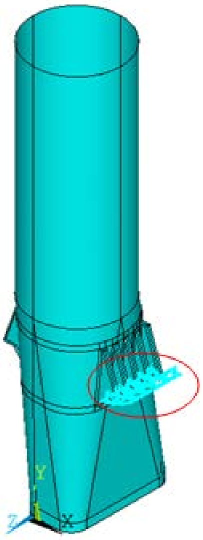

Figure 4.28: Displacement constraints applied on the reinforcement ribs of exhaust system B (shown inside the oval line in red)

4.7.2 Elastic Foundations:

Once exhaust system A is connected to the vessel’s structure by several wire rope isolators and exhaust system B is connected by several elastomers that are specifically applied to protect the structures from shocks and vibrations, elastic foundations were defined in the finite element model in order to simulate the absorption of these shocks and vibrations. These elastic foundations also help to reduce the stresses caused by the vertical and horizontal thermal expansions that occur on the exhaust systems[2].

The elastic foundation stiffness (EFS) is defined as the pressure required to produce a unit normal deflection of the foundation and is defined through the real constants defined for the finite element SHELL63 type.

The EFS value is given by (eq. 4.1):

$$EFS = \frac{k}{A} \tag{4.1}$$

Where k (N/m) is the elastic constant of the wire rope isolators or elastomers and A (m^2) is the area where they are applied. The elastic constant, k (N/m), is given by the force, F (N), applied on the wire rope isolators or elastomers and y (m) represents the vertical displacement that the force applied, F, causes (eq. 4.2).

$$k = \frac{F}{y} \tag{4.2}$$

In order to verify the EFS value calculation, a simple simulation was made in *Ansys*®.

In this simulation, a rectangular plate with 2 m length and a width of 1 m, supported by an elastic foundation, was created and it was applied a force, F, with the direction of the Y axis, equal to 0.01 N on each of its 28 nodes and an EFS value of 5 N/m^2.

Through the use of equation 4.1, using an EFS value of 5 N/m^2 and an area of 2 m^2, an elastic constant of 10 N/m was obtained.

$$EFS = \frac{k}{A} \Leftrightarrow k = EFS.A \Leftrightarrow k = 5 \times 2 = 10\, N/m$$

Finally, through equation 4.2 and using this elastic constant and the defined force, the vertical displacement expected, y, was obtained:

$$k = \frac{F}{y} \Leftrightarrow y = \frac{F}{k} \Leftrightarrow y = \frac{0.01 \times 28}{10} = 0{,}028\, m$$

Figure 4.29 shows the displacement value obtained in this simulation, which corresponds to the displacement value calculated.

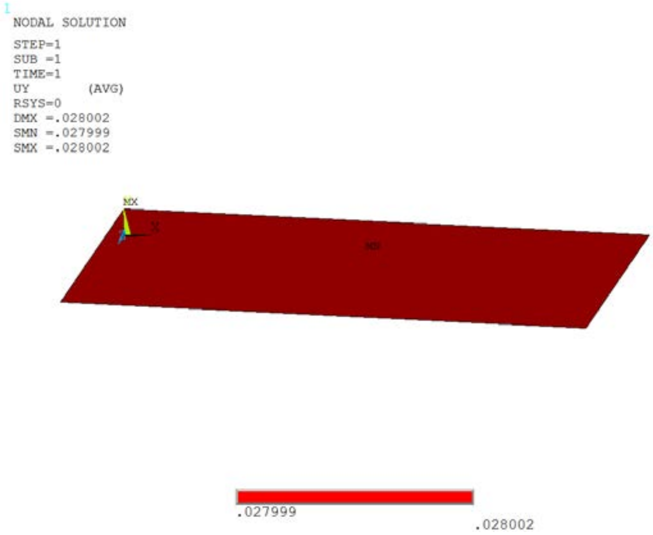

```
1
NODAL SOLUTION

STEP=1
SUB =1
TIME=1
UY        (AVG)
RSYS=0
DMX =.028002
SMN =.027999
SMX =.028002
```

Figure 4.29: Displacement value obtained on a 2 × 1 m^2 plate by the application of a 0,28 N force and an EFS value of 5 N/m^3

Once confirmed that the EFS value is given by equation 4.1, the EFS values for both exhaust system A and B were calculated (section 4.7.2.1), using the elastic constants, k, of the wire rope isolators and of the elastomers, existent in the exhaust system's connection to the vessel's structures and the areas in which they were applied on.

4.7.2.1 Elastic foundations defined on exhaust system A:

Exhaust system A has wire rope isolators on the right and left bottom sides of the lower supporting ring as well as on the right and left sides of the upper supporting ring of the exhaust system, that are specifically applied to protect the structures from shocks and vibrations [1, 2]. These wire rope isolators are submitted to compression, rolling and shear due to the inertial loads applied to exhaust system A (Chapter 4.6.1).

The wire rope isolators chosen to simulate the absorption of the shocks and vibrations were the *Enidine* WR20-200-08 [13], which can support the weight of exhaust system A and have an elastic constant, k, of 62940 N/m (Figure 4.30- Curve 1). Figure 4.30 shows the load diagrams for the WR20 series and the elastic constant, k, obtained for the WR20-200-08 [13].

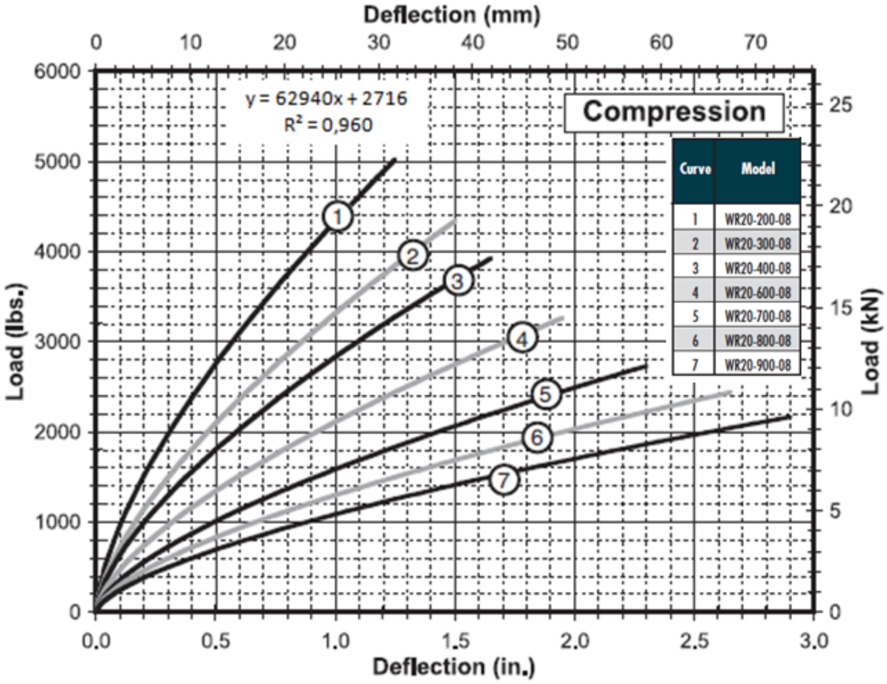

Figure 4.30: Load vs Deflection diagrams – WR20 series

Several elastic foundation stiffness values (EFS) were defined, according to the elastic constant obtained for the wire rope isolators (Figure 4.30) and to the areas where they were applied (Fig. 4.31). These elastic foundation areas were defined in order to simulate the effect of the wire rope isolators in compression.

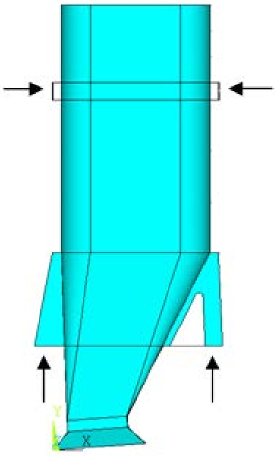

Figure 4.31: Location of the elastic foundations defined on exhaust system A (black arrows)

4.7.2.2 Elastic foundations defined on exhaust system B:

Exhaust system B uses elastomers on the base of the right and left reinforcement ribs as well as in an upper section of the exhaust system, which are specifically applied to protect the structures from shocks and vibrations. These elastomers are submitted to compression due to the inertial loads applied to exhaust system B (Chapter 4.6.1).

The elastomers chosen to simulate the absorption of the shocks and vibrations were the *Vibrostop* flexobloc FX 0-60 [14], which can support the weight of exhaust system B and have an elastic constant, k, of 47969 N/m (Figure 4.32). Figure 4.32 shows the load diagrams for the FX 0 series flexoblocs and the elastic constant, k, obtained for the FX 0-60 *Vibrostop* flexobloc [14].

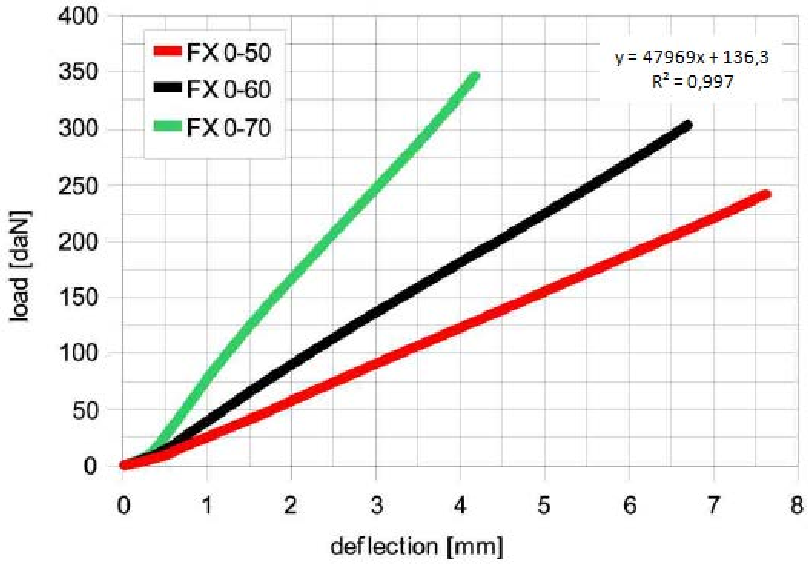

Figure 4.32: Load vs Deflection diagrams - *Vibrostop* flexobloc FX 0 series

Several elastic foundation stiffness values (EFS) were defined, according to the elastic constant, k, obtained for the elastomers (Figure 4.32) and to the areas where they were applied. These elastic foundation areas were defined in order to simulate the effect of the elastomers in compression. Figure 4.33 shows where the elastic foundations were applied.

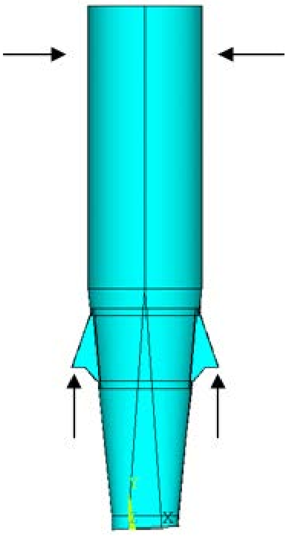

Figure 4.33: Location of the elastic foundations defined on exhaust system B (black arrows)

4.8 Pressure distribution:

Before applying the pressure caused by the flow of the exhaust gases passing through the exhaust systems, the direction of the normal of some areas present in the finite element model was inverted, in order to ensure that positive values of pressure would define an internal pressure, while negative values of pressure would define an external pressure.

The mass flow rate of the exhaust gases, q_m, that passes through each exhaust system was considered to be the maximum mass flow rate that the gas turbine of each vessel generates.

The exhaust gases that flow inside the exhaust systems under study were considered almost air, once 70% of nitrogen existing in it passes through the gas turbine without being modified. Thus, the density of the exhaust gases, ρ, was assumed to be equal to the air density and to remain at a temperature of 500 ºC throughout all the exhaust systems [1, 2, 15]. Therefore, an air density of 0.457 Kg/m^3 (air at 500 ºC) was considered.

Since the pressure varies with the area of the sections through which the mass flow rate of the exhaust gases is passing, the pressure was calculated in different sections of the exhaust systems under study in order to obtain each exhaust systems' pressure distribution.

The pressures were calculated through the Bernoulli's equation (eq. 4.3) [16]:

$$P + \frac{1}{2}.\rho.V^2 = \text{const.} \tag{4.3}$$

where the velocity of the exhaust gases is obtained by equation 4.4:

$$V = \frac{q_m}{\rho.A} \tag{4.4}$$

Therefore, the pressure on each section (P_S) was calculated from equation 4.5, using the atmospheric pressure (P_0) and the area of the outlet section (A_0) as the reference:

$$P_s + \frac{1}{2}.\frac{{q_m}^2}{\rho.{A_s}^2} = P_0 + \frac{1}{2}.\frac{{q_m}^2}{\rho.{A_0}^2} \tag{4.5}$$

The pressures calculated and defined in *Ansys*® are relative pressures.

4.8.1 Pressure distribution in exhaust system A:

The areas of six different sections of the exhaust system were calculated, in order to define the pressure distribution in exhaust system A. Figure 4.34 shows the sections where the areas and the relative pressures were calculated.

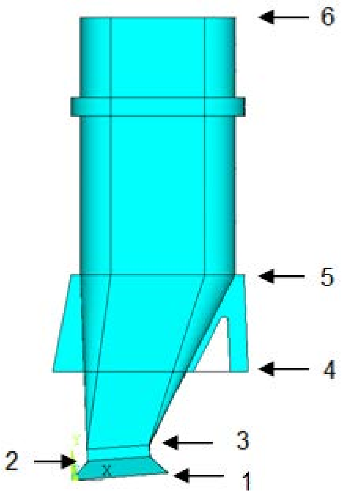

Figure 4.34: Sections of exhaust system A where the areas and relative pressures were calculated

The mass flow rate considered in the calculation of the relative pressures applied on each section shown was the sum of the maximum exhaust gases' mass flow rate that the gas turbine of vessel A generates with a secondary mass flow rate of air, at room temperature, that is mixed with the main flow to diminish the temperature of the fluid that enters in the exhaust system. The fluid's total mass flow rate considered was q_m= 68 Kg/s [2].

Once section 1 has an area of 3.452 m^2 (A_1) and bearing in mind that the mass flow rate of the exhaust gases is 68 Kg/s, the air density at 500 ºC is 0.457 Kg/m^3 and that the outlet area (A_0) has 4.340m^2, the relative pressure in section 1 (P_1) was calculated through equation 4.5:

$$P_1 + \frac{1}{2}.\frac{{q_m}^2}{\rho.{A_1}^2} = P_0 + \frac{1}{2}.\frac{{q_m}^2}{\rho.{A_0}^2} \Leftrightarrow P_1 = P_0 + \frac{1}{2}.\left(\frac{{q_m}^2}{\rho.{A_0}^2} - \frac{{q_m}^2}{\rho.{A_1}^2}\right)$$

$$\Leftrightarrow P_1 = 0 + \frac{1}{2}.\left(\frac{68^2}{0.457\times 4.340^2} - \frac{68^2}{0.457\times 3.452^2}\right)$$

$$P_1 = -156 \text{ Pa}$$

Section 2 has an area of 1.653 m^2 (A_2). Using the same mass flow rate and air density as used for P_1, the relative pressure in section 2 (P_2) was calculated (eq. 4.5):

$$P_2 = P_0 + \frac{1}{2}.\left(\frac{{q_m}^2}{\rho.{A_0}^2} - \frac{{q_m}^2}{\rho.{A_2}^2}\right) \Leftrightarrow P_2 = 0 + \frac{1}{2}.\left(\frac{68^2}{0.457\times 4.340^2} - \frac{68^2}{0.457\times 1.653^2}\right)$$

$$P_2 = -1583 \text{ Pa}$$

Since there is no area variation from section 2 to section 3 (A_2=A_3), the pressure remains constant and equal to the relative pressure in section 2, P_2:

$$P_3 = P_2 = -1583 \text{ Pa}$$

Section 4 has an area of 4.026 m^2 (A_4). Repeating the same calculations (eq. 4.5), the pressure in section 4 was obtained:

$$P_4 = P_0 + \frac{1}{2}.\left(\frac{{q_m}^2}{\rho.{A_0}^2} - \frac{{q_m}^2}{\rho.{A_4}^2}\right) \Leftrightarrow P_4 = 0 + \frac{1}{2}.\left(\frac{68^2}{0.457\times 4.340^2} - \frac{68^2}{0.457\times 4.026^2}\right)$$

$$P_4 = -44 \text{ Pa}$$

Section 5 has a total area of 5.113 m^2. However, from section 5 to section 6 there are three silencers which reduce the exhaust gases flow area to a value of 3.401 m^2(A_5). Using once again equation 4.5 and the given values of mass flow rate and air density at 500 ºC, the pressure in section 5 was calculated:

$$P_5 = P_0 + \frac{1}{2}.\left(\frac{{q_m}^2}{\rho.{A_0}^2} - \frac{{q_m}^2}{\rho.{A_5}^2}\right) \Leftrightarrow P_5 = 0 + \frac{1}{2}.\left(\frac{68^2}{0.457\times 4.340^2} - \frac{68^2}{0.457\times 3.401^2}\right)$$

$$P_5 = -169 \text{ Pa}$$

Since there is no area variation from section 5 to section 6 (A_5=A_6), the pressure remains constant and equal to the pressure in section 5, P_5:

$$P_6 = P_5 = -169 \text{ Pa}$$

These are the theoretical pressures that should be applied to the exhaust system. However, there was a study made to the exhaust gases flow of this exhaust system using a Computational Fluid Dynamics software (CFD), where the predominant pressure obtained is higher than the theoretical pressures obtained for the critical sections in study. Due to this fact, the pressure was defined according to the pressure distribution obtained through this CFD analysis [8, 15].

Figure 4.35 shows the pressure distribution in exhaust system A, obtained through CFD analysis from previous studies made to this exhaust system [15].

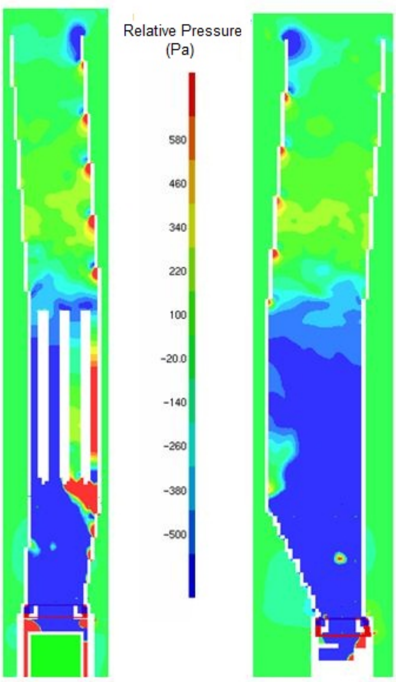

Figure 4.35: Pressure distribution in exhaust system A obtained through CFD analysis

High pressure concentrations were registered near the silencers, due to vortexes caused by the passage of the exhaust gases through the silencers, and also near the inlet section of the exhaust system. However, the pressure defined was the predominant pressure registered in the critical sections of exhaust system A in study. Thus, the defined pressure for the analysis is assumed to be constant through all the exhaust system (from section 1 to section 6), with a value of -500 Pa.

Figure 4.36 shows the pressure distribution obtained for exhaust system A.

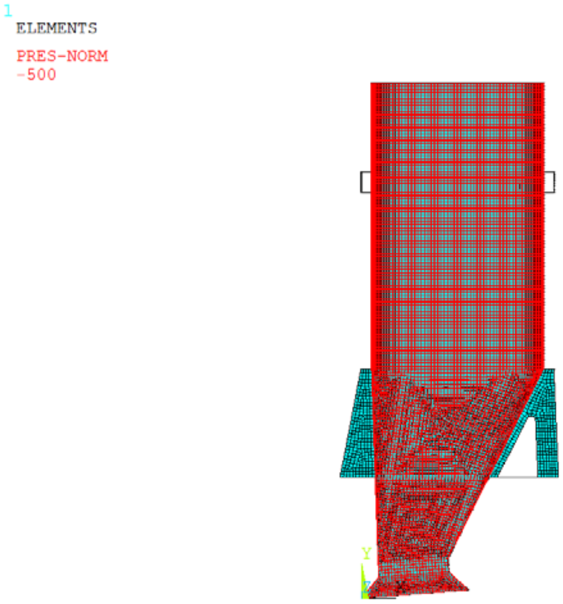

Figure 4.36: Pressure distribution applied in the finite element model of exhaust system A (pressure in Pascal)

Once all the steps referred from chapter 4.1 to 4.4 and 4.6 to 4.8, regarding exhaust system A were fulfilled and the thermal analysis file (.RTH file) obtained (chapter 4.5.1) and loaded, structural analyses using the finite element SHELL63 type (defined in chapter 4.2) were ready to be run. Therefore, these steps defined the program that was written using the Ansys Parametric Design

Language (APDL) to determine the structural response of the current exhaust system's geometry and of all the redesigned structures studied.

4.8.2 Pressure distribution in exhaust system B:

In order to determine the pressure distribution applied on exhaust system B, the areas of four different sections of the exhaust system were calculated. Figure 4.37 shows the sections where the areas and the relative pressures were calculated.

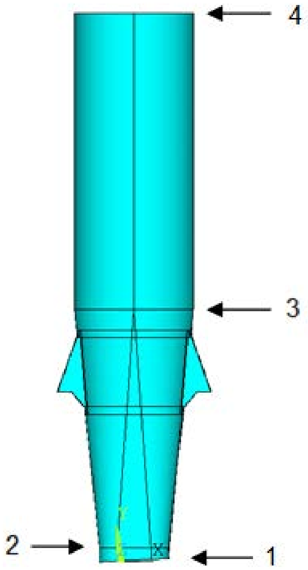

Figure 4.37: Sections of exhaust system B where the areas and relative pressures were calculated

The mass flow rate value considered in the calculation of the relative pressures applied on each section shown is the maximum mass flow rate of exhaust gases that the gas turbine of vessel B generates, q_m= 67 Kg/s [17].

Despite the gas turbine in vessel A being different from the one in vessel B, similar mass flow rates of exhaust gases are generated.

Once section 1 has an area of 1.902 m^2 (A_1) and bearing in mind that the mass flow rate of the exhaust gases is 67 Kg/s, the air density at 500 ºC is 0.457 Kg/m^3 and that the outlet area (A_0) has 2.274m^2, the relative pressure in section 1 (P_1) was calculated through equation 4.5:

$$P_1 + \frac{1}{2}.\frac{{q_m}^2}{\rho.{A_1}^2} = P_0 + \frac{1}{2}.\frac{{q_m}^2}{\rho.{A_0}^2} \Leftrightarrow P_1 = P_0 + \frac{1}{2}.\left(\frac{{q_m}^2}{\rho.{A_0}^2} - \frac{{q_m}^2}{\rho.{A_1}^2}\right)$$

$$\Leftrightarrow P_1 = 0 + \frac{1}{2}.\left(\frac{67^2}{0.457\times 2.274^2} - \frac{67^2}{0.457\times 1.902^2}\right)$$

$$P_1 = -408\ \mathrm{Pa}$$

Once there is no variation of area from section 1 to section 2 (A_1=A_2), the pressure remains constant and equal to the relative pressure applied on section 1, P_1:

$$P_2 = P_1 = -408\ \mathrm{Pa}$$

Section 3 has an area of 2.274 m^2 (A_3). Using the same mass flow rate and air density as used for P_1, the relative pressure applied on section 3 (P_3) was calculated (eq. 4.5):

$$P_3 = P_0 + \frac{1}{2}.\left(\frac{{q_m}^2}{\rho.{A_0}^2} - \frac{{q_m}^2}{\rho.{A_3}^2}\right) \Leftrightarrow P_3 = 0 + \frac{1}{2}.\left(\frac{67^2}{0.457\times 2.274^2} - \frac{67^2}{0.457\times 2.274^2}\right)$$

$$P_3 = 0\ \mathrm{Pa}$$

Since there is no area variation from section 3 to section 4 (A_3=A_4), the pressure remains constant and equal to the pressure in section 3, P_3:

$$P_4 = P_3 = 0\ \mathrm{Pa}$$

From the relative pressure values obtained, one may notice that the highest pressure value occurs from section 1 to section 2 and that there is no relative pressure applied in the exhaust system from section 3 to section 4.

To apply a correct pressure distribution in the finite element model of vessel B's exhaust system, some functions were defined in order to simulate the pressure variations throughout the sections where the area varies.

As mentioned before, due to fact that there is no variation in the areas' values from section 1 to section 2 (A_1=A_2), the pressure remains constant throughout these sections with a constant value of -408 Pa.

From section 2 to section 3, a mathematical function was determined to represent the pressure variation due to the values of the cross section areas of exhaust system B, starting from a pressure of -408 Pa in section 2 to a final pressure of 0 Pa in section 3.

Finally, there was no pressure defined from section 3 to section 4, because the pressure value between these sections is 0 Pa.

Figure 4.38 shows the pressure distribution obtained for exhaust system B.

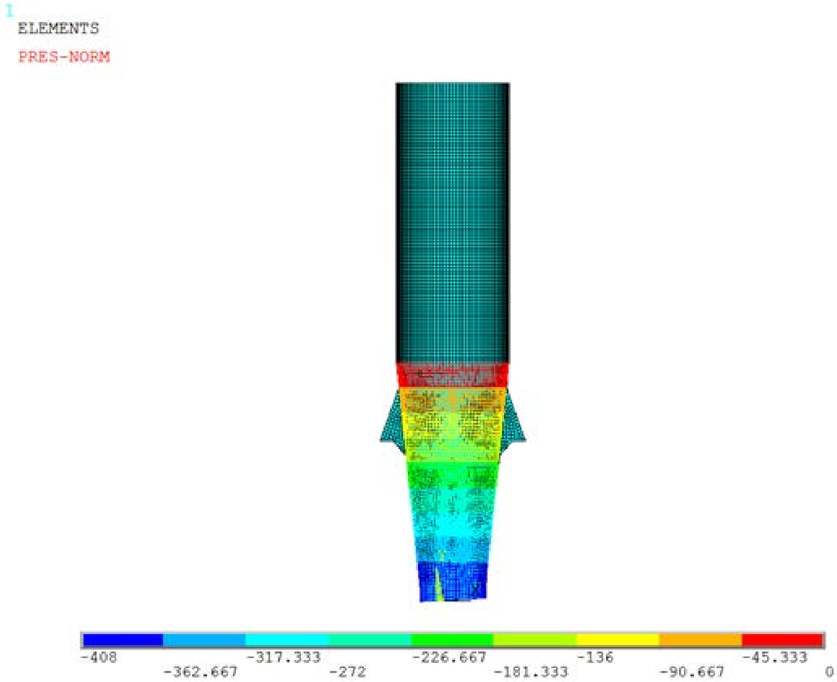

Figure 4.38 Pressure distribution applied in the finite element model of exhaust system B (pressure in Pascal)

Once all the steps referred from chapter 4.1 to 4.4 and 4.6 to 4.8, regarding exhaust system B were fulfilled and the thermal analysis file (.RTH file) obtained (chapter 4.5.2) and loaded, structural analyses using the finite element SHELL63 type (defined in chapter 4.2) were ready to be run. Therefore, these steps defined the program that was written using the Ansys Parametric Design Language (APDL) to determine the structural response of the current exhaust system's geometry and of all the redesigned structures studied.

5. Redesign of the exhaust systems

In order to reduce the stresses induced on the exhaust systems under study and, hence, enhance its fatigue lives, several redesign structures were defined and assessed.

The current exhaust systems (A and B) and many of the redesigned exhaust systems were considered to be entirely fabricated of the AISI 316L austenitic stainless steel and were simulated considering normal in-service conditions (without 2G deceleration) as well as the overload conditions (superposition of the 2G deceleration).

Studies were also made, considering that the current exhaust systems (A and B) and many of the redesigned exhaust systems were entirely fabricated with the 445M2 ferritic stainless steel and were simulated considering normal in-service conditions (without 2G deceleration) as well as the overload conditions (superposition of the 2G deceleration).

The exhaust systems plate thicknesses obtained in this chapter, were applied in chapter 4.2, in order to analyse the thermal and structural behaviour of each redesigned exhaust system under study.

5.1 Modifications proposed to exhaust system A

5.1.1 Current geometry:

The current geometry of exhaust system A and its plate's thicknesses are shown in figure 5.1. In this geometry, the exhaust system's pipe, Figure 5.1-(1), has a wall thickness of 4 mm. The reinforcement ribs on the right side (2) have a thickness of 13 mm, while the left side reinforcement ribs (3) have a thickness of 11 mm. The lower supporting ring (4) has a thickness of 15 mm, the intermediate supporting ring (5) has a thickness of 30 mm and the upper supporting ring (6) has plates 10 mm thick.

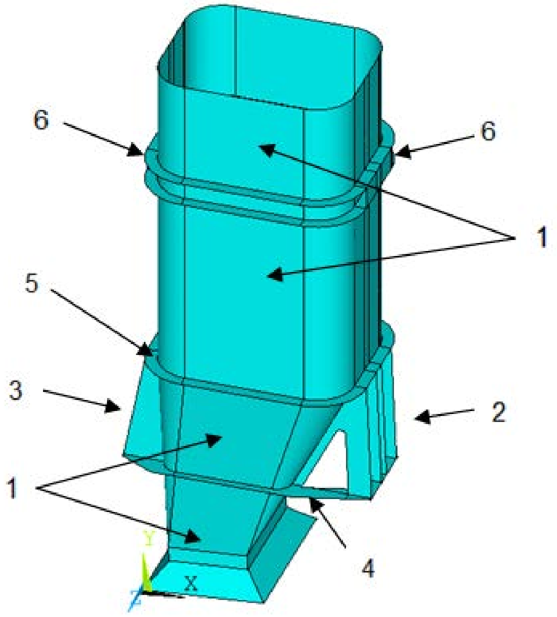

Figure 5.1: Overall view of the current geometry of exhaust system A. Identification of the different plate's thicknesses in the exhaust system A

All the subsequent modifications presented in the present section are based on the current geometry of exhaust system A.

5.1.2 Addition of four vertical reinforcement ribs:

In this modification, four vertical reinforcement ribs (two on each side of the exhaust system) were added to the current geometry of exhaust system A in order to evaluate the mechanical and thermal behaviour of the exhaust system when the intermediate section is vertically reinforced. Figure 5.2 shows an oblique view and a right side view of this modified geometry of exhaust system A.

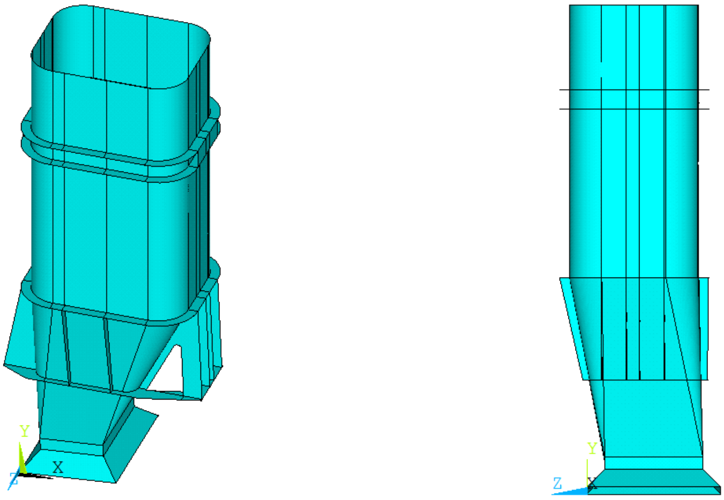

Figure 5.2: Addition of four vertical reinforcement ribs on the current geometry of exhaust system A

A technical drawing with the position and dimensions of the four vertical reinforcement ribs added to exhaust system A, is shown in annex A, A5.

The four vertical reinforcement ribs, Figure 5.3-(7), added to the exhaust system's current geometry were defined with a thickness of 12 mm. Doing this, the reinforcement ribs wil tend to expand in a similar manner to the right and left side reinforcement ribs, Figure 5.3-(2),(3), that have a thickness of 13 mm and 11 mm, respectively.

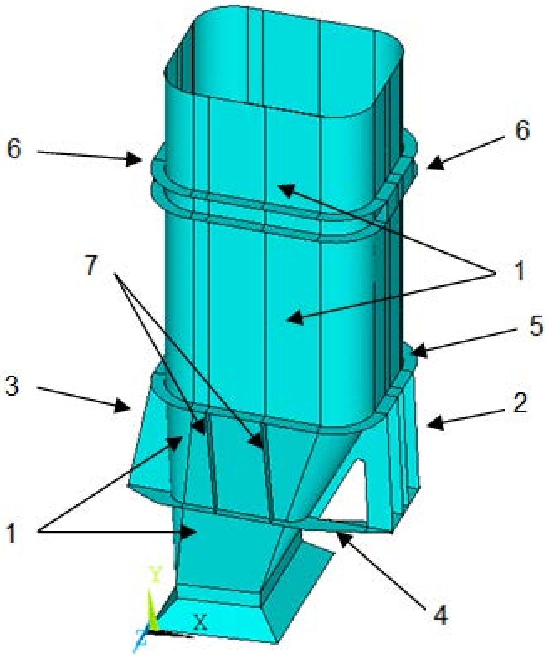

Figure 5.3: Distribution of the plates' thicknesses of a modified geometry of exhaust system A

5.1.3 Addition of two vertical reinforcement ribs:

In this modification, two vertical reinforcement ribs (one on each side of the exhaust system) were added to the current geometry of exhaust system A in order to evaluate the mechanical and thermal behaviour of the exhaust system when the intermediate section is vertically reinforced. Figure 5.4 shows an oblique view and a right side view of this modified geometry of exhaust system A.

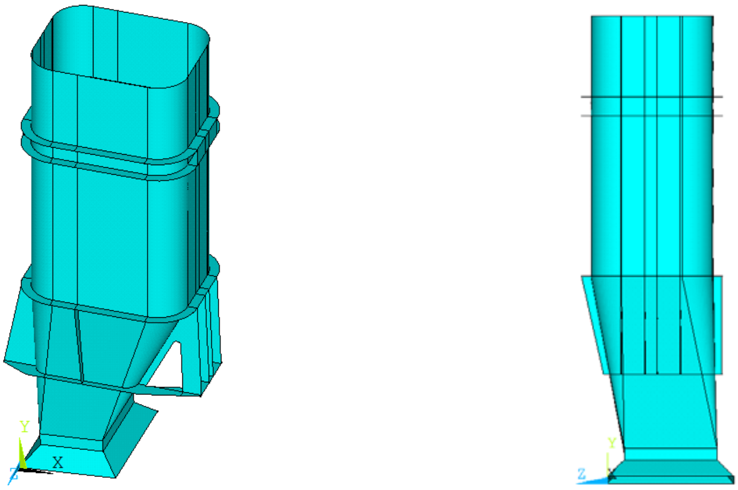

Figure 5.4: Addition of two vertical reinforcement ribs on the current geometry of exhaust system A

A technical drawing with the position and dimensions of the two vertical reinforcement ribs added to exhaust system A, is shown in annex A, A6.

The two vertical reinforcement ribs, Figure 5.5-(7), added to the exhaust system's current geometry were defined with a thickness of 12 mm. Doing this, the reinforcement ribs wil tend to expand in a similar manner to the right and left side reinforcement ribs, Figure 5.5-(2),(3), that have a thickness of 13 mm and 11 mm, respectively.

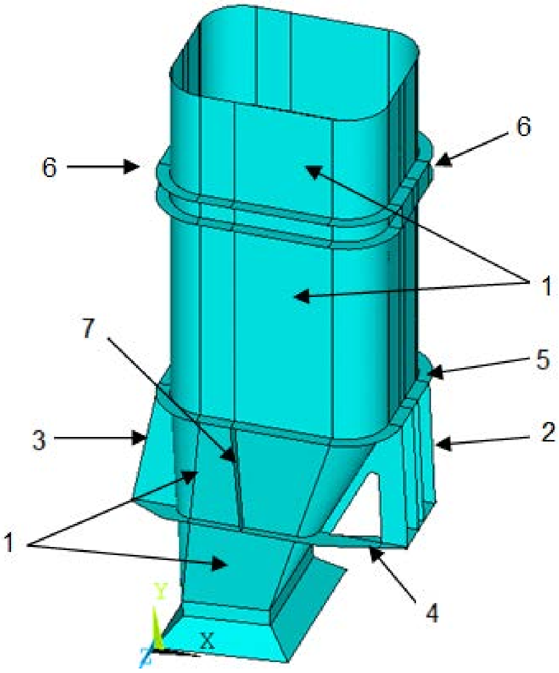

Figure 5.5: Distribution of the plates' thicknesses of a modified geometry of exhaust system A

5.1.4 Addition of one horizontal reinforcement ring:

In this modification, an horizontal reinforcement ring was added to the current geometry of exhaust system A in order to evaluate its mechanical and thermal behaviour when the intermediate section is horizontally reinforced. Figure 5.6 shows an isometric view and a left side view of this modified geometry of exhaust system A.

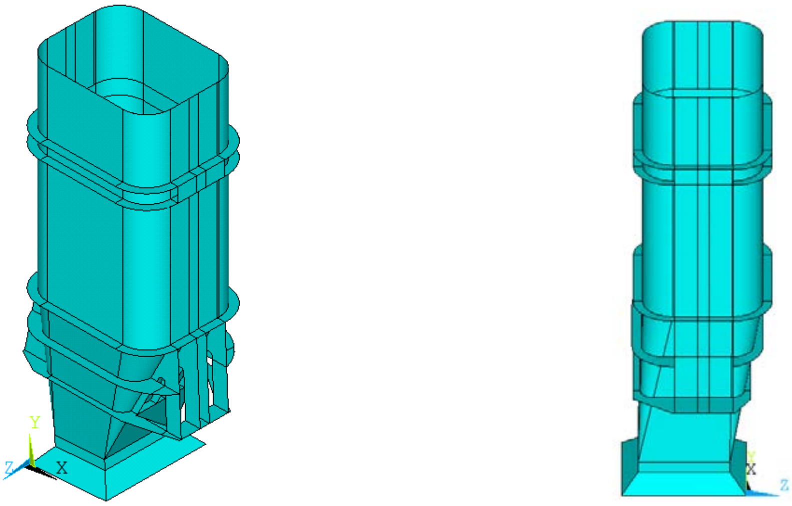

Figure 5.6: Addition of an horizontal reinforcement ring on the current geometry of exhaust system A

A technical drawing with the position and dimensions of the horizontal reinforcement ring added to exhaust system A, is shown in annex A, A7.

The horizontal supporting ring, Figure 5.7-(7), added to the exhaust system's current geometry were defined with a thickness of 12 mm. Figure 5.7 shows the addition of the horizontal reinforcement ring and the distribution of the plate thicknesses on this new geometry.

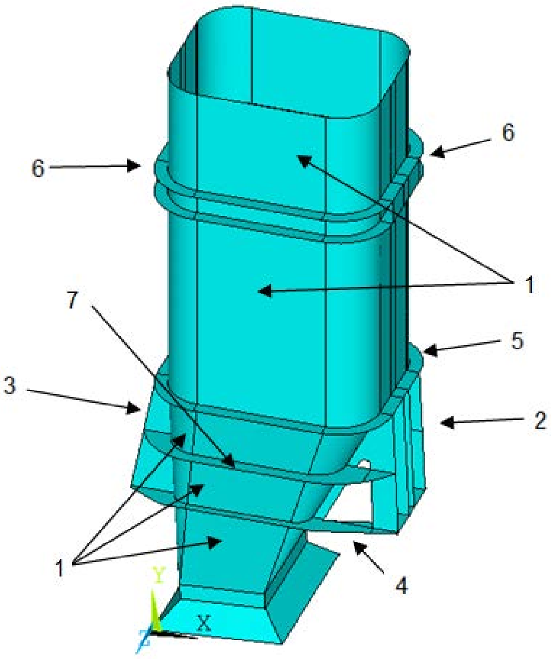

Figure 5.7: Distribution of the plates' thicknesses of a modified geometry of exhaust system A

5.1.5 Thickness change of the intermediate section of the exhaust system from 4 mm to 12 mm:

This modification consisted in the change of the plate thicknesses of the intermediate section of the exhaust system from 4 mm to 12 mm, Fig. 5.8-(7). This was done in order to make this section expand similarly to the right and left side reinforcement ribs, Figure 5.8-(2),(3), that have a thickness of 13 mm and 11 mm, respectively, and enhance the thermal shock response, lowering the thermal stresses induced in the intermediate section. Also it is expected a reduction of the mechanical stresses induced in the section.

In this geometry, the exhaust system pipe, Figure 5.8-(1), has a wall thickness of 4 mm. The reinforcement ribs on the right side (2) have a thickness of 13 mm, while the left side reinforcement ribs (3) have a thickness of 11 mm. The lower supporting ring (4) has a thickness of 15 mm, the intermediate supporting ring (5) has a thickness of 30 mm and the upper supporting ring (6) has plates with 10 mm thickness. The intermediate section of the exhaust system (7) has a wall thickness of 12 mm. Figure 5.8 shows the distribution of the plates' thicknesses on this new geometry.

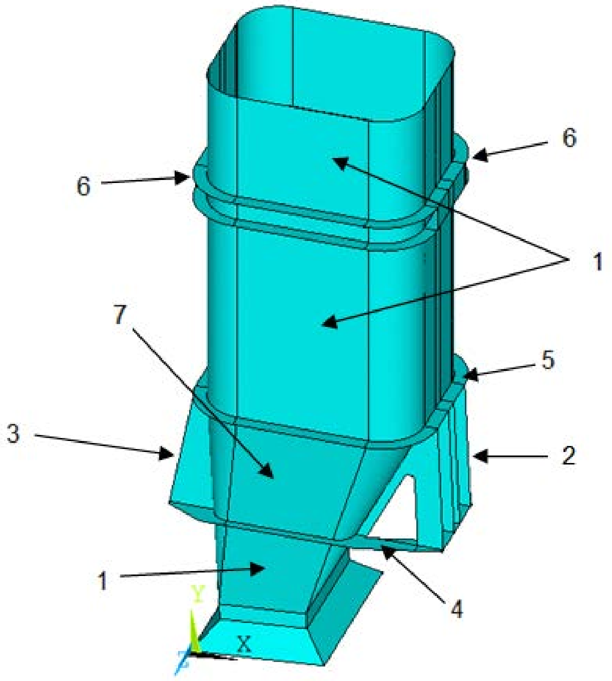

Figure 5.8: Distribution of the plates' thicknesses of a modified geometry of exhaust system A

5.1.6 Thickness change of the intermediate supporting ring from 30 mm to 12 mm:

This modification consisted in the change of the thickness of the intermediate supporting ring from 30 mm to 12 mm, in order to evaluate the mechanical and thermal behaviour of exhaust system A when the thickness of the intermediate supporting ring was decreased.

In this geometry, the exhaust system pipe, Figure 5.9-(1), has a wall thickness of 4 mm. The reinforcement ribs on the right side (2) have a thickness of 13 mm, while the left side reinforcement ribs (3) have a thickness of 11 mm. The lower supporting ring (4) has a 15 mm thickness, the intermediate supporting ring (5) has a 12 mm thickness and the upper supporting ring (6) has plates with 10 mm of thickness. Figure 5.9 shows the distribution of the plate thicknesses on this new geometry.

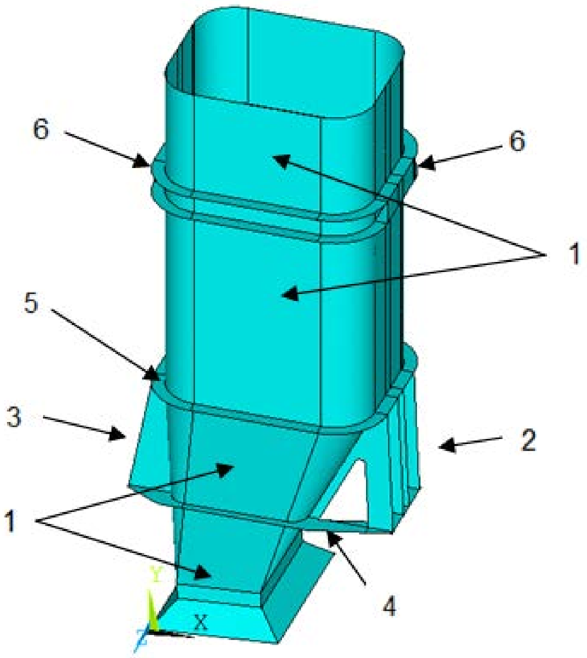

Figure 5.9: Distribution of the plates' thicknesses of a modified geometry of exhaust system A

5.1.7 Thickness change of the lower and intermediate supporting rings to 4 mm:

This modification consisted in the change of the plate's thicknesses of the lower and intermediate supporting rings from 15 mm and 30 mm, respectively, to 4 mm, in order to uniform the thicknesses of almost all the plates that compose the critical section of the exhaust system A.

In this geometry, the exhaust system pipe, Figure 5.10-(1), has a wall thickness of 4 mm. The reinforcement ribs on the right side (2) have a thickness of 13 mm, while the left side reinforcement ribs (3) have a thickness of 11 mm. The lower supporting ring (4) and the intermediate supporting ring (5) have plates' thicknesses equal to 4 mm and the upper supporting ring (6) has plates with 10 mm thick. Figure 5.10 shows the distribution of the plate thicknesses on this new geometry.

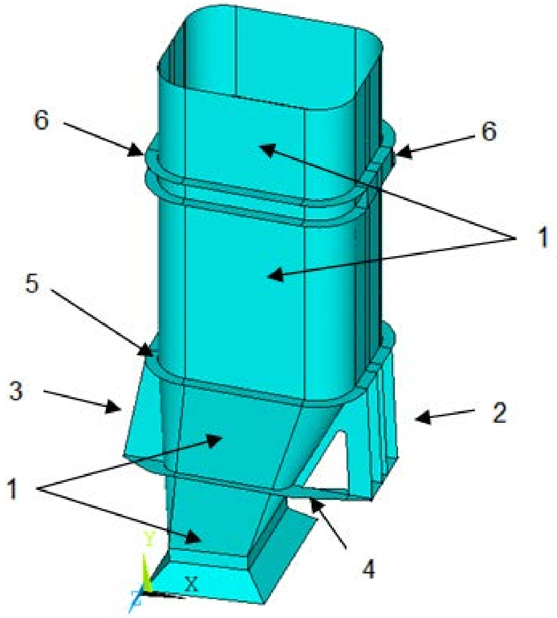

Figure 5.10: Distribution of the plates' thicknesses of a modified geometry of exhaust system A

5.1.8 Thickness change of the vertical reinforcement ribs to 4 mm:

This modification consisted in the change of the thickness of the right and left reinforcement ribs from 13 mm and 11 mm, respectively, to 4 mm, in order to uniform the thicknesses of the vertical reinforcement ribs and the intermediate section of exhaust system A.

In this geometry, the exhaust system pipe, Figure 5.11-(1), has a wall thickness of 4 mm. The reinforcement ribs, on the right and left side, (2) and (3), respectively, have a thickness of 4 mm. The lower supporting ring (4) has a thickness of 15 mm and the intermediate supporting ring (5) a thickness of 30 mm. The upper supporting ring (6) has plates with 10 mm of thickness. Figure 5.11 shows the distribution of the plates' thicknesses on this new geometry.

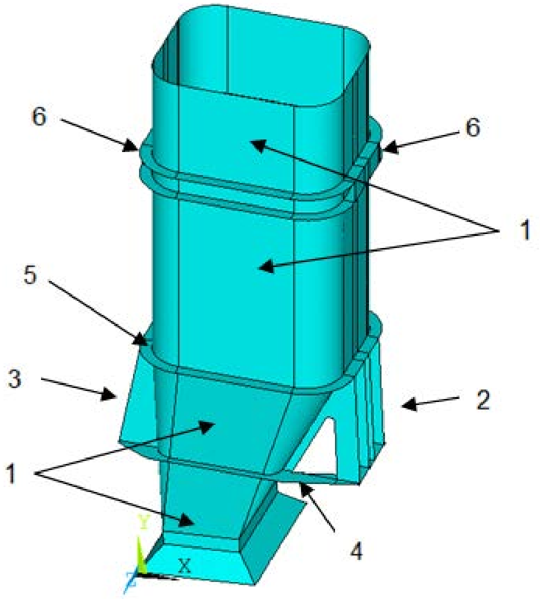

Figure 5.11: Distribution of the plates' thicknesses of a modified geometry of exhaust system A

5.1.9 Thickness change of all the exhaust system's plates to 4 mm:

This modification consisted on changing all the exhaust system's plates to 4 mm, Figure 5.12-(1) to (6), in order to uniform the thermal expansion of all the plates of exhaust system A

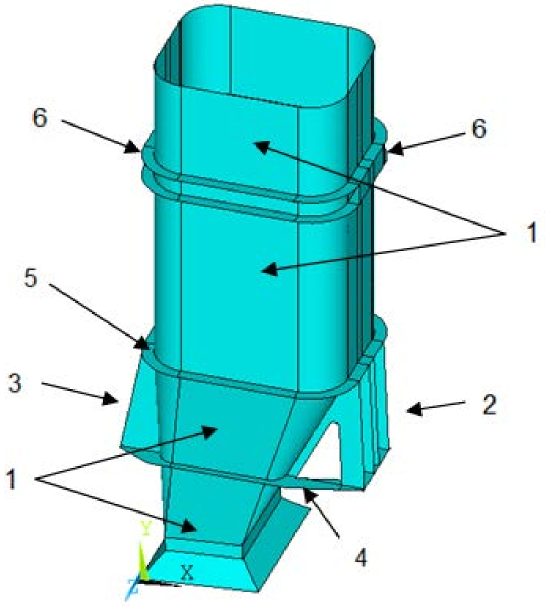

Figure 5.12: Distribution of the plates' thicknesses of a modified geometry of exhaust system A

5.1.10 Thickness change of all the exhaust system's plates to 12 mm:

Similar to what was presented in section 5.1.9, this modification consisted on changing all the exhaust system's plates to 12 mm, Figure 5.13-(1) to (6), in order to uniform the thermal expansion of all the plates of exhaust system A and also improve the mechanical response of the exhaust system.

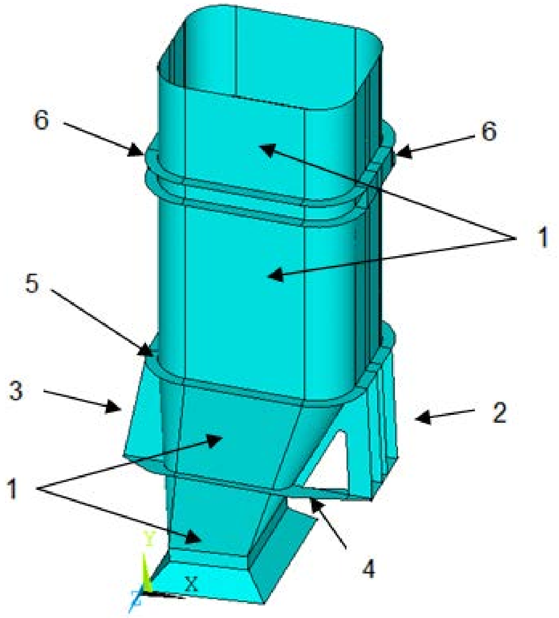

Figure 5.13: Distribution of the plates' thicknesses of a modified geometry of exhaust system A

5.1.11 Removal of the outer vertical reinforcement ribs:

In this modification, the outer vertical reinforcement ribs were removed from the right and left sides of the current geometry of exhaust system A, in order to try to reduce the thermal and mechanical stresses induced in the structure. Figure 5.14 shows a isometric views of this modified geometry of exhaust system A.

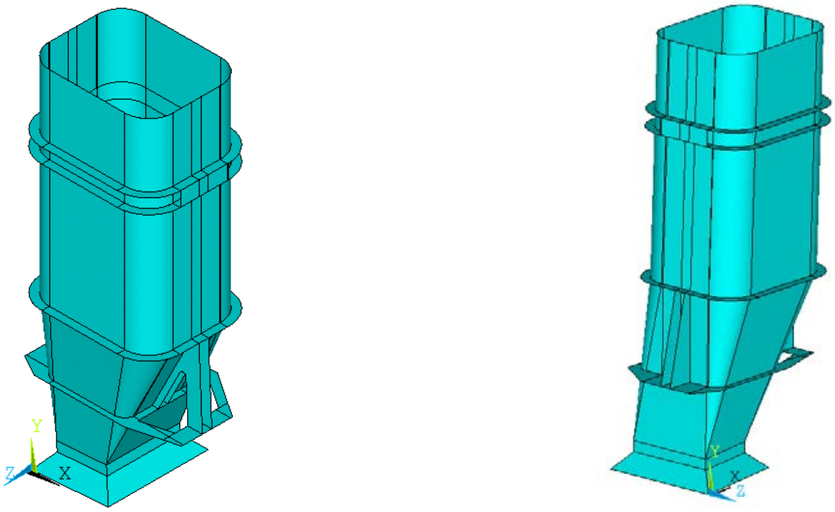

Figure 5.14: Removal of the outer vertical reinforcement ribs of the current geometry of exhaust system A

This modified geometry has the same plates' thicknesses of the current geometry of exhaust system A. Thus, the exhaust system pipe, Figure 5.15-(1), has a wall thickness of 4 mm. The reinforcement ribs on the right side (2) have a thickness of 13 mm, while the left side reinforcement ribs (3) have a thickness of 11 mm. The lower supporting ring (4) has a 15 mm thickness, the intermediate supporting ring (5) has a 30 mm thickness and the upper supporting ring (6) has plates with 10 mm thickness. Figure 5.15 shows the removal of the outer vertical reinforcement ribs and the distribution of the plates' thicknesses on this new geometry.

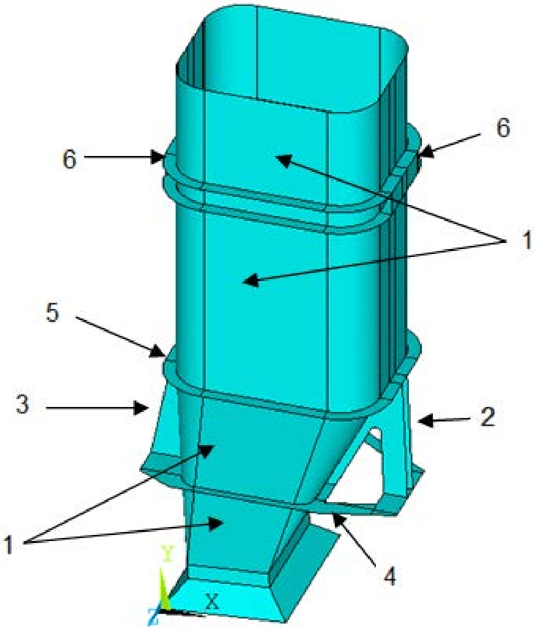

Figure 5.15: Distribution of the plates' thicknesses of a modified geometry of exhaust system A

5.1.12 Removal of the inner vertical reinforcement ribs:

In this modification, the inner vertical reinforcement ribs were removed from the current geometry of exhaust system A, in order to try to reduce the thermal and mechanical stresses induced in the structure. Figure 5.16 shows isometric views of this modified geometry of exhaust system A.

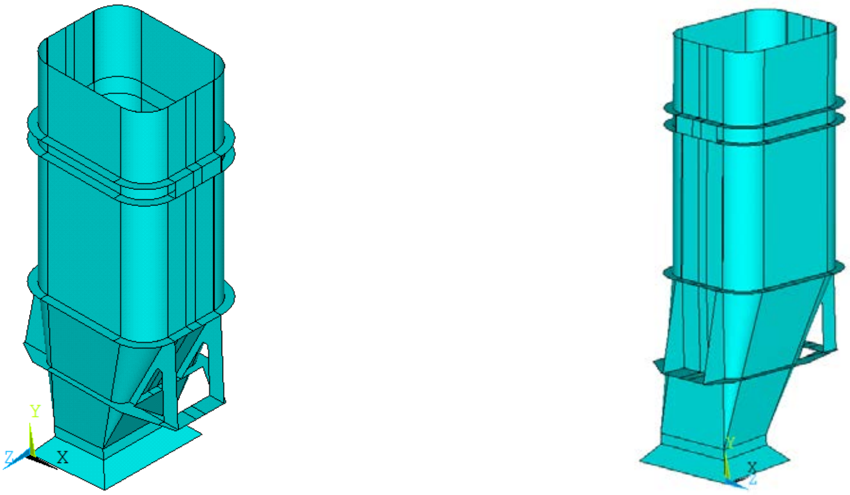

Figure 5.16: Removal of the inner vertical reinforcement ribs of the current geometry of exhaust system A

This modified geometry has the same plates' thicknesses of the current geometry of exhaust system A. Thus, the exhaust system pipe, Figure 5.17-(1), has a wall thickness of 4 mm. The reinforcement ribs on the right side (2) have a thickness of 13 mm, while the left side reinforcement ribs (3) have a thickness of 11 mm. The lower supporting ring (4) has a 15 mm thickness, the intermediate supporting ring (5) has a 30 mm thickness and the upper supporting ring (6) has plates with 10 mm of thickness. Figure 5.17 shows the removal of the inner vertical reinforcement ribs and the distribution of the plate thicknesses on this new geometry.

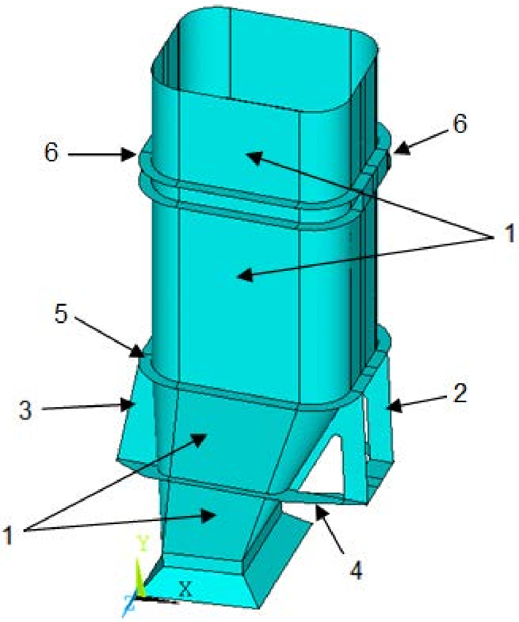

Figure 5.17: Distribution of the plates' thicknesses of a modified geometry of exhaust system A

5.1.13 Partial removal of the lower supporting ring:

In the modification proposed, the lower supporting ring was partially removed from the current geometry of exhaust system A (Fig. 5.18), having remained only the areas where the elastic foundations were defined. This modification attempt was done in order to assess the influence of the lower supporting ring on the mechanical and thermal behaviour of exhaust system A. Figure 5.18 shows a isometric views of this modified geometry of exhaust system A.

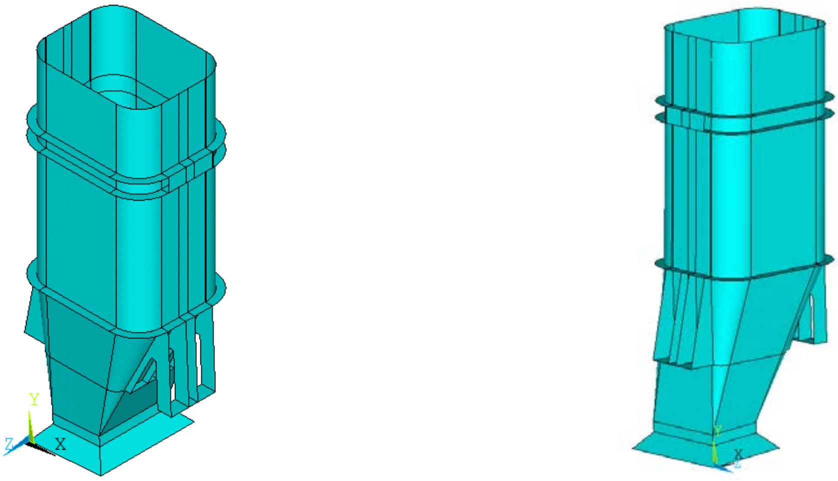

Figure 5.18: Partial removal of the lower supporting ring of the current geometry of exhaust system A

This geometry has the same plates' thicknesses of the current geometry of exhaust system A. So, the exhaust system pipe, Figure 5.19-(1), has a wall thickness of 4 mm. The reinforcement ribs on the right side (2) have a thickness of 13 mm, while the left side reinforcement ribs (3) have a thickness of 11 mm. The lower supporting ring that remained (4) has a thickness of 15 mm, the intermediate supporting ring (5) has a thickness of 30 mm and the upper supporting ring (6) has plates 10 mm thick. Figure 5.19 shows the partial removal of the lower supporting ring and the distribution of the plates' thicknesses on this new geometry.

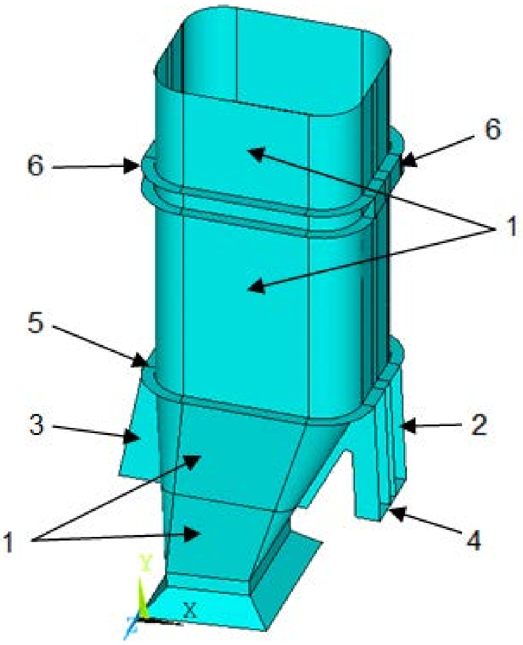

Figure 5.19: Distribution of the plates' thicknesses of a modified geometry of exhaust system A

5.1.14 Partial removal of the intermediate supporting ring:

In this modification, the intermediate supporting ring was partially removed from the current geometry of exhaust system A, remaining only the areas that are attached to the reinforcement ribs. This attempt was done in order to assess the influence of the intermediate supporting ring on the mechanical and thermal behaviour of exhaust system A. Figure 5.20 shows isometric views of this modified geometry of exhaust system A.

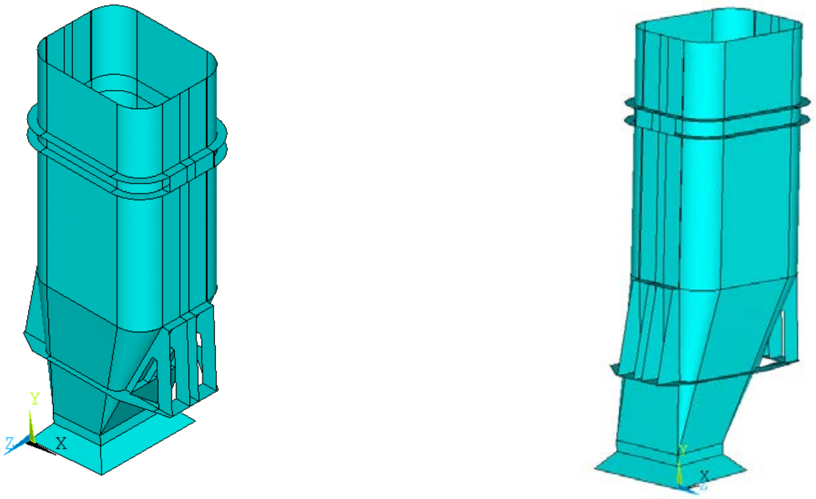

Figure 5.20: Partial removal of the intermediate supporting ring of the current geometry of exhaust system A

This geometry has the same plates' thicknesses of the current geometry of exhaust system A. Thus, the exhaust system pipe, Figure 5.21-(1), has a wall thickness of 4 mm. The reinforcement ribs on the right side (2) have a thickness of 13 mm, while the left side reinforcement ribs (3) have a thickness of 11 mm. The lower supporting ring (4) has a thickness of 15 mm, the partial removed intermediate supporting ring that remained (5) has a thickness of 30 mm and the upper supporting ring (6) has plates 10 mm thick. Figure 5.21 shows the partial removal of the intermediate supporting ring and the distribution of the plates' thicknesses on this new geometry.

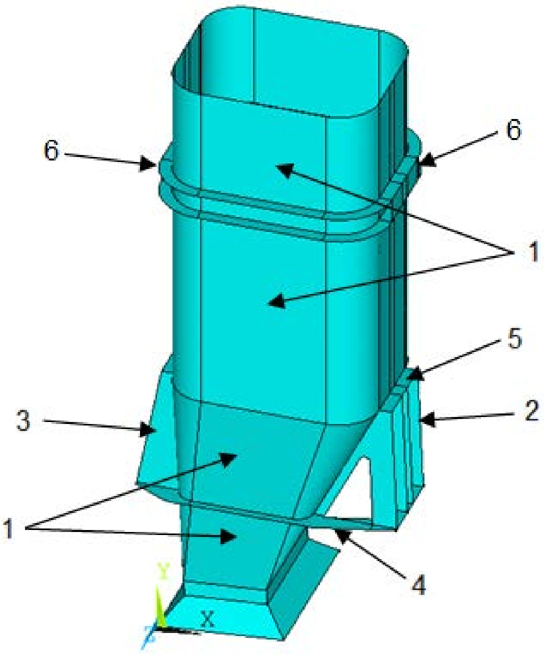

Figure 5.21: Distribution of the plates' thicknesses of a modified geometry of exhaust system A

5.1.15 Entire removal of the intermediate supporting ring:

In this modification, the intermediate supporting ring was completely removed from the current geometry of exhaust system A, in order to assess the influence of the intermediate supporting ring on the mechanical and thermal behaviour of exhaust system A. Figure 5.22 shows isometric views of this modified geometry of exhaust system A.

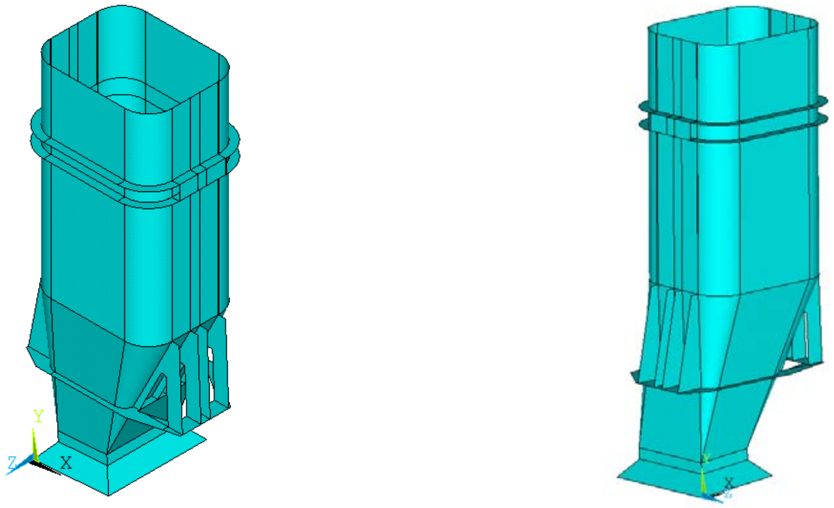

Figure 5.22: Removal of the intermediate supporting ring of the current geometry of exhaust system A

In this geometry, the exhaust system pipe, Figure 5.23-(1), has a wall thickness of 4 mm. The reinforcement ribs on the right side (2) have a thickness of 13 mm, while the left side reinforcement ribs (3) have a thickness of 11 mm. The lower supporting ring (4) has a thickness of 15 mm and the upper supporting ring (5) has plates 10 mm thick. Figure 5.23 shows the complete removal of the intermediate supporting ring and the distribution of the plates' thicknesses on this new geometry.

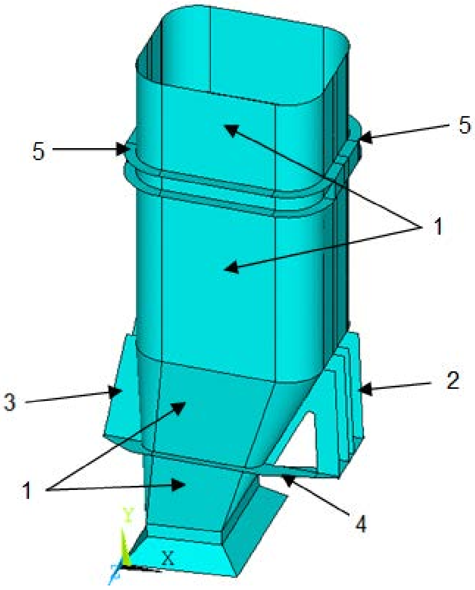

Figure 5.23: Distribution of the plates' thicknesses of a modified geometry of exhaust system A

5.1.16 Material and thickness change of the intermediate section:

This modification consisted in the change of the material and thicknesses of the plates that compose the intermediate section of the exhaust system pipe (Fig. 5.23-(7)). The material in this section was changed from the AISI 316L austenitic stainless steel to the 445M2 ferritic stainless steel and the plates' thicknesses were changed from 4 mm to 12 mm. This modification attempt was done in order to assess the consequences of using dissimilar materials, with very different thermal properties, in the critical section of the exhaust system.

In this geometry, the exhaust system pipe, Figure 5.24-(1), has a wall thickness of 4 mm. The reinforcement ribs on the right side (2) have a thickness of 13 mm, while the left side reinforcement ribs (3) have a thickness of 11 mm. The lower supporting ring (4) has a thickness of 15 mm, the intermediate supporting ring (5) has a thickness of 30 mm and the upper supporting ring (6) has plates 10 mm thick. The intermediate section of the exhaust system pipe (7) has a wall thickness of 12 mm and is made of the 445M2 ferritic stainless. Figure 5.24 shows the distribution of the material and plates' thicknesses on this new geometry.

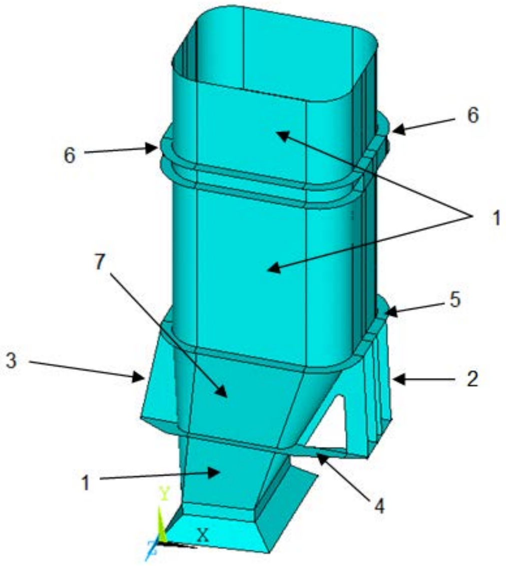

Figure 5.24: Distribution of the plates' thicknesses and material on this modified geometry of exhaust system A

5.1.17 Material change of the intermediate section:

This modification consisted in the change of the material of the plates of the intermediate section of the exhaust system pipe. The material in this section was changed from the AISI 316L austenitic stainless steel to the 445M2 ferritic stainless steel. This modification attempt was done in order to assess the consequences of using dissimilar materials, with very different thermal properties, in the critical section of the exhaust system.

In this geometry, the exhaust system pipe, Figure 5.25-(1), has a wall thickness of 4 mm. The reinforcement ribs on the right side (2) have a thickness of 13 mm, while the left side reinforcement ribs (3) have a thickness of 11 mm. The lower supporting ring (4) has a thickness of 15 mm, the intermediate supporting ring (5) has a thickness of 30 mm and the upper supporting ring (6) has plates 10 mm thick. The intermediate section of the exhaust system pipe (7) has a wall thickness of 4 mm and is made of the 445M2 ferritic stainless steel. Figure 5.25 shows the distribution of the material and plates' thicknesses on this new geometry.

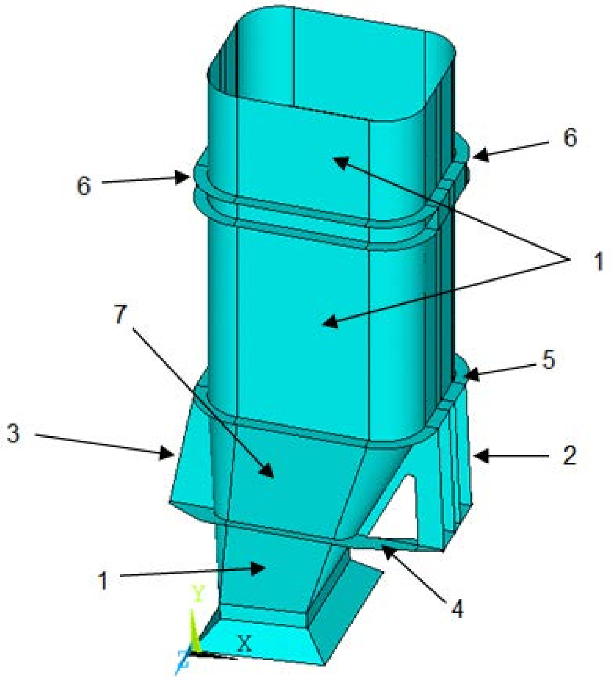

Figure 5.25: Distribution of the plates' thicknesses and material on this modified geometry of exhaust system A

5.2 Modifications proposed to exhaust system B:

5.2.1 Current geometry:

The current geometry and plates' thicknesses of exhaust system B are shown in figure 5.26 and 5.27. In this geometry, the exhaust system pipe, Figure 5.26-(1), has a wall thickness of 4mm, the right and left side reinforcement ribs, Figure 5.26-(2) and Figure 5.27-(2), have a thickness of 12 mm, and the right and left doubler plates, Figure 5.27-(3), also have a thickness of 12 mm. In the APDL programs, the areas that correspond to the overlap of the exhaust system pipe with the doubler plates were defined as having a thickness of 16 mm (4 mm thickness of the exhaust pipe plus 12 mm thickness of the doubler plates).

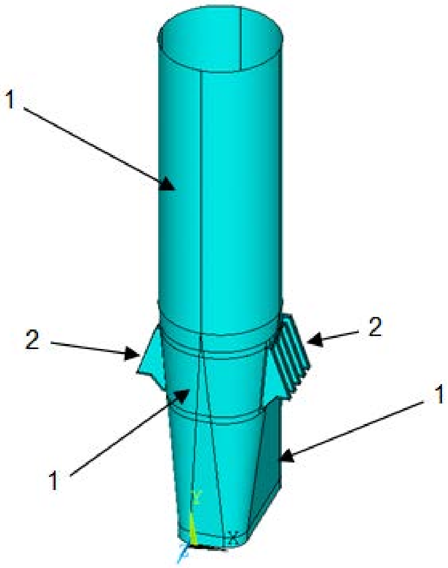

Figure 5.26: Distribution of the plates' thicknesses on the current geometry of exhaust system B

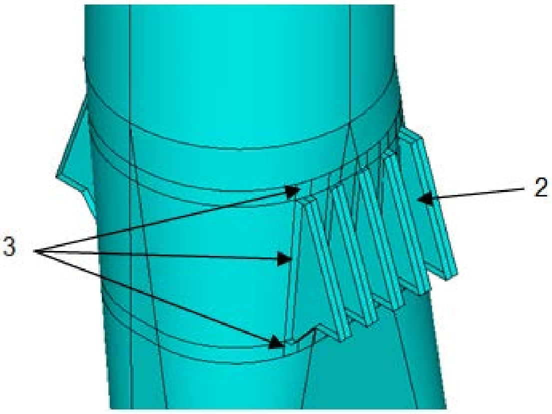

Figure 5.27: Distribution of the plates' thicknesses on the current geometry of exhaust system B (magnification of the right reinforcement ribs and doubler plates)

All the subsequent modifications presented in the present section are based on the current geometry of exhaust system B.

5.2.2 Thickness change of the intermediate section from 4 mm to 12 mm:

This modification consisted on the change of the plates' thicknesses of the intermediate section of the exhaust system pipe from 4 mm to 12 mm. This was done in order to make this section expand similarly to the right and left side reinforcement ribs, Figures 5.28-(2) and 5.29-(2), that have a thickness of 12 mm, and enhance the thermal shock response, lowering the thermal stresses induced in the intermediate section. Also it is expected a reduction of the mechanical stresses induced in the section.

In this geometry, the exhaust system pipe, Figure 5.28-(1), has a wall thickness of 4 mm, the right and left side reinforcement ribs, Figure 5.28-(2) and Figure 5.29-(2), have a thickness of 12 mm, and the right and left doubler plates, Figure 5.29-(3), also have a thickness of 12 mm. The intermediate section, Figure 5.28-(4), has a wall thickness of 12 mm. In the APDL programs, the areas that correspond to the overlap of the exhaust system pipe with the doubler plates were defined as having a thickness of 24 mm (12 mm thickness of the exhaust pipe with the 12 mm thickness of the doubler plates). Figure 5.28 and 5.29 show the distribution of the plates' thicknesses on this new geometry.

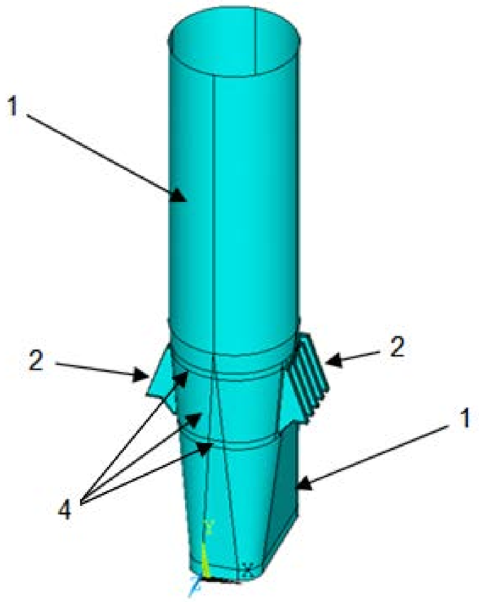

Figure 5.28: Distribution of the plates’ thicknesses on this modified geometry of exhaust system B

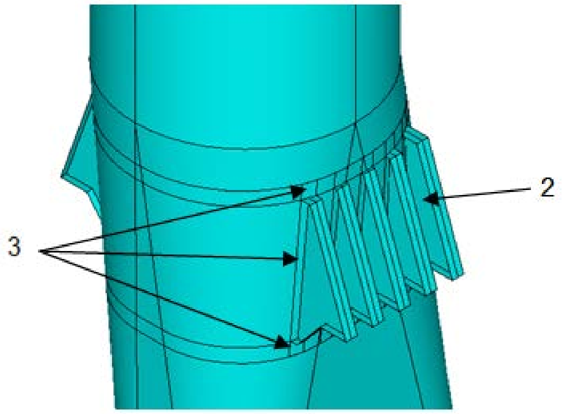

Figure 5.29: Distribution of the plates’ thicknesses on this modified geometry of exhaust system B (magnification of the right reinforcement ribs and doubler plates)

5.2.3 Thickness change of all the exhaust system plates to 4 mm:

This modification consisted on changing all the exhaust system’s plates to 4 mm, Figure 5.30, in order to uniform the thermal expansion of all the plates of exhaust system B.

In this geometry, the exhaust system pipe, Figure 5.30-(1), has a wall thickness of 4 mm, the right and left side reinforcement ribs, Figure 5.30-(2) and Figure 5.31-(2), have a thickness of 4 mm, and the right and left doubler plates, Figure 5.31-(3), also have a thickness of 4 mm. In the APDL programs, the areas that correspond to the overlap of the exhaust system pipe with the doubler plates were defined as having a thickness of 8 mm (4 mm thickness of the exhaust pipe plus the 4 mm thickness of the doubler plates). Figure 5.30 and 5.31 show the distribution of the plates’ thicknesses on this new geometry.

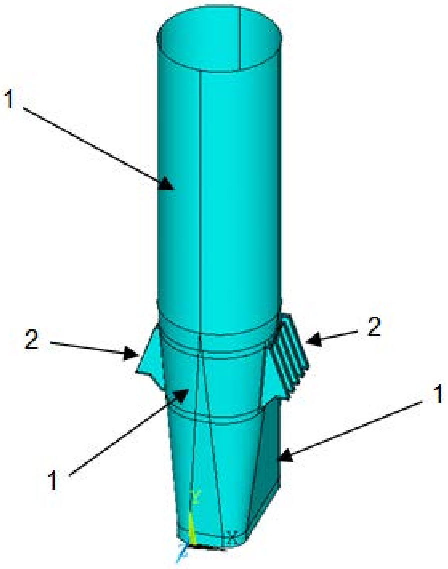

Figure 5.30: Distribution of the plates' thicknesses on this modified geometry of exhaust system B

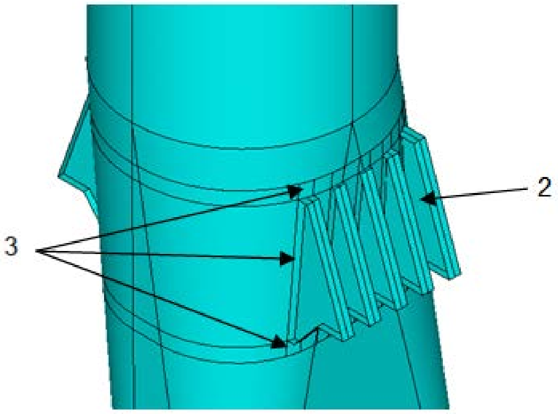

Figure 5.31: Distribution of the plates' thicknesses on this modified geometry of exhaust system B (magnification of the right reinforcement ribs and doubler plates)

5.2.4 Thickness change of all the exhaust system plates to 12 mm:

Similar to what was presented in section 5.2.3, this modification consisted on changing all the exhaust system's plates to 12 mm, Figure 5.32, in order to uniform the thermal expansion of all the plates of exhaust system B and also improve the mechanical response of the exhaust system.

In this geometry, the exhaust system pipe, Figure 5.32-(1), has a wall thickness of 12 mm, the right and left side reinforcement ribs, Figure 5.32-(2) and Figure 5.33-(2), have a thickness of 12 mm, and the right and left doubler plates, Figure 5.33-(3), also have a thickness of 12 mm. In the APDL programs, the areas that correspond to the overlap of the exhaust system pipe with the doubler plates were defined as having a thickness of 24 mm (12 mm thickness of the exhaust pipe plus 12 mm thickness of the doubler plates). Figure 5.32 and 5.33 show the distribution of the plates' thicknesses on this new geometry.

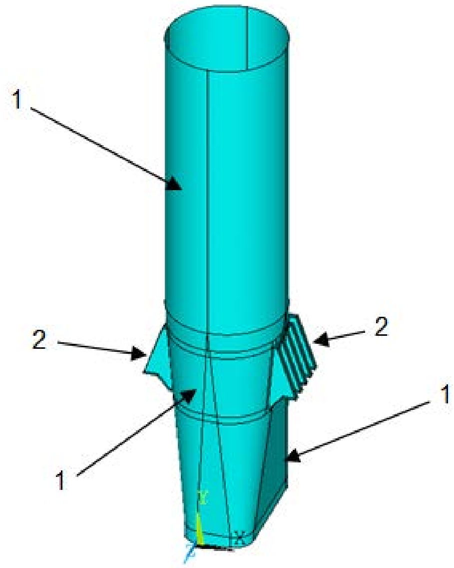

Figure 5.32: Distribution of the plates' thicknesses on this modified geometry of exhaust system B

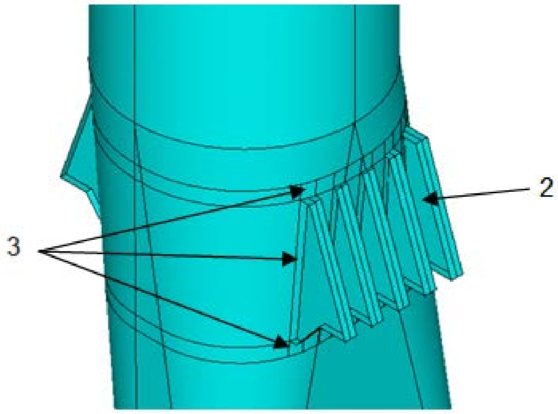

Figure 5.33: Distribution of the plates' thicknesses on this modified geometry of exhaust system B (magnification of the right reinforcement ribs and doubler plates)

5.2.5 Material and thickness change of the intermediate section:

This modification consisted in changing the material and the plates' thicknesses of the intermediate section of the exhaust system pipe (Fig 5.34-(4)), from the AISI 316L austenitic stainless steel to the 445M2 ferritic stainless steel and from 4 mm to 12 mm, with exception for the areas that correspond to the overlap of the exhaust system pipe with the doubler plates. This modification attempt was done in order to assess the consequences of using dissimilar materials, with very different thermal properties, in the critical section of the exhaust system.

In this geometry, the exhaust system pipe, Figure 5.34-(1), has a wall thickness of 4 mm, the right and left side reinforcement ribs, Figures 5.34-(2) and 5.35-(2), have a thickness of 12 mm, and the right and left doubler plates, Figure 5.35-(3), also have a thickness of 12 mm.

In the APDL programs, the areas that correspond to the overlap of the exhaust system pipe with the doubler plates were defined as having a thickness of 16 mm (4 mm thickness of the exhaust pipe plus 12 mm thickness of the doubler plates) and being made of the AISI 316L austenitic stainless steel. Figure 5.34 and 5.35 show the distribution of the material and plates' thicknesses on this new geometry.

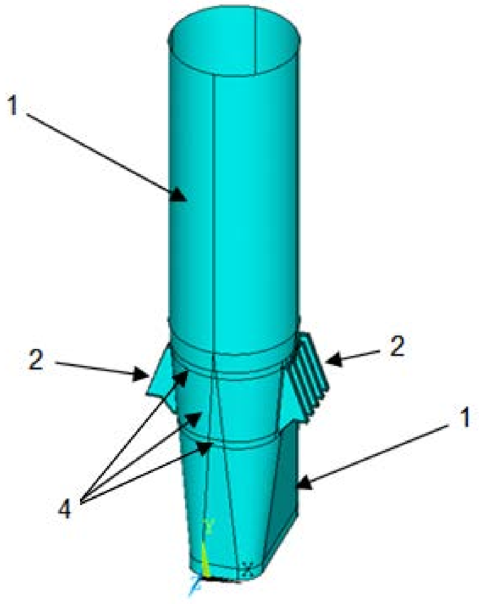

Figure 5.34: Distribution of the plates' thicknesses on this modified geometry of exhaust system B

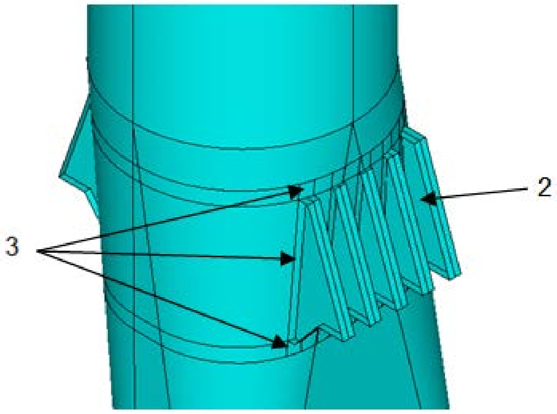

Figure 5.35: Distribution of the plates' thicknesses on this modified geometry of exhaust system B (magnification of the right reinforcement ribs and doubler plates)

5.2.6 Material change of the intermediate section:

This modification consisted in changing the material of the plates of the intermediate section of the exhaust system pipe (Fig 5.36-(4)), from the AISI 316L austenitic stainless steel to the 445M2 ferritic stainless steel, with exception for the areas that correspond to the overlap of the exhaust system pipe with the doubler plates. This modification attempt was done in order to assess the consequences of using dissimilar materials, with very different thermal properties, in the critical section of the exhaust system.

In this geometry, the exhaust system pipe, Figure 5.36-(1), has a wall thickness of 4 mm, the right and left side reinforcement ribs, Figures 5.36-(2) and 5.37-(2), have a thickness of 12 mm, and the right and left doubler plates, Figure 5.37-(3), also have a thickness of 4 mm. As said before, the intermediate section of the exhaust system pipe, Figure 5.36-(4), has a wall thickness of 4 mm and is made of the 445M2 ferritic stainless steel instead.

In the APDL programs, the areas that correspond to the overlap of the exhaust system pipe with the doubler plates were defined as having a thickness of 16 mm (4 mm thickness of the exhaust pipe plus 12 mm thickness of the doubler plates) and being made of the AISI 316L austenitic stainless steel. Figure 5.36 and 5.37 show the distribution of the material and plates' thicknesses on this new geometry.

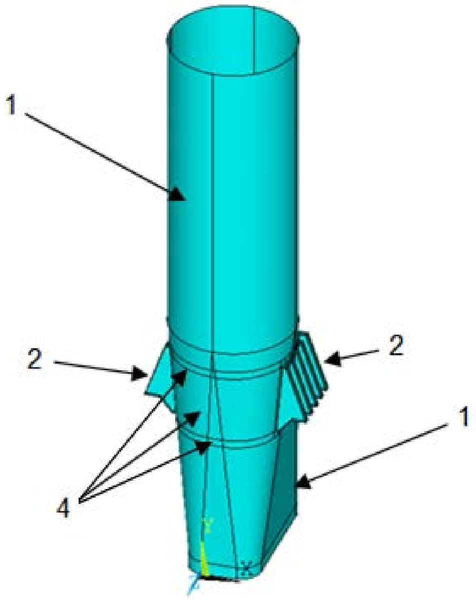

Figure 5.36: Distribution of the plate thicknesses on this modified geometry of exhaust system B

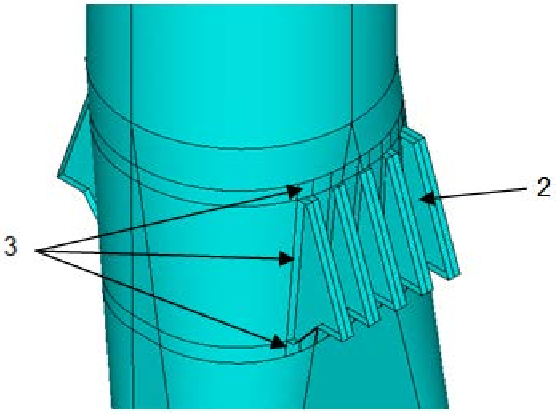

Figure 5.37: Distribution of the plate thicknesses on this modified geometry of exhaust system B (zoom in of the right reinforcement ribs and doubler plates)

6. Fatigue life assessment of the exhaust systems

6.1 Fatigue assessment of classified structural details and welded joints:

The fatigue assessment of classified structural details and welded joints was based on the maximum principal stress range in the sections where potential fatigue crack nucleation and propagation was considered.

A program was made, using APDL, to automatically retrieve, from each redesigned exhaust system analysis, all the graphics with the first principal nodal stress distribution of each section where potential fatigue cracking was considered. Some of these graphics are shown in annex B, B.1 to B.8.

The maximum first principal nodal stress value in each one of these graphics was multiplied by 2, in order to obtain the nominal stress ranges, $\Delta\sigma$, to be used for the fatigue life assessment of each structural detail chosen in chapters 6.1.1 and 6.1.2. This factor of 2 corresponds to a stress ratio, R, approximately equal to -1, correspondent to the heating and cooling cycles to which the exhaust systems are submitted.

For first principal stress values equal or under 18 MPa, which corresponds to a stress range equal or under 36 MPa ($\Delta\sigma \leq 36\ MPa$), it was considered that the details presented an infinite fatigue life.

Each structural detail analysed has a corresponding fatigue class (FAT) which corresponds to the characteristic fatigue strength of that detail at 2 million cycles (Figure 6.1). This relation can be given by the fatigue resistance S-N curves which are given by equation 6.1 [18]:

$$N = \frac{C}{\Delta\sigma^{m}} \tag{6.1}$$

where N is the number of cycles to failure, C is a material constant, $\Delta\sigma$ is the nominal stress range and m is the slope of the fatigue strength curves.

Once the structural details were assessed on the basis of normal stresses and are made of steel, the slope of the fatigue strength curves, m, was considered equal to 3. Figure 6.1 shows the fatigue resistance S-N curves used.

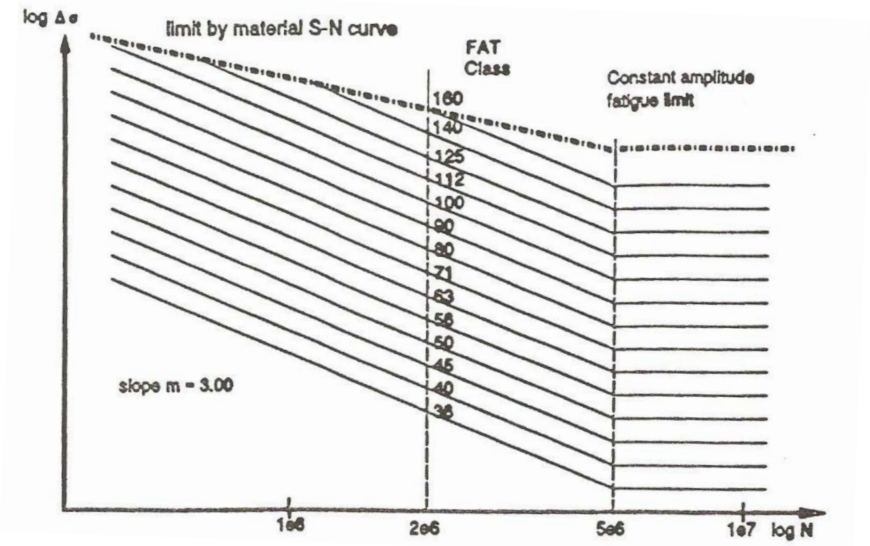

Figure 6.1: Fatigue resistance S-N curves for m=3, normal stress (steel) [18]

The FAT class of each detail can be multiplied by a factor value $f(R)$, to enhance or reduce the fatigue strength of the structural details. The fatigue strength factor, $f(R)$, depends on the stress ratio applied, the plate's thickness and/or the temperature at which the assessed details are submitted to [18].

Once there is no available reliable information on residual stresses actuating at the welded details present in the exhaust system, no enhancement factor was considered due to stress ratios.

Also, the influence of plate's thickness on fatigue strength should be taken into account in cases where cracks start from the weld toe on plates thicker than 25 mm. However, in the case scenario studied, no reduction factor related with thickness was considered since all the plates analysed have a thickness inferior to 25 mm.

Besides, a reducing factor due to the application of high temperatures, was used according to the temperatures calculated by the FEA in each assessed detail. Figure 6.2 shows the relation between fatigue strength reduction factor and temperature.

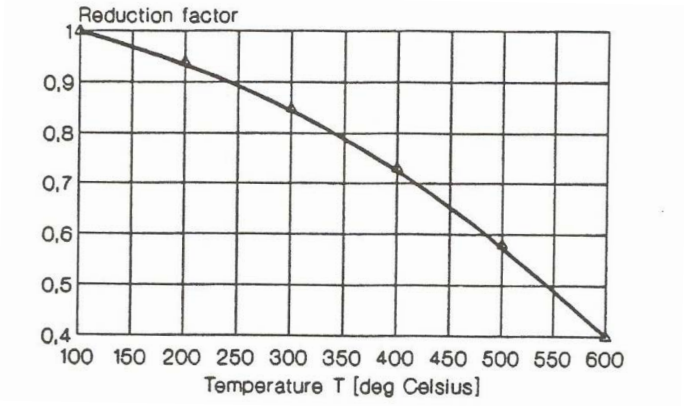

Figure 6.2: Fatigue strength reduction factor for steel at high temperatures [18]

The constant, C, of each S-N curve can be determined by the FAT class and fatigue strength factor of an assessed detail when the number of cycles, N, is 2 million. This relation results from equation 6.1 and is given by equation 6.2 [18]:

$$C = N.\Delta\sigma^{m} = N.[FAT.f(R)]^{m} \tag{6.2}$$

This equation (eq. 6.2) was used to calculate the constant of material, C, of each assessed detail, bearing in mind that m =3.

Once obtained this constant, C, the fatigue life of each section, where potential fatigue cracking was considered, could be assessed. The fatigue life, N, of each detail was obtained through equation 6.1, using the value of C and stress range obtained for each detail.

Since there were a lot of details to be assessed, the fatigue life calculations were done using *Excel*®. In chapter 6.1.1 and 6.1.2, it will be presented all the details of the exhaust systems chosen to be assessed, along with their correspondent location and FAT class.

All fatigue live calculations presented in the document assumed that crack propagation occurred in a high cycle fatigue regime (HCF). For fatigue lives below 3500 cycles, low cycle fatigue was considered to occur (LCF) and the *Coffin-Manson* equation should be applied (eq. 6.3) [19]:

$$\frac{\Delta\varepsilon_p}{2} = \varepsilon_f^{'} \times (2N)^{c'} \tag{6.3}$$

where $\frac{\Delta\varepsilon_p}{2}$ is the plastic strain amplitude, $\varepsilon_f^{'}$ is the fatigue ductility coefficient, N is the number of strain cycles to failure ($2N$ is the number of strain reversals to failure) and c' is the fatigue ductility exponent. Once these parameters were not known for the materials in study, no fatigue life assessments were made for low cycle fatigue.

The transition between LCF and HCF (number of cycles equal to 3500) was determined using a structural detail with a FAT class of 45 and a nominal stress range of $1.5\sigma_y$ [18].

6.1.1 Fatigue resistance values of the assessed structural details of exhaust system A:

Structural detail no. 424:

The structural detail no. 424 [18] was chosen to assess the fatigue life of welded joints between the exhaust system pipe and the lower supporting ring, as well as the welded joint between the exhaust system pipe and the intermediate supporting ring (Table 6.1). For this structural detail, the FAT class was obtained according to the wall thickness of the exhaust system pipe in study (Table 6.1). Table 6.1 shows the assessed structural detail and respective FAT class.

Table 6.1: Fatigue resistance value for structural detail no. 424[1] [18]

Detail number	Structural detail	Structural detail on exhaust system A	Description	FAT class
424	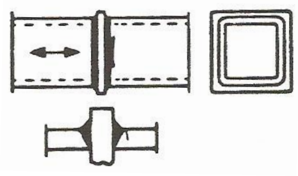	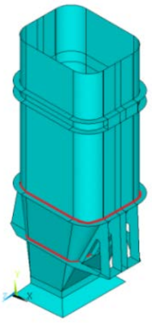	Splice of rectangular hollow section, single-sided butt weld, toe crack.	
			Wall thickness > 8 mm	50
			Wall thickness < 8 mm	45

Temperatures applied on the detail under study were taken from *Ansys*® calculations (Fig. 4.23) in the welded joint of the intermediate supporting ring with the exhaust system pipe and in the welded joint of the lower supporting ring with the exhaust system pipe. Table 6.2 shows the highest temperature calculated in each welded joint and the corresponding fatigue strength reduction factor, $f(R)$, to be applied, that was obtained through figure 6.2.

Table 6.2: Temperatures and fatigue strength reduction factors of the welded joints assessed for structural detail no. 424

Welded joint location	Highest temperature measured (ºC)	Fatigue strength reduction factor, f(R)
Intermediate supporting ring	350	0.78
Lower supporting ring	245	0.89

These fatigue reduction factors were multiplied to the corresponding FAT class chosen for this detail (as shown in equation 6.2).

The fatigue life for this type of detail was assessed in the current geometry of exhaust system A and in all the modifications made to exhaust system A, since it is a section where fatigue cracking has been noticed.

Structural detail no. 234:

The structural detail no. 234 [18] was chosen to assess the fatigue life of butt welds that join the sections of the exhaust system pipe, which have equal wall thicknesses and are welded in regions near from the intermediate supporting ring and the lower supporting ring (Table 6.3). For this structural detail, a FAT class is defined according to the chosen type of root inspection: root inspection or no NDT (Table 6.3). Table 6.3 shows the assessed structural detail and respective FAT class.

---

[1] The fatigue life assessment of the detail category shown in this table was performed taking into account the direction of the maximum first principal stress determined through the FEA.

Table 6.3: Fatigue resistance value for structural detail no. 234[1] [18]

Detail number	Structural detail	Structural detail on exhaust system A	Description	FAT class
234	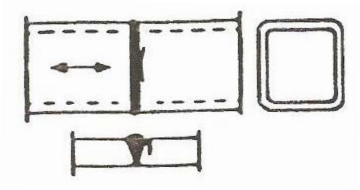	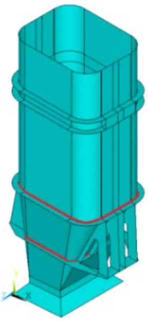	Transverse butt weld splice in rectangular hollow section, welded from one side, full penetration.	
			Root inspected by NDT	56
			No NDT	45

Both root inspected by non destructive test (NDT) and root inspected without NDT were considered, in order to compare the fatigue life of this detail according to the type of root inspection.

Temperatures applied on the detail under study were taken from *Ansys*® calculations (Fig. 4.23) in the butt welds that join the sections of the exhaust system's pipe which have equal wall thicknesses in regions near to the intermediate supporting ring and near to the lower supporting ring. Once these temperatures were assumed to be the same as the ones assessed for detail no. 424, the same fatigue strength reduction factors were used (Table 6.2). These fatigue reduction factors were multiplied by the corresponding FAT class chosen for this detail (as shown in equation 6.2).

The fatigue life for this type of detail was assessed in the current geometry of exhaust system A and in the modifications made to exhaust system A that showed the lowest first principal nodal stress results, since it is a section where potential fatigue cracking was considered.

Structural detail no. 223:

The structural detail no. 223 [18] is similar to structural detail no. 234 and was chosen to assess the fatigue life of butt welds of sections of the exhaust system's pipe which could have, in the future, different wall thicknesses (redesigned structure) and are located near to the intermediate supporting ring and near to the lower supporting ring (Table 6.4). For this structural detail, a FAT class was defined according to the slope between the wall thicknesses of the welded sections of the exhaust system pipe. Table 6.4 shows the assessed structural detail and respective FAT class.

Table 6.4: Fatigue resistance value for structural detail no. 223[1] [18]

Detail number	Structural detail	Structural detail on exhaust system A	Description	FAT class
223	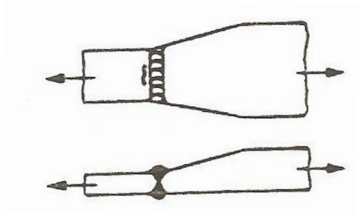	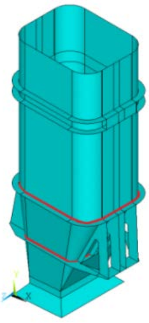	Transverse butt weld, NDT inspection, with transition on thickness and width.	
			Slope 1:5	80
			Slope 1:3	71
			Slope 1:2	63

---

[1] The fatigue life assessment of the detail category shown in this table was performed taking into account the direction of the maximum first principal stress determined through the FEA.

For this type of structural detail it was considered in its fatigue life assessment that a smooth slope (slope 1:5) will be used to weld the sections of the exhaust system pipe.

Temperatures applied on the detail under study were taken from *Ansys*® calculations (Figure 4.23). Once these welded joints were assumed to be in the same location as the ones assessed for detail no. 424, the same temperatures and fatigue strength reduction factors were used (Table 6.2). These fatigue reduction factors were multiplied by the FAT class chosen for this detail (as shown in equation 6.2).

Moreover, the misalignment present in this detail, due to the load transfer between plates with different thicknesses, leads to a local increase of stresses applied in the welded joint due to the occurrence of secondary shell bending stress. The net stress can be calculated, in a simplified way,by the formulae for the stress magnification factor, $\mathrm{k_m}$, which is given by equation 6.4 [20]:

$$\mathrm{k_m} = \frac{t_2}{t_1} \qquad , t_2 \geq t_1 \tag{6.4}$$

where t_1 and t_2 are the thickness of the different welded plates.

Since the fatigue life for this type of detail was only assessed in the modification where there was a thickness change of the intermediate section of the exhaust system pipe, from 4 mm to 12 mm, the stress magnification factor, $\mathrm{k_m}$, obtained through equation 6.4 was equal to 3:

$$\mathrm{k_m} = \frac{t_2}{t_1} = \frac{12}{4} = 3$$

This stress magnification factor was also multiplied by the FAT class and fatigue reduction factors chosen, decreasing more the fatigue life of the assessed detail.

The fatigue life for this type of detail was assessed in the current geometry of exhaust system A and in the modifications made to exhaust system A that showed the lowest first principal nodal stress results, since it is a section where potential fatigue cracking was considered.

Structural detail no. 323:

The structural detail no. 323 [18] was chosen to assess the fatigue life of welded joints between the exhaust system pipe and the left and right side reinforcement ribs (Table 6.5), although the ribs do not have one of the flanges shown (much similar to a T-joint). For this structural detail, a FAT class of 90 was obtained. Table 6.5 shows the assessed structural detail and respective FAT class.

Table 6.5: Fatigue resistance value for structural detail no. 323[1] [18]

Detail number	Structural detail	Structural detail on exhaust system A	Description	FAT class
323	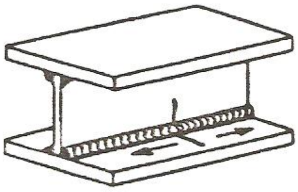	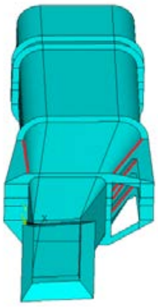	Continuous manual longitudinal fillet or butt weld.	90

Temperatures applied on the detail under study were taken from *Ansys*® calculations (Figure 4.23), in the welds that join the left and right side supporting ribs with the exhaust system's pipe. Table

---

[1] The fatigue life assessment of the detail category shown in this table was performed taking into account the direction of the maximum first principal stress determined through the FEA.

6.6 shows the average temperature measured in the welded joints and the corresponding fatigue strength reduction factor, $f(R)$, obtained through figure 6.2.

Table 6.6: Temperature and fatigue strength reduction factor of the welded joints assessed for structural detail no. 323

Welded joint location	Average temperature measured (ºC)	Fatigue strength reduction factor, f(R)
Left and right reinforcement ribs	275	0.87

This fatigue reduction factor was multiplied to the FAT class chosen for this detail (as shown in equation 6.2).

The fatigue life for this type of detail was assessed in the current geometry of exhaust system A and in the modifications made to exhaust system A that showed the lowest first principal nodal stress results applied to the ribs, since it is a section where potential fatigue cracking was considered.

Structural detail no. 822:

The structural detail no. 822 [18] was chosen to assess the fatigue life of welded joints between the exhaust system's pipe and the intermediate supporting ring, considering that the flange is 15 mm thick and is bolted to another flange with a thickness of 15 mm, in order to simulate the intermediate supporting ring that has a thickness of 30 mm in the FEA (Table 6.7). For this structural detail, a FAT class of 63 was obtained. Table 6.7 shows the assessed structural detail and respective FAT class.

Table 6.7: Fatigue resistance value for structural detail no. 822[1] [18]

Detail number	Structural detail	Structural detail on exhaust system A	Description	FAT class
822	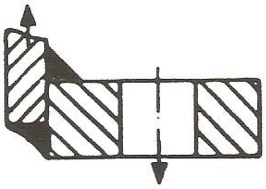	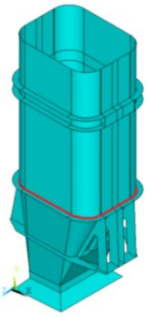	Flat flange with fillet welds, modified nominal stress in pipe, toe crack.	63

Temperatures applied on the detail under study were taken from *Ansys*® calculations (Figure 4.23), in the welded joint of the intermediate supporting ring with the exhaust system's pipe. Table 6.8 shows the highest temperature measured in the region considered in the analysis and the corresponding fatigue strength reduction factor, $f(R)$, obtained through figure 6.2.

Table 6.8: Temperature and fatigue strength reduction factor of the welded joint assessed for structural detail no. 822

Welded joint location	Highest temperature measured (ºC)	Fatigue strength reduction factor, f(R)
Intermediate supporting ring	350	0.78

This fatigue reduction factor was multiplied to the FAT class chosen for this detail (as shown in equation 6.2).

---

[1] The fatigue life assessment of the detail category shown in this table was performed taking into account the direction of the maximum first principal stress determined through the FEA.

The fatigue life for this type of detail was assessed in the current geometry of exhaust system A and in the modifications made to exhaust system A that showed the lower first principal nodal stress results since it is a section where potential fatigue cracking was considered.

6.1.2 Fatigue resistance values of the structural assessed details of exhaust system B:

Structural detail no. 511:

The structural detail no. 511 [18] was chosen to assess the fatigue life of welded joints between the doubler plates and the upper flanges of the right and left side reinforcement ribs, as well as between the doubler plates and the lower flanges of the right and left side reinforcement ribs (Table 6.9). For this structural detail, a FAT class of 80 was chosen once the welded joints were considered to be fillet welds, as welded, and the attachment in not thicker than main plate. Table 6.9 shows the assessed structural detail and respective FAT class.

Table 6.9: Fatigue resistance value for structural detail no. 511[1] [18]

Detail number	Structural detail	Structural detail on exhaust system B	Description	FAT class
511	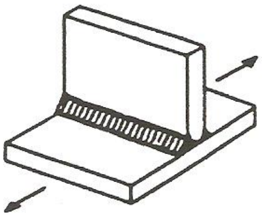	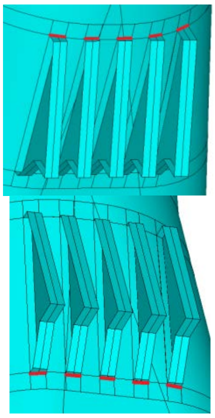	Transverse non-load-carrying attachment, not thicker than main plate.	
			K-butt weld, toe ground	100
			Two-sided fillets, toe ground	100
			Fillet weld(s): as welded	80
			Thicker than main plate	71

Temperatures applied on the detail under study were taken from *Ansys*® calculations (Figure 4.25), in the welded joints of the upper flanges of the right and left side supporting ribs with the doubler plates and in the welded joints of the lower flanges of the right and left side supporting ribs with the reinforcement plates. Table 6.10 shows the highest temperature calculated in the upper and lower welded joints and the corresponding fatigue strength reduction factor, $f(R)$, obtained through figure 6.2.

Table 6.10: Temperatures and fatigue strength reduction factors of the welded joints assessed for structural detail no. 511

Welded joint location	Highest temperature measured (ºC)	Fatigue strength reduction factor, f(R)
Upper flanges	370	0.75
Lower flanges	380	0.74

These fatigue reduction factors were multiplied by the FAT class chosen for this detail (as shown in equation 6.2).

The fatigue life for this type of detail was assessed in the current geometry of exhaust system B and in all the modifications made to exhaust system B since it is a section where fatigue cracking is more likely to occur.

---

[1] The fatigue life assessment of the detail category shown in this table was performed taking into account the direction of the maximum first principal stress determined through the FEA.

Structural detail no. 232:

The structural detail no. 232 [18] was chosen to assess the fatigue life of butt welds that join the circular sections of the exhaust system's pipe which have equal wall thicknesses and are welded in regions located near to the upper and lower ends of the doubler plates (Table 6.11). For this structural detail, a FAT class was obtained according to the chosen type of root inspection. Table 6.11 shows the assessed structural detail and respective FAT class.

Table 6.11: Fatigue resistance value for structural detail no. 232[1] [18]

Detail number	Structural detail	Structural detail on exhaust system B	Description	FAT class
232	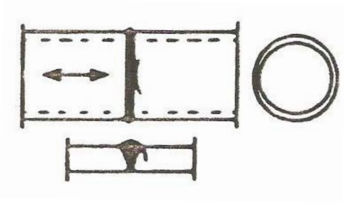	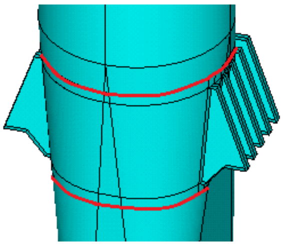	Transverse butt weld splice in circular hollow section, welded from one side, full penetration.	
			Root inspected by NDT	71
			No NDT	45

Both root inspected by non destructive test (NDT) and root inspected without NDT where considered, in order to compare the fatigue life of this detail according to the type of root inspection.

Temperatures applied on the detail under study were taken from *Ansys*® calculations (Figure 4.25), in the welds that join the sections of the circular exhaust system pipe which have equal wall thicknesses and are welded in regions located near to the upper and lower ends of the doubler plates. Table 6.12 shows the highest temperature calculated in each welded joint and the corresponding fatigue strength reduction factor, $f(R)$, obtained through figure 6.2.

Table 6.12: Temperatures and fatigue strength reduction factors of the welded joints assessed for structural detail no. 232

Welded joint location	Highest temperature measured (ºC)	Fatigue strength reduction factor, f(R)
Upper flanges	365	0.76
Lower flanges	395	0.73

These fatigue reduction factors were multiplied by the corresponding FAT class chosen for this detail (as shown in equation 6.2).

The fatigue life for this type of detail was assessed in the current geometry of exhaust system B and in the modifications made to exhaust system B that showed the lower first principal nodal stress results since it is a section where potential fatigue cracking was considered.

Structural detail no. 223:

The structural detail no. 223 [18] is similar to the structural detail no. 232 and was chosen to assess the fatigue life of butt welds of sections of the exhaust system's pipe that could have, in the future, different wall thicknesses (redesigned strutcture) and are located near to the upper and lower ends of the doubler plates (Table 6.13). For this structural detail, a FAT class was obtained according to the slope between the wall thicknesses of the welded sections of the exhaust system pipe. Table 6.13 shows the assessed structural detail and respective FAT class.

---

[1] The fatigue life assessment of the detail category shown in this table was performed taking into account the direction of the maximum first principal stress determined through the FEA.

Table 6.13: Fatigue resistance value for structural detail no. 223[1] [18]

Detail number	**Structural detail**	**Structural detail on exhaust system B**	**Description**	**FAT class**
223	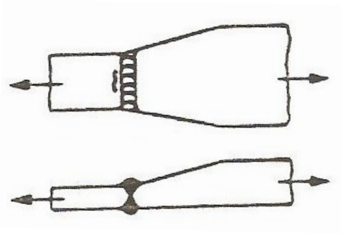	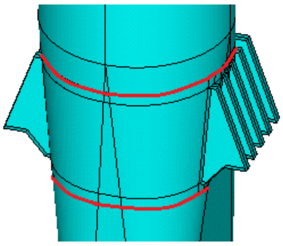	Transverse butt weld, NDT inspection, with transition on thickness and width.	
			Slope 1:5	80
			Slope 1:3	71
			Slope 1:2	63

For this type of structural detail it was considered in its fatigue life assessment that a smooth slope (slope 1:5) will be used to weld the sections of the exhaust system pipe.

Temperatures applied on the detail under study were taken from *Ansys*® calculations (Figure 4.25). Once these welded joints were assumed to be in the same location as the ones assessed for detail no. 232, the same temperatures and fatigue strength reduction factors were used (Table 6.12). These fatigue reduction factors were multiplied by the FAT class chosen for this detail (as shown in equation 6.2).

Moreover, the misalignment present in this detail, due to the load transfer between plates with different thicknesses, leads to a local increase of stresses applied in the welded joint due to the occurrence of secondary shell bending stress. The net stress can be calculated, in a simplified way,by the formulae for the stress magnification factor, $\mathrm{k_m}$, which is given by equation 6.4 [20].

Since the fatigue life for this type of detail was only assessed in the modification where there was a thickness change of the intermediate section of the exhaust system pipe, from 4 mm to 12 mm, the stress magnification factor, $\mathrm{k_m}$, obtained through equation 6.4 was equal to 3.

This stress magnification factor was also multiplied by the FAT class and fatigue reduction factors chosen, decreasing more the fatigue life of the assessed detail.

The fatigue life for this type of detail was assessed in the current geometry of exhaust system B and in the modifications made to exhaust system B that showed the lower first principal nodal stress results since it is a section where potential fatigue cracking was considered.

Structural detail no. 323:

The structural detail no. 323 [18] was chosen to assess the fatigue life of welded joints between the doubler plates and the left and right side reinforcement ribs (Table 6.14). For this structural detail, a FAT class of 90 was obtained. Table 6.14 shows the assessed structural detail and respective FAT class.

---

[1] The fatigue life assessment of the detail category shown in this table was performed taking into account the direction of the maximum first principal stress determined through the FEA.

Table 6.14: Fatigue resistance value for structural detail no. 323[1] [18]

Detail number	Structural detail	Structural detail on exhaust system B	Description	FAT class
323	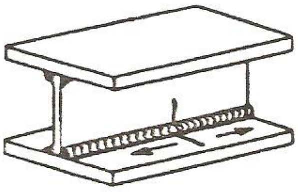	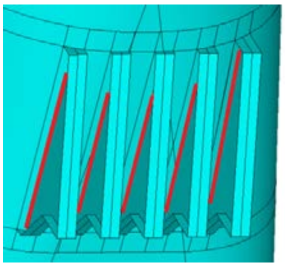	Continuous manual longitudinal fillet or butt weld.	90

Temperatures applied on the detail under study were taken from *Ansys*® calculations (Figure 4.25), in the welds that join the left and right side supporting ribs with the doubler plates. Table 6.15 shows the average temperature measured in the welded joints and the corresponding fatigue strength reduction factor, $f(R)$, obtained through figure 6.2.

Table 6.15: Temperature and fatigue strength reduction factor of the welded joints assessed for structural detail no. 323

Welded joint location	Average temperature measured (ºC)	Fatigue strength reduction factor, f(R)
Left and right reinforcement ribs	385	0.74

This fatigue reduction factor was multiplied by the FAT class chosen for this detail (as shown in equation 6.2).

The fatigue life for this type of detail was assessed in the current geometry of exhaust system B and in the modifications made to exhaust system B that showed the lower first principal nodal stress results since it is a section where potential fatigue cracking was considered.

Structural details no. 712 and no. 721:

Since there is no structural detail which resembles exactly the structural detail that exists in exhaust system B, both structural detail no. 712 and no. 721 [18] were chosen to assess the fatigue life of welded joints between the exhaust system's pipe and the upper ends of the right and left doubler plates and the welded joints between the exhaust system's pipe and the lower ends of the right and left doubler plates (Table 6.16). For the structural detail no. 712, the FAT class was obtained according to the thickness of the exhaust system pipe's wall and the thickness of the doubler plates. Table 6.16 shows the assessed structural detail and respective FAT class.

---

[1] The fatigue life assessment of the detail category shown in this table was performed taking into account the direction of the maximum first principal stress determined through the FEA.

Table 6.16: Fatigue resistance value for structural detail no. 712[1] [18]

Detail number	Structural detail	Structural detail on exhaust system B	Description	FAT class
712	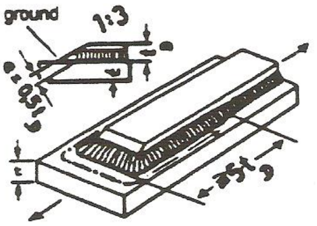	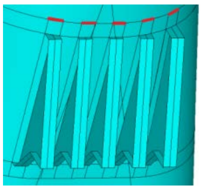 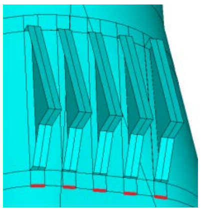	End of long doubling plate on beam, reinforced welded ends ground.	
			$t_D \leq 0{,}8.t$	71
			$0{,}8.t < t_D \leq 1{,}5.t$	63
			$t_D > 1{,}5.t$	56

For the structural detail no. 721, a FAT class of 50 was obtained (Table 6.17). Table 6.17 shows the assessed structural detail and respective FAT class.

Table 6.17: Fatigue resistance value for structural detail no. 721[1] [18]

Detail number	Structural detail	Structural detail on exhaust system B	Description	FAT class
721	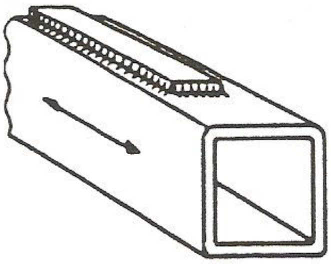	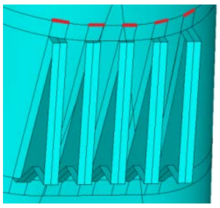 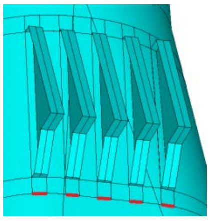	End of reinforcement plate on rectangular hollow section.	
			Wall thickness:	
			$t < 25$ mm	50

Temperatures applied on the details under study were taken from *Ansys*® calculations (Figure 4.25), in the welds that join the exhaust system pipe with the upper ends of the right and left reinforcement plates and the welds that join the exhaust system pipe with the lower ends of the right and left reinforcement plates. Table 6.18 shows the highest temperature measured in the upper and lower welded joints and the corresponding fatigue strength reduction factor, $f(R)$, obtained through figure 6.2.

---

[1] The fatigue life assessment of the detail category shown in this table was performed taking into account the direction of the maximum first principal stress determined through the FEA.

Table 6.18: Temperatures and fatigue strength reduction factors of the welded joints assessed for detail no. 712

Welded joint location	Highest temperature measured (ºC)	Fatigue strength reduction factor, f(R)
Upper ends of the doubler plates	365	0.76
Lower ends of the doubler plates	395	0.73

These fatigue reduction factors were multiplied by the corresponding FAT class chosen for detail no. 712 and to the FAT class value chosen for detail no. 721 (as shown in equation 6.2).

The fatigue life for these type of details was assessed in the current geometry of exhaust system B and in the modifications made to exhaust system B that showed the lower first principal nodal stress results since it is a section where potential fatigue cracking was considered.

6.2 Fatigue crack propagation assessment:

Taking into account the observation of a fracture surface taken out from exhaust system A, where several points of crack nucleation and propagation were detected [5], a fatigue life assessment was carried out considering that there were initial cracks present the exhaust systems, which propagated each time the exhaust systems went through a heating and cooling cycle. These initial cracks reduce the exhaust system's life.

The fatigue crack growth rate of cracks present in a material is dependent on the values of the parameters of the Paris Law, C_0 and m, and is given by (eq. 6.5) [18, 21]:

$$\frac{da}{dN} = C_0.\Delta K^m \tag{6.5}$$

where, C_0 is the constant of the Paris law, m is the exponent of the Paris law, ΔK is the cyclic stress intensity factor range and $\frac{da}{dN}$ is the growth rate of the propagating cracks. For elevated temperatures up to 600 ºC, the exponent of the Paris law, m, is considered to be equal to 3 and the constant of the Paris law is given by (eq. 6.6) [22]:

$$C_0 = 1.65 \times 10^{-11} \times \left(\frac{E_{100\ ^\circ C}}{E_{ET}}\right)^3, \text{ in } MPa.\sqrt{m} \text{ and } m \tag{6.6}$$

where $E_{100\ ^\circ C}$ is the elastic modulus at 100 ºC and E_{ET} is the elastic modulus at the elevated temperature.

For the AISI 316L stainless steel, it was considered $E_{100\ ^\circ C}$=199 GPa; as the temperature near the regions where cracks were assessed was 335 ºC, an Elastic Modulus, E_{ET}, of 183.3 GPa [5] was considered. Once there is no available information on the Elastic Modulus of the ferritic 445M2 stainless steel at 335 ºC, and in order to assess the fatigue crack propagation for the ferritic 445M2 stainless steel, the same Elastic Modulus of the AISI 316L stainless steel was considered. So, from equation 6.6, the constant of Paris law, C_0, was equal to 2.12×10^{-11}.

From equation 6.5, it is possible to calculate the increment on the crack depth and length after N cycles are applied (eq. 6.7).

$$\frac{da}{dN} = C_0.\Delta K^m \Leftrightarrow \frac{a_f - a_i}{N} = C_0.\Delta K^m \Leftrightarrow a_f = a_i + C_0.\Delta K^m.N \tag{6.7}$$

where a_i is the initial crack depth, a_f is the crack depth after N cycles applied, N is the number of cycles applied, m is the exponent of the Paris law and ΔK is the stress intensity factor range that depends on the crack size, crack shape, and welded joint geometry at weld toe (stress concentration factor).

For each new cycle ($N = N + 1$), a new crack depth, a_f, is obtained due to crack propagation. This new crack depth, a_f, is then used in the next cycle, as the new crack depth, a_i (eq. 6.7).

Figure 6.3 shows a surface crack, where c is half the length of the surface crack, a is the depth of the surface crack, t is the thickness of the material in study along which the crack will propagate and b is the distance to the nearest edge of the plate.

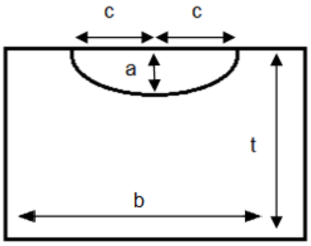

Figure 6.3: Elliptical surface crack

For a surface crack under constant amplitude membrane stress, propagating in the depth direction (figure 6.3), the stress intensity range factor at weld toe, ΔK_I, is given by [18]:

$$\Delta K_I = \Delta\sigma . \sqrt{\frac{\pi . a}{(1{+}1.464{\times}\left(\frac{a}{c}\right)^{1,65})}} . \Bigg[\left(1{,}13 - 0{,}09 \times \left(\frac{a}{c}\right)\right) + \left(-0{,}54 + \frac{0{,}89}{0.2{+}\left(\frac{a}{c}\right)}\right) \times \left(\frac{a}{t}\right)^2 + \Bigg[(0{,}5 - \frac{1}{0.65{+}\left(\frac{a}{c}\right)} + 14 \times \left(1 - \left(\frac{a}{c}\right)^{24}\right)\Bigg] \times \left(\frac{a}{t}\right)^4\Bigg] \times f_w \times M_k \ , \ \frac{a}{c} < 1 \quad (6.8)$$

where ΔK_I is the stress intensity factor range for a type of crack propagation designated as Mode I (crack propagates perpendicular to the direction of the applied maximum principal stress), $\Delta\sigma$ is the nominal stress range applied on the crack, f_w is a finite width correction factor and M_k is a weld local geometry correction factor for the crack at weld toe.

The finite width correction factor, f_w, is given by (eq. 6.9) [18]:

$$f_w = \left[sec\left(\frac{\pi \times c \times \sqrt{\frac{a}{t}}}{2b}\right)\right]^{0.5} \quad (6.9)$$

The value of the distance to the nearest edge, b, was considered to be infinite, since it is much higher than a, c and t, and so, by equation 6.9, the finite width correction factor, f_w, was equal to 1.

The weld local geometry correction factor for crack at weld toe, M_k, depends on the relation between the toe distance, l, and the thickness, t, of the material in study along which the crack will propagate (fig. 6.4).

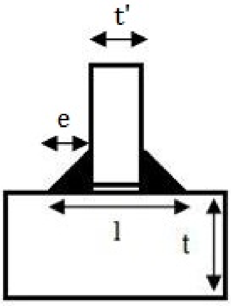

Figure 6.4: T-joint fillet weld

The toe distance, l, is given by (eq. 6.10):

$$l = t' + 2e \quad (6.10)$$

where t' is for example the thickness of the supporting ring of exhaust system A or the thickness of the flanges of exhaust system B and e is the weld toe width, which is related to the thickness t' [23].

Considering that the relation between the toe distance, l, and the thickness, t, of the material in study, along which the crack will propagate, will always be higher than 2, $\frac{l}{t} > 2$, then the local geometry correction factor for the crack at weld toe, M_k, will be given by [18]:

$$M_k = 0.615 \times \left(\frac{a}{t}\right)^{-0.31}, \text{ for } \left(\frac{a}{t}\right) \leq 0.073 \qquad (6.11)$$

or

$$M_k = 0.83 \times \left(\frac{a}{t}\right)^{-0.2}, \text{ for } \left(\frac{a}{t}\right) > 0.073 \qquad (6.12)$$

For the stress intensity factor, ΔK_I, lower than the threshold of the stress intensity factor range, ΔK_{th}, determined at a temperature of 350 ºC, it was considered that no crack propagation would occur [21]. As a result, no fatigue assessment by crack propagation calculation was carried out for stress intensity factor ranges applied, ΔK_I, lower than 6 $MPa.\sqrt{m}$ (ΔK_{th} factor at 350 ºC) [18].

In order to assess the size of the plastic region at the crack tip, important to decide whether to use the Linear Elastic Fracture Mechanics (LEFM) or the Elastic Plastic Fracture Mechanics (EPFM), the flow chart presented in figure 6.5 was used [19]:

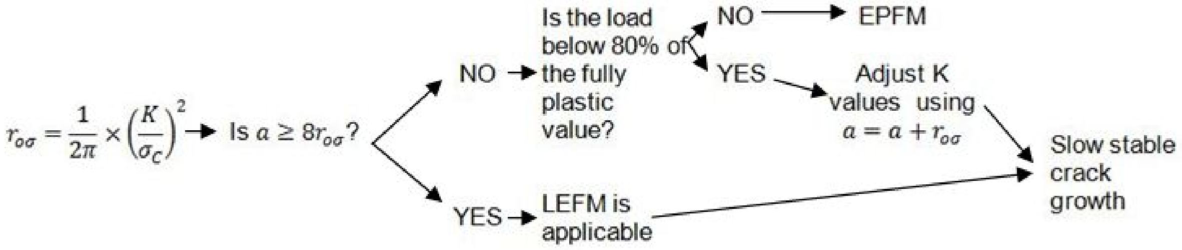

Figure 6.5: Flow chart to assess if LEFM or EPFM should be applied in fatigue life prediction

In this flow chart (Figure 6.5), the stress intensity factor, K, is calculated using equation 6.8, but not considering the nominal stress range, $\Delta\sigma$. Instead, the maximum nominal stress, σ, applied to the crack should be used.

In the cases where the load applied is below 80% of the fully plastic value of the material (yield strength) and the crack size is higher than $8.r_{o\sigma}$, an adjustment on the crack tip size shoud be made ($a = a + r_{o\sigma}$) in order to be possible to apply the LEFM concepts.

For maximum nominal stresses values, σ, higher than the yield strength of the material in study, σ_y, the elastic plastic fracture mechanics concepts (EPFM) should be considered. When this case happened, no fatigue crack life prediction was made and a note (EPFM) was inserted instead.

The fatigue life prediction of the exhaust systems was made using linear elastic fracture mechanics (LEFM), and a program was written, using *MATLAB*® , to accomplish that task. Using equation 6.7, where the cyclic stress intensity factor range, ΔK_I, is calculated using equation 6.8, the program predict the fatigue life of a surface crack under membrane stress (constant stress across the plate's thickness was considered). Based on the results obtained in previous fracture tests that were made, an initial crack depth, a, of 0.3 mm was assumed to exist in the structure, near the weld toe.

A disfunction criteria was defined - when the crack depth reached 75% of the thickness of the material or when the maximum stress intensity factor, $K_{I\,max}$., was higher than the toughness of the material obtained in plane stress condition at 350ºC, K_{IC}=100 $MPa.\sqrt{m}$ [18]. Where the disfunction criteria was exceeded, the program stopped the calculation of the number of the fatigue cycles. In the absence of information, the fatigue threshold value of the stress intensity factor, ΔK_{th}, and the toughness value, K_{IC}, of the austenitic stainless steel, were considered for the ferritic stainless steel.

Also, a constant relation between the surface crack half-length, c, and the crack depth, a, was defined, $c = \frac{a}{0{,}4}$, at the initial condition and during the crack propagation stage. Once all the parameters described earlier were set, the program was run and the number of cycles needed to reach material failure was obtained.

6.2.1 Fatigue life assessment of exhaust system A assuming fatigue crack propagation:

The sections of exhaust system A where fatigue cracking has been noticed are the sections where the exhaust system pipe is welded to the lower supporting ring and the sections where the exhaust system pipe is welded to the intermediate supporting ring. Thus, in these sections, a fatigue life assessment was done, assuming the existence of an initial crack near to the weld toe of the welded details considered, and using the maximum nominal principal stress value calculated in each welded joint by FEM. Figure 6.6 shows the location of the assessed sections of exhaust system A.

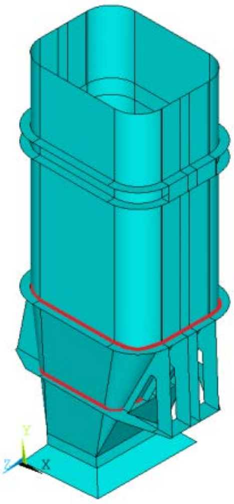

Figure 6.6: Fatigue life assessment of two welded details (line in red), containing an initial crack, at sections of exhaust system A

The fatigue life assessment was performed for the current geometry of exhaust system A and for its redesigned structures where the lowest first principal nodal stress results were obtained.

6.2.2 Fatigue life assessment of exhaust system B assuming fatigue crack propagation:

The sections of exhaust system B where nucleation and fatigue crack propagation are more prone to occur are the sections where the reinforcement plates are welded to the upper flanges of the right and left side supporting ribs and where the reinforcement plates are welded to the lower flanges of the right and left side supporting ribs. So, in these sections, a fatigue life assessment was done assuming the existence of an initial crack near to the weld toe of the welded details considered, and using the maximum nominal principal stress value calculated in each welded joint by FEM. Figure 6.7 shows the location of the assessed sections of exhaust system B.

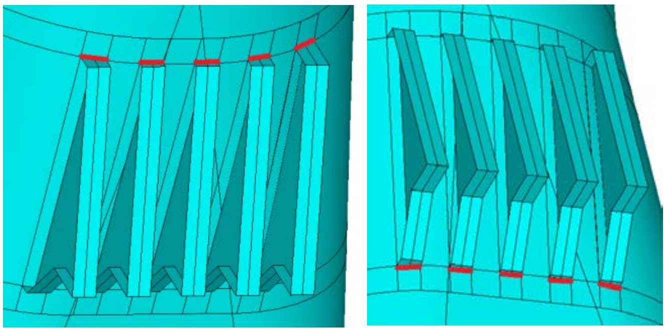

Figure 6.7: Fatigue life assessment of welded details (lines in red), containing an initial crack, where nucleation and propagation of cracks are more prone to occur at exhaust system B

The fatigue life assessment was performed for the current geometry of exhaust system B and for its redesigned structures where the lowest principal nodal stress results were obtained.

7. Results

7.1 First principal nodal stress results:

The first nodal stress results presented herein were obtained for the details chosen in chapter 6 in each modification made to the exhaust systems (chapter 5).

7.1.1 First principal nodal stress results of exhaust system A:

Structural detail no. 424:

Table 7.1 shows the maximum first principal nodal stress values obtained in the welded joint between the exhaust system's pipe and the lower supporting ring, as well as in the welded joint between the exhaust system pipe and the intermediate supporting ring (detail no. 424 - chapter 6.1). These maximum first principal nodal stress values were obtained for the normal in-service condition (without the 2G deceleration) in the current geometry of exhaust system A and in all the modifications made to exhaust system A (chapter 5.1), for both AISI 316L austenitic stainless steel and 445M2 ferritic stainless steel.

Table 7.1: First principal stress values actuating on detail no. 424 in each modification made to exhaust system A – normal in-service conditions (without 2G deceleration)

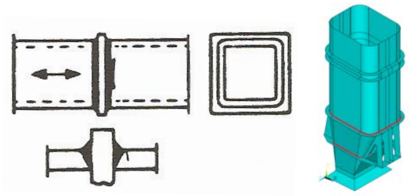	**Material type**			
	AISI 316L austenitic stainless steel		**445 M2 ferritic stainless steel**	
	Intermediate supporting ring (MPa)	**Lower supporting ring (MPa)**	**Intermediate supporting ring (MPa)**	**Lower supporting ring (MPa)**
Current geometry	339	125	235	83
Addition of four vertical reinforcement ribs	345	130	240	86
Addition of two vertical reinforcement ribs	343	128	239	85
Addition of a horizontal supporting ring	177	154	125	103
Thickness change of the intermediate section of the exhaust system pipe from 4 mm to 12 mm	133	91	93	62
Thickness change of the intermediate supporting ring from 30 mm to 12 mm	304	124	211	82
Thickness change of the intermediate and lower supporting rings to 4 mm	251	131	174	84
Thickness change of the vertical reinforcement ribs to 4 mm	209	106	148	72
Thickness change of all the exhaust system plates to 4 mm	156	104	110	69
Thickness change of all the exhaust system plates to 12 mm	134	104	95	69
Removal of the outer vertical reinforcement ribs	227	151	161	101
Removal of the inner vertical reinforcement ribs	314	100	221	67
Partial removal of the lower supporting ring	355	140	244	93
Partial removal of the intermediate supporting ring	323	119	223	79

Total removal of the intermediate supporting ring	---	119	---	79

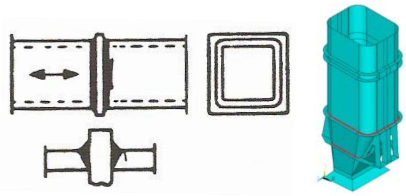	**Use of dissimilar welded joints of an AISI 316L Austenitic and a 445 M2 ferritic stainless steels in the intermediate region of exhaust system**	
	Intermediate supporting ring (MPa)	**Lower supporting ring (MPa)**
Change of material type and thickness in the intermediate section to 445M2 ferritic and 12mm	301	119
Change of material in the intermediate section to 445M2 ferritic	557	175

To confirm the maximum first principal stress values shown in table 7.1, some first principal stress distribution graphics, where these values were obtained from, are shown in annex B, B.1 to B.4. These graphics were obtained for the current geometry of exhaust system A and for the modification where the thickness of the intermediate section of the exhaust system A pipe was changed from 4 mm to 12 mm.

Table 7.2 shows the maximum first principal nodal stress values obtained in the welded joint between the exhaust system's pipe and the lower supporting ring, as well as in the welded joint between the exhaust system pipe and the intermediate supporting ring (detail no. 424 - chapter 6.1). These maximum first principal nodal stress values were obtained for the overload condition (with the 2G deceleration) in the current geometry of exhaust system A and in all the modifications made to exhaust system A (chapter 5.1), for both AISI 316L austenitic stainless steel and 445M2 ferritic stainless steel.

Table 7.2: First principal stress values actuating on detail no. 424 in each modification made to exhaust system A – overload conditions (with 2G deceleration)

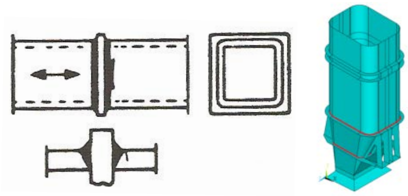	**Material type**			
	AISI 316L austenitic stainless steel		**445M2 ferritic stainless steel**	
	Intermediate supporting ring (MPa)	**Lower supporting ring (MPa)**	**Intermediate supporting ring (MPa)**	**Lower supporting ring (MPa)**
Current geometry	340	118	236	76
Addition of four vertical reinforcement ribs	346	122	241	79
Addition of two vertical reinforcement ribs	346	120	242	77
Addition of a horizontal supporting ring	178	143	126	93
Thickness change of the intermediate section of the exhaust system pipe from 4 mm to 12 mm	130	83	91	54
Thickness change of the intermediate supporting ring from 30 mm to 12 mm	305	116	212	75
Thickness change of the intermediate and lower supporting rings to 4 mm	250	116	173	69
Thickness change of the vertical reinforcement ribs to 4 mm	209	98	149	64
Thickness change of all the exhaust system plates to 4 mm	155	89	110	55

Thickness change of all the exhaust system plates to 12 mm	134	99	94	64
Removal of the outer vertical reinforcement ribs	230	143	164	93
Removal of the inner vertical reinforcement ribs	314	93	222	60
Partial removal of the lower supporting ring	312	637	218	631
Partial removal of the intermediate supporting ring	315	112	215	72
Total removal of the intermediate supporting ring	---	111	---	72

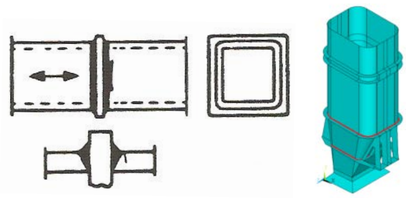	**Use of dissimilar welded joints of an AISI 316L austenitic and a 445 M2 ferritic stainless steels in the intermediate region of exhaust system**	
	Intermediate Supporting ring (MPa)	**Lower supporting ring (MPa)**
Change of material type and thickness in the intermediate section to 445M2 ferritic and 12mm	298	129
Change of material in the intermediate section to 445M2 ferritic	558	190

From all the modifications made to exhaust system A (chapter 5.1), the ones that presented first principal nodal stress values (Tables 7.1 and 7.2) better than the current geometry of exhaust system A were selected to be assessed in the following details. The reason for this selection is discussed in chapter 8.1.1.

Structural detail no. 234:

Table 7.3 shows the maximum first principal nodal stress values obtained in the butt welds that join the sections of the exhaust system's pipe which have equal wall thicknesses and are welded in regions near to the intermediate supporting ring and to the lower supporting ring (detail no. 234 - chapter 6.1). These maximum first principal nodal stress values were obtained for normal in-service conditions (without the 2G deceleration) in the current geometry of exhaust system A and in the selected modifications made to exhaust system A (chapter 8.1.1), for both AISI 316L austenitic stainless steel and 445M2 ferritic stainless steel.

Table 7.3: First principal stress values actuating on detail no. 234 in each modification made to exhaust system A – normal in-service conditions (without 2G deceleration)

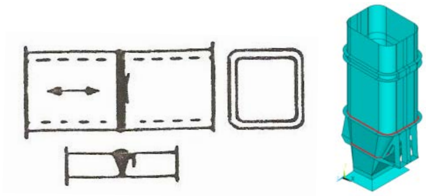	**Material type**			
	AISI 316L austenitic stainless steel		**445M2 ferritic stainless steel**	
	Intermediate supporting ring (MPa)	**Lower supporting ring (MPa)**	**Intermediate supporting ring (MPa)**	**Lower supporting ring (MPa)**
Current geometry	339	125	235	83
Thickness change of the vertical reinforcement ribs to 4 mm	209	106	148	72
Thickness change of all the exhaust system plates to 4 mm	156	104	110	69
Thickness change of all the exhaust system plates to 12 mm	134	104	95	69
Removal of the inner vertical reinforcement ribs	314	100	221	67

For details no. 234, the maximum first principal nodal stress values obtained for the overload condition (with the 2G deceleration) in the current geometry of exhaust system A and in the selected modifications made to exhaust system A (chapter 8.1.1), for both AISI 316L austenitic stainless steel and 445M2 ferritic stainless steel are shown in annex C, table C.1.

Structural detail no. 223:

Table 7.4 shows the maximum first principal nodal stress values obtained in the the butt welds of sections of the exhaust system's pipe which could have, in the future, different wall thicknesses (redesigned structure) and are located near to the intermediate supporting ring and near to the lower supporting ring (detail no. 223 - chapter 6.1). These maximum first principal nodal stress values were obtained for normal in-service conditions (without the 2G deceleration) in the current geometry of exhaust system A and in the selected modifications made to exhaust system A (chapter 8.1.1), for both AISI 316L austenitic stainless steel and 445M2 ferritic stainless steel.

Table 7.4: First principal stress values actuating on detail no. 223 in each modification made to exhaust system A – normal in-service conditions (without 2G deceleration)

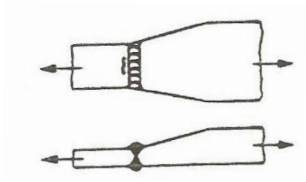 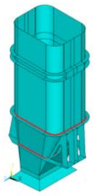	**Material type**			
	AISI 316L austenitic stainless steel		**445M2 ferritic stainless steel**	
	Intermediate supporting ring (MPa)	**Lower supporting ring (MPa)**	**Intermediate supporting ring (MPa)**	**Lower supporting ring (MPa)**
Thickness change of the intermediate section of the exhaust system pipe from 4 mm to 12 mm	133	91	93	62

For detail no. 223, the maximum first principal nodal stress values obtained for the overload condition (with the 2G deceleration) in the current geometry of exhaust system A and in the selected modifications made to exhaust system A (chapter 8.1.1), for both AISI 316L austenitic stainless steel and 445M2 ferritic stainless steel are shown in annex C, table C.2.

Structural detail no. 323:

Table 7.5 shows the maximum first principal nodal stress values obtained in the welded joints between the exhaust system's pipe and the right side reinforcement ribs (detail no. 323 - chapter 6.1). These maximum first principal nodal stress values were obtained for normal in-service conditions (without the 2G deceleration) in the current geometry of exhaust system A and in the selected modifications made to exhaust system A (chapter 8.1.1), for both AISI 316L austenitic stainless steel and 445M2 ferritic stainless steel.

The reinforcement ribs were numbered according to their position in exhaust system A, being the first reinforcement rib, the one seen in the front view of exhaust system A.

Table 7.5: First principal stress values actuating on detail no. 323 in each modification made to exhaust system A – right side reinforcement ribs - normal in-service conditions (without 2G deceleration)

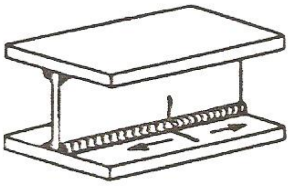 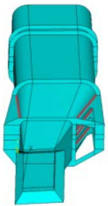	**Material type**			
	AISI 316L austenitic stainless steel			
	1st reinf. rib (MPa)	**2nd reinf. rib (MPa)**	**3rd reinf. rib (MPa)**	**4th reinf. rib (MPa)**
Current geometry	236	119	112	300
Thickness change of the intermediate section of the exhaust system pipe from 4 mm to 12 mm	84	76	76	120

Thickness change of the vertical reinforcement ribs to 4 mm	111	77	80	147
Thickness change of all the exhaust system plates to 4 mm	88	75	77	125
Thickness change of all the exhaust system plates to 12 mm	82	78	81	122
Removal of the inner vertical reinforcement ribs	180	---	---	232
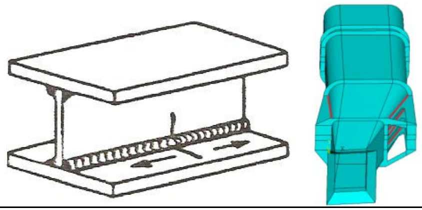	**Material type**			
	445M2 ferritic stainless steel			
	1st reinf. rib (MPa)	**2nd reinf. rib (MPa)**	**3rd reinf. rib (MPa)**	**4th reinf. rib (MPa)**
Current geometry	164	82	77	208
Thickness change of the intermediate section of the exhaust system pipe from 4 mm to 12 mm	61	53	53	86
Thickness change of the vertical reinforcement ribs to 4 mm	79	54	55	104
Thickness change of all the exhaust system plates to 4 mm	63	52	52	89
Thickness change of all the exhaust system plates to 12 mm	60	54	56	87
Removal of the inner vertical reinforcement ribs	127	---	---	164

Table 7.6 shows the maximum first principal nodal stress values obtained in the welded joints between the exhaust system's pipe and the left side reinforcement ribs (detail no. 323 - chapter 6.1). These maximum first principal nodal stress values were obtained for normal in-service conditions (without the 2G deceleration) in the current geometry of exhaust system A and in the selected modifications made to exhaust system A (chapter 8.1.1), for both AISI 316L austenitic stainless steel and 445M2 ferritic stainless steel.

The reinforcement ribs were numbered according to their position in exhaust system A, being the first reinforcement rib, the one seen in the front view of exhaust system A.

Table 7.6: First principal stress values actuating on detail no. 323 in each modification made to exhaust system A – left side reinforcement ribs - normal in-service conditions (without 2G deceleration)

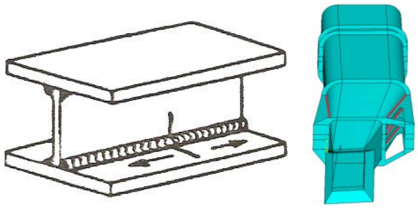	**Material type**			
	AISI 316L austenitic stainless steel			
	1st reinf. rib (MPa)	**2nd reinf. rib (MPa)**	**3rd reinf. rib (MPa)**	**4th reinf. rib (MPa)**
Current geometry	212	133	142	280
Thickness change of the intermediate section of the exhaust system pipe from 4 mm to 12 mm	160	101	107	114
Thickness change of the vertical reinforcement ribs to 4 mm	121	126	148	168
Thickness change of all the exhaust system plates to 4 mm	104	133	150	156
Thickness change of all the exhaust system plates to 12 mm	94	137	154	148
Removal of the inner vertical reinforcement ribs	176	---	---	237

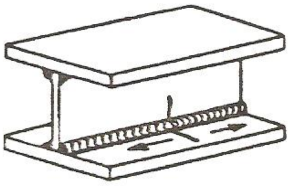 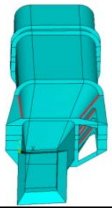	Material type			
	445M2 ferritic stainless steel			
	1st reinf. rib (MPa)	2nd reinf. rib (MPa)	3rd reinf. rib (MPa)	4th reinf. rib (MPa)
Current geometry	148	90	91	193
Thickness change of the intermediate section of the exhaust system pipe from 4 mm to 12 mm	116	67	70	81
Thickness change of the vertical reinforcement ribs to 4 mm	86	83	97	118
Thickness change of all the exhaust system plates to 4 mm	74	89	100	109
Thickness change of all the exhaust system plates to 12 mm	67	90	103	104
Removal of the inner vertical reinforcement ribs	124	---	---	164

For detail no. 323, the maximum first principal nodal stress values obtained for the overload condition (with the 2G deceleration) in the current geometry of exhaust system A and in the selected modifications made to exhaust system A (chapter 8.1.1), for both AISI 316L austenitic stainless steel and 445M2 ferritic stainless steel are shown in annex C, tables C.3 and C.4.

Structural detail no. 822:

Table 7.7 shows the maximum first principal nodal stress values obtained in the welded joint between the exhaust system's pipe and the intermediate supporting ring, considering that the intermediate supporting ring, which has a thickness of 30 mm, is infact two 15 mm thick flanges, that are bolted together (detail no. 822 - chapter 6.1).The aforementioned was done, in order to simulate the real conditions of the intermediate supporting ring. These maximum first principal nodal stress values were obtained for normal in-service conditions (without the 2G deceleration) in the current geometry of exhaust system A and in the selected modifications made to exhaust system A (chapter 8.1.1), for both AISI 316L austenitic stainless steel and 445M2 ferritic stainless steel.

Table 7.7: First principal stress values actuating on detail no. 822 in each modification made to exhaust system A – normal in-service conditions (without 2G deceleration)

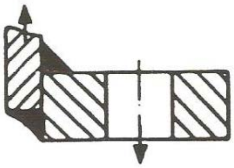 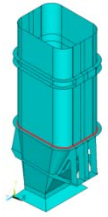	Material type	
	AISI 316L austenitic stainless steel	445M2 ferritic stainless steel
	Intermediate supporting ring (MPa)	Intermediate supporting ring (MPa)
Current geometry	339	235
Thickness change of the intermediate section of the exhaust system pipe from 4 mm to 12 mm	133	93
Thickness change of the vertical reinforcement ribs to 4 mm	209	148
Thickness change of all the exhaust system plates to 4 mm	156	110
Thickness change of all the exhaust system plates to 12 mm	134	95
Removal of the inner vertical reinforcement ribs	314	221

For detail no. 822, the maximum first principal nodal stress values obtained for the overload condition (with the 2G deceleration) in the current geometry of exhaust system A and in the selected modifications made to exhaust system A (chapter 8.1.1), for both AISI 316L austenitic stainless steel and 445M2 ferritic stainless steel are shown in annex C, table C.5.

7.1.2 First nodal stress results of exhaust system B:

Structural detail no. 511:

Table 7.8 shows the maximum first principal nodal stress values obtained in the welded joints between the doubler plates and the upper flanges of the right and left side reinforcement ribs, as well as between the doubler plates and the lower flanges of the right and left side reinforcement ribs (detail no. 511 - chapter 6.2). These maximum first principal nodal stress values were obtained for normal in-service conditions (without the 2G deceleration) in the current geometry of exhaust system B and in all the modifications made to exhaust system B (chapter 5.2), for both AISI 316L austenitic stainless steel and 445M2 ferritic stainless steel.

Table 7.8: First principal stress values actuating on detail no. 511 in each modification made to exhaust system B – normal in-service conditions (without 2G deceleration)

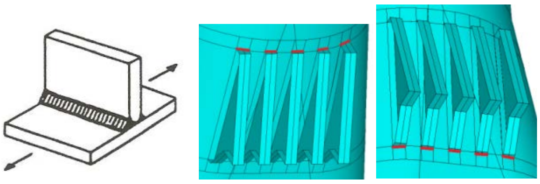	**Material type**			
	AISI 316L austenitic stainless steel		**445M2 ferritic stainless steel**	
	Upper flanges (MPa)	**Lower flanges (MPa)**	**Upper flanges (MPa)**	**Lower flanges (MPa)**
Current geometry	14	239	8	161
Thickness change of the intermediate section of the exhaust system pipe from 4 mm to 12 mm	17	186	9	125
Thickness change of all the exhaust system plates to 4 mm	15	156	11	107
Thickness change of all the exhaust system plates to 12 mm	21	152	13	102

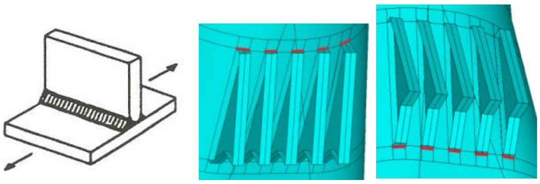	**Use of dissimilar welded joints of an AISI 316L austenitic and a 445 M2 ferritic stainless steels in the intermediate region of exhaust system**	
	Upper flanges (MPa)	**Lower flanges (MPa)**
Change of material type and thickness in the intermediate section to 445M2 ferritic and 12mm	198	289
Change of material type in the intermediate section to 445M2 ferritic	341	429

To confirm the maximum first principal stress values shown in table 7.8, some first principal stress distribution graphics, where these values were obtained from, are shown in annex B, B.5 to B.8. These graphics were obtained for the current geometry of exhaust system B and for the modification where the thickness of all the exhaust system B plates were changed to 12 mm.

Table 7.9 shows the maximum first principal nodal stress values obtained in the welded joints between the doubler plates and the upper flanges of the right and left side reinforcement ribs, as well as between the doubler plates and the lower flanges of the right and left side reinforcement ribs (detail no. 511 - chapter 6.2). These maximum first principal nodal stress values were obtained for the overload condition (with the 2G deceleration) in the current geometry of exhaust system B and in all the modifications made to exhaust system B (chapter 5.2), for both AISI 316L austenitic stainless steel and 445M2 ferritic stainless steel.

Table 7.9: First principal stress values actuating on detail no. 511 in each modification made to exhaust system B – overload conditions (with 2G deceleration)

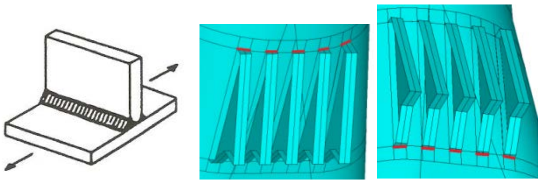	**Material type**			
	AISI 316L austenitic stainless steel		**445M2 ferritic stainless steel**	
	Upper flanges (MPa)	**Lower flanges (MPa)**	**Upper flanges (MPa)**	**Lower flanges (MPa)**
Current geometry	133	219	123	207
Thickness change of the intermediate section of the exhaust system pipe from 4 mm to 12 mm	49	198	43	168
Thickness change of all the exhaust system plates to 4 mm	91	346	89	317
Thickness change of all the exhaust system plates to 12 mm	42	180	42	150
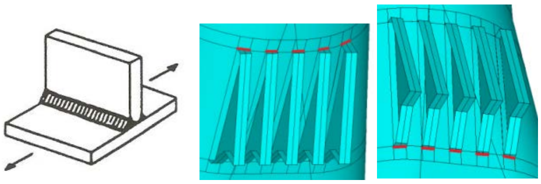	**Use of dissimilar welded joints of an AISI 316L austenitic and a 445 M2 ferritic stainless steels in the intermediate region of exhaust system**			
	Upper flanges (MPa)		**Lower flanges (MPa)**	
Change of material type and thickness in the intermediate section to 445M2 ferritic and 12mm	215		258	
Change of material type in the intermediate section to 445M2 ferritic	376		403	

From all the modifications made to exhaust system B (chapter 5.2), the ones that presented first principal nodal stress values (Tables 7.8 and 7.9) better than the current geometry of exhaust system B, were selected to be assessed in the following details. The reason for this selection is discussed in chapter 8.1.2.

Structural detail no. 232:

Table 7.10 shows the maximum first principal nodal stress values obtained in the butt welds that join the sections of the exhaust system's pipe which have equal wall thicknesses and are welded in regions near to the upper and lower ends of the doubler plates (detail no. 232 - chapter 6.2). These maximum first principal nodal stress values were obtained for normal in-service conditions (without the 2G deceleration) in the current geometry of exhaust system B and in the selected modifications made to exhaust system B (chapter 8.1.2), for both AISI 316L austenitic stainless steel and 445M2 ferritic stainless steel.

Table 7.10: First principal stress values actuating on detail no. 232 in each modification made to exhaust system B – normal in-service conditions (without 2G deceleration)

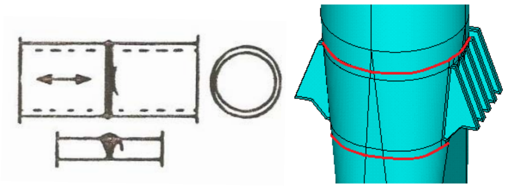	**Material type**			
	AISI 316L austenitic stainless steel		**445M2 ferritic stainless steel**	
	Upper end (MPa)	**Lower end (MPa)**	**Upper end (MPa)**	**Lower end (MPa)**
Current geometry	30	144	17	98
Thickness change of all the exhaust system plates to 4 mm	6	36	5	25
Thickness change of all the exhaust system plates to 12 mm	7	20	4	14

For detail no. 232, the maximum first principal nodal stress values obtained for the overload condition (with the 2G deceleration) in the current geometry of exhaust system B and in the selected modifications made to exhaust system B (chapter 8.1.2), for both AISI 316L austenitic stainless steel and 445M2 ferritic stainless steel are shown in annex D, table D.1.

Structural detail no. 223:

Table 7.11 shows the maximum first principal nodal stress values obtained in the butt welds of sections of the exhaust system’s pipe that could have, in the future, different wall thicknesses (redesigned strutcture) and are located near to the upper and lower ends of the doubler plates (detail no. 223 - chapter 6.2). These maximum first principal nodal stress values were obtained for normal in-service conditions (without the 2G deceleration) in the current geometry of exhaust system B and in the selected modifications made to exhaust system B (chapter 8.1.2), for both AISI 316L austenitic stainless steel and 445M2 ferritic stainless steel.

Table 7.11: First principal stress values actuating on detail no. 223 in each modification made to exhaust system B – normal in-service conditions (without 2G deceleration)

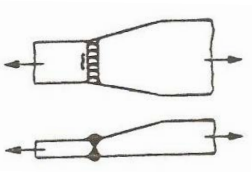 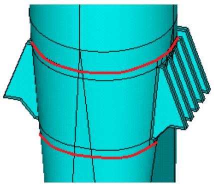	**Material type**			
	AISI 316L austenitic stainless steel		**445M2 ferritic stainless steel**	
	Upper end (MPa)	**Lower end (MPa)**	**Upper end (MPa)**	**Lower end (MPa)**
Thickness change of the intermediate section of the exhaust system pipe from 4 mm to 12 mm	7	20	5	18

For detail no. 223, the maximum first principal nodal stress values obtained for the overload condition (with the 2G deceleration) in the current geometry of exhaust system B and in the selected modifications made to exhaust system B (chapter 8.1.2), for both AISI 316L austenitic stainless steel and 445M2 ferritic stainless steel are shown in annex D, table D.2.

Structural detail no. 323:

Table 7.12 shows the maximum first principal nodal stress values obtained in the welded joints between the doubler plates and the right side reinforcement ribs (detail no. 323 - chapter 6.2). These maximum first principal nodal stress values were obtained for normal in-service conditions (without the 2G deceleration) in the current geometry of exhaust system B and in the selected modifications made to exhaust system B (chapter 8.1.2), for both AISI 316L austenitic stainless steel and 445M2 ferritic stainless steel.

The reinforcement ribs were numbered according to their position in exhaust system B, being the first reinforcement rib, the one seen in the front view of exhaust system B.

Table 7.12: First principal stress values actuating on detail no. 323 in each modification made to exhaust system B – right reinforcement ribs - normal in-service conditions (without 2G deceleration)

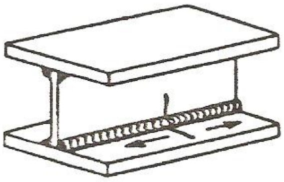 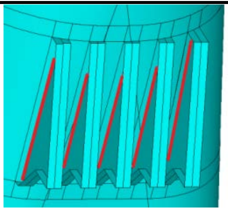	**Material type**				
	AISI 316L austenitic stainless steel				
	1st reinf. rib (MPa)	**2nd reinf. rib (MPa)**	**3rd reinf. rib (MPa)**	**4th reinf. rib (MPa)**	**5th reinf. rib (MPa)**
Current geometry	27	23	13	16	15
Thickness change of the intermediate section of the exhaust system pipe from 4 mm to 12 mm	69	51	15	20	33
Thickness change of all the exhaust system plates to 4 mm	43	40	14	22	24

Thickness change of all the exhaust system plates to 12 mm	69	51	15	20	33
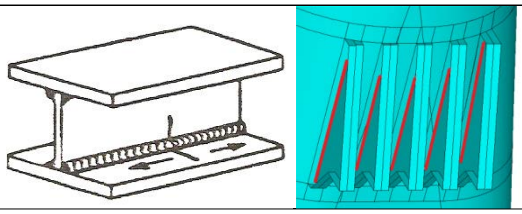	**Material type**				
	445M2 ferritic stainless steel				
	1st reinf. rib (MPa)	**2nd reinf. rib (MPa)**	**3rd reinf. rib (MPa)**	**4th reinf. rib (MPa)**	**5th reinf. rib (MPa)**
Current geometry	18	15	9	11	9
Thickness change of the intermediate section of the exhaust system pipe from 4 mm to 12 mm	39	31	7	14	27
Thickness change of all the exhaust system plates to 4 mm	28	27	11	16	16
Thickness change of all the exhaust system plates to 12 mm	46	33	10	14	22

Table 7.13 shows the maximum first principal nodal stress values obtained in the welded joints between the doubler plates and the left side reinforcement ribs (detail no. 323 - chapter 6.2). These maximum first principal nodal stress values were obtained for normal in-service conditions (without the 2G deceleration) in the current geometry of exhaust system B and in the selected modifications made to exhaust system B (chapter 8.1.2), for both AISI 316L austenitic stainless steel and 445M2 ferritic stainless steel. The reinforcement ribs were numbered according to their position in exhaust system B, being the first reinforcement rib, the one seen in the front view of exhaust system B.

Table 7.13: First principal stress values actuating on detail no. 323 in each modification made to exhaust system B – left reinforcement ribs - normal in-service conditions (without 2G deceleration)

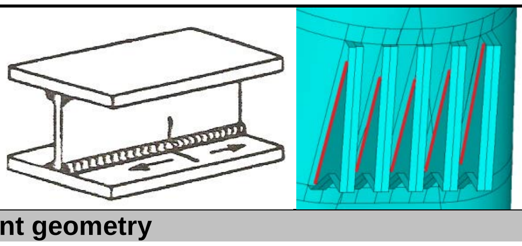	**Material type**				
	AISI 316L austenitic stainless steel				
	1st reinf. rib (MPa)	**2nd reinf. rib (MPa)**	**3rd reinf. rib (MPa)**	**4th reinf. rib (MPa)**	**5th reinf. rib (MPa)**
Current geometry	4	3	5	3	3
Thickness change of the intermediate section of the exhaust system pipe from 4 mm to 12 mm	5	3	5	4	3
Thickness change of all the exhaust system plates to 4 mm	4	4	10	6	3
Thickness change of all the exhaust system plates to 12 mm	5	3	5	4	3
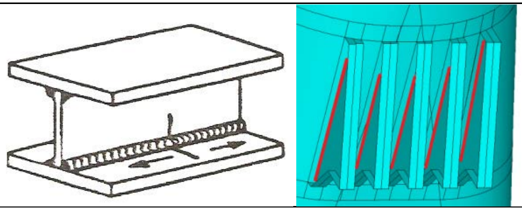	**Material type**				
	445M2 ferritic stainless steel				
	1st reinf. rib (MPa)	**2nd reinf. rib (MPa)**	**3rd reinf. rib (MPa)**	**4th reinf. rib (MPa)**	**5th reinf. rib (MPa)**
Current geometry	3	2	4	3	2
Thickness change of the intermediate section of the exhaust system pipe from 4 mm to 12 mm	1	2	3	2	1
Thickness change of all the exhaust system plates to 4 mm	3	4	9	5	2
Thickness change of all the exhaust system plates to 12 mm	3	2	4	3	1

For detail no. 323, the maximum first principal nodal stress values obtained for the overload condition (with the 2G deceleration) in the current geometry of exhaust system B and in the selected modifications made to exhaust system B (chapter 8.1.2), for both AISI 316L austenitic stainless steel and 445M2 ferritic stainless steel are shown in annex D, tables D.3 and D.4.

Structural details no. 712 and no. 721:

Table 7.14 shows the maximum first principal nodal stress values obtained in the welded joints between the exhaust system's pipe and the upper ends of the right doubler plates and the welded joints between the exhaust system's pipe and the lower ends of the right doubler plates (details no. 712 and no. 721 - chapter 6.2). These maximum first principal nodal stress values were obtained for normal in-service conditions (without the 2G deceleration) in the current geometry of exhaust system B and in the selected modifications made to exhaust system B (chapter 8.1.2), for both AISI 316L austenitic stainless steel and 445M2 ferritic stainless steel.

The doubler plates were numbered according to their position in exhaust system B, being the first reinforcement plate, the one seen in the front view of exhaust system B. The first principal nodal stress values presented in table 7.14, are the values obtained for the upper and for the lower ends of the right side doubler plates, respectively.

Table 7.14: First principal stress values actuating on details no. 712 and no.721 in each modification made to exhaust system B – upper and lower ends of the right side doubler plates - normal in-service conditions (without 2G deceleration)

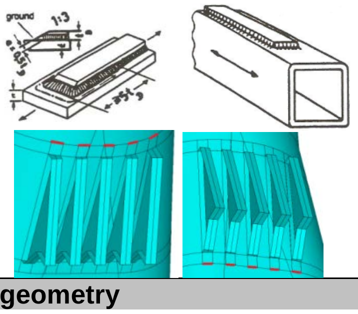	**Material type**				
	AISI 316L austenitic stainless steel				
	1st doubler plate (MPa)	**2nd doubler plate (MPa)**	**3rd doubler plate (MPa)**	**4th doubler plate (MPa)**	**5th doubler plate (MPa)**
Current geometry	3/3	11/13	2/43	16/144	11/27
Thickness change of the intermediate section of the exhaust system pipe from 4 mm to 12 mm	7/14	1/15	3/13	6/20	6/20
Thickness change of all the exhaust system plates to 4 mm	1/3	5/29	6/15	3/36	4/2
Thickness change of all the exhaust system plates to 12 mm	7/14	1/15	3/13	6/20	6/20
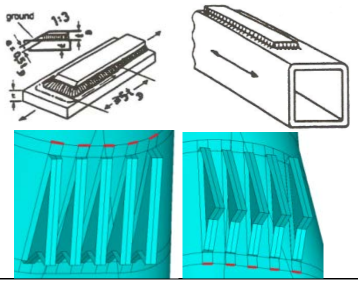	**Material type**				
	445M2 ferritic stainless steel				
	1st doubler plate (MPa)	**2nd doubler plate (MPa)**	**3rd doubler plate (MPa)**	**4th doubler plate (MPa)**	**5th doubler plate (MPa)**
Current geometry	17/3	4/86	0/30	10/98	8/18
Thickness change of the intermediate section of the exhaust system pipe from 4 mm to 12 mm	1/0	3/11	1/11	5/18	5/0
Thickness change of all the exhaust system plates to 4 mm	1/1	3/20	5/12	2/25	3/0
Thickness change of all the exhaust system plates to 12 mm	4/11	0/11	1/9	3/14	3/14

Table 7.15 shows the maximum first principal nodal stress values obtained in the welded joints between the exhaust system's pipe and the upper ends of the left doubler plates and the welded joints between the exhaust system's pipe and the lower ends of the left doubler plates (details no. 712 and

no. 721 - chapter 6.2). These maximum first principal nodal stress values were obtained for normal in-service conditions (without the 2G deceleration) in the current geometry of exhaust system B and in the selected modifications made to exhaust system B (chapter 8.1.2), for both AISI 316L austenitic stainless steel and 445M2 ferritic stainless steel.

The doubler plates were numbered according to their position in exhaust system B, being the first reinforcement plate, the one seen in the front view of exhaust system B. The first principal nodal stress values presented in table 7.15, are the values obtained for the upper and for the lower ends of the left side doubler plates, respectively.

Table 7.15: First principal stress values actuating on details no. 712 and no.721 in each modification made to exhaust system B – upper and lower ends of the left side doubler plates - normal in-service conditions (without 2G deceleration)

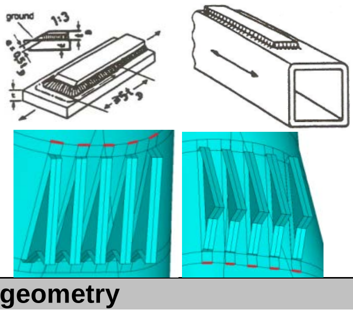	**Material type** **AISI 316L austenitic stainless steel**				
	1st doubler plate (MPa)	**2nd doubler plate (MPa)**	**3rd doubler plate (MPa)**	**4th doubler plate (MPa)**	**5th doubler plate (MPa)**
Current geometry	7/0	9/5	9/23	9/11	15/0
Thickness change of the intermediate section of the exhaust system pipe from 4 mm to 12 mm	4/0	4/4	5/10	4/6	4/0
Thickness change of all the exhaust system plates to 4 mm	1/0	1/8	5/17	3/11	4/0
Thickness change of all the exhaust system plates to 12 mm	4/0	4/4	5/10	4/6	4/0
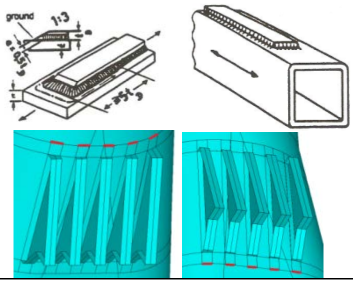	**Material type** **445M2 ferritic stainless steel**				
	1st doubler plate (MPa)	**2nd doubler plate (MPa)**	**3rd doubler plate (MPa)**	**4th doubler plate (MPa)**	**5th doubler plate (MPa)**
Current geometry	3/0	6/5	5/18	7/10	11/0
Thickness change of the intermediate section of the exhaust system pipe from 4 mm to 12 mm	3/0	2/4	1/9	5/7	5/0
Thickness change of all the exhaust system plates to 4 mm	1/0	0/8	5/15	2/10	3/0
Thickness change of all the exhaust system plates to 12 mm	2/0	1/4	2/8	3/6	2/0

For details no. 712 and no. 721, the maximum first principal nodal stress values obtained for the overload condition (with the 2G deceleration) in the current geometry of exhaust system B and in the selected modifications made to exhaust system B (chapter 8.1.2), for both AISI 316L austenitic stainless steel and 445M2 ferritic stainless steel are shown in annex D, tables D.5 and D.6.

7.2 Fatigue life prediction of classified structural details and welded joints:

The fatigue life assessment of the exhaust systems of naval gas turbines under study was performed on the structural details chosen in chapter 6.1, assuming that no crack like defect are present in the structural details. Hence, S-N Curves were used and through equations 6.1 and 6.2 and with the FAT class and the first principal nodal stress values obtained in chapters 6.1 and 7.1, respectively, the fatigue life of the chosen details, was calculated. It should be noted that, as previously mentioned, the nominal stress ranges used in the fatigue life assessment presented in this chapter were obtained by multiplying by 2 (R=-1) the first principal nodal stress values shown in section 7.1.

All the fatigue life values that present a fatigue life of over 5 million cycles (5 $\times 10^{6}$ cycles), were considered to have an infinite fatigue life. For first principal stress values equal or under 18 MPa, which corresponds to a stress range equal or under 36 MPa ($\Delta\sigma \leq 36\ MPa$), it was also considered that the details presented an infinite fatigue life [18].

One should note that these calculations were made considering high cycle fatigue (HCF). For fatigue lives below 3500 cycles, it is considered to be low cycle fatigue (LCF). For LCF, the fatigue lives should be calculated through the *Coffin-Manson* relation.

7.2.1 Fatigue life prediction of classified structural details of exhaust system A:

Structural detail no. 424:

Table 7.16 shows the fatigue life prediction made for detail no. 424 (chapter 6.1.1) for normal in-service conditions (without the 2G deceleration) in the current geometry of exhaust system A and in all the modifications made to exhaust system A (chapter 5.1). The fatigue life of this detail was predicted according to the FAT class chosen (Table 6.1), the first principal nodal stress values obtained (Table 7.1) and the material constants, C, calculated.

One shall note that in table 7.16, a FAT class of 45 was used for the fatigue life calculation for the current geometry of exhaust system A and for all the modifications made to exhaust system A, with exception to the modification where the thickness of all the exhaust system plates was changed to 12 mm. For this modification, a FAT class of 50 was used.

Table 7.16: Fatigue life prediction of detail no. 424 considering a FAT class of 45 – normal in-service conditions - exhaust system A (C = 8.65x10^{10}, T=350 ºC; C = 1.28x10^{11}, T=245 ºC)

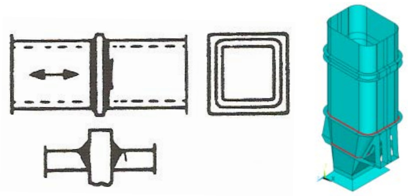	**Material type**			
	AISI 316L austenitic stainless steel		**445 M2 ferritic stainless steel**	
	Intermediate supporting ring (cycles)	**Lower supporting ring (cycles)**	**Intermediate supporting ring (cycles)**	**Lower supporting ring (cycles)**
Current geometry	<3500	8220	<3500	28100
Addition of four vertical reinforcement ribs	<3500	7310	<3500	25200
Addition of two vertical reinforcement ribs	<3500	7660	5540	14700
Addition of a horizontal supporting ring	<3500	4400	<3500	26200
Thickness change of the intermediate section of the exhaust system pipe from 4 mm to 12 mm	4600	21300	13400	67400
Thickness change of the intermediate supporting ring from 30 mm to 12 mm	<3500	8420	<3500	29100
Thickness change of the intermediate and lower supporting rings to 4 mm	<3500	7140	<3500	27100

Thickness change of the vertical reinforcement ribs to 4 mm	<3500	13500	<3500	43000
Thickness change of all the exhaust system plates to 4 mm	<3500	14300	8120	48900
Thickness change of all the exhaust system plates to 12 mm	6160	19600	17300	67100
Removal of the outer vertical reinforcement ribs	<3500	4660	<3500	15600
Removal of the inner vertical reinforcement ribs	<3500	16100	<3500	53400
Partial removal of the lower supporting ring	<3500	5850	<3500	20000
Partial removal of the intermediate supporting ring	<3500	9530	<3500	32600
Total removal of the intermediate supporting ring	---	9530	---	32600

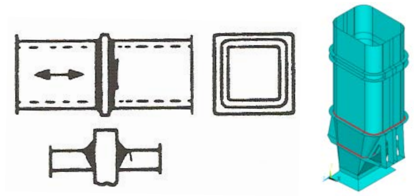	**Use of dissimilar welded joints of an AISI 316L Austenitic and a 445 M2 ferritic stainless steels in the intermediate region of exhaust system**	
	Intermediate supporting ring (cycles)	**Lower supporting ring (cycles)**
Change of material type and thickness in the intermediate section to 445M2 ferritic and 12mm	<3500	9530
Change of material in the intermediate section to 445M2 ferritic	<3500	<3500

Structural detail no. 234:

Table 7.17 shows the fatigue life prediction made for detail no. 234 (chapter 6.1.1) for normal in-service conditions (without the 2G deceleration) in the current geometry of exhaust system A and in the selected modifications made to exhaust system A (chapter 8.1.1), considering that it was root inspected without the use of non destructive tests (no NDT). The fatigue life of such detail was predicted according to the FAT class chosen (Table 6.3), the first principal nodal stress values obtained (Table 7.3) and the material constants, C, calculated.

Table 7.17: Fatigue life prediction of detail no. 234 considering a FAT class of 45 – normal in-service conditions - exhaust system A (C = 8.65x10^{10}, T=350 °C; C = 1.28x10^{11}, T=245 °C)

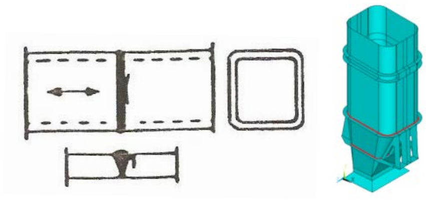	**Material type**			
	AISI 316L austenitic stainless steel		**445M2 ferritic stainless steel**	
	Intermediate supporting ring (cycles)	**Lower supporting ring (cycles)**	**Intermediate supporting ring (cycles)**	**Lower supporting ring (cycles)**
Current geometry	<3500	8220	<3500	28100
Thickness change of the vertical reinforcement ribs to 4 mm	<3500	13500	<3500	43000
Thickness change of all the exhaust system plates to 4 mm	<3500	14300	8120	48900
Thickness change of all the exhaust system plates to 12 mm	4490	14300	12600	48900
Removal of the inner vertical reinforcement ribs	<3500	16100	<3500	53400

Table 7.18 shows the fatigue life prediction made for detail no. 234 (chapter 6.1.1) for normal in-service conditions (without the 2G deceleration) in the current geometry of exhaust system A and in the selected modifications made to exhaust system A (chapter 8.1.1), considering that it was root inspected by NDT. The fatigue life of this detail was predicted according to the FAT class chosen (Table 6.3), the first principal nodal stress values obtained (Table 7.3) and the material constants, C, calculated.

Table 7.18: Fatigue life prediction of detail no. 234 considering a FAT class of 56 – normal in-service conditions - exhaust system A (C = $1.67\text{x}10^{11}$, T=350 ºC; C = $2.48\text{x}10^{11}$, T=245 ºC)

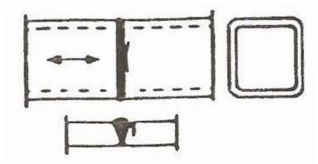 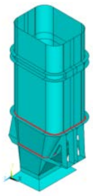	**Material type**			
	AISI 316L austenitic stainless steel		**445M2 ferritic stainless steel**	
	Intermediate supporting ring (cycles)	**Lower supporting ring (cycles)**	**Intermediate supporting ring (cycles)**	**Lower supporting ring (cycles)**
Current geometry	<3500	15800	<3500	54100
Thickness change of the vertical reinforcement ribs to 4 mm	<3500	26000	6430	82900
Thickness change of all the exhaust system plates to 4 mm	5490	27500	15700	94200
Thickness change of all the exhaust system plates to 12 mm	8660	27500	24300	94200
Removal of the inner vertical reinforcement ribs	<3500	31000	<3500	103000

Structural detail no. 223:

Table 7.19 shows the fatigue life prediction made for detail no. 223 (chapter 6.1.1) for normal in-service conditions (without the 2G deceleration) in the current geometry of exhaust system A and in the selected modifications made to exhaust system A (chapter 8.1.1). The fatigue life of this detail was predicted according to the FAT class chosen (Table 6.4), the first principal nodal stress values obtained (Table 7.4) and the material constants, C, calculated.

Table 7.19: Fatigue life prediction of detail no. 223 considering a FAT class of 80 (with $\mathrm{k_m}$ = 3) – normal in-service conditions - exhaust system A (C = $1.80\text{x}10^{10}$, T=350 ºC; C = $2.67\text{x}10^{10}$, T=245 ºC)

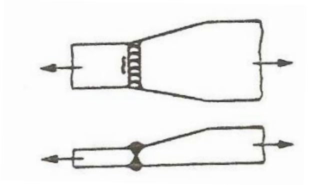 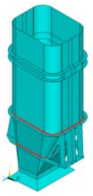	**Material type**			
	AISI 316L austenitic stainless steel		**445M2 ferritic stainless steel**	
	Intermediate supporting ring (cycles)	**Lower supporting ring (cycles)**	**Intermediate supporting ring (cycles)**	**Lower supporting ring (cycles)**
Thickness change of the intermediate section of the exhaust system pipe from 4 mm to 12 mm	<3500	4440	<3500	14000

Structural detail no. 323:

Table 7.20 shows the fatigue life prediction made for detail no. 323 (chapter 6.1.1) for normal in-service conditions (without the 2G deceleration) in the current geometry of exhaust system A and in the selected modifications made to exhaust system A (chapter 8.1.1). The fatigue life of such detail was predicted according to the FAT class chosen (Table 6.5), the first principal nodal stress values obtained (Table 7.5) and the material constant, C, calculated.

Table 7.20: Fatigue life prediction of detail no. 323 for a FAT class of 90 - right side reinforcement ribs – normal in-service conditions - exhaust system A (C = 9.60x10^{11}, T=275 ºC)

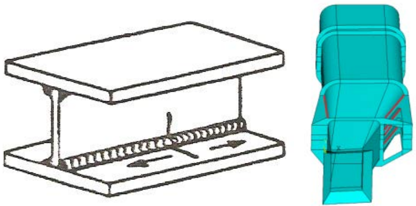	**Material type**			
	AISI 316L austenitic stainless steel			
	1st reinf. rib (cycles)	**2nd reinf. rib (cycles)**	**3rd reinf. rib (cycles)**	**4th reinf. rib (cycles)**
Current geometry	9130	71200	85400	4440
Thickness change of the intermediate section of the exhaust system pipe from 4 mm to 12 mm	202000	273000	273000	69500
Thickness change of the vertical reinforcement ribs to 4 mm	87800	263000	234000	37800
Thickness change of all the exhaust system plates to 4 mm	176000	284000	263000	61400
Thickness change of all the exhaust system plates to 12 mm	218000	253000	226000	66100
Removal of the inner vertical reinforcement ribs	20600	---	---	9610
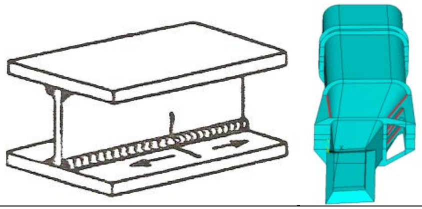	**Material type**			
	445M2 ferritic stainless steel			
	1st reinf. rib (cycles)	**2nd reinf. rib (cycles)**	**3rd reinf. rib (cycles)**	**4th reinf. rib (cycles)**
Current geometry	27200	218000	263000	13300
Thickness change of the intermediate section of the exhaust system pipe from 4 mm to 12 mm	529000	806000	806000	189000
Thickness change of the vertical reinforcement ribs to 4 mm	243000	762000	762000	107000
Thickness change of all the exhaust system plates to 4 mm	480000	854000	854000	170000
Thickness change of all the exhaust system plates to 12 mm	556000	762000	683000	182000
Removal of the inner vertical reinforcement ribs	58600	---	---	27200

Table 7.21 shows the fatigue life prediction made for detail no. 323 (chapter 6.1.1) for normal in-service conditions (without the 2G deceleration) in the current geometry of exhaust system A and in the selected modifications made to exhaust system A (chapter 8.1.1). The fatigue life of this detail was predicted according to the FAT class chosen (Table 6.5), the first principal nodal stress values obtained (Table 7.6) and the material constant, C, calculated.

Table 7.21: Fatigue life prediction of detail no. 323 for a FAT class of 90 - left side reinforcement ribs – normal in-service conditions - exhaust system A (C = 9.60x10^{11}, T=275 ºC)

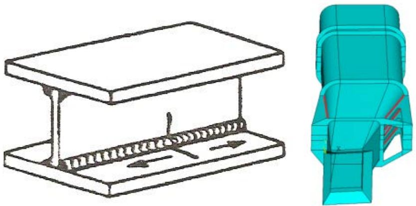	**Material type**			
	AISI 316L austenitic stainless steel			
	1st reinf. rib (cycles)	**2nd reinf. rib (cycles)**	**3rd reinf. rib (cycles)**	**4th reinf. rib (cycles)**
Current geometry	12600	51000	41900	5470
Thickness change of the intermediate section of the exhaust system pipe from 4 mm to 12 mm	29300	116000	98000	81000
Thickness change of the vertical reinforcement ribs to 4 mm	67700	60000	37000	25300

Thickness change of all the exhaust system plates to 4 mm	107000	51000	35600	31600
Thickness change of all the exhaust system plates to 12 mm	144000	46700	32900	37000
Removal of the inner vertical reinforcement ribs	22000	---	---	9020

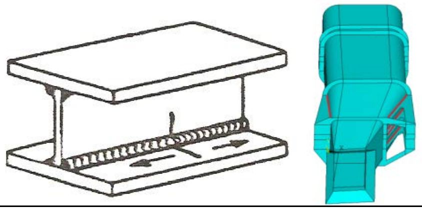	**Material type**			
	445M2 ferritic stainless steel			
	1st reinf. rib (cycles)	**2nd reinf. rib (cycles)**	**3rd reinf. rib (cycles)**	**4th reinf. rib (cycles)**
Current geometry	37000	165000	159000	16700
Thickness change of the intermediate section of the exhaust system pipe from 4 mm to 12 mm	76900	399000	350000	226000
Thickness change of the vertical reinforcement ribs to 4 mm	189000	210000	131000	73000
Thickness change of all the exhaust system plates to 4 mm	296000	170000	120000	92700
Thickness change of all the exhaust system plates to 12 mm	399000	165000	110000	107000
Removal of the inner vertical reinforcement ribs	62900	---	---	27200

Structural detail no. 822:

Table 7.22 shows the fatigue life prediction made for detail no. 822 (chapter 6.1.1) for normal in-service conditions (without the 2G deceleration) in the current geometry of exhaust system A and in the selected modifications made to exhaust system A (chapter 8.1.1). The fatigue life of this detail was predicted according to the FAT class chosen (Table 6.7), the first principal nodal stress values obtained (Table 7.7) and the material constant, C, calculated.

Table 7.22: Fatigue life prediction of detail no. 822 for a FAT class of 63 – normal in-service conditions - exhaust system A (C = 2.37x10^{11}, T=350 ºC)

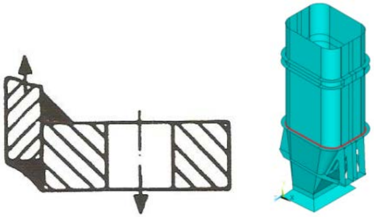	**Material type**	
	AISI 316L austenitic stainless steel	**445M2 ferritic stainless steel**
	Intermediate supporting ring (cycles)	**Intermediate supporting ring (cycles)**
Current geometry	<3500	<3500
Thickness change of the intermediate section of the exhaust system pipe from 4 mm to 12 mm	12600	36900
Thickness change of the vertical reinforcement ribs to 4 mm	<3500	9150
Thickness change of all the exhaust system plates to 4 mm	7810	22300
Thickness change of all the exhaust system plates to 12 mm	12300	34600
Removal of the inner vertical reinforcement ribs	<3500	<3500

7.2.2 Fatigue life prediction of classified structural details of exhaust system B:

Structural detail no. 511:

Table 7.23 shows the fatigue life prediction made for detail no. 511 (chapter 6.1.2) for normal in-service conditions (without the 2G deceleration) in the current geometry of exhaust system B and in all the modifications made to exhaust system B (chapter 5.2). The fatigue life of this detail was predicted according to the FAT class chosen (Table 6.9), the first principal nodal stress values obtained (Table 7.8) and the material constants, C, calculated.

Table 7.23: Fatigue life prediction of detail no. 511 for a FAT class of 80 – normal in-service conditions - exhaust system B (C = 4.32x10^{11}, T=370 ºC; C = 4.15x10^{11}, T=380 ºC)

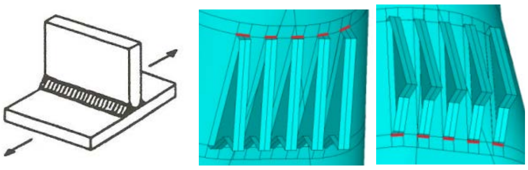	**Material type**			
	AISI 316L austenitic stainless steel		**445M2 ferritic stainless steel**	
	Upper flanges (cycles)	**Lower flanges (cycles)**	**Upper flanges (cycles)**	**Lower flanges (cycles)**
Current geometry	$>5 \times 10^{6}$	3800	$>5 \times 10^{6}$	12400
Thickness change of the intermediate section of the exhaust system pipe from 4 mm to 12 mm	$>5 \times 10^{6}$	8060	$>5 \times 10^{6}$	26600
Thickness change of all the exhaust system plates to 4 mm	$>5 \times 10^{6}$	13700	$>5 \times 10^{6}$	42300
Thickness change of all the exhaust system plates to 12 mm	$>5 \times 10^{6}$	14800	$>5 \times 10^{6}$	48900
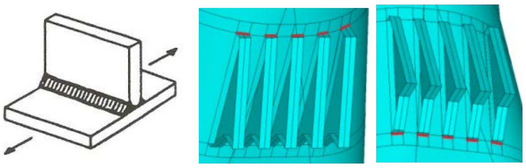	**Use of dissimilar welded joints of an AISI 316L austenitic and a 445 M2 ferritic stainless steels in the intermediate region of exhaust system**			
	Upper flanges (cycles)		**Lower flanges (cycles)**	
Change of material type and thickness in the intermediate section to 445M2 ferritic and 12mm	6960		<3500	
Change of material type in the intermediate section to 445M2 ferritic	<3500		<3500	

Structural detail no. 232:

Table 7.24 shows the fatigue life prediction made for detail no. 232 (chapter 6.1.2) for normal in-service conditions (without the 2G deceleration) in the current geometry of exhaust system B and in the selected modifications made to exhaust system B (chapter 8.1.2), considering that it was root inspected without the use of non destructive tests (no NDT). The fatigue life of this detail was predicted according to the FAT class chosen (Table 6.11), the first principal nodal stress values obtained (Table 7.10) and the material constants, C, calculated.

Table 7.24: Fatigue life prediction of detail no. 232 for a FAT class of 45 – normal in-service conditions - exhaust system B (C = 8.00x10^{10}, T=365 ºC; C = 7.09x10^{10}, T=395 ºC)

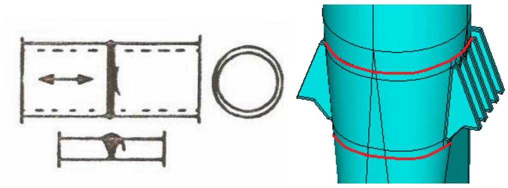	**Material type**			
	AISI 316L austenitic stainless steel		**445M2 ferritic stainless steel**	
	Upper end (cycles)	**Lower end (cycles)**	**Upper end (cycles)**	**Lower end (cycles)**
Current geometry	370000	<3500	2.04×10^{6}	9420
Thickness change of all the exhaust system plates to 4 mm	$>5 \times 10^{6}$	190000	$>5 \times 10^{6}$	567000
Thickness change of all the exhaust system plates to 12 mm	$>5 \times 10^{6}$	1.10×10^{6}	$>5 \times 10^{6}$	3.23×10^{6}

Table 7.25 shows the fatigue life prediction made for detail no. 232 (chapter 6.1.2) for normal in-service conditions (without the 2G deceleration) in the current geometry of exhaust system B and in the selected modifications made to exhaust system B (chapter 8.1.2), considering that it was root inspected with the use of NDT. The fatigue life of this detail was predicted according to the FAT class chosen (Table 6.11), the first principal nodal stress values obtained (Table 7.10) and the material constants, C, calculated.

Table 7.25: Fatigue life prediction of detail no. 232 for a FAT class of 71 – normal in-service conditions - exhaust system B (C = 3.14x10^{11}, T=365 ºC; C = 2.78x10^{11}, T=395 ºC)

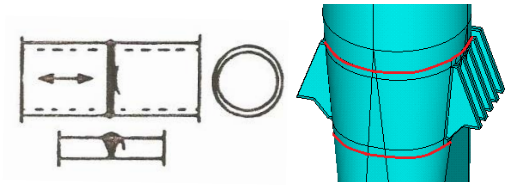	Material type			
	AISI 316L austenitic stainless steel		445M2 ferritic stainless steel	
	Upper end (cycles)	Lower end (cycles)	Upper end (cycles)	Lower end (cycles)
Current geometry	1.45×10^6	11700	$>5 \times 10^6$	37000
Thickness change of all the exhaust system plates to 4 mm	$>5 \times 10^6$	746000	$>5 \times 10^6$	2.23×10^6
Thickness change of all the exhaust system plates to 12 mm	$>5 \times 10^6$	4.35×10^6	$>5 \times 10^6$	$>5 \times 10^6$

Structural detail no. 223:

Table 7.26 shows the fatigue life prediction made for detail no. 223 (chapter 6.1.2) for normal in-service conditions (without the 2G deceleration) in the current geometry of exhaust system B and in the selected modifications made to exhaust system B (chapter 8.1.2). The fatigue life of this detail was predicted according to the FAT class chosen (Table 6.13), the first principal nodal stress values obtained (Table 7.11) and the material constants, C, calculated.

Table 7.26: Fatigue life prediction of detail no. 223 for a FAT class of 80 (with k_m = 3) – normal in-service conditions - exhaust system B (C = 1.67x10^{10}, T=365 ºC; C = 1.48x10^{10}, T=395 ºC)

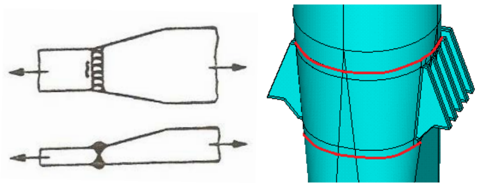	Material type			
	AISI 316L austenitic stainless steel		445M2 ferritic stainless steel	
	Upper end (cycles)	Lower end (cycles)	Upper end (cycles)	Lower end (cycles)
Thickness change of the intermediate section of the exhaust system pipe from 4 mm to 12 mm	$>5 \times 10^6$	231000	$>5 \times 10^6$	316000

Structural detail no. 323:

Table 7.27 shows the fatigue life prediction made for detail no. 323 (chapter 6.1.2) for normal in-service conditions (without the 2G deceleration) in the current geometry of exhaust system B and in the selected modifications made to exhaust system B (chapter 8.1.2). The fatigue life of this detail was predicted according to the FAT class chosen (Table 6.14), the first principal nodal stress values obtained (Table 7.12) and the material constant, C, calculated.

Table 7.27: Fatigue life prediction of detail no. 323 for a FAT class of 90 - right side reinforcement ribs – normal in-service conditions - exhaust system B (C = 5.91x10^{11}, T=385 ºC)

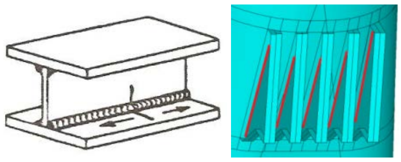	**Material type**				
	AISI 316L austenitic stainless steel				
	1st reinf. rib (cycles)	**2nd reinf. rib (cycles)**	**3rd reinf. rib (cycles)**	**4th reinf. rib (cycles)**	**5th reinf. rib (cycles)**
Current geometry	3.75×10^6	$>5\times10^6$	$>5\times10^6$	$>5\times10^6$	$>5\times10^6$
Thickness change of the intermediate section of the exhaust system pipe from 4 mm to 12 mm	225000	557000	$>5\times10^6$	$>5\times10^6$	2.06×10^6
Thickness change of all the exhaust system plates to 4 mm	929000	1.15×10^6	$>5\times10^6$	$>5\times10^6$	$>5\times10^6$
Thickness change of all the exhaust system plates to 12 mm	225000	557000	$>5\times10^6$	$>5\times10^6$	2.06×10^6
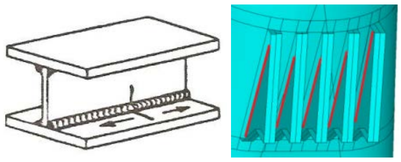	**Material type**				
	445M2 ferritic stainless steel				
	1st reinf. rib (cycles)	**2nd reinf. rib (cycles)**	**3rd reinf. rib (cycles)**	**4th reinf. rib (cycles)**	**5th reinf. rib (cycles)**
Current geometry	$>5\times10^6$	$>5\times10^6$	$>5\times10^6$	$>5\times10^6$	$>5\times10^6$
Thickness change of the intermediate section of the exhaust system pipe from 4 mm to 12 mm	1.24×10^6	2.48×10^6	$>5\times10^6$	$>5\times10^6$	3.75×10^6
Thickness change of all the exhaust system plates to 4 mm	3.36×10^6	3.75×10^6	$>5\times10^6$	$>5\times10^6$	$>5\times10^6$
Thickness change of all the exhaust system plates to 12 mm	759000	2.06×10^6	$>5\times10^6$	$>5\times10^6$	$>5\times10^6$

Table 7.28 shows the fatigue life prediction made for detail no. 323 (chapter 6.1.2) for normal in-service conditions (without the 2G deceleration) in the current geometry of exhaust system B and in the selected modifications made to exhaust system B (chapter 8.1.2). The fatigue life of this detail was predicted according to the FAT class chosen (Table 6.14), the first principal nodal stress values obtained (Table 7.13) and the material constant, C, calculated.

Table 7.28: Fatigue life prediction of detail no. 323 for a FAT class of 90 - left side reinforcement ribs – normal in-service conditions - exhaust system B (C = 5.91x10^{11}, T=385 ºC)

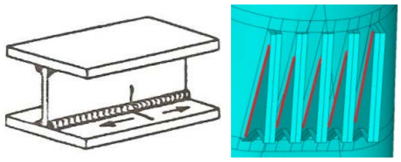	**Material type**				
	AISI 316L austenitic stainless steel				
	1st reinf. rib (cycles)	**2nd reinf. rib (cycles)**	**3rd reinf. rib (cycles)**	**4th reinf. rib (cycles)**	**5th reinf. rib (cycles)**
Current geometry	$>5\times10^6$	$>5\times10^6$	$>5\times10^6$	$>5\times10^6$	$>5\times10^6$
Thickness change of the intermediate section of the exhaust system pipe from 4 mm to 12 mm	$>5\times10^6$	$>5\times10^6$	$>5\times10^6$	$>5\times10^6$	$>5\times10^6$
Thickness change of all the exhaust system plates to 4 mm	$>5\times10^6$	$>5\times10^6$	$>5\times10^6$	$>5\times10^6$	$>5\times10^6$
Thickness change of all the exhaust system plates to 12 mm	$>5\times10^6$	$>5\times10^6$	$>5\times10^6$	$>5\times10^6$	$>5\times10^6$

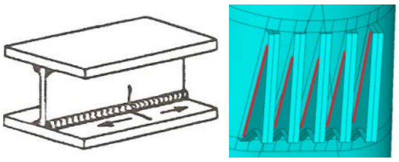	Material type				
	445M2 ferritic stainless steel				
	1st reinf. rib (cycles)	**2nd reinf. rib (cycles)**	**3rd reinf. rib (cycles)**	**4th reinf. rib (cycles)**	**5th reinf. rib (cycles)**
Current geometry	>5 ×10^6	>5 ×10^6	>5 ×10^6	>5 ×10^6	>5 ×10^6
Thickness change of the intermediate section of the exhaust system pipe from 4 mm to 12 mm	>5 ×10^6	>5 ×10^6	>5 ×10^6	>5 ×10^6	>5 ×10^6
Thickness change of all the exhaust system plates to 4 mm	>5 ×10^6	>5 ×10^6	>5 ×10^6	>5 ×10^6	>5 ×10^6
Thickness change of all the exhaust system plates to 12 mm	>5 ×10^6	>5 ×10^6	>5 ×10^6	>5 ×10^6	>5 ×10^6

Structural detail no. 712:

Table 7.29 shows the fatigue life prediction made for detail no. 712 (chapter 6.1.2) for normal in-service conditions (without the 2G deceleration) in the current geometry of exhaust system B and in the selected modifications made to exhaust system B (chapter 8.1.2). The fatigue life of this detail was predicted according to the FAT class chosen (Table 6.16), the first principal nodal stress values obtained (Table 7.14) and the material constants, C, calculated.

It should be noted that in table 7.29, a FAT class of 56 was used for the fatigue life calculation for the current geometry of exhaust system B, due to the relation between the exhaust system pipe thickness and the reinforcement plate thicknesses (Table 6.16). For the remaining modifications made to exhaust system B, a FAT class of 63 was used. The values presented in table 7.29 correspond to the fatigue life of the upper and lower ends, respectively, of each of the right side doubler plates.

Table 7.29: Fatigue life prediction of detail no. 712 for a FAT class of 63 - upper and lower ends of the right side doubler plates – normal in-service conditions - exhaust system B (C = 2.20x10^{11}, T=365 ºC / C = 1.95x10^{11}, T=395 ºC)

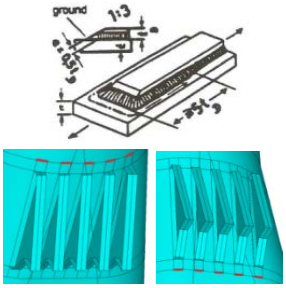	Material type				
	AISI 316L austenitic stainless steel				
	1st doubler plate (cycles)	**2nd doubler plate (cycles)**	**3rd doubler plate (cycles)**	**4th doubler plate (cycles)**	**5th doubler plate (cycles)**
Current geometry	>5 ×10^6/ >5 ×10^6	>5 ×10^6/ >5 ×10^6	>5 ×10^6/ 215000	>5 ×10^6/ 5720	>5 ×10^6/ 868000
Thickness change of the intermediate section of the exhaust system pipe from 4 mm to 12 mm	>5 ×10^6/ >5 ×10^6	>5 ×10^6/ >5 ×10^6	>5 ×10^6/ >5 ×10^6	>5 ×10^6/ 3.04 ×10^6	>5 ×10^6/ 3.04 ×10^6
Thickness change of all the exhaust system plates to 4 mm	>5 ×10^6/ >5 ×10^6	>5 ×10^6/ 997000	>5 ×10^6/ >5 ×10^6	>5 ×10^6/ 521000	>5 ×10^6/ >5 ×10^6
Thickness change of all the exhaust system plates to 12 mm	>5 ×10^6/ >5 ×10^6	>5 ×10^6/ >5 ×10^6	>5 ×10^6/ >5 ×10^6	>5 ×10^6/ 3.04 ×10^6	>5 ×10^6/ 3.04 ×10^6

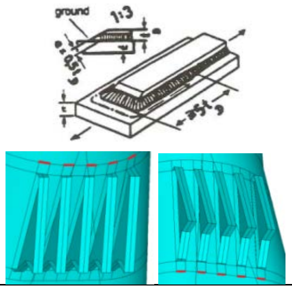	Material type				
	445M2 ferritic stainless steel				
	1st doubler plate (cycles)	2nd doubler plate (cycles)	3rd doubler plate (cycles)	4th doubler plate (cycles)	5th doubler plate (cycles)
Current geometry	3.92×10^6/ $>5 \times 10^6$	$>5 \times 10^6$/ 26900	$>5 \times 10^6$/ 633000	$>5 \times 10^6$/ 18100	$>5 \times 10^6$/ 2.93×10^6
Thickness change of the intermediate section of the exhaust system pipe from 4 mm to 12 mm	$>5 \times 10^6$/ $>5 \times 10^6$	$>5 \times 10^6$/ $>5 \times 10^6$	$>5 \times 10^6$/ $>5 \times 10^6$	$>5 \times 10^6$/ 4.17×10^6	$>5 \times 10^6$/ $>5 \times 10^6$
Thickness change of all the exhaust system plates to 4 mm	$>5 \times 10^6$/ $>5 \times 10^6$	$>5 \times 10^6$/ 3.04×10^6	$>5 \times 10^6$/ $>5 \times 10^6$	$>5 \times 10^6$/ 1.56×10^6	$>5 \times 10^6$/ $>5 \times 10^6$
Thickness change of all the exhaust system plates to 12 mm	$>5 \times 10^6$/ $>5 \times 10^6$	$>5 \times 10^6$/ $>5 \times 10^6$	$>5 \times 10^6$/ $>5 \times 10^6$	$>5 \times 10^6$/ $>5 \times 10^6$	$>5 \times 10^6$/ $>5 \times 10^6$

Table 7.30 shows the fatigue life prediction made for detail no. 712 (chapter 6.1.2) for normal in-service conditions (without the 2G deceleration) in the current geometry of exhaust system B and in the selected modifications made to exhaust system B (chapter 8.1.2). The fatigue life of this detail was predicted according to the FAT class chosen (Table 6.16), the first principal nodal stress values obtained (Table 7.15) and the material constants, C, calculated.

It should be noted that in table 7.30, a FAT class of 56 was used for the fatigue life calculation for the current geometry of exhaust system B, due to the relation between the exhaust system pipe thickness and the reinforcement plate thicknesses (Table 6.16). For the remaining modifications made to exhaust system B, a FAT class of 63 was used. The values presented in table 7.30 correspond to the fatigue life of the upper and lower ends, respectively, of each of the left side doubler plates.

Table 7.30: Fatigue life prediction of detail no. 712 for a FAT class of 63 - upper and lower ends of the left side doubler plates – normal in-service conditions - exhaust system B (C = 2.20x10^{11}, T=365 ºC / C = 1.95x10^{11}, T=395 ºC)

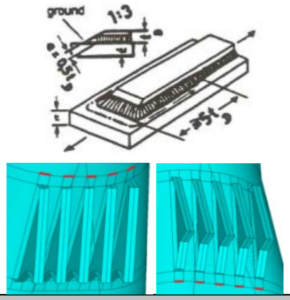	Material type				
	AISI 316L austenitic stainless steel				
	1st doubler plate (cycles)	2nd doubler plate (cycles)	3rd doubler plate (cycles)	4th doubler plate (cycles)	5th doubler plate (cycles)
Current geometry	$>5 \times 10^6$/ $>5 \times 10^6$	$>5 \times 10^6$/ $>5 \times 10^6$	$>5 \times 10^6$/ 1.40×10^6	$>5 \times 10^6$/ $>5 \times 10^6$	$>5 \times 10^6$/ $>5 \times 10^6$
Thickness change of the intermediate section of the exhaust system pipe from 4 mm to 12 mm	$>5 \times 10^6$/ $>5 \times 10^6$	$>5 \times 10^6$/ $>5 \times 10^6$	$>5 \times 10^6$/ $>5 \times 10^6$	$>5 \times 10^6$/ $>5 \times 10^6$	$>5 \times 10^6$/ $>5 \times 10^6$
Thickness change of all the exhaust system plates to 4 mm	$>5 \times 10^6$/ $>5 \times 10^6$	$>5 \times 10^6$/ $>5 \times 10^6$	$>5 \times 10^6$/ 4.95×10^6	$>5 \times 10^6$/ $>5 \times 10^6$	$>5 \times 10^6$/ $>5 \times 10^6$
Thickness change of all the exhaust system plates to 12 mm	$>5 \times 10^6$/ $>5 \times 10^6$	$>5 \times 10^6$/ $>5 \times 10^6$	$>5 \times 10^6$/ $>5 \times 10^6$	$>5 \times 10^6$/ $>5 \times 10^6$	$>5 \times 10^6$/ $>5 \times 10^6$

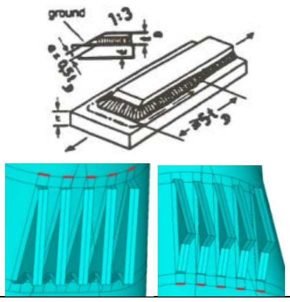	Material type				
	445M2 ferritic stainless steel				
	1st doubler plate (cycles)	2nd doubler plate (cycles)	3rd doubler plate (cycles)	4th doubler plate (cycles)	5th doubler plate (cycles)
Current geometry	$>5\times10^{6}$/ $>5\times10^{6}$	$>5\times10^{6}$/ $>5\times10^{6}$	$>5\times10^{6}$/ 2.93×10^{6}	$>5\times10^{6}$/ $>5\times10^{6}$	$>5\times10^{6}$/ $>5\times10^{6}$
Thickness change of the intermediate section of the exhaust system pipe from 4 mm to 12 mm	$>5\times10^{6}$/ $>5\times10^{6}$	$>5\times10^{6}$/ $>5\times10^{6}$	$>5\times10^{6}$/ $>5\times10^{6}$	$>5\times10^{6}$/ $>5\times10^{6}$	$>5\times10^{6}$/ $>5\times10^{6}$
Thickness change of all the exhaust system plates to 4 mm	$>5\times10^{6}$/ $>5\times10^{6}$	$>5\times10^{6}$/ $>5\times10^{6}$	$>5\times10^{6}$/ $>5\times10^{6}$	$>5\times10^{6}$/ $>5\times10^{6}$	$>5\times10^{6}$/ $>5\times10^{6}$
Thickness change of all the exhaust system plates to 12 mm	$>5\times10^{6}$/ $>5\times10^{6}$	$>5\times10^{6}$/ $>5\times10^{6}$	$>5\times10^{6}$/ $>5\times10^{6}$	$>5\times10^{6}$/ $>5\times10^{6}$	$>5\times10^{6}$/ $>5\times10^{6}$

Structural detail no. 721:

Table 7.31 shows the fatigue life prediction made for detail no. 721 (chapter 6.1.2) for normal in-service conditions (without the 2G deceleration) in the current geometry of exhaust system B and in the selected modifications made to exhaust system B (chapter 8.1.2). The fatigue life of this detail was predicted according to the FAT class chosen (Table 6.17), the first principal nodal stress values obtained (Table 7.14) and the material constants, C, calculated. The values presented in table 7.31 correspond to the fatigue life of the upper and lower ends, respectively, of each of the right side doubler plates.

Table 7.31: Fatigue life prediction of detail no. 721 for a FAT class of 50 - upper and lower ends of the right side doubler plates – normal in-service conditions - exhaust system B (C = 1.10x10^{11}, T=365 ºC / C = 9.73x10^{10}, T=395 ºC)

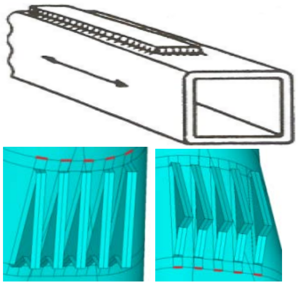	Material type				
	AISI 316L austenitic stainless steel				
	1st doubler plate (cycles)	2nd doubler plate (cycles)	3rd doubler plate (cycles)	4th doubler plate (cycles)	5th doubler plate (cycles)
Current geometry	$>5\times10^{6}$/ $>5\times10^{6}$	$>5\times10^{6}$/ $>5\times10^{6}$	$>5\times10^{6}$/ 153000	3.35×10^{6}/ 4070	$>5\times10^{6}$/ 618000
Thickness change of the intermediate section of the exhaust system pipe from 4 mm to 12 mm	$>5\times10^{6}$/ 4.43×10^{6}	$>5\times10^{6}$/ 3.60×10^{6}	$>5\times10^{6}$/ $>5\times10^{6}$	$>5\times10^{6}$/ 1.52×10^{6}	$>5\times10^{6}$/ 1.52×10^{6}
Thickness change of all the exhaust system plates to 4 mm	$>5\times10^{6}$/ $>5\times10^{6}$	$>5\times10^{6}$/ 498000	$>5\times10^{6}$/ 3.60×10^{6}	$>5\times10^{6}$/ 261000	$>5\times10^{6}$/ $>5\times10^{6}$
Thickness change of all the exhaust system plates to 12 mm	$>5\times10^{6}$/ 4.43×10^{6}	$>5\times10^{6}$/ 3.60×10^{6}	$>5\times10^{6}$/ $>5\times10^{6}$	$>5\times10^{6}$/ 1.52×10^{6}	$>5\times10^{6}$/ 1.52×10^{6}

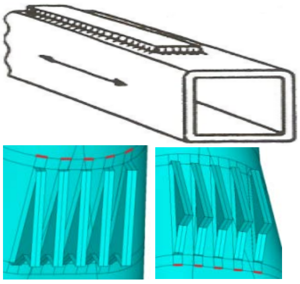	Material type				
	445M2 ferritic stainless steel				
	1st doubler plate (cycles)	2nd doubler plate (cycles)	3rd doubler plate (cycles)	4th doubler plate (cycles)	5th doubler plate (cycles)
Current geometry	2.79 $\times10^{6}$/ $>5\times10^{6}$	$>5\times10^{6}$/ 19100	$>5\times10^{6}$/ 450000	$>5\times10^{6}$/ 12900	$>5\times10^{6}$/ 2.08 $\times10^{6}$
Thickness change of the intermediate section of the exhaust system pipe from 4 mm to 12 mm	$>5\times10^{6}$/ $>5\times10^{6}$	$>5\times10^{6}$/ $>5\times10^{6}$	$>5\times10^{6}$/ $>5\times10^{6}$	$>5\times10^{6}$/ 2.08 $\times10^{6}$	$>5\times10^{6}$/ $>5\times10^{6}$
Thickness change of all the exhaust system plates to 4 mm	$>5\times10^{6}$/ $>5\times10^{6}$	$>5\times10^{6}$/ 1.52 $\times10^{6}$	$>5\times10^{6}$/ $>5\times10^{6}$	$>5\times10^{6}$/ 778000	$>5\times10^{6}$/ $>5\times10^{6}$
Thickness change of all the exhaust system plates to 12 mm	$>5\times10^{6}$/ $>5\times10^{6}$	$>5\times10^{6}$/ $>5\times10^{6}$	$>5\times10^{6}$/ $>5\times10^{6}$	$>5\times10^{6}$/ 4.43 $\times10^{6}$	$>5\times10^{6}$/ 4.43 $\times10^{6}$

Table 7.32 shows the fatigue life prediction made for detail no. 721 (chapter 6.1.2) for normal in-service conditions (without the 2G deceleration) in the current geometry of exhaust system B and in the selected modifications made to exhaust system B (chapter 8.1.2). The fatigue life of this detail was predicted according to the FAT class chosen (Table 6.17), the first principal nodal stress values obtained (Table 7.15) and the material constants, C, calculated. The values presented in table 7.32 correspond to the fatigue life of the upper and lower ends, respectively, of each of the left side doubler plates.

Table 7.32: Fatigue life prediction of detail no. 721 for a FAT class of 50 - upper and lower ends of the left side doubler plates – normal in-service conditions - exhaust system B (C = 1.10x10^{11}, T=365 ºC / C = 9.73x10^{10}, T=395 ºC)

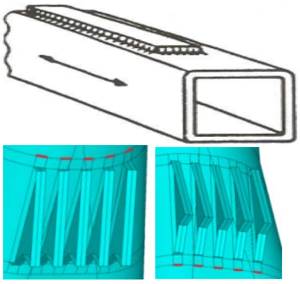	Material type				
	AISI 316L austenitic stainless steel				
	1st doubler plate (cycles)	2nd doubler plate (cycles)	3rd doubler plate (cycles)	4th doubler plate (cycles)	5th doubler plate (cycles)
Current geometry	$>5\times10^{6}$/ $>5\times10^{6}$	$>5\times10^{6}$/ $>5\times10^{6}$	$>5\times10^{6}$/ 999000	$>5\times10^{6}$/ $>5\times10^{6}$	4.06 $\times10^{6}$/ $>5\times10^{6}$
Thickness change of the intermediate section of the exhaust system pipe from 4 mm to 12 mm	$>5\times10^{6}$/ $>5\times10^{6}$	$>5\times10^{6}$/ $>5\times10^{6}$	$>5\times10^{6}$/ $>5\times10^{6}$	$>5\times10^{6}$/ $>5\times10^{6}$	$>5\times10^{6}$/ $>5\times10^{6}$
Thickness change of all the exhaust system plates to 4 mm	$>5\times10^{6}$/ $>5\times10^{6}$	$>5\times10^{6}$/ $>5\times10^{6}$	$>5\times10^{6}$/ 2.47 $\times10^{6}$	$>5\times10^{6}$/ $>5\times10^{6}$	$>5\times10^{6}$/ $>5\times10^{6}$
Thickness change of all the exhaust system plates to 12 mm	$>5\times10^{6}$/ $>5\times10^{6}$	$>5\times10^{6}$/ $>5\times10^{6}$	$>5\times10^{6}$/ $>5\times10^{6}$	$>5\times10^{6}$/ $>5\times10^{6}$	$>5\times10^{6}$/ $>5\times10^{6}$

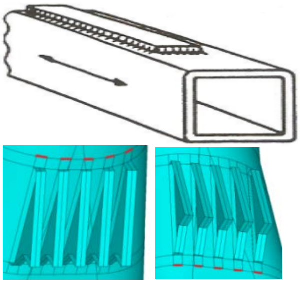	Material type				
	445M2 ferritic stainless steel				
	1st doubler plate (cycles)	**2nd doubler plate (cycles)**	**3rd doubler plate (cycles)**	**4th doubler plate (cycles)**	**5th doubler plate (cycles)**
Current geometry	$>5\times10^6$/ $>5\times10^6$	$>5\times10^6$/ $>5\times10^6$	$>5\times10^6$/ 2.08×10^6	$>5\times10^6$/ $>5\times10^6$	$>5\times10^6$/ $>5\times10^6$
Thickness change of the intermediate section of the exhaust system pipe from 4 mm to 12 mm	$>5\times10^6$/ $>5\times10^6$	$>5\times10^6$/ $>5\times10^6$	$>5\times10^6$/ $>5\times10^6$	$>5\times10^6$/ $>5\times10^6$	$>5\times10^6$/ $>5\times10^6$
Thickness change of all the exhaust system plates to 4 mm	$>5\times10^6$/ $>5\times10^6$	$>5\times10^6$/ $>5\times10^6$	$>5\times10^6$/ 3.60×10^6	$>5\times10^6$/ $>5\times10^6$	$>5\times10^6$/ $>5\times10^6$
Thickness change of all the exhaust system plates to 12 mm	$>5\times10^6$/ $>5\times10^6$	$>5\times10^6$/ $>5\times10^6$	$>5\times10^6$/ $>5\times10^6$	$>5\times10^6$/ $>5\times10^6$	$>5\times10^6$/ $>5\times10^6$

7.3 Fatigue life prediction assuming the existence of initial cracks:

The fatigue life assessment of the exhaust systems assuming the presence of initial cracks was carried out on the sections of the exhaust systems of naval gas turbines where fatigue cracking has been noticed or is more prone to exist. Using equations 6.7 and 6.8 and the first principal nodal stress values presented in section 7.2, the fatigue lives were calculated. It should be noted that the stresses used in equation 6.8 (which were then used in equation 6.7) were obtained by multiplying the first principal nodal stress values obtained in chapters 7.2 by 2 (stress ratio, R=-1).

7.3.1 Fatigue life prediction assuming the existence of initial cracks on exhaust system A:

Table 7.33 shows the fatigue life prediction for the sections of exhaust system A where fatigue crack has been noticed, considering the existence of a crack with an initial depth of 0.3 mm. These fatigue life results were obtained for normal in-service condition (without the 2G deceleration) in the current geometry of exhaust system A and in some redesigned geometries made to exhaust system A (chapter 8.1.1). The values presented in table 7.33 were obtained using the first principal nodal stress values obtained in table 7.1 and correspond to the number of cycles needed for the crack to reach a depth equal to 75% of the thickness of the sections assessed.

One should note that, for fatigue life prediction assuming the existence of initial cracks, it was considered that all the assessed sections have a plate's thickness of 4 mm, except for the exhaust system modification where the plates' thicknesses where changed to 12 mm.

The acronym NP in table 7.33 means that no crack propagation occurred, since the stress intensity range factors actuating at the crack tip were lower than 6 $MPa.\sqrt{m}$ (ΔK_{th} factor at 350 ºC) and EPFM means that the fatigue life should be predicted according to elastic plastic fracture mechanics.

Table 7.33: Fatigue life prediction of exhaust system A assuming the existence of initial cracks with a depth of 0.3 mm – normal in-service condition (without 2G deceleration)

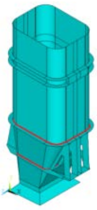	**Material type**			
	AISI 316L austenitic stainless steel		**445M2 ferritic stainless steel**	
	Intermediate supporting ring (cycles)	**Lower supporting ring (cycles)**	**Intermediate supporting ring (cycles)**	**Lower supporting ring (cycles)**
Current geometry	EPFM	14	EPFM	436
Thickness change of the intermediate section of the exhaust system pipe from 4 mm to 12 mm	12	356	332	NP
Thickness change of the vertical reinforcement ribs to 4 mm	EPFM	175	10	NP
Thickness change of all the exhaust system plates to 4 mm	9	207	17	NP
Thickness change of all the exhaust system plates to 12 mm	15	157	233	500
Removal of the inner vertical reinforcement ribs	EPFM	257	EPFM	NP

7.3.2 Fatigue life prediction assuming the existence of initial cracks on exhaust system B:

Table 7.34 shows the fatigue life prediction for the sections of exhaust system B where fatigue crack is more likely to occur, considering the existence of a crack with an initial depth of 0.3 mm. These fatigue life results were obtained for normal in-service condition (without the 2G deceleration) in the current geometry of exhaust system A and in some redesigned geometries made to exhaust system A (chapter 8.1.2). The values presented in table 7.34 were obtained using the first principal nodal stress values obtained in table 7.8 and correspond to the number of cycles needed for the crack to reach a depth equal to 75% of the thickness of the sections assessed.

One should note that, for fatigue life prediction assuming the existence of initial cracks, it was considered that all the assessed sections have a plate’s thickness of 12 mm (doubler plates thickness), with exception for the exhaust system modification where all the plates’ thicknesses where changed to 4 mm.

The acronym NP in table 7.34 means that no crack propagation occurred, since the stress intensity range factors actuating at the crack tip were lower than 6 $MPa.\sqrt{m}$ (ΔK_{th} factor at 350 ºC) and EPFM means that the fatigue life should be predicted according to elastic plastic fracture mechanics.

Table 7.34: Fatigue life prediction of exhaust system B assuming the existence of initial cracks with a depth of 0.3 mm – normal in-service conditions (without 2G deceleration)

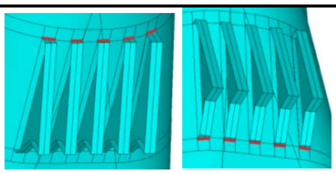	**Material type**			
	AISI 316L austenitic stainless steel		**445M2 ferritic stainless steel**	
	Upper flanges (cycles)	**Lower flanges (cycles)**	**Upper flanges (cycles)**	**Lower flanges (cycles)**
Current geometry	NP	EPFM	NP	11
Thickness change of the intermediate section of the exhaust system pipe from 4 mm to 12 mm	NP	9	NP	17
Thickness change of all the exhaust system plates to 4 mm	NP	9	NP	164
Thickness change of all the exhaust system plates to 12 mm	NP	12	NP	179

8. Discussion of results

8.1 Discussion of the first principal nodal stress results:

In this chapter, a discussion will be made about the first principal nodal stress results obtained for all the structural details chosen to be assessed in each modification made to the exhaust systems under study (chapter 7.1).

8.1.1 Discussion of the first principal nodal stress results obtained for exhaust system A:

Structural detail no. 424:

The following discussion is related with the maximum first principal stress results obtained in the assessment made of the in-service fatigue life of structural detail no. 424 (Table 7.1 – without the 2G deceleration). The first principal stresses obtained in the redesigned structures were compared with the results obtained for the current geometry of exhaust system A for this same structural detail:

- The addition of vertical reinforcement ribs in the current geometry of exhaust system A led to an increase of the first principal stresses in both lower and intermediate supporting rings. It was also noticed that the addition of more vertical ribs led to an extra-increase of the first principal stresses. As a result, the addition of vertical reinforcement ribs was not considered a good solution to solve the high stress problems.

- Adding an horizontal reinforcement ring in the critical region of exhaust A resulted in the reduction of the first principal stresses values applied on the intermediate supporting ring by 48%; however, this modification resulted in the increase of the first principal stresses values applied on the lower supporting ring by 19%. Despite having been obtained a considerable reduction of the first principal stresses applied in the lower supporting ring, this was not considered a good solution to be implemented due to the increase of the first principal stresses in the intermediate supporting ring.

- Changing the thickness of the intermediate section of the exhaust system's pipe from 4 mm to 12 mm led to a reduction of 61% (from 339 MPa to 133 MPa) of the first principal stresses applied in the intermediate supporting ring and a reduction of 27% (from 125 MPa to 91 MPa) in the lower supporting ring. These results show that a uniformization of the plates thicknesses reduce the thermal expansion problems that occur in the current geometry of exhaust system A. Due to the results obtained, this redesigned structure was considered a good solution to be implemented in order to reduce the stresses that occur in the intermediate section (critical section).

- Reducing the thickness of the intermediate supporting ring form 30 mm to 12 mm led to a small decrease of the first principal stresses induced in the intermediate supporting ring. The first principal stresses induced in the lower supporting ring remained the same as the ones obtained in the current geometry of exhaust system A. This modification was not deemed a good solution to be implemented as it only contributed to a small reduction of the first principal stresses in the intermediate ring.

- Changing the plate's thickness of the intermediate and lower supporting rings from 30 mm and 15 mm, respectively, to 4 mm was tested in order to reduce the thermal expansion problems. This modification led to a reduction of 26% in the first principal stresses induced in the intermediate supporting ring. However the first principal stresses in the lower supporting ring increased 5%. In consequence, it was not considered a good solution to be implemented.

- Changing the plate's thickness of the vertical supporting ribs from 11 and 13mm to 4 mm resulted in a decrease of the first principal stresses induced in the intermediate and lower supporting rings of 38% and 15% (from 339 MPa to 209 MPa and from 125 MPa to 106 MPa), respectively. These results show, once again, that a uniformization of the plates thicknesses reduce the thermal expansion problems that occur in the current geometry of exhaust system A. Due to the results obtained, this solution could be considered to be implemented in order to reduce the stresses that occur in the intermediate section (critical section). However a buckling analysis of these plates should be done when the exhaust system is submitted to high acceleration/deceleration in order to avoid that mode of failure.

- When the thicknesses of all the exhaust system’s plates were changed, led to good results since less thermal expansion problems occurred. Changing all the plates’ thicknesses to 4 mm, led to a reduction of 54% and 17% (from 339 MPa to 156 MPa and from 125 MPa to 104 MPa) of the first principal stresses induced in the intermediate and lower supporting ring, respectively. In the modification where the thickness of all the exhaust system’s plates was changed to 12 mm, it was noticed a reduction of 61% and 17% (from 339 MPa to 134 MPa and from 125 MPa to 104 MPa) of the first principal stresses induced in the intermediate and lower supporting ring, respectively. The difference between the first principal stresses obtained for each modification in the intermediate supporting ring, indicates that a better mechanical behaviour is achieved when using plates with thickness of 12 mm,although the mass of the structure would be much higher. Due to the obtained results, these modifications can be considered alternative solutions to be implemented in order to reduce the stresses that occur in the intermediate section (critical section) and in the rest of the exhaust system.

- The removal of the outer vertical supporting ribs led to a reduction of 33% in the first principal stresses in the intermediate supporting ring but the first principal stresses in the lower supporting ring increased 17%. Although this modification solves some vertical thermal expansion problems, caused by vertical expansion restrictions, the removal of the outer vertical supporting ribs leads to higher structural problems in the lower supporting ring. Thus, the above mentioned was not considered a good solution to be implemented.

- The removal of the inner vertical supporting ribs, led to a reduction of 7% and 20% (from 339 MPa to 314 MPa and from 125 MPa to 100 MPa) of the first principal stresses induced in the intermediate and lower supporting rings, respectively. Although the results obtained are not as impressive as the ones in other modifications, it can be considered an alternative solution that can easily be implemented in the current geometry of exhaust system A. However a buckling analysis of these plates should be done when the exhaust system is submitted to high acceleration/deceleration in order to avoid that mode of failure.

- The partial removal of the lower supporting ring led to an increase of the first principal stresses induced in the intermediate and lower supporting ring. Since this modification weakens the structural support of the exhaust system, it was not considered a good solution.

- The partial removal of the intermediate supporting ring led to lower the first principal stresses induced in the intermediate and lower supporting ring. This modification was not considered a very effective solution to be implemented, once the percentage of decrease of the first principal stresses was not significant.

- Like the previous modification, the complete removal of the intermediate supporting ring does not greatly improve the first principal stresses that occur in the lower supporting ring. So, it was not considered a good solution to be implemented.

- Changing the material in the intermediate section to a 445M2 ferritic stainless steel, led to a great increase on the stresses induced in the intermediate and lower supporting rings. Even when the intermediate section was changed to a 445M2ferritic stainless steel with a wall thickness of 12 mm, the first principal stresses remained higher than the ones obtained in the thickness change of the intermediate section to 12 mm of exhaust system A made entirely of the austenitic AISI 316L stainless steel. These modifications were only made in order to prove that these two types of materials should not be welded together due to their different thermal expansion/conductivity properties, which will cause greater local thermal expansion problems on exhaust system A.

Structural details no. 234 and no. 223:

- The same conclusions, as the ones stated for the first principal stress results obtained for the structural detail no. 424, can be applied to details no. 234 and no. 223 (Tables 7.3 and 7.4 – without the 2G deceleration), once the first principal stress results obtained are the same.

Structural detail no. 323:

The following discussion is related with the maximum first principal stress results obtained in the assessment made of the in-service fatigue life of structural detail no. 323 (Tables 7.5 and 7.6 – without the 2G deceleration) and is based on the comparison with the results obtained for the current geometry of exhaust system A for this same structural detail:

- The maximum first principal nodal stress results obtained, revealed that the outer vertical supporting ribs (first and fourth vertical supporting ribs) have higher first principal stress values applied on, which indicates that they are more requested in terms of mechanical and thermal forces.
- The first principal stress values registered in these welded joints are significant which indicates that these are also critical sections where fatigue cracking might occur.

Structural detail no. 822:

The following discussion is related with the maximum first principal stress results obtained in the assessment made of the in-service fatigue life of structural detail no. 822 (Table 7.7 – without the 2G deceleration) and is based on the comparison with the results obtained for the current geometry of exhaust system A for this same structural detail:

- Changing the thickness of the intermediate section of the exhaust system pipe from 4 mm to 12 mm, led to a 61% reduction (from 339 MPa to 133 MPa) of the first principal stresses in the intermediate supporting ring.
- Changing the thickness of the vertical supporting ribs to 4 mm results in a decrease of 38% (from 339 MPa to 209 MPa) of the first principal stresses in the intermediate supporting ring.
- Changing all the plates' thicknesses to 4 mm led to a 54% reduction (from 339 MPa to 156 MPa) of the first principal stresses that occurred in the intermediate supporting ring.
- In the modification where the thickness of all the exhaust system plates was changed to 12 mm, a reduction of 61% (from 339 MPa to 134 MPa) of the first principal stresses in the intermediate was achieved. The difference between the first principal stresses obtained for each modification in the intermediate supporting ring, indicates that a better mechanical behaviour is achieved by using 12 mm thickness plates.
- The removal of the inner vertical supporting ribs led to a reduction of 7% (from 339 MPa to 314 MPa) of the first principal stresses in the intermediate supporting ring.

Changing the material which exhaust system A is made of:

- The change of the type of material in which exhaust system A is made of proved to be a good solution to be implemented in order to reduce the stresses that occur in the exhaust system. For example, the change from the AISI 316L austenitic stainless steel to the 445M2 ferritic stainless steel led to a decrease in the first principal stresses of around 30% in the intermediate supporting ring and around 34% in the lower supporting ring (critical sections) in the current geometry of exhaust system A and in all the modifications made. These results are due to the lower thermal expansion coefficients of the 445M2 ferritic stainless steel which improves the exhaust system thermal behaviour.

Overload condition:

- The comparison between the results obtained for normal in-service conditions (without the 2G deceleration) and the results obtained for the overload condition (with the 2G deceleration) revealed that exhaust system A was designed to withstand great structural impacts, since the application of the 2G deceleration (crashstop manoeuvre) did not produce any considerable increase in the stresses that occur in the exhaust system.

8.1.2 Discussion of the first principal nodal stress results obtained for exhaust system B:

Structural detail no. 511:

The following discussion is related with the maximum first principal stress results obtained in the assessment made of the in-service fatigue life of structural detail no. 511 (Table 7.8 – without the 2G deceleration) and is based on the comparation with the results obtained for the current geometry of exhaust system B for this same structural detail:

- Changing the thickness of the intermediate section of the exhaust system pipe from 4 mm to 12 mm, led to a slight increase of the first principal stresses in the upper flanges (from 14 MPa to 17 MPa) but decreased the first principal stresses by 22% (from 239 MPa to 186 MPa) in the lower flanges.These results show that a uniformization of the plates' thicknesses reduces the thermal expansion problems that occur in the current geometry of exhaust system B. Due to the obtained results, this can be considered a good solution to be implemented in order to reduce the stresses that occur in the intermediate section (critical section).
- When the thicknesses of all the exhaust system's plates were changed, led to similar results as the ones obtained in the previous modification. Changing all the plates' thicknesses to 4 mm, led to an insignificant increase of the first principal stresses induced in the upper flanges but decreased the first principal stresses induced in the lower flanges by 35% (from 239 MPa to 156 MPa). In the modification where the thickness of all the exhaust system's plates was changed to 12 mm, it was noticed a slight increase of the first principal stresses induced in the upper flanges (from 14 MPa to 21 MPa) and a decrease of the first principal stresses induced in the lower flanges by 36% (from 239 MPa to 152 MPa). Due to the obtained results, these modifications can be considered alternative solutions to be implemented in order to reduce the stresses that occur in the intermediate section (critical section) and in the rest of the exhaust system.
- Changing the material of the intermediate section to a 445M2 ferritic stainless steel, led to a great increase on the stresses that occur in the upper and lower flanges. Even when the intermediate section was changed to the 445M2 ferritic stainless steel with a wall thickness of 12 mm, the first principal stresses remained higher than the ones obtained in the thickness change of the intermediate section to 12 mm of exhaust system B made entirely of the austenitic AISI 316L stainless steel. These modifications were only made in order to prove that these two types of materials should not be welded together due to their different thermal expansion properties, which cause greater thermal expansion problems on exhaust system B.

Structural details no. 232 and no. 223:

The following discussion is related with the maximum first principal stress results obtained in the assessment made of the in-service fatigue life of structural details no. 232 and no. 223 (Tables 7.10 and 7.11 – without the 2G deceleration) and is based on the comparison with the results obtained for the current geometry of exhaust system B for this same structural detail:

- The first principal stresses calculated in the lower end of the section of the exhaust system pipe that is welded to the reinforcement plates are significantly higher than the ones registered in the upper end.
- Changing all the plates' thicknesses to 4 mm, led to a 80% and 75% reduction (from 30 MPa to 6 MPa and from 144 MPa to 36 MPa) of the first principal stresses that occurred in the upper and lower ends, respectively, of the section of the exhaust system pipe that is welded to the reinforcement plates.
- In the modification where the thickness of all the exhaust system plates was changed to 12 mm, it was noticed a reduction of 77% and 86% (from 30 MPa to 7 MPa and from 144 MPa to 20 MPa) of the first principal stresses in the upper and lower ends, respectively, of the section of the exhaust system pipe that is welded to the reinforcement plates.
- The difference between the first principal stresses obtained for the two modifications stated above indicates that a better mechanical behaviour is achieved by using 12 mm thickness plates.

- Changing the thickness of the intermediate section of the exhaust system pipe from 4 mm to 12 mm, led to the same results as those obtained for the thickness change of all the exhaust system plates to 12 mm.

Structural detail no. 323:

- The following discussion is related with the maximum first principal stress results obtained in the assessment made of the in-service fatigue life of structural detail no. 323 (Tables 7.12 and 7.13 – without the 2G deceleration) and is based on the comparison with the results obtained for the current geometry of exhaust system B for this same structural detail:

- The maximum first principal nodal stress results obtained, revealed that the first and second right side vertical reinforcement ribs have the highest first principal stress values, which indicates that they are more requested in terms of mechanical forces.

- The left side vertical reinforcement ribs registered very low first principal stress values when compared to the ones in the right side vertical reinforcement ribs. This difference is related with the boundary conditions applied (chapter 4.7.1.2).

- The first principal stress values registered in these welded joints are not as significant as the ones registered in the welded joints between the reinforcement plates and the upper and lower flanges of the supporting ribs. But since all these welded joints are near to each other and welded to the reinforcement plates, fatigue crack propagation might occur.

Structural details no. 712 and no. 721:

- The following discussion is related with the maximum first principal stress results obtained inr the assessment of the in-service fatigue life of structural details no. 712 and no. 721 (Tables 7.14 and 7.15 – without the 2G deceleration) and is based on the comparison with the results obtained for the current geometry of exhaust system B for this same structural detail:

- The maximum first principal nodal stress results obtained, revealed that the third and fourth right side reinforcement plate ends have the highest first principal stress values, which indicates that they are more requested in terms of mechanical forces.

- The left side reinforcement plate ends registered lower first principal stress values when compared to the ones in the right side reinforcement plate ends. This difference is related with the boundary conditions applied (chapter 4.7.1.2).

- The first principal stress values registered in these welded joints are significant and since they are also near the other assessed welded joints, fatigue crack propagation might occur.

Changing the material which exhaust system B is made of:

- The change of the type of material from which exhaust system B is made of, proved to be a very good solution to be implemented in order to reduce the stresses that occur in the exhaust system. For example, the change from the AISI 316L austenitic stainless steel to the 445M2 ferritic stainless steel led to a decrease in the first principal stresses of around 40% in the upper flanges and around 28% in the lower flanges (critical sections) in the current geometry of exhaust system A and in all the modifications made. These results are due to the lower thermal expansion coefficients of the ferritic 445M2 stainless steel which improves the exhaust system thermal behaviour.

Overload condition:

- The comparison between the results obtained for normal in-service conditions (without the 2G deceleration) and the results obtained for the overload condition (with the 2G deceleration) revealed that exhaust system B was not designed to withstand great structural impacts, since the application of the 2G deceleration (crashstop manoeuvre) increased the stresses that occur in the exhaust system. It was also noticed that, even when the exhaust system material was changed to the 445M2 ferritic stainless steel, the first principal stresses remained high, which indicates that this exhaust system was designed to withstand thermal shocks rather than structural impacts.

8.2 Discussion on the fatigue life assessment results:

In this chapter, a discussion will be made about the fatigue life results obtained for all the structural details chosen to be assessed in each modification made to the exhaust systems. These fatigue life results were obtained by using S-N Curves of classified structural details categories (chapter 7.2) and admiting fatigue crack propagation of an initial crack present at some structural details (chapter 7.3).

8.2.1 Discussion of the fatigue life predictions of exhaust system A:

Structural detail no. 424:

The following discussions are related to the in-service fatigue life results obtained for structural detail no. 424 (Table 7.16 – without the 2G deceleration) and are based on the comparison with the results obtained for the current geometry of exhaust system A for this same structural detail:

- Changing the thickness of the intermediate section of the exhaust system pipe from 4 mm to 12 mm, led to an increase of the fatigue life in the intermediate supporting ring and a increase of 159% (from 8220 cycles to 21300 cycles) in the lower supporting ring.
- Changing the thickness of the vertical reinforcement ribs to 4 mm, results in a increase of the fatigue life in the lower supporting ring of 64% (from 8220 cycles to 13500 cycles).
- Changing all the plates thicknesses to 4 mm, led to a 74% increase (from 8220 cycles to 14300 cycles), of the fatigue life predicted for the lower supporting ring.
- In the modification where the thickness of all the exhaust system plates was changed to 12 mm, it was noticed an increase of the fatigue life predicted for the intermediate supporting ring and an increase of 138% of the fatigue life predicted for the lower supporting ring (from 8220 cycles to 19600 cycles).
- The removal of the inner vertical reinforcement ribs, led to a 96% increase (from 8220 cycles to 16100 cycles) of the fatigue life predicted for the lower supporting ring.

Structural details no. 234 and no. 223:

The following discussions are related to the in-service fatigue life results obtained for structural details no. 234 and no. 223 (Tables 7.17, 7.18 and 7.19 – without the 2G deceleration) and are based on the comparison with the results obtained for the current geometry of exhaust system A for this same structural detail:

- The fatigue life predicted for the intermediate section of the exhaust pipe, near the intermediate supporting ring, is significantly lower than the fatigue life predicted for the same intermediate section of the exhaust pipe, near the lower supporting ring.
- Changing the thickness of the vertical reinforcement ribs to 4 mm, led to a 64% increase (from 8220 cycles to 13500 cycles) of the fatigue life in the lower ends of the section of the exhaust system pipe that is welded to the supporting rings.
- In the modifications where the thickness of all the exhaust system plates was changed, an increase of the fatigue life, of the intermediate section of the exhaust pipe, near the lower supporting ring, was noticed. This increase was of 74% for both the modifications where the thickness of all the exhaust system plates was changed to 4 mm and 12 mm.
- The removal of the inner vertical reinforcement ribs led to an increase of 96% (from 8220 cycles to 16100 cycles) in the fatigue life of the intermediate section of the exhaust pipe, near the lower supporting ring. For this same modification, the fatigue life predicted for the intermediate section of the exhaust pipe, near the lower supporting ring is higher than the fatigue life predicted in the other modifications.
- The fatigue life of detail no. 234 also depended on the type of root inspection used. Root inspecting with the use of non destructive tests (NDT) led to an increase of 93% on the fatigue life in comparison to the fatigue life obtained for a root inspection without the use of NDT(Tables 7.18 and 7.17, respectively).

- The first principal stress results obtained for the modification, where the intermediate section of exhaust system A was changed to 12 mm, are lower than those obtained for the other above stated modifications. However, due to the existent misalignment between the plates, a stress magnification factor had to be accounted, reducing this way the fatigue class of detail no. 223. As such, considering this modification, the fatigue life of detail no. 223 is lower in the intermediate section of the exhaust pipe, near the lower supporting ring.

Structural detail no. 323:

The following discussion is related to the in-service fatigue life results obtained for structural detail no. 323 (Tables 7.20 and 7.21 – without the 2G deceleration) and are based on the comparison with the results obtained for the current geometry of exhaust system A for this same structural detail:

- The welded joints between the exhaust system pipe and the right and left side reinforcement ribs (Tables 7.20 and 7.21) presented a long fatigue life. Once again, all the modifications made increased the fatigue life of these sections.

Structural detail no. 822:

The following discussions are related to the in-service fatigue life results obtained for structural detail no. 822 (Table 7.22 – without the 2G deceleration) and are based on the comparison with the results obtained for the current geometry of exhaust system A for this same structural detail:

- By considering that the intermediate supporting ring is composed by two 15 mm thick flanges bolted together, as it is actually, instead of the 30 mm thickness supporting ring, a better fatigue life was obtained.
- In the other suggested modifications, a substantial increase in the fatigue life of the exhaust system was noticed.

Changing the material which exhaust system A is made of:

- The change of the type of material which exhaust system A is made of, proved to be a great solution to be implemented in order to increase the fatigue life of the exhaust system. For example, the change from the AISI 316L austenitic stainless steel to the 445M2 ferritic stainless steel led to an increase of the fatigue life of around 240% in the lower supporting ring (critical section) in the current geometry of exhaust system A and in all the modifications made.

Surface with initial cracks:

The following discussions are related to the normal in-service fatigue life results obtained for a surface with an initial crack depth of 0.3 mm (Table 7.33 – without the 2G deceleration) and are based on the comparison with the results obtained for the current geometry of exhaust system A for this same structural detail:

- The modification of the thickness of the intermediate section of the exhaust system pipe from 4 mm to 12 mm, led to a 2543% increase of the fatigue life of the plates near the lower supporting ring (from just 14 cycles to 356 cycles).
- Changing the thickness of the vertical reinforcement ribs to 4 mm, increases the fatigue life in the plates near the lower supporting ring. However, in the intermediate supporting ring, it still occurs plastification of the material at the crack tip.
- The modifications where the intermediate section of the exhaust system pipe has a wall thickness of 12 mm, led to a considerable increase of the fatigue life in the plates near the intermediate and lower supporting rings.
- The change of the type of material which exhaust system A is made, to the 445M2 ferritic stainless steel, led to an increase of the fatigue life of the plates near the lower supporting ring (from 14 cycles to 436 cycles).

- Changing the material, which the suggested redesign exhaust systems' are made of, to the 445M2 ferritic stainless steel leads to no crack propagation on the plates near the lower supporting ring.

- This kind of fatigue life prediction is more conservative, leading to a prediction of a very short fatigue life for these critical sections of exhaust system A.

- The overall results show that the size of the plastic region at the crack tip plays an importante role in the fatigue life.

8.2.2 Discussion of the fatigue life predictions of exhaust system B:

Structural detail no. 511:

The following discussions are related to the in-service fatigue life results obtained for structural detail no. 511 (Table 7.23 – without the 2G deceleration) and are based on the comparison with the results obtained for the current geometry of exhaust system B for this same structural detail:

- For this detail, the upper flanges revealed an infinite fatigue life in the current geometry and in the modifications made to exhaust system B.

- Changing the thickness of the intermediate section of the exhaust system pipe from 4 mm to 12 mm, led to a 262% increase (from 3800 cycles to 8060 cycles) of the fatigue life in the lower flanges.

- Changing all the plates thicknesses to 4 mm, led to a 260% increase (from 3800 cycles to 13700 cycles) of the fatigue life in the lower flanges.

- In the modification where the thickness of all the exhaust system plates was changed to 12 mm, the results were the same as those obtained for the thickness change of the intermediate section of the exhaust system pipe from 4 mm to 12 mm.

Structural details no. 232 and no. 223:

The following discussions are related to the in-service fatigue life results obtained for structural details no. 232 and no. 223 (Tables 7.24, 7.25 and 7.26 – without the 2G deceleration) and are based on the comparison with the results obtained for the current geometry of exhaust system B for this same structural detail:

- Overall, the fatigue life results obtained for detail no. 232 are very high in the upper end of the intermediate section of the exhaust system pipe.

- The fatigue life results of the lower end of the intermediate section of the exhaust system pipe are lower than the ones in the upper end, which indicates that, if fatigue cracks should occur, they will start to propagate in the lower end of this section.

- The fatigue life of detail no. 232 also dependeds on the type of root inspection used. Root inspecting with the use of non destructive tests (NDT) led to an increase around 293% of the fatigue life in comparison to the fatigue life obtained for a root inspection without the use of NDT(Tables 7.25 and 7.24, respectively).

- The first principal stress results obtained for the modification, where the intermediate section of exhaust system B was changed from 4 mm to 12 mm, are as low as those obtained for the other above stated modifications. However, due to the existent misalignment between the plates, a stress magnification factor had to be accounted, reducing this way the fatigue class of detail no. 223. As such, considering this modification, the fatigue life of detail no. 223 is lower in the lower ends of the intermediate section of the exhaust system pipe.

Structural detail no. 323:

The following discussions are related to the in-service fatigue life results obtained for structural detail no. 323 (Tables 7.27 and 7.28 – without the 2G deceleration) and are based on the comparison with the results obtained for the current geometry of exhaust system B for this same structural detail:

- The right side reinforcement ribs (Table 7.27) denoted a long fatigue life.
- The left side reinforcement ribs (Table 7.28) revealed an infinite fatigue life, due to the low stresses registered in the welded joint of the left side reinforcement ribs with the doubler plates.
- No cracks should occur in these welded joints, due to the high fatigue life results obtained.

Structural details no. 712 and no. 721:

The following discussions are related to the in-service fatigue life results obtained for structural details no. 712 and no. 721 (Tables 7.29, 7.30, 7.31 and 7.32 – without the 2G deceleration) and are based on the comparison with the results obtained for the current geometry of exhaust system B for this same structural detail:

- The right side lower end of the fourth reinforcement plate revealed a lower fatigue life result than the ones obtained for the remaining lower ends of the doubler plates (Table 7.29). This low fatigue life result was increased in the modifications suggested.
- All the upper ends of the right side doubler plates revealed an infinite fatigue life.
- The left side upper and lower ends of the doubler plates (Table 7.30) revealed an infinite fatigue life, due to the low stresses registered in these welds.
- If fatigue cracking should occur, it will start and propagate near the fourth right side reinforcement plate (Tables 7.29 and 7.31).
- The fatigue life results obtained with the detail no. 721 are more conservative.

Changing the material which exhaust system B is made of:

- The change of the type of material which exhaust system B is made of, proved to be a great solution to be implemented in order to increase the fatigue life of the exhaust system. For example, the change from the AISI 316L austenitic stainless steel to the 445M2 ferritic stainless steel led to an increase of the fatigue life of around 430% in the upper flanges and around 220% in the lower flanges (critical sections) in the current geometry of exhaust system B and in all the modifications made.

Surface with initial cracks:

The following discussions are related to the normal in-service fatigue life results obtained for a surface with an initial crack depth of 0.3 mm (Table 7.34 – without the 2G deceleration) and are based on the comparison with the results obtained for the current geometry of exhaust system B for this same structural detail:

- With an initial crack depth of 0.3 mm on the plates near the upper flanges, no crack propagation should occur.
- A low fatigue life is expected for the plates near the lower flange
- The change of the type of material which the current geometry of exhaust system B is made, to the 445M2 ferritic stainless steel, increases the fatigue life of the plates near the lower flanges especially in the modifications where the thicknesses of all the exhaust system's plates were changed.
- This kind of fatigue life prediction is more conservative, leading to a prediction of a very short fatigue life for these critical sections of exhaust system B.
- The overall results show that the size of the plastic region at the crack tip plays an importante role in the fatigue life.

9. Final conclusions and future work proposals

The following overall conclusions result from the present study:

- The two exhaust systems in study have different mechanical and thermal behaviours.
- Exhaust system A was designed to withstand great structural impacts, therefore it revealed good mechanical behaviour when the crashstop manoeuvre was simulated (overload condition).
- This exhaust system's design led to a bad thermal behaviour, since thermal expansion on exhaust system A is very restricted. This restriction is due to all the reinforcement ribs and rings and due to the big difference between the plates' thicknesses of exhaust system A.
- To enhance the thermal behaviour of exhaust system A, some modifications were made towards the reduction of thermal expansion differences between the exhaust system plates.
- The modifications made, where an uniformization of the plate thicknesses was tried, led to good results, reducing the stresses that occur in the exhaust system and therefore increasing its fatigue life.
- No considerable stress variations occurred between the simulation of exhaust system A in normal in-service conditions (without 2G deceleration) and in overload condition (with 2G deceleration).
- Exhaust system B has better thermal behaviour than exhaust system A, once there is a smaller difference between the plates' thicknesses and thermal expansion is less restricted due to the simple supporting design of the exhaust system.
- For this exhaust system, some modifications were made in order to improve even more its thermal behaviour. These modifications consisted in the uniformization of the plates' thicknesses which led to a reduction of the stresses that occur in the exhaust system, therefore increasing its fatigue life.
- The application of the overload condition in exhaust system B increased the stresses that occur in the exhaust system, revealing that this exhaust system was designed towards a more effective thermal behaviour than a good mechanical behaviour.
- Thermal expansion is the main cause of high stress concentrations in the exhaust systems.
- Exhaust system B proved to have a better fatigue life than exhaust system A, since it was designed to have an effective thermal behaviour rather than good mechanical behaviour.
- The fatigue life assessment of structural details showed to be more optimist, once good welding and surface finish was considered.
- The fatigue life assessment, considering that an initial surface crack existed, led to more conservative results.
- Frequent inspections during service should be done to the welds of the exhaust systems, in order to prevent crack propagation from the weld toes, increasing this way the overall fatigue life of the exhaust systems. Also, high quality fabrication is required in order to avoid the presence of initial defects in the structure.
- The use of the austenitic Chromium-Manganese stainless steel can lead to a better fatigue life, once it has the same mechanical strength resistance at 500 ºC as the current material used in the exhaust systems has at room temperature. However its pitting corrosion resistance is lower than the corrosion resistance of the material used in the current design of the exhaust systems A and B.
- The use of the 445M2 ferritic marine type stainless steel resulted in better stress results which leads to an increase in the fatigue life of the exhaust systems. These results are due to the lower thermal expansion coefficients of the ferritic stainless steel in comparison to the austenitic stainless steels in study.
- Finally, some simulations were made in order to confirm that welding the ferritic stainless steel to the austenitic stainless steels should be avoided, once higher stress concentrations occur due to the big difference between the thermal expansion coefficients of the dissimilar materials joined.

Future work proposals:

- More modifications should be made to exhaust system B, in order to improve its mechanical behaviour in the overload condition while remaining its good thermal behaviour.
- Considerable design changes in the exhaust systems should be made, in order to obtain an exhaust system with the mechanical behavior of exhaust system A along with the good thermal behavior of exhaust system B.
- A use of a Duplex stainless steel should be studied, in order to assess the behavior of these types of materials in the design of exhaust systems.
- For the fatigue life predictions under 3500 cycles, material testing should be made in order to obtain specific material parameters and characteristics for low cycle fatigue calculations. Doing so, more accurate fatigue life predictions could be achieved.
- Axial tensile and fatigue tests should be made to ferritic 445M2 stainless steel specimens in order to obtain more accurate mechanical properties for different temperatures.
- An assessment of the costs related to the modifications proposed for the exhaust systems should be made.
- The weight of the proposed modified exhaust systems should be analysed in order to determine the viability of its construction in future vessels.
- Analyses should be made considering that the gas turbines can work at 110% of their capability (overload condition).

10. References

[1] R. F. Martins, C. M. Branco, A. M. Goncalves-Coelho, and E. C. Gomes, "A failure analysis of exhaust systems for naval gas turbines. Part I: Fatigue life assessment," *Engineering Failure Analysis,* vol. 16, pp. 1314-1323, 2009.

[2] R. F. Martins, C. M. Branco, A. M. Goncalves-Coelho, and E. C. Gomes, "A failure analysis of exhaust systems for naval gas turbines. Part II: Design changes," *Engineering Failure Analysis,* vol. 16, pp. 1324-1338, 2009.

[3] R. F. Martins, C. M. Branco, A. M. Goncalves-Coelho, and E. C. Gomes, "Failure Mechanisms on Exhaust Systems of Naval Gas Turbines," *Advanced Materials Forum Iv,* vol. 587-588, pp. 946-950, 2008.

[4] M. V. A. Nagesha, R. Kannan, K. Bhanu Sankara Rao, V. Bauer, H.J. Christ, Vakil Singh, "Thermomechanical fatigue evaluation and life prediction of 316L stainless steel," ed. International Journal of Fatigue 21, 2009.

[5] R. F. Martins, "Análise de Falha de Condutas de Evacuação de Gases de Turbinas a Gás utilizadas para Propulsão Naval," ed. IST/UNL, 2005.

[6] (18/01/2011). *http://www.matweb.com*.

[7] R. F. Martins, Viegas, J., Branco, C.M., "Relatório de Execução Material e de Execução Financeira Intercalar, referente ao ano de 2008, do Projecto de Investigação Científica e Desenvolvimento Tecnológico no âmbito do PIDDAC: "Projecto de desenvolvimento tecnológico de condutas de evacuação de gases de turbinas a gás"," ed: PTDC/EME/67071/2006, 2008.

[8] H. J. T. Cruz, R. F. Martins, J. C. G. Veigas, and J. L. G. Aveiro, "Redesign of Exhaust Systems for Naval Gas Turbines: Usage of a New Cr-Mn Austenitic Stainless Steel," *Advanced Materials Forum V, Pt 1 and 2,* vol. 636-637, pp. 497-503, 2010.

[9] (06/04/2011). *http://www.australwright.com.au*.

[10] (19/08/2011). *http://www.welding-technology-machines.info*.

[11] Y. Xiang-mi, J. Zhou-hua, and L. I. Hua-bing, "Ultra-Pure Ferritic Stainless Steels—Grade, Refining Operation, and Application," vol. - 14, pp. - 30, 2007.

[12] (15/04/2011). *http://www.micometals.co.nz*.

[13] (17/04/2011). *http://www.enidine.com*.

[14] (13/05/2011). *http://www.vibrostop.it*.

[15] J. L. G. Aveiro, "Estudo do escoamento dos produtos da combustão no interior de uma conduta de evacuação de turbinas a gás utilizadas para propulsão naval," ed. FCT/UNL, 2009.

[16] F. White, "Fluid Mechanics," ed. McGraw-Hill international editions – mechanical engineering series, 1986, pp. 689, 266, 321–22.

[17] (18/04/2011). *http://www.rolls-royce.com*.

[18] H. A., *Fatigue design of welded joints and components*: Abington publishing, 1996.

[19] N. E. Dowling, *Mechanical Behaviour of Materials*, Second Edition ed.

[20] G. Lloyd, *Rules for Classification and Construction, III Naval Ship Technology*: Germanischer Lloyd, 2004.

[21] J. William D. Calister, *Materials Science and Engineering: An Introduction*, Seventh Edition ed., 2006.

[22] *Guide on methods for assessing the acceptability of flaws in structures*, BS 7910: 1997 ed., 1997.

[23] L. V. d. Cunha, *Desenho Técnico*, 13ª Edição ed., 2003.

Annexes

Annex A – Technical drawings of the exhaust systems

A1: Technical drawing of exhaust system A (dimensions in meters)[1]

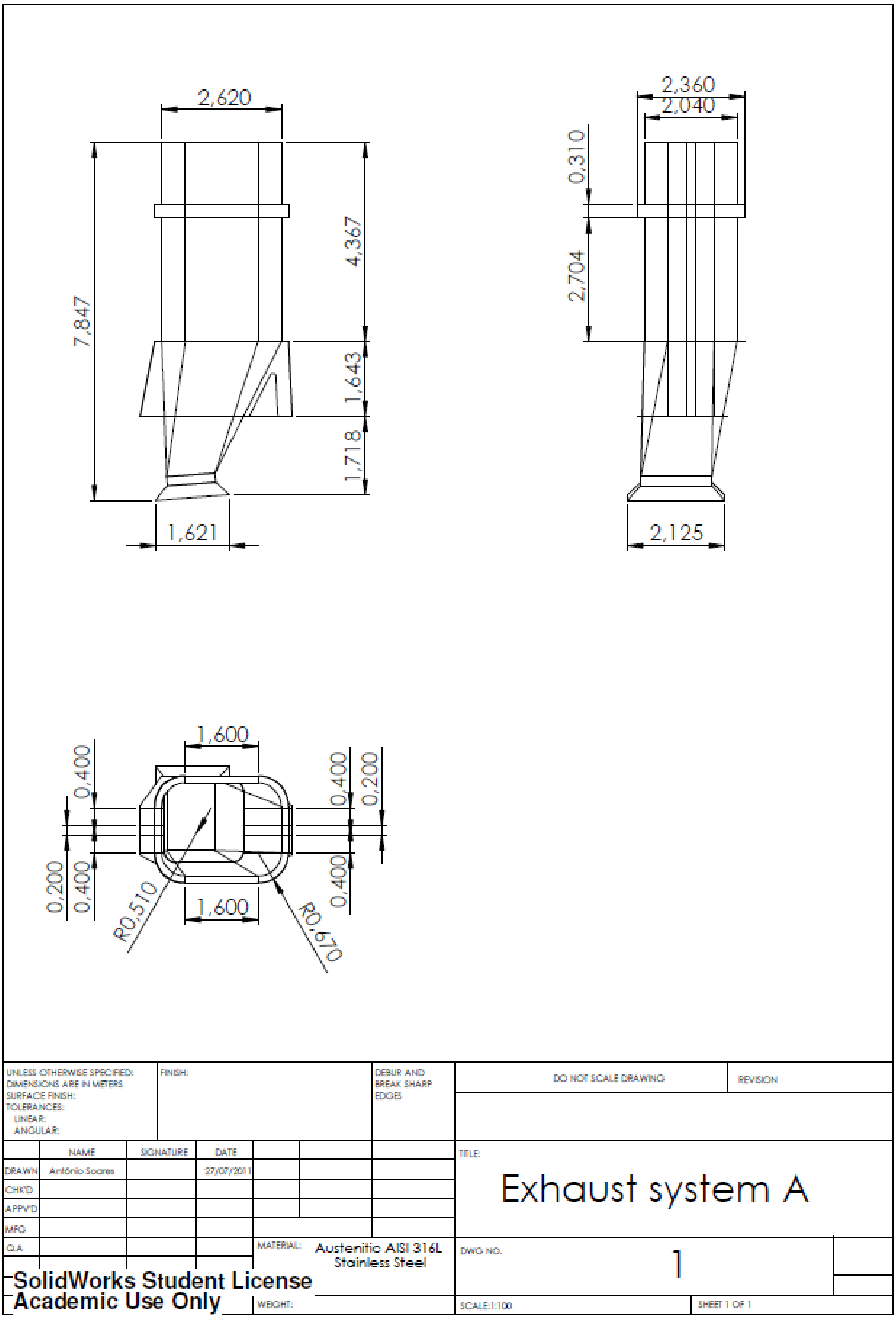

UNLESS OTHERWISE SPECIFIED:
DIMENSIONS ARE IN METERS
SURFACE FINISH:
TOLERANCES:
LINEAR:
ANGULAR:

FINISH:

DEBUR AND BREAK SHARP EDGES

DO NOT SCALE DRAWING

REVISION

	NAME	SIGNATURE	DATE
DRAWN	António Soares		27/07/2011
CHK'D			
APPV'D			
MFG			
Q.A			

TITLE: Exhaust system A

MATERIAL: Austenitic AISI 316L Stainless Steel

DWG NO. 1

WEIGHT:

SCALE:1:100

SHEET 1 OF 1

SolidWorks Student License
Academic Use Only

---

[1] This drawing was resized to fit the document borders. The scale presented in this technical drawing corresponds to a full A4 technical drawing.

A2: Technical drawing of exhaust system A lower and intermediate sections (dimensions in meters)[1]

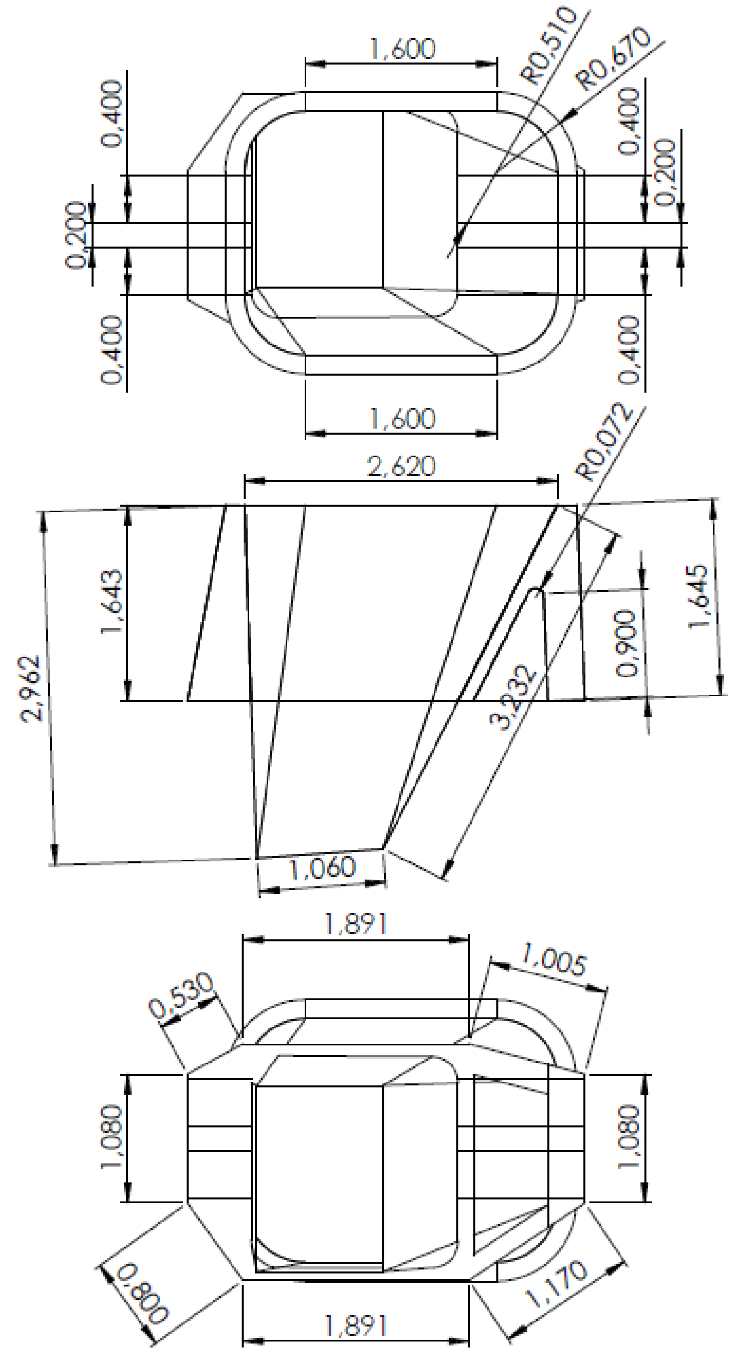

UNLESS OTHERWISE SPECIFIED:
DIMENSIONS ARE IN METERS
SURFACE FINISH:
TOLERANCES:
LINEAR:
ANGULAR:

FINISH:

DEBUR AND
BREAK SHARP
EDGES

DO NOT SCALE DRAWING

REVISION

	NAME	SIGNATURE	DATE
DRAWN	António Soares		27/07/2011
CHK'D			
APPV'D			
MFG			
Q.A			

MATERIAL: Austenitic AISI 316L
Stainless Steel

WEIGHT:

TITLE: Exhaust system A
(Lower and intermediate section)

DWG NO. 2

SCALE:1:50

SHEET 1 OF 1

---

[1] This drawing was resized to fit the document borders. The scale presented in this technical drawing corresponds to a full A4 technical drawing.

A3: Technical drawing of exhaust system B (dimensions in meters)[1]

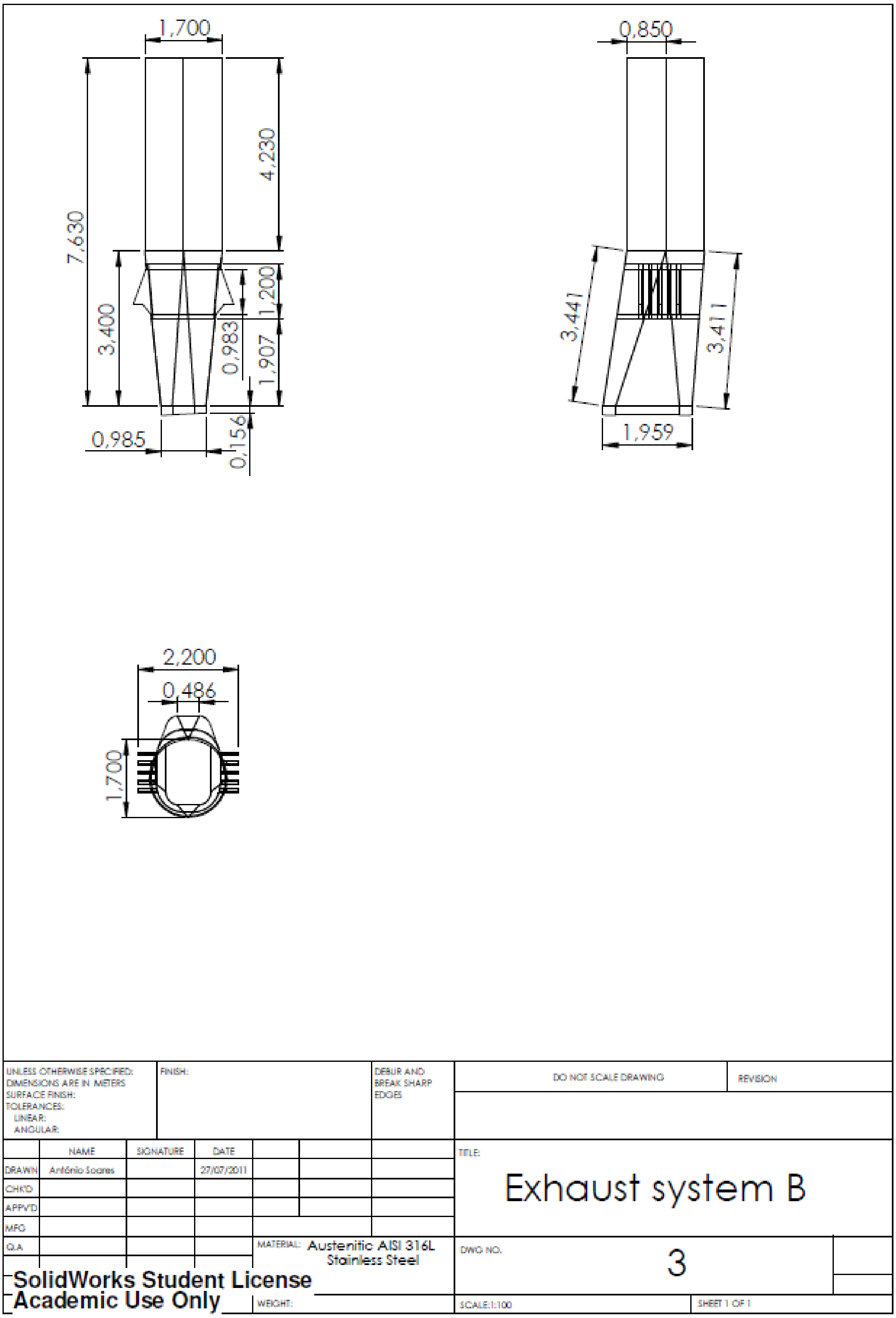

---

[1] This drawing was resized to fit the document borders. The scale presented in this technical drawing corresponds to a full A4 technical drawing.

A4: Technical drawing of exhaust system B lower and intermediate sections (dimensions in meters)[1]

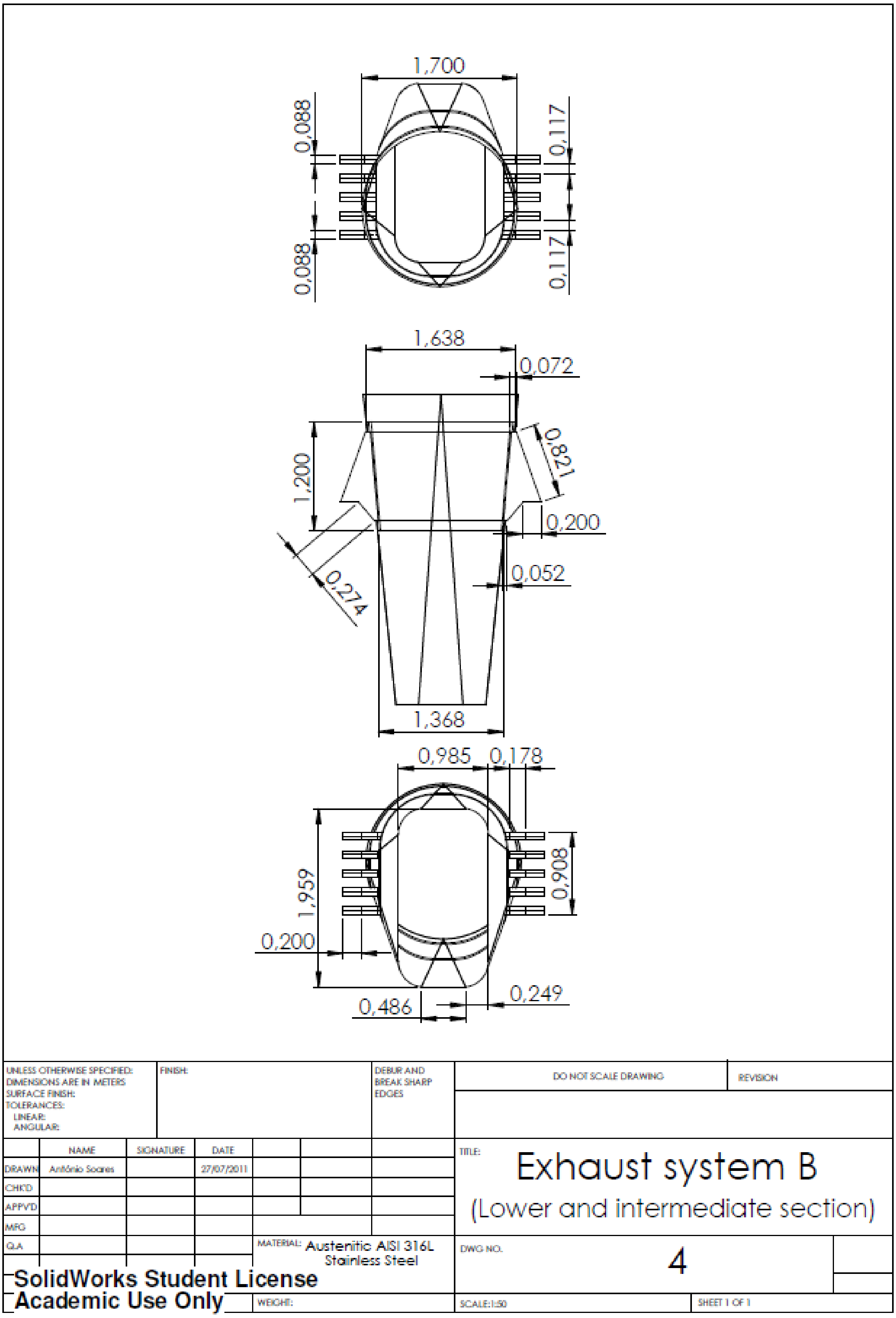

---

[1] This drawing was resized to fit the document borders. The scale presented in this technical drawing corresponds to a full A4 technical drawing.

A5: Technical drawing of exhaust system A with the addition of four vertical reinforcement rib (dimensions in meters)[1]

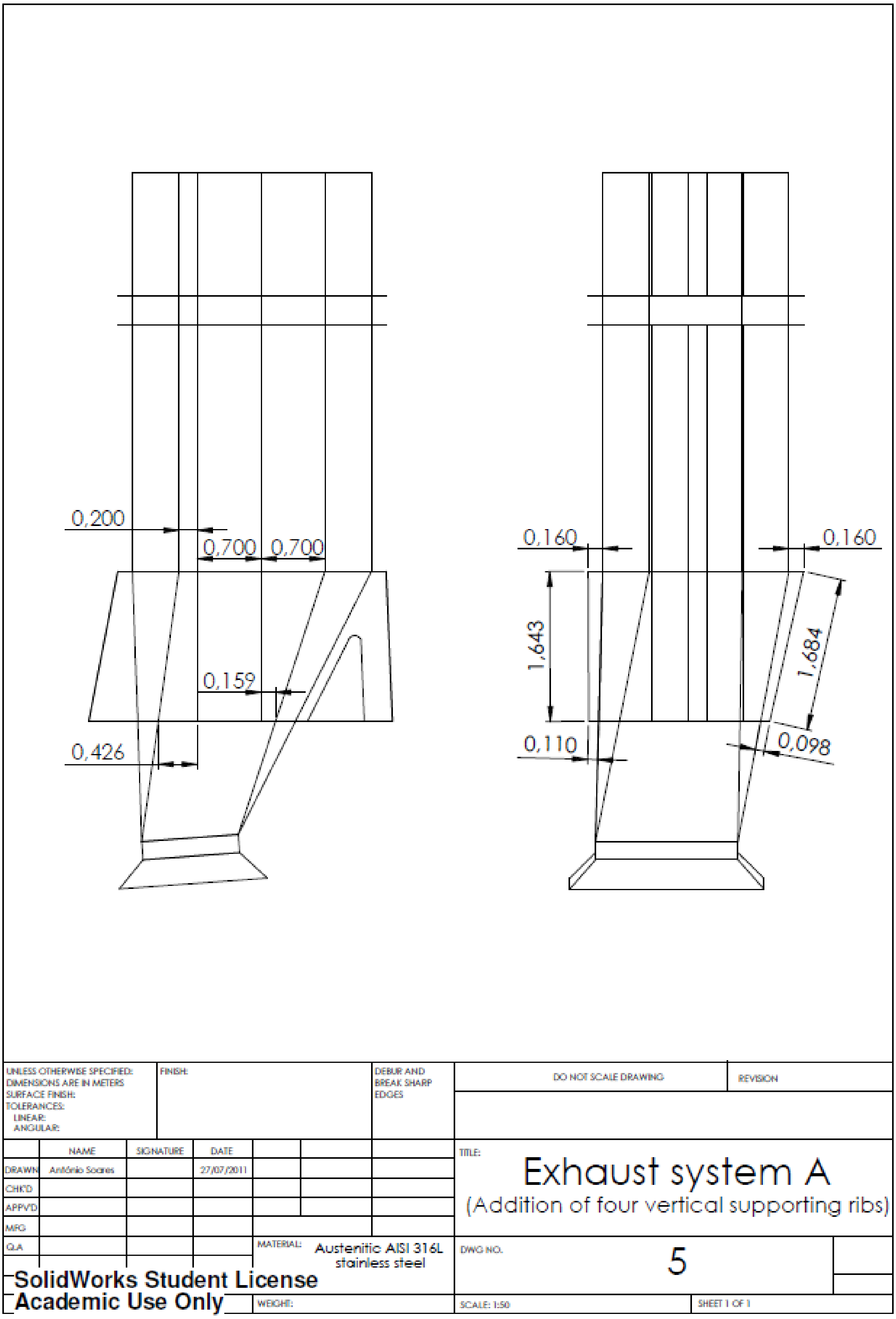

---

[1] This drawing was resized to fit the document borders. The scale presented in this technical drawing corresponds to a full A4 technical drawing.

A6: Technical drawing of exhaust system A with the addition of two vertical reinforcement rib (dimensions in meters)[1]

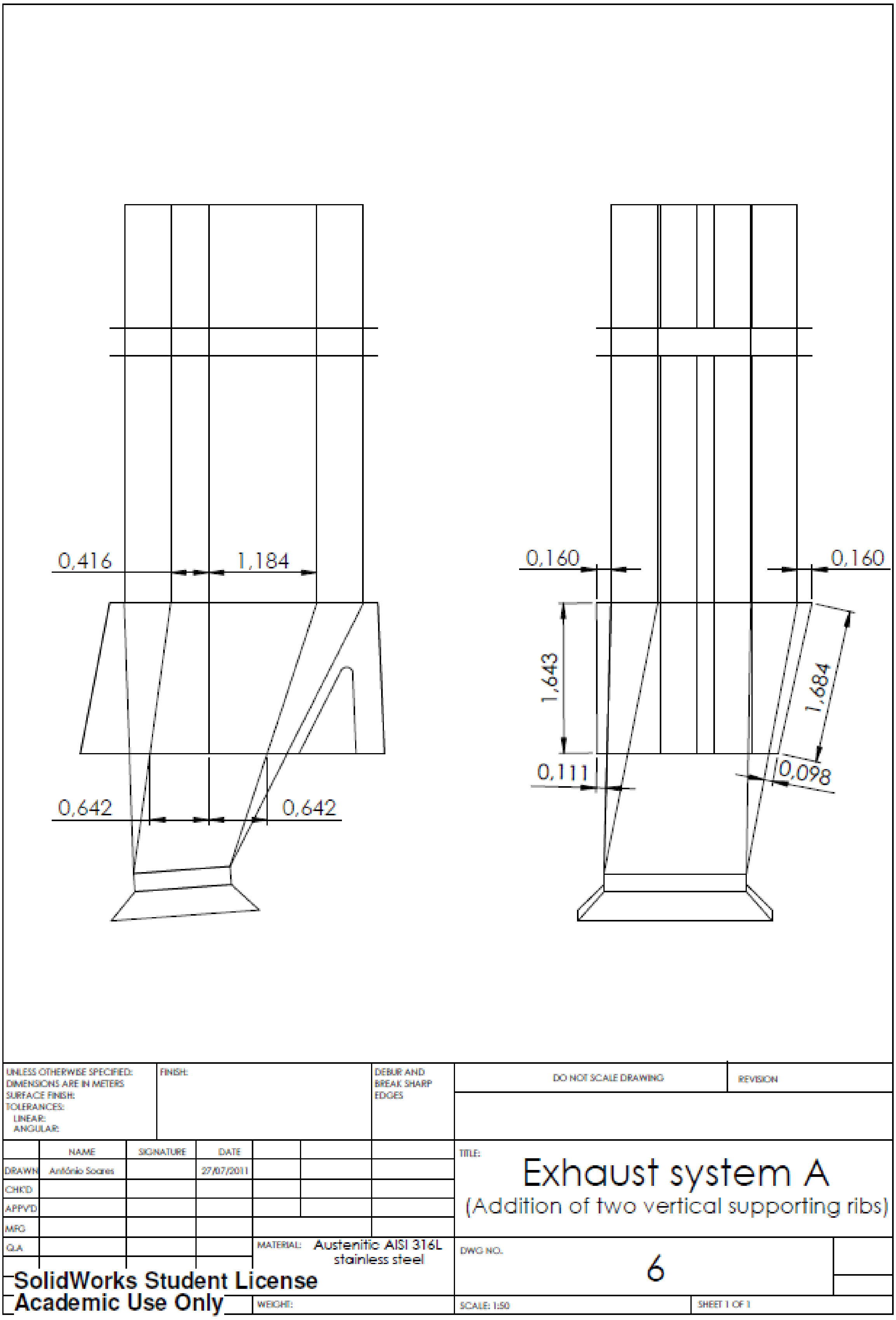

---

[1] This drawing was resized to fit the document borders. The scale presented in this technical drawing corresponds to a full A4 technical drawing.

A7: Technical drawing of exhaust system A with the addition of a horizontal supporting ring (dimensions in meters)[1]

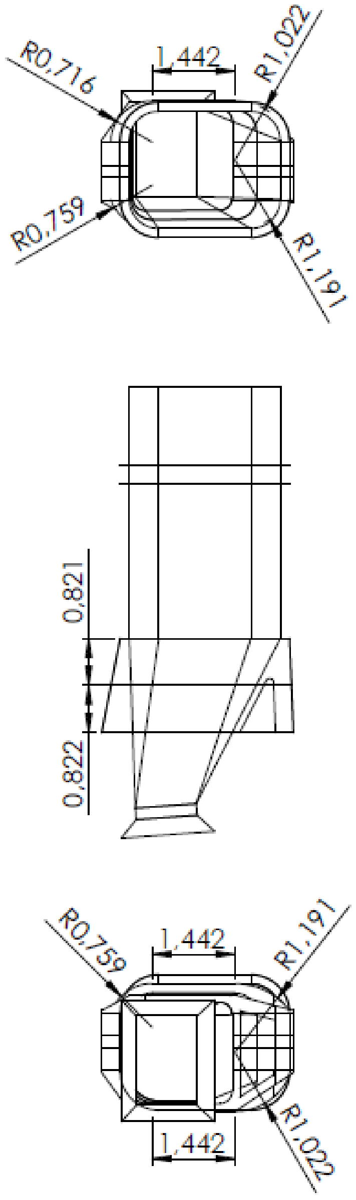

UNLESS OTHERWISE SPECIFIED:
DIMENSIONS ARE IN METERS
SURFACE FINISH:
TOLERANCES:
LINEAR:
ANGULAR:

FINISH:

DEBUR AND BREAK SHARP EDGES

DO NOT SCALE DRAWING

REVISION

	NAME	SIGNATURE	DATE
DRAWN	António Soares		27/07/2011
CHK'D			
APPV'D			
MFG			
Q.A			

MATERIAL: Austenitic AISI 316L stainless steel

WEIGHT:

TITLE: Exhaust system A (Addition of a horizontal supporting ring)

DWG NO. 7

SCALE:1:100

SHEET 1 OF 1

---

[1] This drawing was resized to fit the document borders. The scale presented in this technical drawing corresponds to a full A4 technical drawing.

X

X

Annex B – First principal stress distributions (graphics)

Figure B.1 shows the first principal stress distribution on the welded joint between the exhaust system pipe and the intermediate supporting ring (a) and on the welded joint between the exhaust system pipe and the lower supporting ring (b). These graphics were obtained through *Ansys*®, for normal in-service conditions (without the 2G deceleration) in the current geometry of exhaust system A made of the AISI 316L austenitic stainless steel.

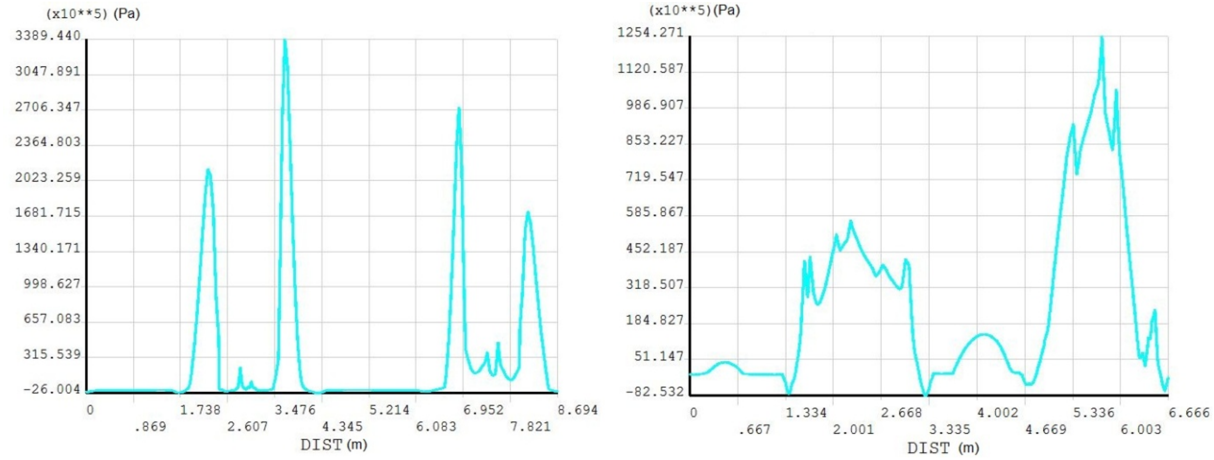

(a) (b)

Figure B.1: Intermediate supporting ring (a) and lower supporting ring (b) - Current geometry of exhaust system A – AISI 316L austenitic stainless steel

Figure B.2 shows the first principal stress distribution on the welded joint between the exhaust system pipe and the intermediate supporting ring (a) and on the welded joint between the exhaust system pipe and the lower supporting ring (b). These graphics were obtained through *Ansys*®, for normal in-service conditions (without the 2G deceleration) in the current geometry of exhaust system A made of the 445M2 ferritic stainless steel.

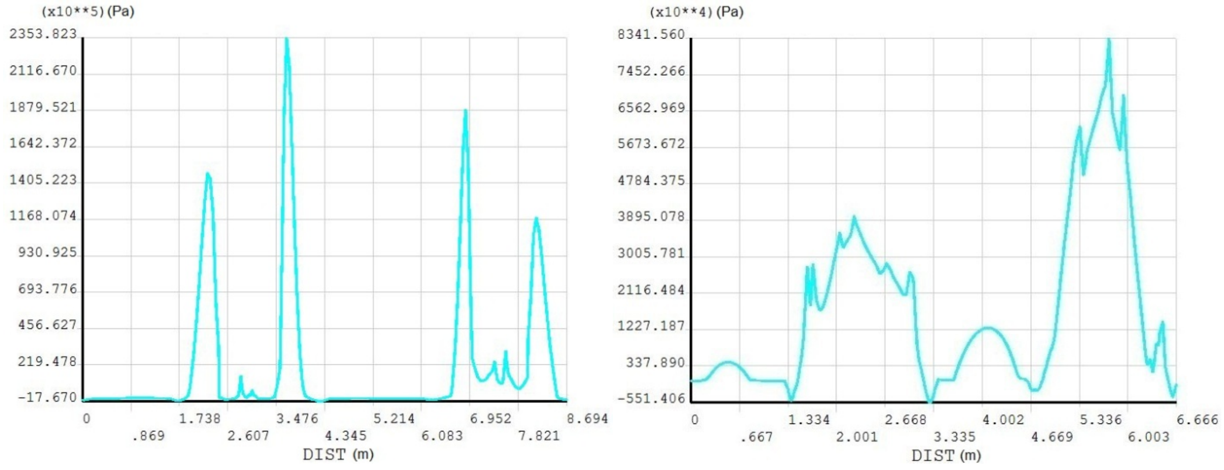

(a) (b)

Figure B.2: Intermediate supporting ring (a) and lower supporting ring (b) - Current geometry of exhaust system A – 445M2 ferritic stainless steel

Figure B.3 shows the first principal stress distribution on the welded joint between the exhaust system pipe and the intermediate supporting ring (a) and on the welded joint between the exhaust system pipe and the lower supporting ring (b). These graphics were obtained through *Ansys*®, for normal in-service conditions (without the 2G deceleration) in the modification where the thickness of the intermediate section of the exhaust system A pipe was changed from 4 mm to 12 mm. In this modification, the exhaust system was considered to be made of the AISI 316L austenitic stainless steel.

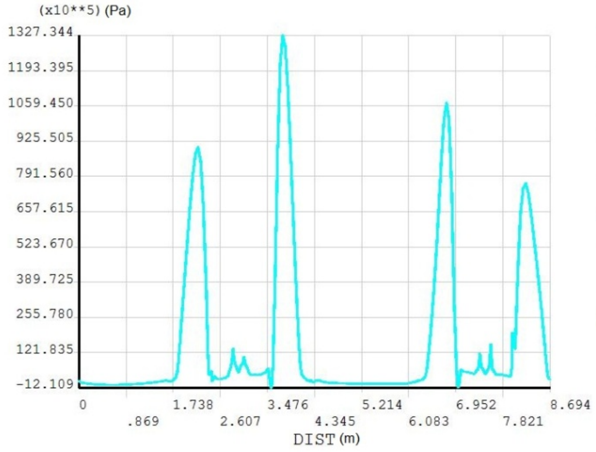

(a) (b)

Figure B.3: Intermediate supporting ring (a) and lower supporting ring (b) – Thickness change of the intermediate section of the exhaust system A pipe from 4 mm to 12 mm – AISI 316L austenitic stainless steel

Figure B.4 shows the first principal stress distribution on the welded joint between the exhaust system pipe and the intermediate supporting ring (a) and on the welded joint between the exhaust system pipe and the lower supporting ring (b). These graphics were obtained through *Ansys*®, for normal in-service conditions (without the 2G deceleration) in the modification where the thickness of the intermediate section of the exhaust system A pipe was changed from 4 mm to 12 mm. In this modification, the exhaust system was considered to be made of the 445M2 ferritic stainless steel.

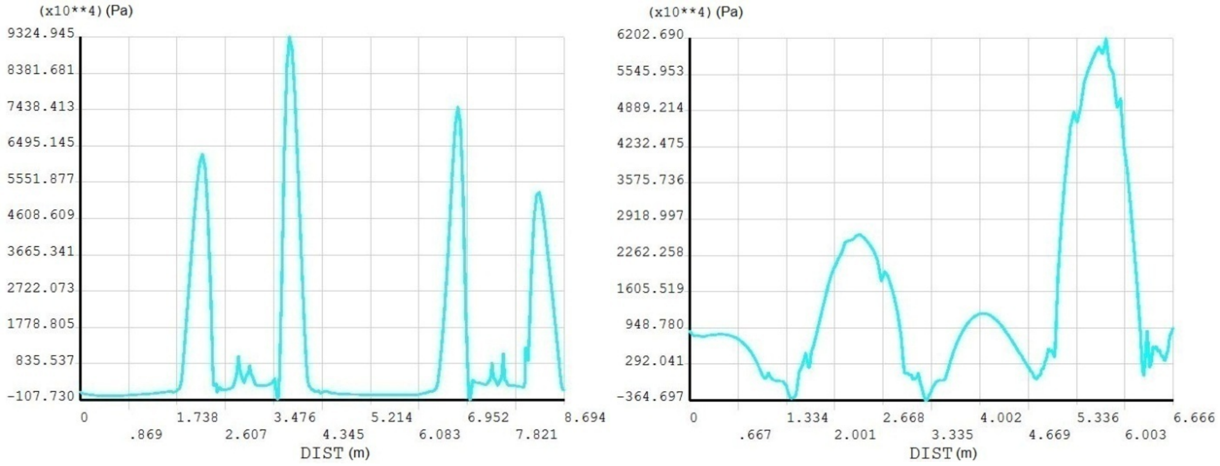

(a) (b)

Figure B.4: Intermediate supporting ring (a) and lower supporting ring (b) - Thickness change of the intermediate section of the exhaust system A pipe from 4 mm to 12 mm – 445M2 ferritic stainless steel

Figure B.5 shows the first principal stress distribution on the welded joints between the doubler plates and the upper flanges of the right and left side reinforcement ribs (a) and on the welded joints between the doubler plates and the lower flanges of the right and left side reinforcement ribs (b). These graphics were obtained through *Ansys*®, for normal in-service conditions (without the 2G deceleration) in the current geometry of exhaust system B made of the AISI 316L austenitic stainless steel.

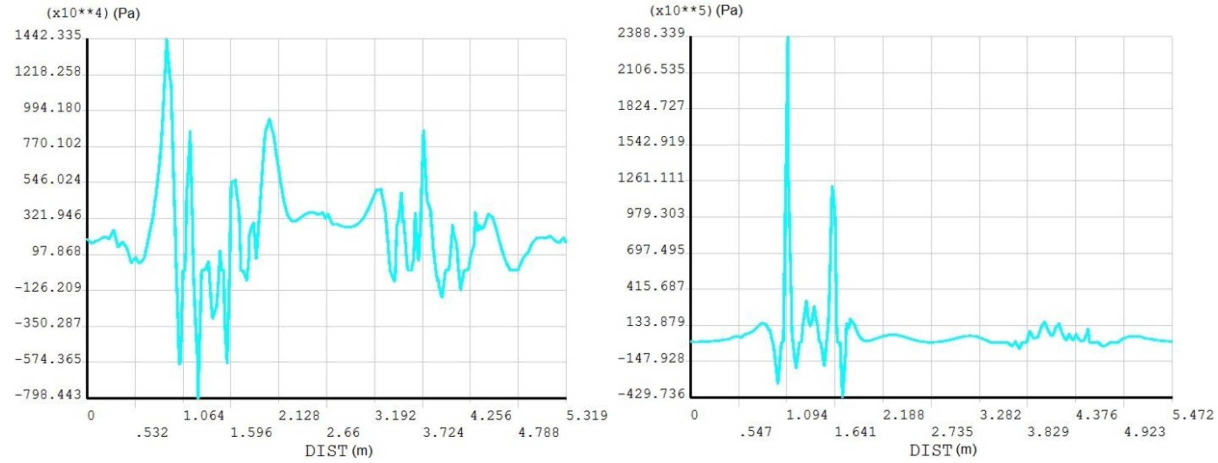

(a) (b)

Figure B.5: Upper flanges (a) and lower flanges (b) - Current geometry of exhaust system B – AISI 316L austenitic stainless steel

Figure B.6 shows the first principal stress distribution on the welded joints between the doubler plates and the upper flanges of the right and left side reinforcement ribs (a) and on the welded joints between the doubler plates and the lower flanges of the right and left side reinforcement ribs (b). These graphics were obtained through *Ansys*®, for normal in-service conditions (without the 2G deceleration) in the current geometry of exhaust system B made of the 445M2 ferritic stainless steel.

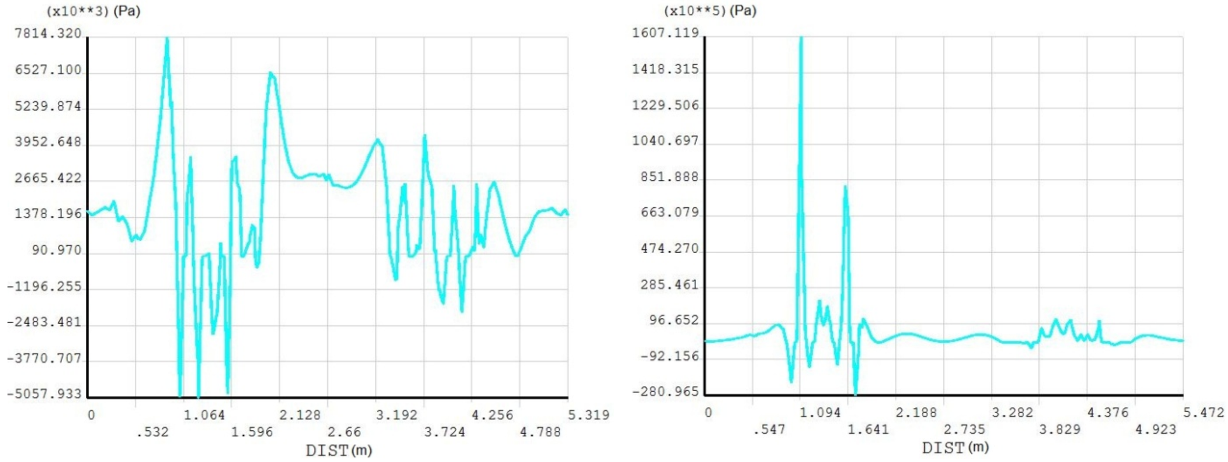

(a) (b)

Figure B.6: Upper flanges (a) and lower flanges (b) - Current geometry of exhaust system B – 445M2 ferritic stainless steel

Figure B.7 shows the first principal stress distribution on the welded joints between the doubler plates and the upper flanges of the right and left side reinforcement ribs (a) and on the welded joints between the doubler plates and the lower flanges of the right and left side reinforcement ribs (b). These graphics were obtained through *Ansys*®, for normal in-service conditions (without the 2G deceleration) in the modification where the thicknesses of all the exhaust system B plates were changed to 12 mm. In this modification, the exhaust system was considered to be made of the austenitic 316L stainless steel.

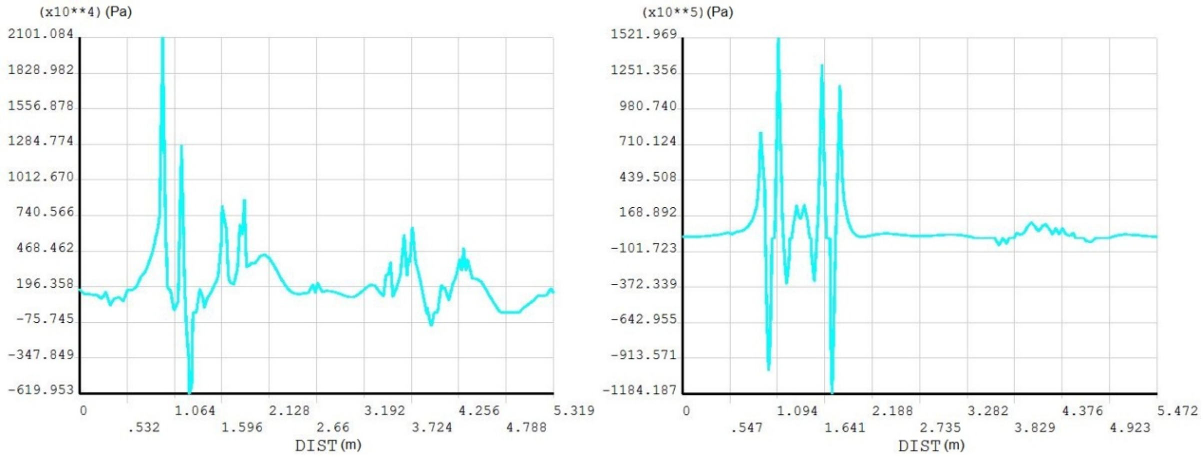

(a) (b)

Figure B.7: Upper flanges (a) and lower flanges (b) – Thickness change of all the exhaust system B plates to 12 mm – AISI 316L austenitic stainless steel

Figure B.8 shows the first principal stress distribution on the welded joints between the doubler plates and the upper flanges of the right and left side reinforcement ribs (a) and on the welded joints between the doubler plates and the lower flanges of the right and left side reinforcement ribs (b). These graphics were obtained through *Ansys*®, for normal in-service conditions (without the 2G deceleration) in the modification where the thicknesses of all the exhaust system B plates were changed to 12 mm. In this modification, the exhaust system was considered to be made of the 445M2 ferritic stainless steel.

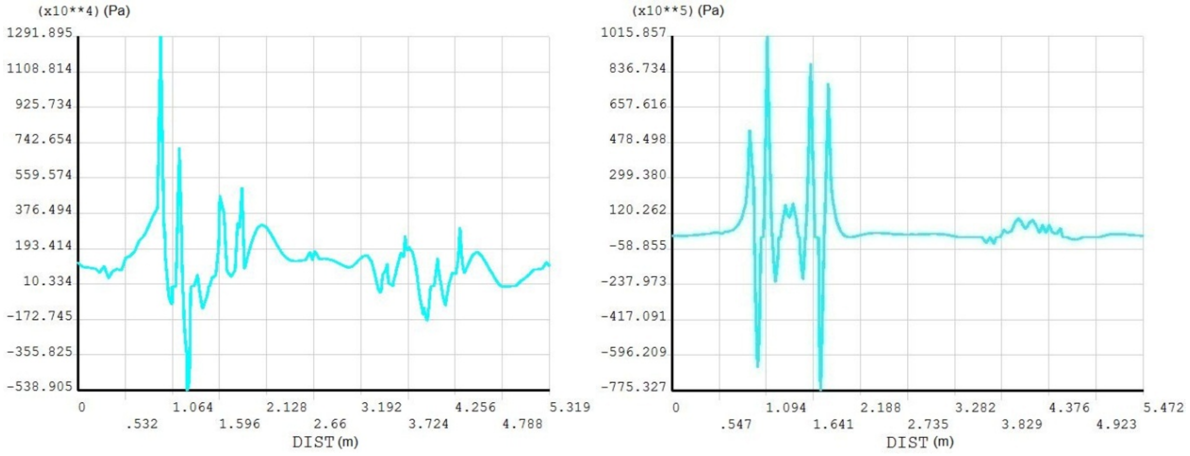

(a) (b)

Figure B.8: Upper flanges (a) and lower flanges (b) - Thickness change of all the exhaust system B plates to 12 mm – 445M2 ferritic stainless steel

Annex C – Exhaust system A – First principal stress results for overload conditions (without 2G deceleration)

Structural detail no. 234:

Table C.1 shows the maximum first principal nodal stress values obtained in the butt welds that join the sections of the exhaust system's pipe which have equal wall thicknesses and are welded in regions near the intermediate supporting ring and to the lower supporting ring (detail no. 234 - chapter 6.1). These maximum first principal nodal stress values were obtained for the overload condition (with the 2G deceleration) in the current geometry of exhaust system A and in the selected modifications made to exhaust system A (chapter 8.1.1), for both AISI 316L austenitic stainless steel and 445M2 ferritic stainless steel.

Table C.1: First principal stress values actuating on detail no. 234 in each modification made to exhaust system A – overload conditions (with 2G deceleration)

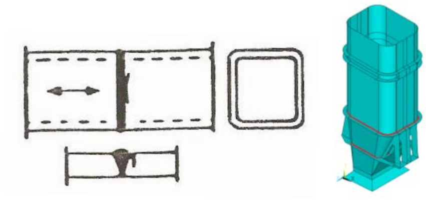	**Material type**			
	AISI 316L austenitic stainless steel		**445M2 ferritic stainless steel**	
	Intermediate supporting ring (MPa)	**Lower supporting ring (MPa)**	**Intermediate supporting ring (MPa)**	**Lower supporting ring (MPa)**
Current geometry	340	118	236	76
Thickness change of the vertical reinforcement ribs to 4 mm	209	98	149	64
Thickness change of all the exhaust system plates to 4 mm	155	89	110	55
Thickness change of all the exhaust system plates to 12 mm	134	99	94	64
Removal of the inner vertical reinforcement ribs	314	93	222	60

Structural detail no. 223:

Table C.2 shows the maximum first principal nodal stress values obtained in the butt welds of sections of the exhaust system's pipe which could have, in the future, different wall thicknesses (redesigned structure) and are located near to the intermediate supporting ring and near to the lower supporting ring (detail no. 223 - chapter 6.1). These maximum first principal nodal stress values were obtained for the overload condition (without the 2G deceleration) in the current geometry of exhaust system A and in the selected modifications made to exhaust system A (chapter 8.1.1), for both AISI 316L austenitic stainless steel and 445M2 ferritic stainless steel.

Table C.2: First principal stress values actuating on detail no. 223 in each modification made to exhaust system A – overload conditions (with 2G deceleration)

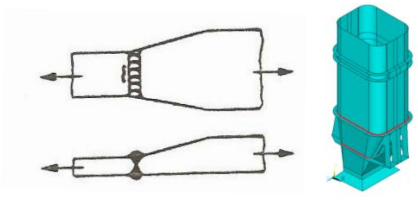	**Material type**			
	AISI 316L austenitic stainless steel		**445M2 ferritic stainless steel**	
	Intermediate supporting ring (MPa)	**Lower supporting ring (MPa)**	**Intermediate supporting ring (MPa)**	**Lower supporting ring (MPa)**
Thickness change of the intermediate section of the exhaust system pipe from 4 mm to 12 mm	130	83	91	54

Structural detail no. 323:

Tables C.3 shows the maximum first principal nodal stress values obtained in the welded joints between the exhaust system's pipe and right side reinforcement ribs (detail no. 323 - chapter 6.1). These maximum first principal nodal stress values were obtained for the overload condition (with the 2G deceleration) in the current geometry of exhaust system A and in the selected modifications made to exhaust system A (chapter 8.1.1), for both AISI 316L austenitic stainless steel and 445M2 ferritic stainless steel.

The reinforcement ribs were numbered according to their position in exhaust system A, being the first reinforcement rib, the one seen in the front view of exhaust system A.

Table C.3: First principal stress values actuating on detail no. 323 in each modification made to exhaust system A – right side reinforcement ribs - overload conditions (with 2G deceleration)

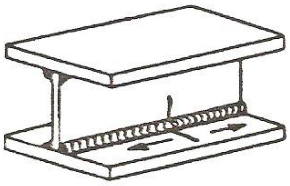 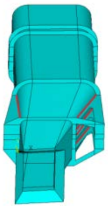	**Material type**			
	AISI 316L austenitic stainless steel			
	1st reinf. rib (MPa)	**2nd reinf. rib (MPa)**	**3rd reinf. rib (MPa)**	**4th reinf. rib (MPa)**
Current geometry	236	120	113	301
Thickness change of the intermediate section of the exhaust system pipe from 4 mm to 12 mm	84	77	76	121
Thickness change of the vertical reinforcement ribs to 4 mm	111	78	79	148
Thickness change of all the exhaust system plates to 4 mm	89	75	77	126
Thickness change of all the exhaust system plates to 12 mm	83	79	79	123
Removal of the inner vertical reinforcement ribs	181	---	---	234

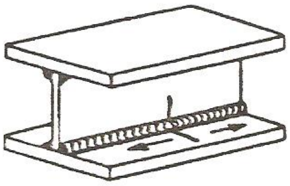 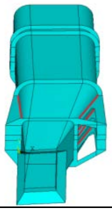	**Material type**			
	445M2 ferritic stainless steel			
	1st reinf. rib (MPa)	**2nd reinf. rib (MPa)**	**3rd reinf. rib (MPa)**	**4th reinf. rib (MPa)**
Current geometry	164	83	78	208
Thickness change of the intermediate section of the exhaust system pipe from 4 mm to 12 mm	61	53	52	87
Thickness change of the vertical reinforcement ribs to 4 mm	80	54	55	105
Thickness change of all the exhaust system plates to 4 mm	64	52	52	90
Thickness change of all the exhaust system plates to 12 mm	60	54	55	88
Removal of the inner vertical reinforcement ribs	129	---	---	165

Tables C.4 shows the maximum first principal nodal stress values obtained in the welded joints between the exhaust system's pipe and leftside reinforcement ribs (detail no. 323 - chapter 6.1). These maximum first principal nodal stress values were obtained for the overload condition (with the 2G deceleration) in the current geometry of exhaust system A and in the selected modifications made to exhaust system A (chapter 8.1.1), for both AISI 316L austenitic stainless steel and 445M2 ferritic stainless steel.

The reinforcement ribs were numbered according to their position in exhaust system A, being the first reinforcement rib, the one seen in the front view of exhaust system A.

Table C.4: First principal stress values actuating on detail no. 323 in each modification made to exhaust system A – left side reinforcement ribs - overload conditions (with 2G deceleration)

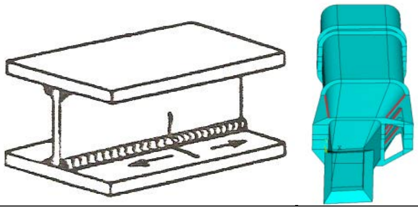	**Material type**			
	AISI 316L austenitic stainless steel			
	1st reinf. rib (MPa)	**2nd reinf. rib (MPa)**	**3rd reinf. rib (MPa)**	**4th reinf. rib (MPa)**
Current geometry	211	132	142	278
Thickness change of the intermediate section of the exhaust system pipe from 4 mm to 12 mm	160	100	106	113
Thickness change of the vertical reinforcement ribs to 4 mm	120	125	149	167
Thickness change of all the exhaust system plates to 4 mm	104	139	156	154
Thickness change of all the exhaust system plates to 12 mm	94	137	156	147
Removal of the inner vertical reinforcement ribs	174	---	---	234
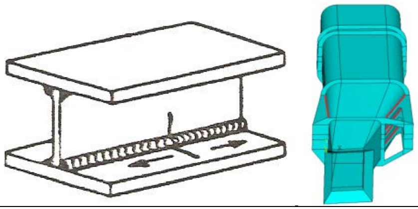	**Material type**			
	445M2 ferritic stainless steel			
	1st reinf. rib (MPa)	**2nd reinf. rib (MPa)**	**3rd reinf. rib (MPa)**	**4th reinf. rib (MPa)**
Current geometry	147	88	92	191
Thickness change of the intermediate section of the exhaust system pipe from 4 mm to 12 mm	115	66	70	80
Thickness change of the vertical reinforcement ribs to 4 mm	85	82	98	116
Thickness change of all the exhaust system plates to 4 mm	73	95	105	107
Thickness change of all the exhaust system plates to 12 mm	67	91	105	103
Removal of the inner vertical reinforcement ribs	122	---	---	162

Structural detail no. 822:

Table C.5 shows the maximum first principal nodal stress values obtained in the welded joint between the exhaust system's pipe and the intermediate supporting ring, considering that the intermediate supporting ring, that has a thickness of 30 mm, is infact two 15 mm thick flanges, that are bolted together(detail no. 822 - chapter 6.1). The aforementioned was done, in order to simulate the real conditions of the intermediate supporting ring. These maximum first principal nodal stress values were obtained for the overload condition (with the 2G deceleration) in the current geometry of exhaust system A and in the selected modifications made to exhaust system A (chapter 8.1.1), for both AISI 316L austenitic stainless steel and 445M2 ferritic stainless steel.

Table C.5: First principal stress values actuating on detail no. 822 in each modification made to exhaust system A – overload conditions (with 2G deceleration)

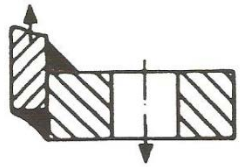 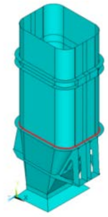	**Material type**	
	AISI 316L austenitic stainless steel	**445M2 ferritic stainless steel**
	Intermediate supporting ring (MPa)	**Intermediate supporting ring (MPa)**
Current geometry	340	236
Thickness change of the intermediate section of the exhaust system pipe from 4 mm to 12 mm	130	91
Thickness change of the vertical reinforcement ribs to 4 mm	209	149
Thickness change of all the exhaust system plates to 4 mm	155	110
Thickness change of all the exhaust system plates to 12 mm	134	94
Removal of the inner vertical reinforcement ribs	314	222

Annex D – Exhaust system B – First principal stress results for overload conditions (without 2G deceleration)

Structural detail no. 232:

Table D.1 shows the maximum first principal nodal stress values obtained in the welds that join the sections of the exhaust system's pipe which have equal wall thicknesses and are welded in regions near to the upper and lower ends of the doubler plates (detail no. 232 - chapter 6.2). These maximum first principal nodal stress values were obtained for the overload condition (with the 2G deceleration) in the current geometry of exhaust system B and in the selected modifications made to exhaust system B (chapter 8.1.2), for both AISI 316L austenitic stainless steel and 445M2 ferritic stainless steel.

Table D.1: First principal stress values actuating on detail no. 232 in each modification made to exhaust system B – overload conditions (with 2G deceleration)

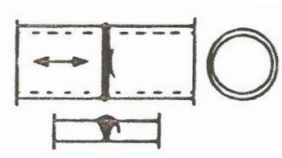 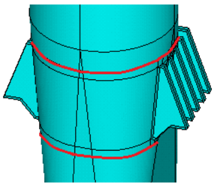	**Material type**			
	AISI 316L austenitic stainless steel		**445M2 ferritic stainless steel**	
	Upper end (MPa)	**Lower end (MPa)**	**Upper end (MPa)**	**Lower end (MPa)**
Current geometry	231	263	212	255
Thickness change of all the exhaust system plates to 4 mm	91	152	88	146
Thickness change of all the exhaust system plates to 12 mm	42	95	40	89

Structural detail no. 223:

Table D.2 shows the maximum first principal nodal stress values obtained in the butt welds of sections of the exhaust system's pipe that could have, in the future, different wall thicknesses (redesigned strutcture) and are located near to the upper and lower ends of the doubler plates (detail no. 223 - chapter 6.2). These maximum first principal nodal stress values were obtained for the overload condition (with the 2G deceleration) in the current geometry of exhaust system B and in the selected modifications made to exhaust system B (chapter 8.1.2), for both AISI 316L austenitic stainless steel and 445M2 ferritic stainless steel.

Table D.2: First principal stress values actuating on detail no. 223 in each modification made to exhaust system B – overload conditions (with 2G deceleration)

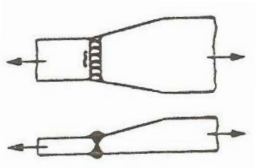 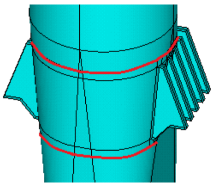	**Material type**			
	AISI 316L austenitic stainless steel		**445M2 ferritic stainless steel**	
	Upper end (MPa)	**Lower end (MPa)**	**Upper end (MPa)**	**Lower end (MPa)**
Thickness change of the intermediate section of the exhaust system pipe from 4 mm to 12 mm	36	86	33	80

Structural detail no. 323:

Table D.3 shows the maximum first principal nodal stress values obtained in the welded joints between the doubler plates and the right side reinforcement ribs (detail no. 323 - chapter 6.2). These maximum first principal nodal stress values were obtained for the overload condition (with the 2G deceleration) in the current geometry of exhaust system B and in the selected modifications made to exhaust system B (chapter 8.1.2), for both AISI 316L austenitic stainless steel and 445M2 ferritic stainless steel.

The reinforcement ribs were numbered according to their position in exhaust system B, being the first reinforcement rib, the one seen in the front view of exhaust system B.

Table D.3: First principal stress values actuating on detail no. 323 in each modification made to exhaust system B – right side reinforcement ribs - overload conditions (with 2G deceleration)

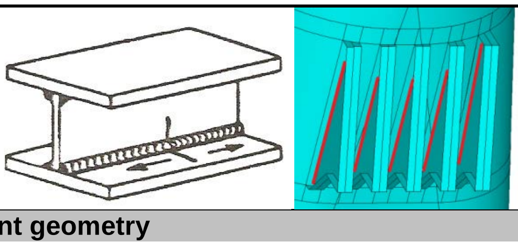	**Material type**				
	AISI 316L austenitic stainless steel				
	1st reinf. rib (MPa)	**2nd reinf. rib (MPa)**	**3rd reinf. rib (MPa)**	**4th reinf. rib (MPa)**	**5th reinf. rib (MPa)**
Current geometry	40	24	11	10	12
Thickness change of the intermediate section of the exhaust system pipe from 4 mm to 12 mm	79	40	11	16	39
Thickness change of all the exhaust system plates to 4 mm	87	27	16	14	56
Thickness change of all the exhaust system plates to 12 mm	89	46	11	13	36
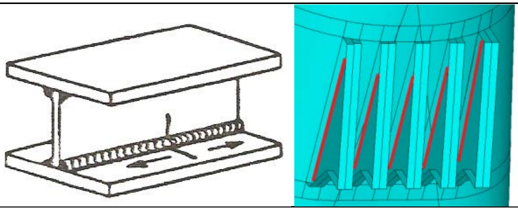	**Material type**				
	445M2 ferritic stainless steel				
	1st reinf. rib (MPa)	**2nd reinf. rib (MPa)**	**3rd reinf. rib (MPa)**	**4th reinf. rib (MPa)**	**5th reinf. rib (MPa)**
Current geometry	31	16	7	6	12
Thickness change of the intermediate section of the exhaust system pipe from 4 mm to 12 mm	60	25	8	10	26
Thickness change of all the exhaust system plates to 4 mm	71	19	16	14	56
Thickness change of all the exhaust system plates to 12 mm	66	29	9	10	28

Table D.4 shows the maximum first principal nodal stress values obtained in the welded joints between the doubler plates and the left side reinforcement ribs (detail no. 323 - chapter 6.2). These maximum first principal nodal stress values were obtained for the overload condition (with the 2G deceleration) in the current geometry of exhaust system B and in the selected modifications made to exhaust system B (chapter 8.1.2), for both AISI 316L austenitic stainless steel and 445M2 ferritic stainless steel.

The reinforcement ribs were numbered according to their position in exhaust system B, being the first reinforcement rib, the one seen in the front view of exhaust system B.

Table D.4: First principal stress values actuating on detail no. 323 in each modification made to exhaust system B– left side reinforcement ribs - overload conditions (with 2G deceleration)

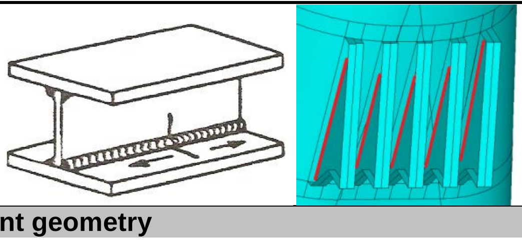	Material type				
	AISI 316L austenitic stainless steel				
	1st reinf. rib (MPa)	2nd reinf. rib (MPa)	3rd reinf. rib (MPa)	4th reinf. rib (MPa)	5th reinf. rib (MPa)
Current geometry	11	8	15	16	10
Thickness change of the intermediate section of the exhaust system pipe from 4 mm to 12 mm	16	16	17	19	18
Thickness change of all the exhaust system plates to 4 mm	11	13	19	22	19
Thickness change of all the exhaust system plates to 12 mm	6	6	8	10	5
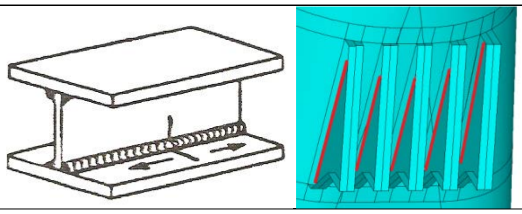	Material type				
	445M2 ferritic stainless steel				
	1st reinf. rib (MPa)	2nd reinf. rib (MPa)	3rd reinf. rib (MPa)	4th reinf. rib (MPa)	5th reinf. rib (MPa)
Current geometry	10	7	15	15	10
Thickness change of the intermediate section of the exhaust system pipe from 4 mm to 12 mm	15	15	17	18	19
Thickness change of all the exhaust system plates to 4 mm	10	12	19	21	19
Thickness change of all the exhaust system plates to 12 mm	4	5	7	8	5

Structural details no. 712 and no. 721:

Table D.5 shows the maximum first principal nodal stress values obtained in the welded joints between the exhaust system's pipe and the upper ends of the right doubler plates and the welded joints between the exhaust system's pipe and the lower ends of the right doubler plates (details no. 712 and no. 721 - chapter 6.2). These maximum first principal nodal stress values were obtained for the overload condition (with the 2G deceleration) in the current geometry of exhaust system B and in the selected modifications made to exhaust system B (chapter 8.1.2), for both AISI 316L austenitic stainless steel and 445M2 ferritic stainless steel.

The doubler plates were numbered according to their position in exhaust system B, being the first reinforcement plate, the one seen in the front view of exhaust system B. The first principal nodal stress values presented in table D.5, are the values obtained for the upper and for the lower ends of the doubler plates, respectively.

Table D.5: First principal stress values actuating on details no. 712 and no. 721 in each modification made to exhaust system B – upper and lower ends of the right side doubler plates - overload conditions (with 2G deceleration)

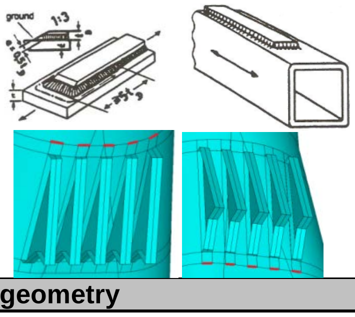	Material type				
	AISI 316L austenitic stainless steel				
	1st doubler plate (MPa)	2nd doubler plate (MPa)	3rd doubler plate (MPa)	4th doubler plate (MPa)	5th doubler plate (MPa)
Current geometry	171/263	62/62	36/56	63/91	231/142

Thickness change of the intermediate section of the exhaust system pipe from 4 mm to 12 mm	27/56	18/9	7/16	23/22	26/46
Thickness change of all the exhaust system plates to 4 mm	47/153	39/4	10/14	91/11	50/102
Thickness change of all the exhaust system plates to 12 mm	30/95	26/25	15/7	42/26	36/77
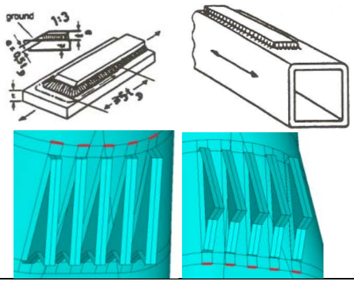	**Material type** **445M2 ferritic stainless steel**				
	1st doubler plate (MPa)	**2nd doubler plate (MPa)**	**3rd doubler plate (MPa)**	**4th doubler plate (MPa)**	**5th doubler plate (MPa)**
Current geometry	153/255	44/26	35/43	58/46	212/129
Thickness change of the intermediate section of the exhaust system pipe from 4 mm to 12 mm	25/56	17/6	7/12	22/14	23/45
Thickness change of all the exhaust system plates to 4 mm	45/146	36/0	9/11	89/2	47/97
Thickness change of all the exhaust system plates to 12 mm	26/89	24/21	13/5	40/19	31/69

Table D.6 shows the maximum first principal nodal stress values obtained in the welded joints between the exhaust system's pipe and the upper ends of the left doubler plates and the welded joints between the exhaust system's pipe and the lower ends of the left doubler plates (details no. 712 and no. 721 - chapter 6.2). These maximum first principal nodal stress values were obtained for the overload condition (with the 2G deceleration) in the current geometry of exhaust system B and in the selected modifications made to exhaust system B (chapter 8.1.2), for both AISI 316L austenitic stainless steel and 445M2 ferritic stainless steel.

The doubler plates were numbered according to their position in exhaust system B, being the first reinforcement plate, the one seen in the front view of exhaust system B. The first principal nodal stress values presented in table D.6, are the values obtained for the upper and for the lower ends of the doubler plates, respectively.

Table D.6: First principal stress values actuating on details no. 712 and no. 721 in each modification made to exhaust system B – upper and lower ends of the left side doubler plates - overload conditions (with 2G deceleration)

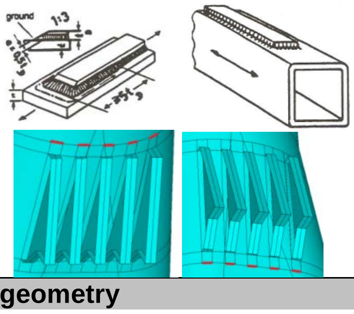	**Material type** **AISI 316L austenitic stainless steel**				
	1st doubler plate (MPa)	**2nd doubler plate (MPa)**	**3rd doubler plate (MPa)**	**4th doubler plate (MPa)**	**5th doubler plate (MPa)**
Current geometry	44/57	61/43	68/79	58/60	36/80
Thickness change of the intermediate section of the exhaust system pipe from 4 mm to 12 mm	16/29	22/23	32/22	25/16	6/13
Thickness change of all the exhaust system plates to 4 mm	11/22	19/31	37/43	61/29	16/38
Thickness change of all the exhaust system plates to 12 mm	9/2	13/16	19/28	21/23	13/8

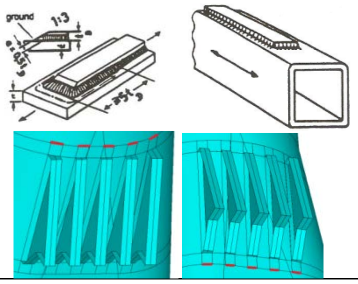	Material type				
	445M2 ferritic stainless steel				
	1st doubler plate (MPa)	**2nd doubler plate (MPa)**	**3rd doubler plate (MPa)**	**4th doubler plate (MPa)**	**5th doubler plate (MPa)**
Current geometry	43/63	56/47	62/74	56/57	29/82
Thickness change of the intermediate section of the exhaust system pipe from 4 mm to 12 mm	14/30	19/24	29/20	23/14	5/14
Thickness change of all the exhaust system plates to 4 mm	11/23	17/32	35/41	60/28	15/38
Thickness change of all the exhaust system plates to 12 mm	8/5	10/15	16/26	20/22	10/10